Martin Gotter

Fusion and Fission of Fluid Amphiphilic Bilayers: a Kinetic Study

Dissertation

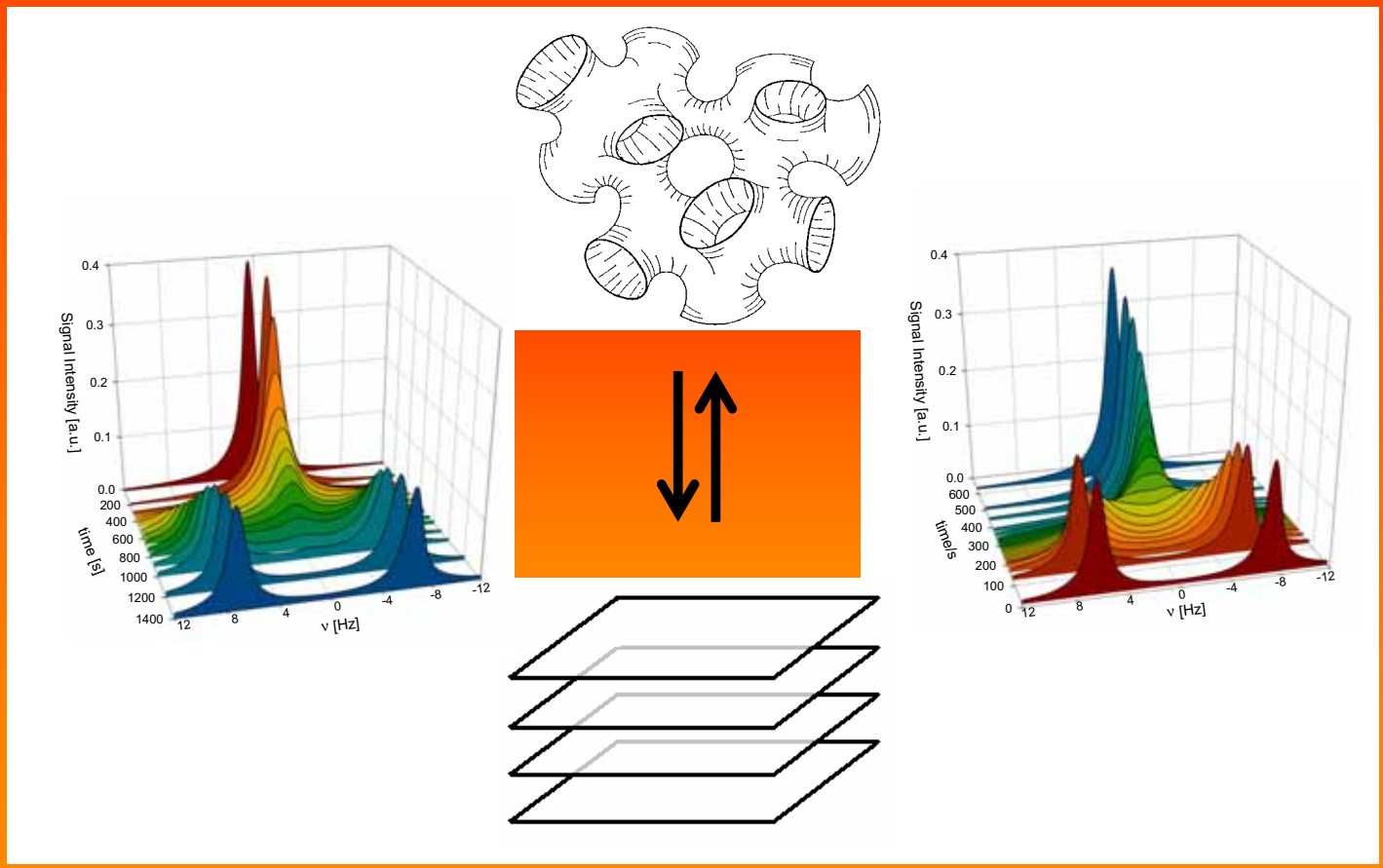

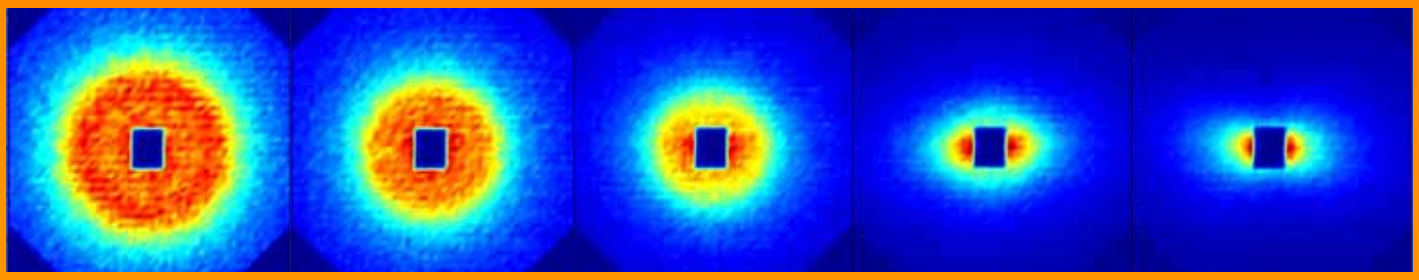

Cuvillier Verlag Göttingen

Fusion and Fission of Fluid Amphiphilic Bilayers: a Kinetic Study

Inaugural-Dissertation

zur

Erlangung des Doktorgrades

der Mathematisch-Naturwissenschaftlichen Fakultät

der Universität zu Köln

vorgelegt von

Martin Gotter

aus Bonn

Köln 2006

Bibliografische Information Der Deutschen Bibliothek
Die Deutsche Bibliothek verzeichnet diese Publikation in der Deutschen Nationalbibliografie; detaillierte bibliografische Daten sind im Internet über http://dnb.ddb.de abrufbar.
1. Aufl. - Göttingen : Cuvillier, 2007
Zugl.: Köln, Univ., Diss., 2006

978-3-86727-160-8

Berichterstatter:	**Prof. Dr. Reinhard Strey**
	Prof. Dr. Ulrich Deiters
Tag der mündlichen Prüfung:	**18.01.2007**

Nonnenstieg 8, 37075 Göttingen
Telefon: 0551-54724-0
Telefax: 0551-54724-21
www.cuvillier.de

1. Auflage, 2007
Gedruckt auf säurefreiem Papier

978-3-86727-160-8

For Magda

***The most exciting phrase to hear in science, the one that heralds new discoveries, is not 'Eureka!' (I found it!) but 'That's funny…'* – Isaac Asimov**

Abstract

The fusion and fission of fluid amphiphilic bilayers is a key process in biology, occurring both on the cellular and subcellular level. In a model system of excess water (D_2O), oil (*n*-decane) and nonionic surfactant ($C_{12}E_5$) the kinetics and mechanisms of transitions between two phase types of extended amphiphilic bilayers, i.e. the lamellar and sponge phase, are investigated. An abrupt change in temperature is used to initiate these phase transitions. The isotropic sponge or L_3-phase consist of a continuous membrane of multiply connected passages extending in three dimensions, while the anisotropic lamellar or L_α-phase is composed of stacks of bilayer sheets. Thus the L_3-to-L_α transition involves passage annihilation/bilayer fission, while passage formation/bilayer fusion marks the reverse case. By employing time resolved ^{2}H-NMR spectroscopy and SANS, it is found that these transitions occur through essentially different mechanisms: nucleation and growth in the case of the L_3-to-L_α transition and the formation of locally uncorrelated passages in the reverse case. The kinetics of the L_3-to-L_α transition (successfully described by the *Avrami* model) are strongly dependent on the change in temperature, the bilayer volume fraction, and viscosity, and slow (ca. 300-4000s) when compared to the opposite course (ca. 600s). Although initial (<200s) passage formation occurs very quickly in the fast L_α-to-L_3 transition, it appears that this slows considerably once a critical passage density is attained. Evidence suggests that disruption of long range lamellar order might also be a rate limiting process in this case. In the L_3-to-L_α transition, it is found that lamellar nuclei form at considerably higher bilayer volume fraction, than the equilibrium value. This can inhibit progressive nucleation at an advanced point in time. The work presented here represents the first systematic study on nucleation and growth phenomena in a microemulsion-type system. The results form the basis for improving the theoretical description of bilayer fusion and fission.

Kurzzusammenfassung

Das Verschmelzen, d.h. die Fusion, sowie die Teilung von fluiden Amphiphil-Doppelschichten (Bilayern) ist ein Schlüsselprozess in der Biologie, sowohl auf zellulärer wie subzellulärer Ebene. In einem Modelsystem, bestehend aus Wasser im Überschuss (D_2O), Öl (*n*-Dekan) und nichtionischem Tensid ($C_{12}E_5$), werden die Kinetik und die Mechanismen von Übergängen zwischen zwei Phasentypen mit ausgedehnten Bilayerstrukturen, d.h. der lamellaren L_α- und der L_3-Schwammphase, untersucht. Eine sprunghafte Temperaturänderung dient dazu, die Phasenumwandlungen zu initiieren. In der isotropen L_3-phase bildet eine kontinuierliche Amphiphil-Membran, von dreidimensionaler Ausdehnung, mehrfach verbundene Passagen aus, während die anisotrope, L_α-phase eine planare Doppelschichtstruktur smektischer Fernordnung aufweist. Dementsprechend umfasst der Phasenübergang von L_3 nach L_α Passagenzerstörung/ Bilayerteilung, während die L_α nach L_3 Umwandlung durch Passagenbildung/ Bilayerfusion gekennzeichnet ist. Durch Anwendung zeitaufgelöster ^{2}H-NMR Spektroskopie und Kleinwinkelneutronenstreuung (SANS) kann gezeigt werden, dass die zwei Umwandlungen durch grundlegend unterschiedliche Mechanismen bestimmt werden: Keimbildung und Wachstum im Falle von L_3 nach L_α und aufeinanderfolgende, nicht korrelierte Passagenbildung im umgekehrten Fall. Die Kinetik der L_3 nach L_α Umwandlung, erfolgreich beschrieben durch das *Avrami* Model, ist stark abhängig vom Grad der Temperaturänderung, dem Bilayervolumenanteil, sowie der Viskosität und sie ist langsam (ca. 300-4000s) gegenüber dem Umkehrprozess (ca. 600s). Obwohl dort zu Beginn (<200s) Passagenbildung sehr schnell erfolgt, scheint es, dass sich der Prozess merklich verlangsamt, sobald eine kritische Passagendichte erreicht ist. Auch gibt es Hinweise, dass die Auflösung der lamellaren Fernordnung ein geschwindigkeitsbestimmender Faktor sein könnte. Ferner findet man, dass in der L_3 nach L_α Umwandlung die L_α-Keime einen wesentlich höheren Bilayervolumenanteil enthalten, als von der Gleichgewichtskonzentration vorhergesagt. Dies kann progressive Keimbildung zu einem fortgeschrittenen Zeitpunkt der Umwandlung eindämmen. Die vorliegende Arbeit stellt die erste systematische Untersuchung von Keimbildungs- und Wachstumsphänomenen in einem Mikroemulsionssystem dar. Die gezeigten Resultate bilden die Grundlage zur Verbesserung der theoretischen Beschreibung von Bilayerfusion und Bilayerteilung.

Acknowledgements

The present work was accomplished from February 2003 to November 2006 at the Department of Physical Chemistry of the University of Cologne under guidance of *Prof. Dr. Reinhard Strey*. Thank you Reinhard for setting me on the challenging, yet intriguing path of investigating the kinetics of phase transitions. Your advice and counsel were always welcome and the discussions, especially towards completion of this dissertation, have been invaluable. Last but not least, I am very grateful to you for enabling my journeys to Sweden.

I would really like to thank *Prof. Dr. Ulf Olsson* from the Department of Physical Chemistry 1 (Fkem1), Lund University, for urging me in the direction of NMR investigations. The many discussions we had in that subject area and the theory of bilayers, face to face and in extended telephone conferences, have given me deep insights into the fields. Without your assistance and support, this work would have needed to take a different direction.

My sincere gratitude goes to *Prof. Dr. Håkan Wennerström* for familiarising me with many aspects of NMR spectroscopy theory, and specifically for deriving the extended McConnell equation. I am very happy that you took the time to come to Cologne and aided in finalising my first publication.

I thank *Markus Nilsson* for supporting me in my first steps towards managing an NMR apparatus. In general, I acknowledge the highly international Fkem1 'crowd' of 2003, that through volleyball, BBQs, Rock concerts and Midsummer merrymaking made it impossible to forget that there is more to life than science. I will always remember this special time in my life. Thank you all!

Special thanks goes to *Hans Lilja* for his incredible support above and beyond the call of duty with the technicalities of the Varian 360, Linux and bulk data management in my 2005 stay. Thank you so much Hans!

I specifically would like to thank *Dr. Thomas Sottmann* for his support in all aspects of this work no matter what the hour, but especially his Grenoble night shifts and mopping up that thermostat tsunami. I also thank *Sandra, Tobias* (who was also busy mopping) and *Lorentz* for their work, be it day and night, during the SANS measurements.

Many thanks for the ILL assistance received from *Dr. David Bowyer* and *Dr. Ralf Schweins*. Thank you Ralf for your patience in repeatedly creating online accounts and guiding me through the intricacies and pitfalls of online data processing.

I would also like to thank the Cologne nucleation group of *Jan*, *David* and *Dr. Judith Wölk* for the discussions on, surprise, nucleation.

I thank all my colleagues of the Department of Physical Chemistry in Cologne for the friendly working atmosphere and cooperation.

Finally, my very special thanks goes to my partner *Dr. Magdalena Baciu*, who always believed in me and was at my side through all the highs and lows, and my friends and family for their love and support through all the years. It will be great to start seeing you all more often again.

Symbols and Abbreviations

(note that vectorial variables are denoted with an arrow $\vec{x}$)

a_c	surface area of a surfactant molecule in an interface
A	water component of a system
A	specified area
A_{in}	internal lamellar area of a nucleus
A_s	surface area of a spherical nucleus
b	factor of a power law
b	bound coherent scattering length of an atom
B	oil component of a system
$\vec{B}$	static magnetic field of an NMR spectrometer (magnetic flux density)
$\vec{B}_{local}$	local magnetic field at the site of a single atomic nucleus
C	surfactant component of a system
c_0	spontaneous curvature
c_1	and c_2, principal curvatures
d	bilayer repeat distance in general
$\vec{d}$	director of a phase
d_3	repeat distance of the L_3-phase
d_{sd}	sample detector distance
d_α	repeat distance of the L_α-phase
$d_{\alpha,1}$	repeat distance of the L_α-phase of a standard sphere at $\phi_{B+C} = 0.01$
D	deuterium atom, i.e. ^2H
D	diffusion coefficient
e	elementary charge, $e = 1.602177 \cdot 10^{-19}$ C
E	energy, specifically the bending energy
E_{m_I}	energies of m_I dependant orientations of nuclear magnetic moments in a magnetic field
E_A	energy barrier of passage formation
g_I	g-factor of a nucleus
G	Gibbs free enthalpy
h	Planck constant, $h = 6.6260755 \cdot 10^{-34}$ Js
$\hbar$	$\hbar = h/2\pi$

H mean curvature

$J(\omega)$ spectral density function

I spin quantum number of an atomic nucleus or simply 'spin'

I_0 intensity of an incident beam

I^{max} maximum intensity of a peak of Lorentzian lineshape in an NMR spectrum

$I(q)$ absolute intensity in a SANS experiment as function of q

$I(\nu)$ intensity in an NMR spectrum as function of frequency

J nucleation rate

J_{AX} coupling constant between a nucleus A and a nucleus X

k rate constant

k_B Boltzmann constant, $k_B = 1.38066 \cdot 10^{-23}$ JK^{-1}

K_J kinetic factor

$\vec{k}$ wave vector

K Gaussian curvature

$\vec{L}$ spin angular momentum of an atomic nucleus

$\vec{L}_z$ component of the spin angular moment (along $\vec{B}$)

m exponent of a power law

M molar mass

$\vec{M}$ macroscopic magnetisation of an NMR sample

m_I magnetic quantum number

m_n rest mass of a neutron, $m_n = 1.6749286 \cdot 10^{-27}$ kg

n number of MAPA D_2O per surfactant molecule *or* the refractive index *or* dimension term of the KJMA exponent α

n^* particle number of a critical nucleus

$\vec{n}$ local symmetry axis of the anisotropic molecular motion *or* a surface normal

N total number of particles (atomic nuclei) of a system

N_A *Avogadro*'s number, $N_A = 6.0221367 \cdot 10^{23}$

N_{td} number of data points in the time domain

N_α number of atomic nuclei of spin α

p momentum

p_i fraction of given particles at a given site

p_x mole fraction of MAPA D_2O

P probability of exchange between to states or sites

$\vec{q}$	scattering vector, and $q = \left\|\vec{q}\right\|$
$\vec{q}_{zz}$	principal component of an efg tensor (field)
Q	a quantity that is usually referred to as the quadrupole moment
r	specified distance
r_s	radius of a spherical nucleus
r^*	radius of critical nucleus
R	dipolar coupling constant
S	entropy
S_{xy}	order parameter specified by subscript (section 7.1.8), see also θ
t	time *or* variance of monolayer diffuseness
t_{ac}	acquisition time
t_{dw}	dwell time
t_{sac}	time to required for the acquisition of an NMR spectrum
T	absolute temperature *or* transmittance
$\overline{T}$	phase inversion temperature PIT
T'	time constant due to inhomogeneity of a magnetic field
T_1	time constant of the longitudinal relaxation
T_{1Q}	time constant of the longitudinal relaxation stemming from quadrupolar interactions
T_2	time constant of the transverse relaxation
T_{2Q}	time constant of the transverse relaxation stemming from quadrupolar interactions
T_2^*	effective time constant of the transverse relaxation
v	velocity
v_c	volume of a surfactant molecule
V	electric potential
W_{sp}	spectrum width in Hertz
x	molar fraction of a stated component
α	exponent of the *Avrami* equation
γ	gyromagnetic ratio
δ	chemical shift *or* the bilayer (membrane) thickness
ΔG^*	nucleation energy barrier
Δμ	supersaturation
$\Delta\nu_{1/2}$	width at half height of a peak of Lorentzian lineshape in an NMR spectrum

$\Delta\nu_{dd}$ splitting caused by *direct* magnetic dipole-dipole interactions

$\Delta\nu_{Q}$ quadrupolar splitting

$\Delta\nu_{Q,L}$ quadrupolar splitting of the steady state lamellar phase

ε half bilayer thickness

ζ wandering exponent

η viscosity

θ angle between a vector and $\vec{B}$

θ_{db} angle between the director of an anisotropic phase and the magnetic field

θ_{nb} angle between surfactant layer normal and the magnetic field

θ_{nd} angle between surfactant layer normal and the director of the liquid crystal

θ_{qn} angle between the efg and the normal of a layer which impedes molecular tumbling

κ rigidity modulus

$\bar{\kappa}$ saddle splay modulus

λ *de Broglie* wavelength *or* elongation factor

μ chemical potential

$\vec{\mu}$ magnetic moment of an atomic nucleus

μ_0 permeability of a vacuum $\mu_0 = 4\pi\cdot 10^{-7}\ \mathrm{T^2J^{-1}m^3}$

μ_N nuclear magneton $\mu_N = 5.0507866\cdot 10^{-27}\ \mathrm{JT^{-1}}$

ν frequency

ν_L Larmor frequency

$\nu_{L,0}$ Larmor frequency of nucleus of reference

ν_Q resonance frequency for the transition between energy states modified through nuclear quadrupolar interactions

ν^+, ν^- resonance frequencies of a quadrupolar doublet ($I = 1$ condition)

ρ macroscopic density

$\rho(t)$ autocorrelation function

ρ_s scattering length density

ρ_d scattering length density of a domain consisting of several components

σ shielding constant *or* surface energy *or* invariance of a bilayer

τ relaxation time constant *or* another specified amount of time

τ_c correlation time

τ_l life time

τ_P^{-1}	rate of bilayer contact (indirectly a probability)
φ	volume fraction of the lamellar phase
ϕ_{B+C}	bilayer = membrane volume fraction
ϕ_C	surfactant volume fraction
$\phi_{C,i}$	surfactant volume fraction of the interface
χ	nuclear quadrupole coupling constant
χ_E	Euler-Poincaré characteristic
χ_P	coalescence parameter
ψ	mass fraction of a stated component *or*
	constant of the *Avrami* equation determining the type of nucleation
ω	angular velocity in rad/s
ω_b	surfactant to oil plus surfactant volume ratio
ω_L	Larmor angular velocity in rad/s

cps	counts per second
efg	electric field gradient
EPM	'equal peak moment', the point in time where the coexisting peaks in the NMR spectrum of an L_3 to L_α transition have the same intensities
FID	free induction decay
KJMA	*Kolmogorov*, *Johnson*, *Mehl* and *Avrami*
MAPA	'mobile, through adsorption partially aligned'
ME	microemulsion
*n*D-	*n* dimensional
NMR	nuclear magnetic resonance
NQR	nuclear quadrupole resonance
r.f.	radiofrequency
SANS	small angel neutron scattering
T-jump	temperature jump
TR-SANS	time resolved SANS

Table of Contents

1. Introduction **1**

1.1 Complex Fluids **1**
1.2 Motivation and Objectives **3**

2. Phase Behaviour **7**

2.1 Binary System H_2O-$C_{12}E_5$ **8**
2.2 Ternary System H_2O - n-decane - $C_{12}E_5$ **9**
2.3. Phase Behaviour Measurements **13**

3. Theoretical Description of Bilayer Characteristics **16**

3.1 Curvature of Amphiphilic Films **16**
3.2 Bending Energy **18**

4. Mechanisms of Passage Formation and Destruction **20**

4.1 Passage Formation **20**
4.2 Passage Destruction **21**

5. Relaxation Kinetics **25**

6. Nucleation **28**

6.1 Classical Nucleation Theory **28**
6.2 The KJMA Model **31**

7. NMR-Spectroscopy **33**

7.1 Basic Principles **34**

7.1.1 Spin Angular Momentum and Magnetic Moment 34
7.1.2 The Influence of a Magnetic Field 36
7.1.3 The Influence of Radiofrequency Radiation 39
7.1.4 Signal Detection, Free Induction Decay (FID) and Lineshape 41
7.1.5 Relaxation and Correlation Time τ_c 45
7.1.6 Magnetic Shielding, Chemical Shift and Equivalent Nuclei 49
7.1.7 Spin-Spin Coupling 51
7.1.8 Quadrupolar Interactions 52
7.1.9 NMR Experiment Time Scale and Chemical Exchange 57

7.2 The NMR Experiments **60**

7.2.1 D_2O, the Probe Molecule 60
7.2.2 The Two-Sites Model 63

7.2.3 Direct Dipole-Dipole Interactions 65
7.2.4 NMR Signal of the Steady State Isotropic L_3-Phase 66
7.2.5 NMR Signal of the Steady State Anisotropic L_α-Phase 67
7.2.6 L_3/L_α Transition Experiments 69

7.2.6.1 Experimental Procedure 69
7.2.6.2 L_3 to L_α Transitions 70
7.2.6.3 L_α to L_3 Transitions 78
7.2.6.4 Additional Experiments 82

7.3 Analysis of the Experimental Findings 85

7.3.1 L_3 to L_α Transitions 85

7.3.1.1 Kinetic Analysis and Re-Evaluation of the Preliminary Experiments 89
7.3.1.2 Kinetic Analysis of the Established Experiments 93
7.3.1.3 Trends in the Development of the L_α-Phase Volume Fraction φ 102
7.3.1.4 General Kinetic Behaviour 107
7.3.1.5 Splitting Development 112
7.3.1.6 Sponge and Lamellar Peak Width Development 116

7.3.2 L_α to L_3 Transitions 119

7.3.2.1 The Two States Model and the McConnell Equation 119
7.3.2.2 Failure of the Two States Model 122
7.3.2.3 Spectra Fitting 122
7.3.2.4. Trends in the Development of the Fitting Parameters 127

7.3.3 Kinetics of the 'Additional Experiments' 132
7.3.4 Experiments Separating Nucleation from Growth 134

7.4 Interpretations of the Experimental Findings 137

7.4.1 The Driving Force of the L_3/L_α Phase Transition 137
7.4.2 Influence of the Magnetic Field 138
7.4.3 Shift of Resonance Frequency 139
7.4.4. Experimental Data vs. Fits and Simulation 140
7.4.5 L_3 to L_α Transitions 141

7.4.5.1 Characteristics of the Nucleation and Growth Mechanism 141
7.4.5.2 Quadrupolar Splitting of the Steady State Lamellar Phase 144
7.4.5.3 Significances of the Quadrupolar Splitting Development 146
The Effects of Initial Nuclei Orientation on Lineshape 147
Splitting Development Comparisons at Varying Amplitude of the T-Jump 148
Diffusion and the Dilution Effect 150
Splitting Development: Comparisons at Varying Concentration 153

7.4.5.4 Development of Peak Width 155
7.4.5.5 The L_3 to L_α Phase Transition Kinetics 156

The Kinetics in the Light of the CNT 157
Kinetics in the Light of the Passage Destruction Mechanism 163

7.4.6 L_α to L_3Transitions 168

7.4.6.1 Characteristics of the Phase Transition Mechanism 168
7.4.6.2 The L_α to L_3 Phase Transition Kinetics 169
7.4.6.3 The Kinetics in Light of the Passage Formation Mechanism 172
7.4.7 The 'Additional Experiments' 176

8. Small Angle Neutron Scattering (SANS) 177

8.1 Fundamentals of Scattering 177
8.2 Geometry of the SANS Experiments 179
8.3 Contrast Variation 181
8.4 Data Processing 183
8.5 The Equilibrium L_3 State 185
8.6 Temperature Jump Experiments 188
8.6.1 The L_3 to L_α Phase Transition 189
8.6.2 The Equilibrium L_α State 196
8.6.3 The L_α to L_3 Phase Transition 198
8.7 Interpretations of the Experimental Findings 202
8.7.1 The Sponge and Lamellar Steady States 202
8.7.2 TR-SANS, the Kinetic Investigations 204

9. Summary 213

10. Appendices 218

11. Tables 240

12. References 253

1. Introduction

1.1 Complex Fluids

An elemental principle of chemistry concerned with the solution of a component (the solute) in a solvent is generally known even by non-scientists through the simple rule of thumb 'like dissolves like'. This rule refers of course to the polarity of a substance, differentiating simply between polar and nonpolar components, which are regularly termed as being hydrophilic and lipophilic respectively. The latter expressions stem from Greek and are associated with the two main classes of biological solvents, i.e. water on one hand and fats or oils on the other.

Both living nature and modern industry are faced with the problem of intermingling components of the two opposite groups on microscopic length scales and thus resort to using amphiphiles, i.e. molecules that contain both a hydrophilic and lipophilic moiety. These molecules necessarily situate themselves between domains of hydrophilic and lipophilic character (i.e. they reside in the *interface*[1,2,3,4]) because of lowest energy considerations, as the components reduce the interfacial tension between the opposing substances. This in turn results in increasing the miscibility of fluids or, in case of a solid surface and a liquid phase, facilitates wetting and spreading. When amphiphiles function in this manner, they are normally denoted as surfactants. The term 'surfactant' is a linguistic blend of '**surf**ace **act**ive **a**ge**nt**'.

When a water (**A**) and an oil (**B**) component form a macroscopically homogenous mixture due to the presence of a surfactant (**C**) and the input of energy through mechanical perturbation, one speaks of an emulsion. The dispersed phase is present in surfactant coated spherical droplets of the micrometer scale and the internal interface is relatively small. Such mixtures are only kinetically stabilised and degrade over time[4,5,6], i.e. phase separation occurs. If however surfactant concentration is increased the formation of so called microemulsions (ME) becomes feasible. In these mixtures, the required interfacial energy is so extraordinarily low that the present thermal energy suffices to ensure thermodynamic, i.e. indefinite, stability. Thus, microemulsions are nanostructured, thermodynamically stable and macroscopically isotropic homogeneous mixtures of water-oil-surfactant[7,8,9]. Compared with the emulsions, ME have a much larger internal interfacial area and accordingly the structures they exhibit exist on the nanometer scale.

These structures can be surprisingly intricate and can be separated into two general categories, namely discrete aggregates and extended structures. The former include the well-known spherical micelles, but also rod-shaped or disc-like aggregates, while the latter contain extended surfactant films which form structures of various symmetry (e.g. cubic and hexagonal), but also far-reaching tubular networks or simply stacks of sheets. In all of the described cases the surfactant films separate the hydrophilic from the lipophilic domain(s) with a *monolayer* of amphiphilic molecules. It is not surprising that mixtures of this kind are allocated to a general class termed complex fluids, i.e. fluids containing some sort of structure.

Interestingly, complex structures similar to the afore mentioned exist even in the case of simple two component systems, i.e. oil - surfactant and water - surfactant mixtures. That is to say, amphiphilic molecules are not randomly dispersed within their solvent, but rather tend to form a variety of structures through self-assembly, provided that they are present in a critical (but low) concentration. The exact type of present structure is dependant on the existing physical conditions, mainly system composition and temperature. However, in contrast to the three component systems, the surfactant films of two component mixtures are inevitably composed of a *bilayer* of amphiphilic molecules, so that the molecular region of opposite characteristic is isolated from the solvent. The importance of the phenomenon of self-assembly can not be overestimated as life is only possible through compartmentalisation, which is brought about by the existence of biological membranes and amphiphiles in the form of phospholipids are one of their main constituents.

Due to the fluidity of the systems in which they are contained, surfactant bilayers as well as monolayers are highly dynamic in character and it is important to bear this in mind even when a phase and therefore its structures, are in thermodynamic equilibrium. Owing to over half a century of study, equilibrium phase behaviour and the existence of the exhibited structures of water-oil-surfactant systems are by in large understood and accordingly theoretically described[10,11]. Consequently, the focus has shifted to the investigations of phase transitions and specifically their associated kinetics[12,13].

While phase transitions *per se* are a phenomenon that transcends all the natural sciences from astrophysics to zoology[14,15], phase transitions involving membranes/bilayers are mainly a focus of biochemistry and biophysics, as bilayer fusion and fission is an integral part of many cellular processes (e.g. cell division, exocytosis, endocytosis, chemical synapses in neurons, mitochondrial[16] and peroxosimal[17] division). In particular, the investigation of lipid bilayer fusion has received much attention and in that topic especially a proposed mechanism

where an intermediate 'stalk' structure[18,19,20,21] is followed by 'pore formation'[22,23]. However, most of the associated studies are either of a purely theoretical nature or numerical simulations, that is little experimental work has actually been performed and the current state of affairs appears as yet unsatisfactory[24]. Also, biological systems are by their very nature excessively complex and in order to gain underlying understanding of the topic, experiments on simplified model systems are needed. Ternary microemulsions of water, oil and surfactant with their well described bilayer physics can represent such a system.

1.2 Motivation and Objectives

This thesis approaches the subject of amphiphilic bilayer fusion and fission on a most basic level. In essence, it deals with the transition between two bilayer structures of fundamentally different topologies, those of the lamellar or L_α-phase and those of the sponge or L_3-phase (fig. 1.2(1)). These structures are examined in a very dilute system, i.e. the dominating component is water, in resemblance of biological systems. Accordingly, the hydrophilic region of the surfactant molecules faces 'outward', while the hydrophobic region is contained within the bilayer. The L_α-structure consists of stacks of planar, in theory infinite, bilayer sheets and can thus be considered a lyotropic liquid crystalline phase of long-range smectic order. The L_3-phase consist of a single, multiply connected bilayer without seams or edges, which separates two continuous, interwoven water domains that are independent of each other. The bilayer itself can be seen as a network of interconnected 'passages' or 'handles' of somewhat hourglass-like shape (similar to a catenoid). In fact, the morphology of the L_3-phase has been described as a 'melted' cubic phase[25,26,27,28].

From fig. 1.2(1) it is rather obvious that a transition from the L_α to the L_3 phase requires the formation of the mentioned 'handles' or 'passages' and that this inevitably includes bilayer fusion, while the opposite is true in the reverse case. (Formally this can be understood by the fact that the topologies, in the mathematical sense, of the two structures are different, i.e. the Euler-Poincaré characteristic χ_E of an infinite bilayer sheet is zero, while χ_E is negative for the sponge phase[3].) In fact, in the above mentioned bilayer fusion mechanism with intermediate stalk and ultimate formation of a pore, an expanded pore corresponds to just such a passage (fig 1.2(1b)). Although bilayer fusion/fission processes occur by necessity in all cases where there is a change in membrane topology, the chosen transition is particularly advantageous, because the number of passages in an ideal lamellar phase is exactly defined, i.e. there are none. Furthermore, this transition is of additional interest as the isotropic sponge

phase can be considered to 'crystallise' when converting to the anisotropic lamellar state, while 'melting' occurs in the reverse case (and indeed the phase transitions in question are achieved through an alteration of system temperature). Attaining macroscopic length scale order through controlled crystallisation is an essential part of producing modern materials for functional devices. Hence, basic research concerned with melting and crystallisation processes is always useful.

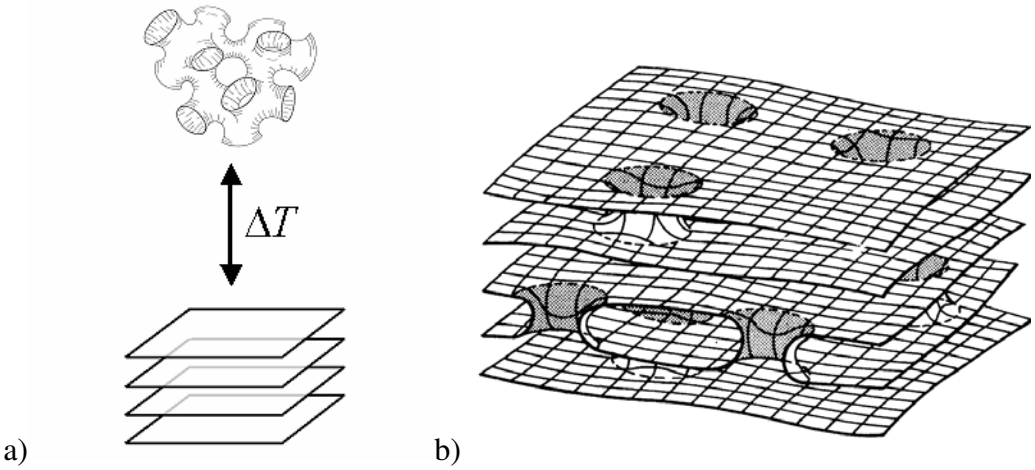

Fig. 1.2(1): a) schematic illustration of the lamellar and sponge phase structures which form after thermally induced phase transitions. The stack of sheets and the continuous passage network represent surfactant bilayers containing the minority oil component. The bilayers themselves are located within bulk water. b) passage formation between lamellae corresponding transition state towards the sponge phase. Concept and figure taken from ref. [29].

All investigations presented in this dissertation were performed on highly dilute microemulsions of the water - *n*-decane - $C_{12}E_5$ system, where $C_{12}E_5$ corresponds to the nonionic surfactant *n*-dodecylpentaoxyethylene. Additionally, the surfactant to oil plus surfactant volume ratio ω_b was kept constant at $\omega_b = 0.45$. Thus, since the water component is excessively dominating and there is respectively little hydrocarbon oil, the membrane structures of the sponge and lamellar phases are still essentially bilayers, even though they are somewhat 'swollen' with *n*-decane. The primary reason for the choice of this particular system with its specific ω_b is the fact that it has been intensely studied, i.e. its equilibrium thermodynamic and bilayer elastic properties have been determined. Also, and notably, the dynamics of its L_3-phase have been thoroughly investigated in close cooperation with *Prof. Dr. Olsson* from the Department of Physical Chemistry 1, Lund University, Sweden. This thesis is in effect the result of the continuation of this fruitful cooperation. However, the original selection of the system in question was of course anything but arbitrary.

Firstly, the use of a nonionic surfactant avoids complications with long-range electrostatic interactions[30]. Secondly, employing *n*-decane ensures that the $C_{12}E_5$ monolayers are simultaneously saturated both with respect to oil and water. This is advantageous for theoretical considerations[31]. Also, since *n*-decane is insoluble in water the ternary system at hand can be modelled as a *pseudo*-binary one. Finally, the L_3 and lamellar phases are situated at temperatures which are better manageable experimentally, that is to say they are located at lower values, when compared to the simpler binary system of H_2O - $C_{12}E_5$.

Although the lamellar and sponge phases have both been the subject of intense study, transitions between them, especially the involved kinetics, have not. Indeed, quite a few studies have focused on sponge to lamellar transitions, but almost all of them resorted to shearing as the means of inducing this transition. In fact, only two studies were found that actually utilised the change of temperature instead[32,33] and only the first of these focused on the transition kinetics. However, this investigation was carried out using purely visual methods, so termed dark-field *macroscopy* and polarisation microscopy. In addition, the lamellar phase developed in the form of multi lamellar vesicles, i.e. not the classical layer structure investigated here. Finally, the focus was on describing a kinetic pathway when observing transitions, where the initial state consisted of two phases (L_α and L_3) or even three phases (L_1, L_α and L_3) in equilibrium.

L_3/L_α transitions have been previously investigated almost exclusively with scattering techniques. However, since the sponge phase is isotropic and the lamellar phase anisotropic the interesting possibility arises to use heavy water and employ deuterium nuclear magnetic resonance (^{2}H-NMR), as the two phase types then lead to different signals. In general, the application of ^{2}H-NMR to notice phase transitions or to aid in the identification of a particular phase due to symmetry considerations is well established[34]. However, it appears that this method was first used in investigating an L_3 to L_α transition by *Fischer et. al.* only recently[35], while the investigation of the reverse process in this way seems not to have been performed at all. In the study in question, a single time constant was determined by simply monitoring signal intensity and fitting a single exponential. However, the transition itself was induced through a chemical reaction associated with an increasing change of system composition and the opportunity to vary system parameters or conduct a more detailed evaluation was passed by. Nevertheless, the ^{2}H-NMR experiments presented in this dissertation are essentially modelled after that exemplary work.

The aim of this thesis is to examine the kinetics of L_3/L_α transitions by employing time resolved ^{2}H-NMR and small angle neutron scattering (TR-SANS). The majority of the experiments are of the former kind and they were all performed at Lund University during two extended stays, while the latter were performed on two different occasions at the D11 instrument of the Institut Laue-Langevin (ILL) in Grenoble, France. Insight into the importance of key parameters is to be gained by altering the size of the temperature jumps ΔT, the bilayer volume fraction ϕ_{B+C}, and sample viscosity η (through the addition of sucrose). Furthermore, the study is intended to acquire knowledge of the actual mechanisms involved in the process of the two phase transitions.

2. Phase Behaviour

As stated in the introduction, the investigations in this thesis involve transitions between lamellar (L_α) phase and sponge (L_3) phase. A typical L_α phase[1,4] consists of flat bilayers, which are layered arrangements of amphiphilic molecules, possessing one-dimensional order and being separated from each other by water layers (see fig. 2(1,*left*)).

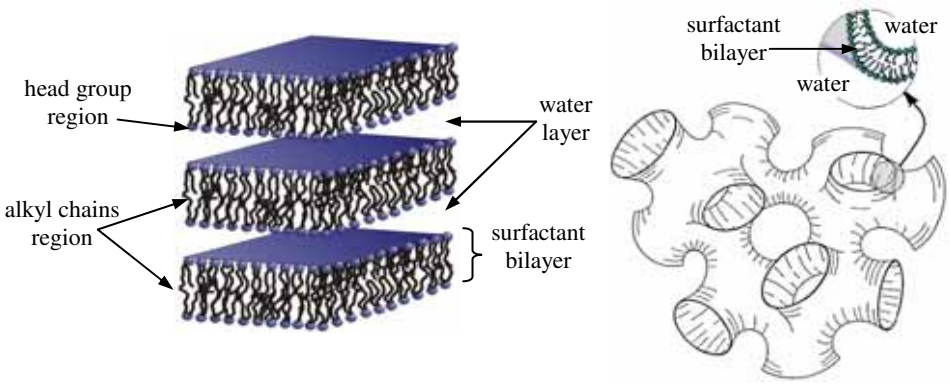

Fig.2(1): structures of extended bilayers: lamellar phase (*left*) and sponge phase (*right*).

Sponge or L_3 phase (see fig. 2(1, *right*)) is an isotropic solution and has up to now only been found in the vicinity of a lamellar phase (L_α)[36,37,38]. Because of its macroscopic appearance, this phase was termed 'anomalous'. It may show strong opalescence and flow birefringence, properties that become increasingly pronounced with dilution. Data resulting from conductivity measurements upon L_3 phase, are quantitatively comparable with what is expected from a bilayer continuous cubic phase, hence the L_3-phase is sometime referred to as a *melted or distorted cubic* phase[25,26,28]. SANS results are consistent with a local bilayer structure. In addition, Freeze Fracture Electron Microscopy (FFEM) investigations upon the topological transformation from dilute lamellar phase to L_3 phase support the idea that there are two main structural differences between L_α phase and L_3 phase: the positional order and the topology[29]. Thus, L_α phase shows long-range smectic order and its bilayers are flat planes, whilst L_3 phase is a liquid-like disordered phase, consisting of 3D multiply connected bilayers and possessing negative monolayer curvature[29,39,40].

2.1 Binary System H_2O - $C_{12}E_5$

Lamellar phase L_α and sponge phase L_3 can be found in the dilute region of the aqueous solutions of surfactants that belong to the well-known class of *n*-alkyl polyoxyethylene (H - $(CH_2)_i$ – $(OCH_2CH_2)_j$ – OH), commonly denoted as C_iE_j . Here *i* informs about the length of the hydrophobic alkyl chain, whilst *j* represents the number of the ethylene oxide groups within the molecule. For the present work the surfactant of choice is $C_{12}E_5$, which when in mixture with water forms a rich variety of phases (see fig. 2.1(2)), with lamellar phase L_α and sponge phase L_3 exhibited at high dilutions.

At very low concentrations the surfactant monomerically dissolves in the water phase. Above a surfactant concentration denoted as *cmc* (critical micelle concentration) the surfactant concentration is sufficient to form microstructures. At low temperatures and low surfactant concentrations these are droplet structures namely micelles which elongate with increasing temperature. At high temperatures the miscibility gap is found.

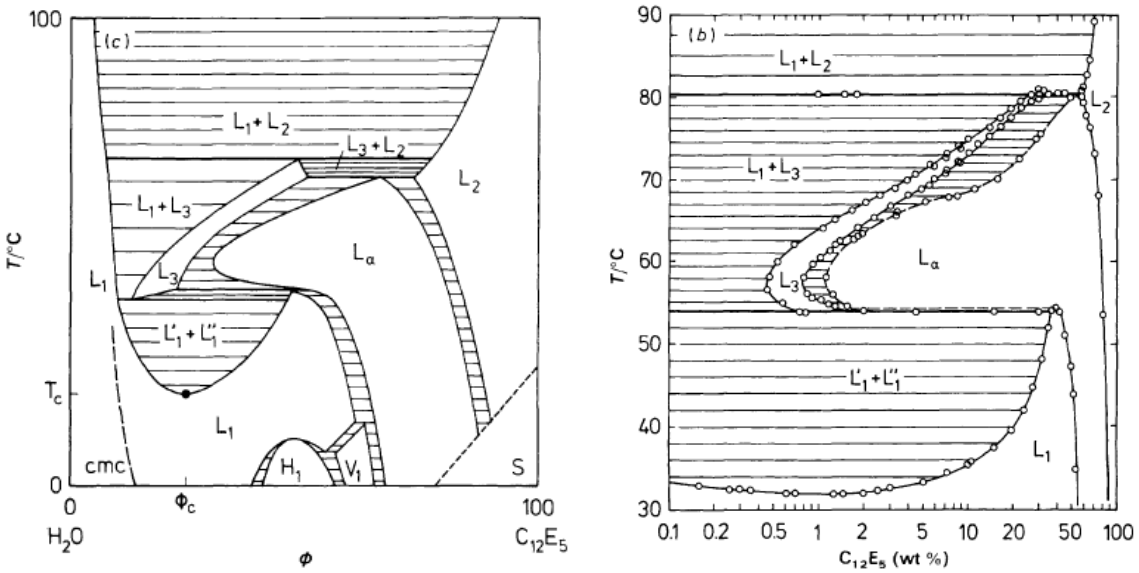

Fig. 2.1(1): a schematic depiction (*left*) and an experimentally determined (*right*) phase diagram of the binary system H_2O-$C_{12}E_5$. Figures taken from ref.[26]

At higher surfactant concentrations, liquid crystalline phases such as hexagonal phase H_1, cubic phase V_1 and lamellar phase L_α are formed. The latter is stable over a wide range of temperature and composition into very dilute regions. In direct vicinity of the L_α phase, towards higher temperatures, separated only by a narrow two-phase coexistence region, the L_3-phase is located. It is evident, that the L_3-phase is stable only over a narrow temperature interval, while extending over a large concentration range. Therefore, one often refers to an

'L_3-channel'. At higher temperatures, the sponge phase is in coexistence with the L_1' phase, a phase similar to the micellar L_1 phase but of higher dilution, i.e. water content.

However, no matter how attractive the simplicity of the above mentioned binary system is, for the study of the L_α / L_3 phase transition there are a few serious limitations from practical, as well as from theoretical perspective (see section 1.2). This limitations can be overcome by introducing a third component, namely an oil (here *n*-decane). This does not only bring the L_α and L_3 phases closer to room temperature, but at the same time ensures the saturation of the $C_{12}E_5$ monolayer in both water and oil.

2.2 Ternary system H_2O - n-decane - $C_{12}E_5$

In general, when describing the phase behaviour of three component systems as function of their composition, it is sensible to resort to using a *Gibbs triangle* spanned by the three components, in order to avoid the complications associated with a three dimensional depiction. Choosing the classical notations from the microemulsions: the water is referred to as the (A) component, the oil as the (B) component and the surfactant as the (C) component. Since the phase behaviour of microemulsion consisting of water (A), hydrocarbon oil (B) and nonionic surfactant(C) is also strongly dependant on temperature, this parameter is added as an ordinate to the triangular base and the result is a phase prism (fig. 2.2(1)). Fortunately, microemulsions of the mentioned type are very insensitive to changes in pressure (an increase of 10 MPa causes a shift of the phase behaviour to higher temperatures by approximately 2-3 K)[41,42], so that for all measurements at the respective ambient condition this parameter is neglected.

The investigations presented in this thesis deal with temperature induced L_3/L_α transitions in the dilute region of the microemulsion-type system H_2O - *n*-decane - $C_{12}E_5$. A schematic phase diagram, inserted into a phase prism, is given in fig. 2.2(1), the area of interest being denoted by a circle.

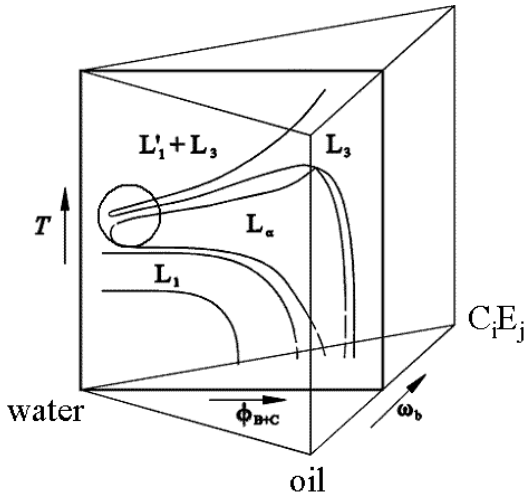

Fig. 2.2(1): phase prism including a schematic phase diagram of a water – hydrocarbon oil – C_iE_j surfactant system superimposed on a cut corresponding to a constant value of the surfactant to oil plus surfactant volume ratio ω_b. The phase diagram on the cut is a function of temperature *T* and the bilayer volume fraction ϕ_{B+C}. The experiments of this thesis are conducted in the dilute, i.e. high water content, region. The area of interest is denoted by the circle.

Depending on the temperature and the bilayer volume fraction ϕ_{B+C} (see eq. 2.2(1)) one finds the same phase sequence as in the binary system. Again the L_3-phase can be found in direct vicinity to the L_α-phase, separated from it by a narrow two-phase region. The extent of both the L_3- and the L_α-phase increases with increasing bilayer volume fraction.

When focusing on the geometries of surfactant structures in solution, neither the mole nor the mass concentration of the components is of direct importance, but rather the volume that they occupy. For this reason, the system compositions of this thesis are described by two parameters, the bilayer volume fraction ϕ_{B+C} and the surfactant to oil plus surfactant volume ratio ω_b. They are defined as follows

$$\phi_{B+C} = \frac{V_B + V_C}{V_A + V_B + V_C} \qquad \text{eq. 2.2(1)}$$

$$\omega_b = \frac{V_C}{V_B + V_C} \qquad \text{eq. 2.2(2)}$$

V_X corresponds to the volume of the water (A), oil (B) or surfactant (C) component, respectively and can be calculated simply via the known component mass and by accounting for a substance's bulk density. Thus, any deviations due to the true partial molar volumes are disregarded. The meaning of the two parameters ϕ_{B+C} and ω_b within isothermal *Gibbs* triangles is further elucidated via lines corresponding to constant values (fig. 2.2(2)). Note

that ϕ_{B+C} and ω_b together are sufficient to describe the exact composition of a sample. Since ϕ_{B+C} includes the oil component, it will also be referred to as the membrane volume fraction.

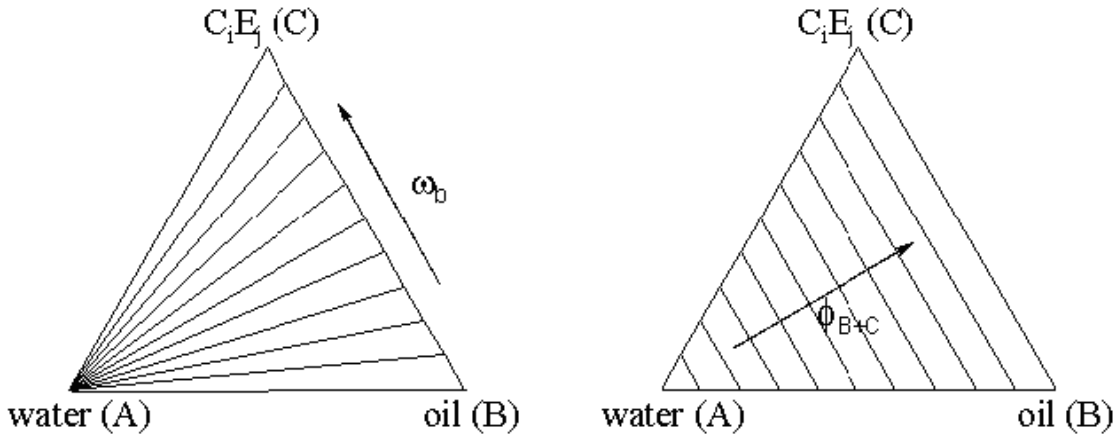

Fig. 2.2(2): isothermal Gibbs triangles with lines corresponding to constant values of the surfactant to oil plus surfactant volume ration ω_b (*left*) and bilayer volume faction ϕ_{B+C} (*right*). The arrows indicate the direction of increasing values for the two parameters.

Another useful relation is

$$\phi_{B+C} \cdot \omega_b = \phi_C \qquad \text{eq. 2.2(3)}$$

Hence the surfactant volume fraction ϕ_C can be calculated easily for any given composition.

In addition to employing a single system throughout all the experiments, the surfactant to oil plus surfactant volume ratio ω_b is kept constant. In doing so, one effectively looks at a single 'cut' through the phase prism, i.e. a two-dimensional phase diagram as function of ϕ_{B+C} and temperature *T*. (fig. 2.2(1)).

For the system employed in this thesis (water - *n*-decane - $C_{12}E_5$), the parameter ω_b is fixed at $\omega_b = 0.45$ and for this particular case, a comprehensive phase diagram, representing the mentioned 'cut' through the phase prism, has been previously determined.

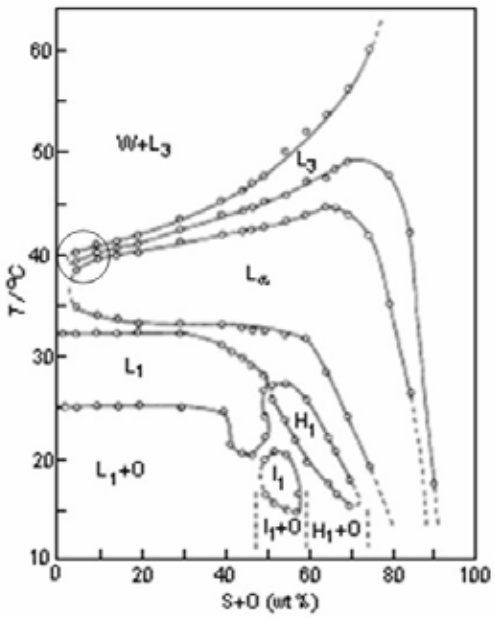

Fig. 2.2(3): phase diagram of the H_2O - *n*-decane - $C_{12}E_5$ system at $\omega_b = 0.45$. The area of interest is denoted by a circle. (S+O represents the surfactant + oil weight fraction). Figure taken from ref [43]

Due to the dominance of the water component and the relatively small volume fraction of *n*-decane used, the surfactant structures in the sponge and lamellar phases can still be considered to consist of bilayers, albeit of ones 'swollen' with oil. These swollen bilayers are also referred to as membranes and accordingly ϕ_{B+C} as the membrane volume fraction. As the ω_b parameter is kept constant, the degree to which the bilayers are swollen is also constant, regardless of the bilayer volume fraction present. Thus, when one assumes conservation of volume and constant membrane thickness δ, ideal one-dimensional swelling of a lamellar phase upon dilution with water is described via

$$d = \frac{\delta}{\phi_{B+C}} \qquad \text{eq. 2.2(4)}$$

where *d* is the repeat distance of the bilayers. Investigations on the binary system H_2O - $C_{12}E_5$ showed that this type of swelling indeed occurs over the entire concentration range in which the lamellar phase is stable[26]. At high dilution there is a deviation towards higher values of *d* stemming from possible defects in the lamellar structure and bilayer undulations. It is however small enough to be neglected in the discussions of this thesis. Additionally, several studies[44,45,46,27] showed that dilution of an L_3-phase also occurs according to ideal one-dimensional swelling, so that $d \propto \phi_{B+C}^{-1}$.

2.3 Phase Behaviour Measurements

As stated in section 2.2 the phase behaviour of H_2O - *n*-decane - $C_{12}E_5$ system at $\omega_b = 0.45$ has been determined in detail over basically the entire concentration and relevant temperature range by *Leaver et. al.*[43]. However, in order to enable the ^{2}H-NMR and SANS investigations of this study, the hydrophilic water component needed to be exchanged with its deuterated equivalent. When in a water-surfactant or water-oil-surfactant system, the water component is replaced by D_2O, this causes a small but characteristic shift of the phase behaviour in temperature (see below).

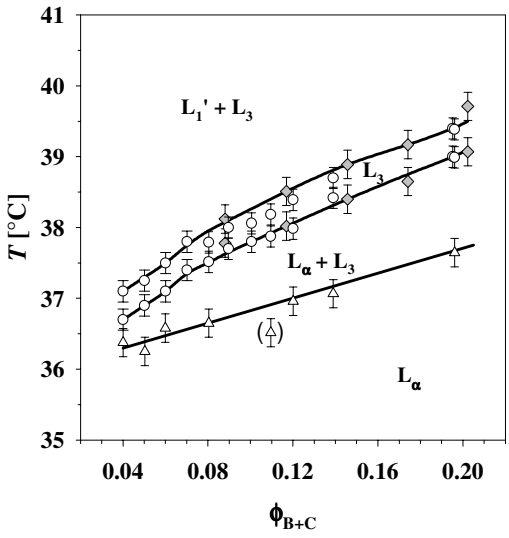

Fig. 2.3(1): phase diagram of the D_2O - *n*-decane - $C_{12}E_5$ system at $\omega_b = 0.45$ as a function of ϕ_{B+C} and temperature *T*. Empty circles represent the boundaries of the L_3-phase and empty triangles the $L_\alpha/L_\alpha+L_3$ boundary. Grey diamonds were extrapolated by shifting L_3-boundary data from a system with H_2O/NaCl (0.1 molar) as the water component[46] by 0.6°C to lower temperatures.

For the D_2O - *n*-decane - $C_{12}E_5$ system, the phase boundaries of the L_3-phase and the L_3/L_α coexistence region were determined for all samples prior to performing the actual phase transition experiments, although they could be easily estimated from the phase diagram from the data of fig. 2.2(3). Phase behaviour measurements are generally necessary, in order to exclude the possibility of error during sample preparation (section 10.2) and potential surfactant impurity.

In fig. 2.3(1) the results of these measurements are shown. The L_3 phase is stable only within a narrow temperature interval of approximately 0.5°C for the entirety of this range and so one can most certainly denote an L_3-channel. This channel is located around 37°C for low bilayer volume fractions ($\phi_{B+C} \approx 0.04$) and extends to 39°C for higher ones ($\phi_{B+C} \approx 0.20$). At temperatures above this channel, the L_3 phase is in equilibrium with excess, almost pure, water, while at lower temperatures, it is separated from the L_α-phase by a coexistence region.

This region is narrow (approx. 0.7°C wide) at $\phi_{B+C} \approx 0.04$, but widens steadily to approx. 1.4°C at $\phi_{B+C} \approx 0.20$. The phase boundary temperatures of the system are in good agreement with those found in a previous study[47] and the afore mentioned complete phase diagram of *Leaver et. al.*

When using $C_{10}D_{22}$ instead of the protonated component in order to achieve film contrast in the SANS experiments (see section 8.3), the phase behaviour is shifted minimally (0.3°C) to higher temperatures (data not shown). In general, replacing system components with their isotope doped counterparts or incorporating additives which solubilise completely in either the water or oil domains, simply causes a shift in phase behaviour to either higher or lower temperatures, i.e. it does not significantly alter the relative location of the phases nor their extension. This is demonstrated in fig. 3a, where the location of the studied L_3-channel can be reproduced by shifting L_3-boundary data[46], from a system with H_2O/NaCl (0.1 molar) as its aqueous component, by a constant value of -0.6°C (grey diamonds).

An important parameter influencing phase transition kinetics is the viscosity of the medium. Through the addition of sucrose the viscosity η of the system can be tuned. Sucrose and other additives such as salt, glycerol influence the phase behaviour in a well-known and well-defined way[48,9,49]. Analogue to the addition of lyotropic salts and glycerol, sucrose competes for the hydration water with the ethylene oxide groups of the surfactant molecules[50]. As a result, the solubility of the surfactant in water is reduced and accordingly the phase behaviour shifts to lower temperatures.

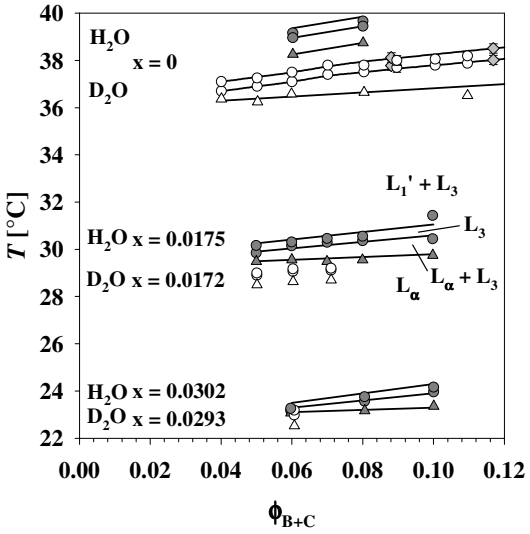

Fig. 2.3(2): phase behaviour upon the addition of sucrose. Depicted are the boundaries of the L_3-phase (circles) and the $L_\alpha/L_\alpha+L_3$ boundary (triangles) of six slightly different systems. All are of the water - *n*-decane - $C_{12}E_5$ type, however three contain H_2O as the aqueous component (dark symbols) and three D_2O (empty symbols). All contain different molar fractions x of sucrose with respect to the water component (specified in the figure). Notice that the data points of the D_2O system without sucrose (x=0) are the ones from fig. 2.3(1).

In the system at hand, sucrose can be regarded as a pseudocomponent since it completely solubilises in water. Thus, the sucrose in water solution is regarded as the system hydrophilic component. The mass fraction of sucrose in the mixture of sucrose and water is given according to the following equation

$$\psi = \frac{m_{sucrose}}{m_{water} + m_{sucrose}} \qquad \text{eq. 2.3(1)}$$

Fig.2.3(2), depicts the effect of sucrose addition upon the phase behaviour of D_2O - *n*-decane - $C_{12}E_5$ and H_2O - *n*-decane - $C_{12}E_5$ systems. With respect to the sucrose free system of fig. 2.3(1), the phase-boundaries shift to lower temperatures, as is expected. D_2O/sucrose samples with a sucrose molar fraction of x=0.0172 (regarding D_2O only) are shifted by -8.4°C, while those with x=0.0293 are shifted by -14.3°C. This corresponds to a mass fraction of ψ=0.230 and 0.340 respectively. The viscosities of the two D_2O/sucrose mixtures at 20°C were determined to be $\eta_{D2O/S}$=2.828 and 5.404 cP which corresponds to $\eta_{D2O/S} = \eta_0 \cdot 2.261$ and $\eta_{D2O/S} = \eta_0 \cdot 4.320$ of the D_2O viscosity η_0=1.251 cP. Note that the viscosities of the complex fluids themselves were not determined and that viscosity is a function of temperature.

In addition, by comparing the H_2O with the respective D_2O systems of fig. 2.3(2), the isotopic effect on phase boundaries can be discerned. The replacement of H_2O by D_2O causes a shift of -1.8°C for x=0, -1.3°C for x≈0.017 and approx. -0.35°C for x≈0.03. Notice that when comparing H_2O/sucrose with D_2O/sucrose systems, this shift is less distinct with increasing sucrose concentration. Also, the extent of the already narrow L_3-channel appears to be somewhat reduced when sucrose is added.

3. Theoretical Description of Bilayer Characteristics

In order to understand the stability of the sponge and lamellar phases, the properties of the surfactant bilayers (which, in the experiments presented here, are additionally swollen with an oil component) must be described for the respective topologies. *Helfrich* [51] developed the so called *flexible surface model* which gives a theoretical description for both mono- and bilayers in terms of their curvatures and bending energies. This model and some elaborations on it will be briefly presented in this chapter.

3.1 Curvature of Amphiphilic Films

The curvature at any point of a two dimensional surface can be described via the principal curvatures c_1 and c_2, which are reciprocals of the principal curvature radii

$$r_1 = \frac{1}{c_1}; r_2 = \frac{1}{c_2} \qquad \text{eq. 3.1(1)}$$

By convention, a curvature towards a hydrophilic domain is defined as negative and curvature towards a hydrophobic domain accordingly positive. Thus *on average*, for micelles of surfactant in water $c_1 = c_2 < 0$, while for the lamellar phase $c_1 = c_2 = 0$ and for the saddle-like structures of the sponge and bicontinuous phases $c_1 = -c_2$ (fig. 3.1(1)).

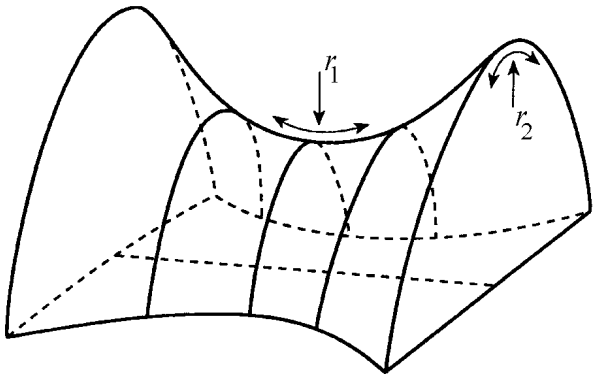

Fig. 3.1(1): depiction of a saddle-like surface and its principal radii of opposite sign[4]

The mean curvature H of an arbitrary point on the surface is defined by

$$H = \frac{1}{2}\left(\frac{1}{r_1} + \frac{1}{r_2}\right) = \frac{1}{2}(c_1 + c_2) \qquad \text{eq. 3.1(2)}$$

while the Gaussian curvature K is given by

$$K = \frac{1}{r_1} \cdot \frac{1}{r_2} = c_1 c_2 \qquad \text{eq. 3.1(3)}$$

It is stated in section 2, that the phase behaviour of systems consisting of water, hydrocarbon oil and nonionic surfactant, is strongly temperature dependent. This stems mainly from the interaction of water molecules with the ethylene oxide groups of the nonionic surfactant[52], i.e. the hydration of the EO-groups decreases with increasing temperature[53,54]. This in turn effects the preferred curvature of a surfactant film, which leads accordingly to different topologies. It could be shown by Strey[55], that the mean curvature H of systems of the type water – *n*-alkane – nonionic surfactant (C_iE_j) can be described linearly over a large temperature interval according to

$$H = c\left(\overline{T} - T\right) \qquad \text{eq. 3.1(4)}$$

where c is the temperature coefficient of curvature and $\overline{T}$ the phase inversion temperature, i.e. the mean temperature of the three phase body[56]. Similarly, the development of the principal curvatures is given by

$$c_1 = c(T_u - T) \quad \text{und} \quad c_2 = c(T_l - T) \qquad \text{eq. 3.1(5)}$$

with T_u and T_l being the upper and lower temperatures of the three-phase body respectively. Fig. 3.1(2) depicts the stated developments.

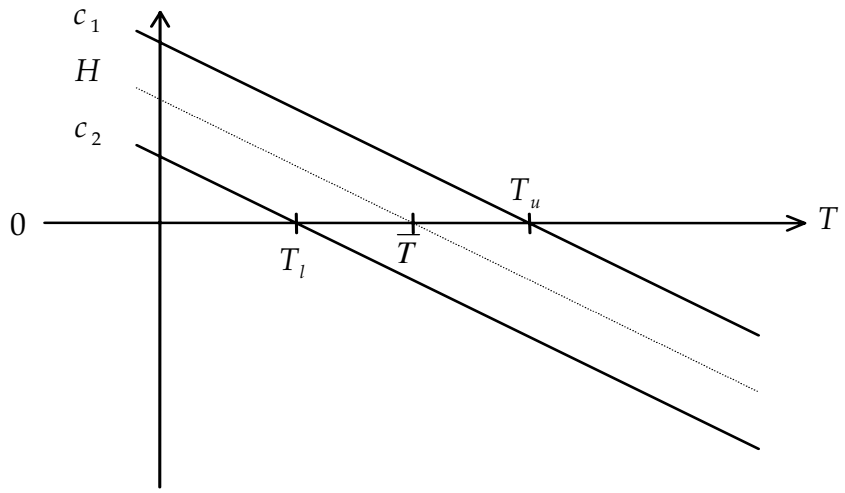

Fig. 3.1(2): temperature dependence of the principal curvatures c_1 and c_2 and the mean curvature H for a nonionic surfactant system.

Which curvature of a surfactant film is energetically favourable at a given temperature is determined by the *Helfrich* bending energy of the flexible surface model.

3.2 Bending Energy

The general expression of the bending energy E of an area element A is given by *Helfrich* via

$$E = \int \mathrm{d}A\left(2\kappa(H - 2c_0)^2 + \bar{\kappa}K\right) \qquad \text{eq. 3.2(1)}$$

where c_0 is the spontaneous curvature of the film (a theoretical quantity that signifies a film's minimum energy configuration in the absence of restrictions), and κ and $\bar{\kappa}$ are the elastic bending moduli. κ is the rigidity modulus, which quantifies a film's resistance to deformation, and $\bar{\kappa}$ is the saddle splay modulus, which defines its preferred topology. Eq. 3.2(1) is given for properties of monolayers, the corresponding adaptation for bilayers is given as part of a discussion chapter (see section 7.4.1). c_0 cannot be determined experimentally, however it is generally assumed that it should be similarly temperature dependent as the mean curvature and is therefore given by

$$c_{0,\mathrm{mono}} = c\left(\overline{T} - T\right) \qquad \text{eq. 3.2(2)}$$

It is clear from eq. 3.2(1) that the contribution to the two summation terms to the bending energy E is dependent on the film curvature, i.e. type of microstructure present. However, for the dilution of bilayer structures, *Porte et al.* [57,58] could demonstrate a *scaling invariance* of E.

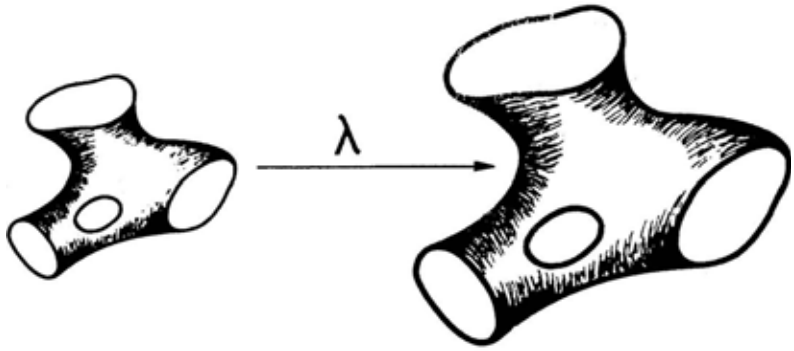

$c_1 \rightarrow c_1/\lambda$
$c_2 \rightarrow c_2/\lambda$
$dA \rightarrow \lambda^2 dA$

Fig. 3.2(1): scaling invariance of an L_3-strucuture, when experiencing a factor of elongation λ[57].

When a given structure is elongated by a given factor λ, the principal curvatures are reduced accordingly. Yet, when integrating over an increased area $\lambda^2 dA$, the value of the bending energy is constant, i.e. $E(1) = E(\lambda)$.

The lamellar and sponge phase structures are related much more closely than is apparent from their different topologies (see fig. 1.2(1)). In fact, the sponge phase is always found to border a lamellar phase in phase diagrams. The mean curvature H of the *bilayers* is zero in both cases (the monolayer mean curvature of the L_3-phase is slightly negative, i.e. curved towards the water domain). However, while the bilayer Gaussian curvature K is also zero for the L_α-phase, it is negative for the L_3-phase. Hence, it could be shown by Morse[59], that the key parameter of L_3/L_α phase stability is the saddle splay modulus $\bar{\kappa}$. Indeed, he was able to express the boundary of stability between the two phases via

$$\ln \phi_C = \frac{6\pi}{5}\left(\frac{\bar{\kappa}}{k_B T}\right) \qquad \text{eq. 3.2(3)}$$

The stability between the L_3 and L_α phase is elucidated in more detail in section 7.4.1.

4. Mechanisms of Passage Formation and Destruction

In the introduction chapter, the structures of the lamellar and sponge phases have been presented in fig. 1.2(1). Since the L_3-phase consists of a network of interconnected catenoid-like passages and the L_α-phase simply of stacks of planar sheets, it is clear that said passages must be formed when a transition from the L_α to L_3 phase occurs. Respectively passage destruction takes place in the reverse case.

4.1 Passage Formation

The creation of a passage in the lamellar phase must involve membrane fusion between two adjacent bilayers and thus can only come to pass in case of bilayer contact. In biological systems, the fusion of cell membranes is mediated and controlled by fusion proteins[60,61]. However, the thermal energy of membranes suffices to cause contact between bilayers through undulations and subsequently an intermediate structure termed a *stalk* can be formed[62,63]. This structure is of central importance in the model of membrane fusion widely accepted today and applies equally for protein-involved 'biological' fusion, as for model amphiphilic bilayer fusion. Since the stability of the stalk is calculated on the basis of the flexible surface model (section 3), which is applicable to surfactant films in general, the structure must be expected to similarly occur in the fusion of *n*-decane swollen $C_{12}E_5$ bilayers.

Although the stalk concept was first developed in the 1980s[64,65], experimental confirmation occurred only recently in a system of pure phospholipid bilayers via electron density reconstruction of lipid mesophases[66,67]. Also, details regarding its appearance and stability are still a controversial topic of current research. For the purposes of this thesis however, the actual form of the fusion intermediate is not so much of an issue as the fact that an intermediate exists at all and hence that passage formation is a two-step process[68], consisting of bilayer contact and subsequent passage formation (see section 7.4.5.5).

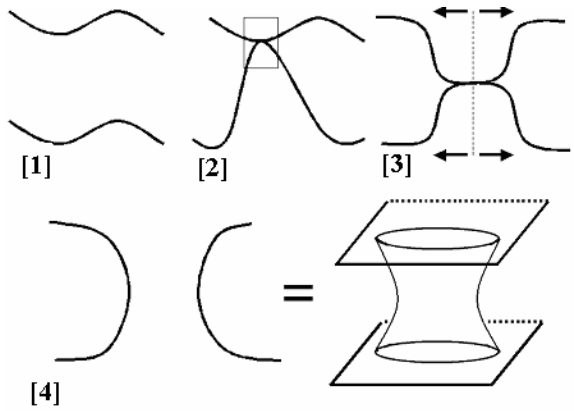

Fig. 4.1(1): schematic representation of passage formation, the individual steps are described in the text below. Each line represents a surfactant bilayer, swollen with the oil component. The depicted structures should be envisaged as cylindrically symmetric. Note that the figure merely serves as a guide in visualising the passage formation as a two-step process and that no great significance should be given to the depicted distances and bilayer curvatures.

Fig. 4.1(1) illustrates the process of bilayer fusion. [1] represents two adjacent bilayers in a lamellar phase experiencing undulations. In [2] an extraordinarily strong undulation causes bilayer contact and the formation of a metastable, intermediate structure, presumably the stalk. It is located in the boxed area and is detailed further on in fig. 4.2(3) [2], which will be explained in detail when the subject of passage destruction is addressed (see below). The bilayer configuration at this time is high in bending energy and accordingly will relax toward a structure, where the tension is more evenly distributed [3]. The bilayer is then ruptured at or near the centre via pore formation in the vertical (signified by the dashed line) and this pore expands as indicated by the arrows. Thus the structure is transformed into a catanoid-like passage [4].

4.2 Passage Destruction

In order for the lamellar phase to form within the sponge phase, the passages that form the latter must be destroyed. However, a passage cannot simply rupture, as this would result in leaving an exposed bilayer edge (with a highly curved surfactant film) of considerable length, but must separate via an energetically more favourable intermediate. The boundary region between the bulk L_3-phase and the nucleating L_α-phase (see section 7.4.5.5 and fig. 7.4.5(9)) demands continuity of the bilayers across the L_3/L_α interface[69,70]. A likely bilayer conformation that can occur at this interface is depicted in fig. 4.2(1).

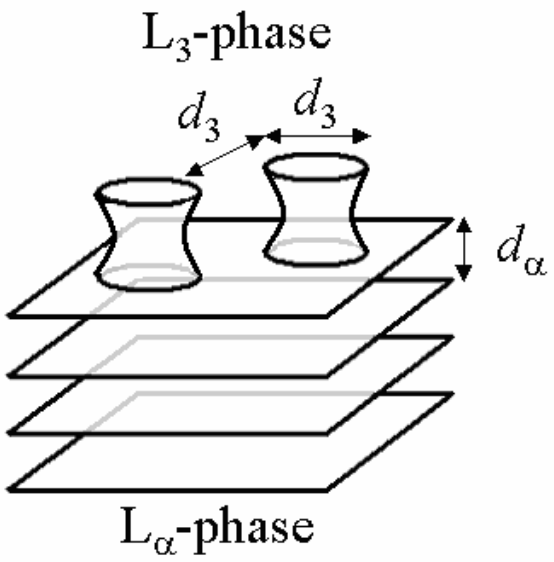

Fig. 4.2(1): schematic representation of the boundary region between the lamellar and sponge phase. The interface between the two phases corresponds to the upper lamellar layer with 'attached' passages. Each line represents a surfactant bilayer, swollen with the oil component. Note that the interbilayer distance of the lamellar phase d_α in *equilibrium* is smaller than the respective distance in the sponge phase d_3.

The actual process of passage destruction (i.e. bilayer fission) necessarily involves both the fusion and fission of monolayers. On the basis of reversing passage formation, fig. 4.2(2) illustrates the proposed mechanism. [1] represents a passage of the L_3-phase at the L_3/L_α interface akin to fig. 4.2(1). [2] An unusually strong undulation of the continuous membrane brings it into contact with itself, spanning a distance of circa d_3. (The box marks the area where membrane fusion/fission transpires. The event is detailed in fig. 4.2(3).) [3] Membrane fission has occurred and the unfavourable conformation with high bending energy can convert into the desired one of the lamellar phase, i.e. planer bilayers [4].

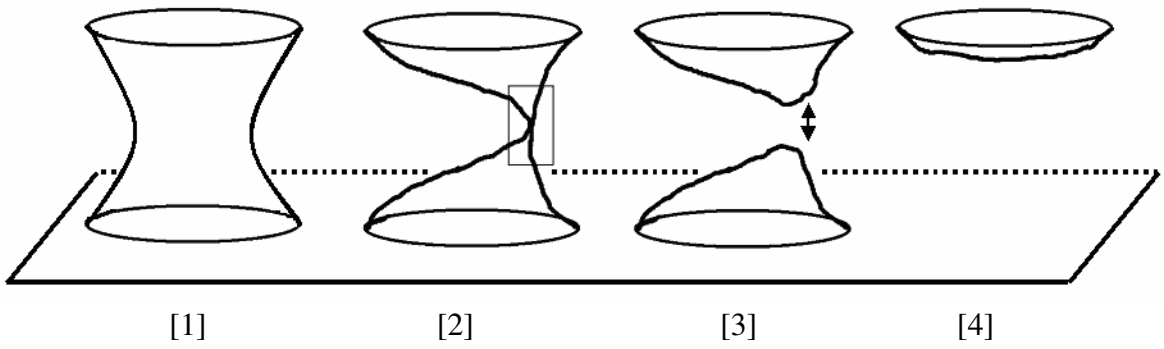

Fig. 4.2(2): the process of passage destruction in stages 1 to 4. Description is given in the text above.

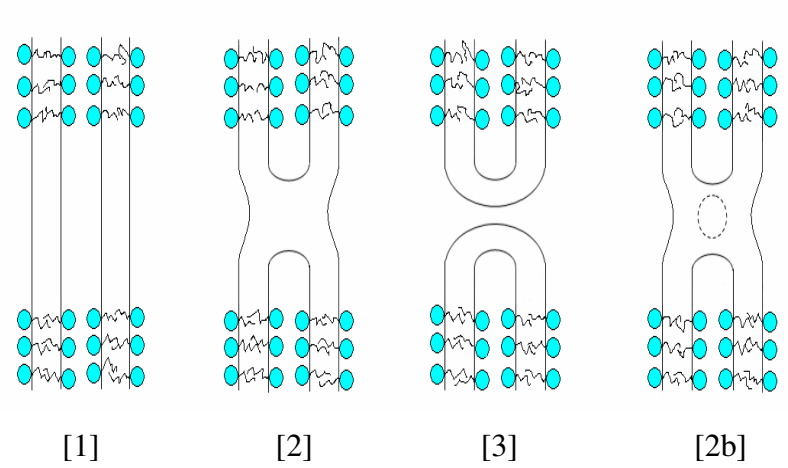

Fig. 4.2(3): detail of stalk [2] and fusion pore [3] formation as intermediates of passage destruction. The involved membranes are composed of surfactant bilayers. The circles represent the hydrophilic head groups and the squiggly lines the hydrophobic alkyl chains of the amphiphilic molecules. The structures are similar when incorporating an oil component into the bilayers.

In fig. 4.2(3) two '2-dimensional' bilayer sheets (seen from the side) approach each other to a close distance [1]. They go on to connect in a point, causing the fusion and simultaneous fission of the two touching monolayers. The result is most likely a structure termed a *stalk* [2]. Literature often continues to then classify an event termed *trans* monolayer contact[71] (TMC), before through subsequent fusion/fission of said opposed monolayers a fusion pore is formed [3]. This latter process however only leads to separation of two membrane sheets (as is shown in fig. 4.2(2) step [2] to [3]) if the stalk [2] has no noteworthy extension in any direction. Otherwise the pore will have to extend (horizontally in the example of fig. 4.2(3)) until its entrance and exit holes meet and there the membrane will have to rupture. (Imagine two holes on opposite sides of an upright cylinder. The holes expand, mainly horizontally, until they meet at two points. Both these points need to 'rupture' in order to separate the cylinder in two.)

In fig. 4.2(3), illustration [2b] serves to demonstrate the necessity of the just described rupturing. If the stalk of [2, 2b] is thought of as a 3D object of cylindrical symmetry along the vertical axis, the fusion pore might as well form in the dimension perpendicular to the sheet of paper in front of you (indicated by the dashed circle). This still leaves a small amount of surface on the right and left of the pore to rupture. However, the distance of rupturing is literally on the molecular scale and does accordingly not pose an insurmountable energy barrier as the severing of a complete passage (fig. 4.2(2)[1]), which would leave an edge of high curvature on the order of $\pi \cdot d_3$ length.

In the case of stalk formation as part of bilayer fusion, i.e. passage formation (see above), the fusion pore formed in [3] needs to expand in two dimensions. Here, these

dimensions correspond to the vertical and the dimension perpendicular to the paper. As the pore expands, the extreme curvature in its vicinity will diminish until the curvature of the resulting catenoid-like passage is attained (fig. 4.2(2)[1]).

5. Relaxation Kinetics

If the conditions in which a system exists in equilibrium are altered, then this system is perturbed and as a result will *relax* towards a new equilibrium state, corresponding to the new conditions. The speed at which this adjustment of equilibrium occurs signifies the relaxation kinetics. In order to investigate this kinetics, one requires an appropriate means of perturbation and a property of the system, which changes characteristically during the equilibration process and can be thereby monitored accurately. It is essential, that the disturbance of the system occurs significantly faster than the relaxation, as otherwise only the speed at which the disturbance transpires can be observed. Also, it is advantageous for the examined property to change considerably in magnitude, since then the sensitivity with which it is detected becomes less significant. Finally, as the property is investigated as a function of time, it is crucial for the time resolution of the detection method to be sufficiently high.

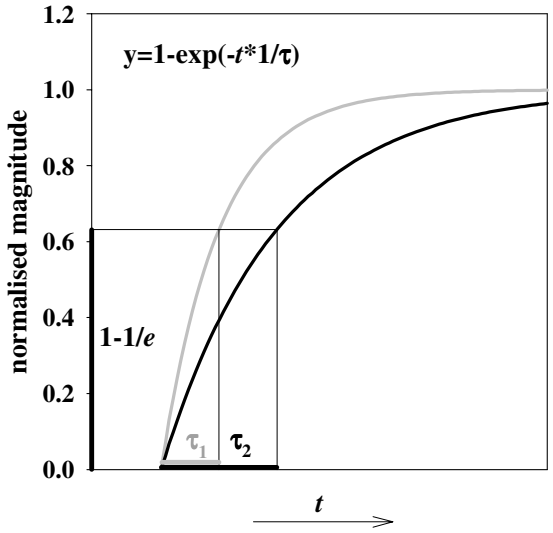

Fig. 5(1): the development of the magnitude of a parameter observed as a function of time *t*, yielding the characteristic time τ.

Often, and when the relaxation behaviour is governed by a single process, the manner in which the parameters of a system will reach their new equilibrium value can be described by a function of the form

$$y = 1 - \exp(-t \cdot 1/\tau) \qquad \text{eq. 5(1)}$$

where y is the normalised, absolute value of the investigated parameter, t the time and τ the relaxation time constant. The meaning of τ is illustrated in fig. 5(1). It corresponds to the

amount of time, starting with the initiation of the relaxation process, after which the magnitude of a parameter reaches the value 1-1/*e* ≈ 0.632 and this time is characteristic of a process.

In this thesis complex fluids of water, hydrocarbon oil and nonionic surfactant are perturbed by changing the ambient temperature and thereby initiating a change in the surfactant bilayer conformation from the sponge L_3 to the lamellar L_α structure or *vice versa*. Primarily, this phase transition is monitored by ^{2}H-NMR spectroscopy. The changes of temperature required to achieve the transitions are relatively small (~1 to 2°C). However, temperature within NMR spectrometers is simply controlled via an air flow, so that a few minutes are required to reach thermal equilibrium when dealing with samples on the order of cubic centimetres in volume. One of the incentives, to attempt this type of investigation in the first place was the fact, that the relaxation kinetics *within the L_3-phase* of the system of interest, at high dilution, are very slow (on the order of tens of minutes)(fig. 5(2)).

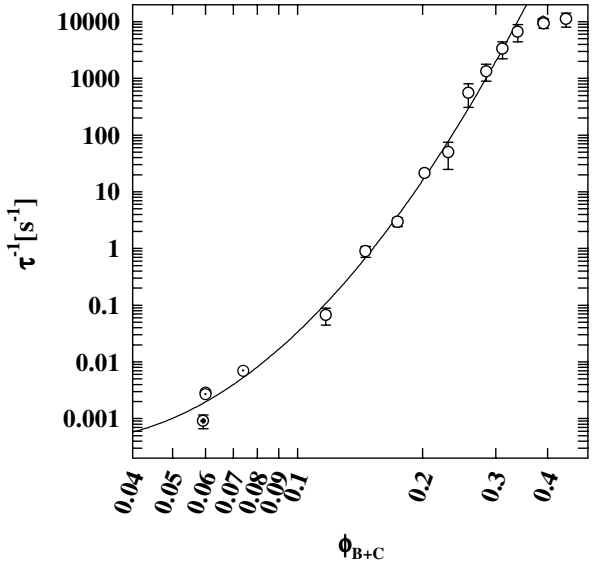

Fig. 5(2): plot of relaxation rates τ^{-1} obtained from small temperature jumps performed within the sponge phase of the water/NaCl – *n*-decane – $C_{12}E_5$ system at ω_b=0.45. Data are taken from refs. [72] and [46].

Fig 5(2) plots the relaxation rates τ^{-1} as a function of the bilayer volume fraction. For $0.1 < \phi_{B+C} < 0.4$ fast temperature jumps were performed using the Joule- heating technique[72]. At lower bilayer concentrations ($\phi_{B+C} < 0.1$) the relaxation times become greater than the temperature reequilibration time of the *T*-jump apparatus (~20s). The data in this region was therefore determined by transferring samples from a water bath to a spectrometer set at slightly higher temperature or via isothermal shearing[46]. For the temperature jump experiments, the method of detection was light scattering and it was found that the relaxation times were independent of the probing length scale, i.e. the magnitude of the scattering vector.

It was concluded that the relaxation time has to be associated with structural change. Based on the theoretical model of the sponge phase[73], a temperature increase should result in a bilayer structure with more passages, i.e. a more negative Euler- Poincaré characteristic χ_E. As it seemed reasonable to assume, that global phase transformation from L_3 to L_α, or *vice versa*, (which is associated with a similar structural change), should not occur at faster rates, the use of alternative, slower detection methods therefore became conceivable.

While NMR has a time resolution that is far inferior to light scattering, it turned out that this is not an issue, since spectra of great signal to noise ratio could have been taken circa every 2s (see section 10.4.4). Thus, for these experiments only the rate of temperature change is of importance (see section 7.2.6.1). Additionally a second method of investigation, namely small angle neutron scattering (SANS), is employed in this work. Its time resolution depends of course on just how well a sample scatters and the intensity of the neutron beam (see section 10.5). Unfortunately, high dilution is not conducive to strong scattering and neutron flux cannot compare to photon flux. Hence, acquisition of a single spectrum of good signal to noise ratio requires tens of seconds. However, with long relaxation times being determined in the NMR experiments, SANS experiments of moderate time resolution (120s/spectrum) became possible.

6. Nucleation

6.1 Classical Nucleation Theory

The experiments dealing with the sponge to lamellar phase transition presented in this thesis will demonstrate that said transition occurs through a *nucleation and growth* process. This means that the lamellar phase first appears within the sponge phase in a small volume, a nucleus, which then goes on to expand in size, all the time converting volume of the sponge structure into the lamellar structure. This expansion is defined as 'growth'. In general, many nuclei of an emerging phase form during a (first order) phase transition at random or given sites (see below) within the phase of origin and each of these nuclei will experience growth until the entire volume in question is converted. The process of nucleation, i.e. the formation of centres which have the ability to grow, is most basically described by what nowadays is known as the Classical Nucleation Theory or simply, CNT [74,75].

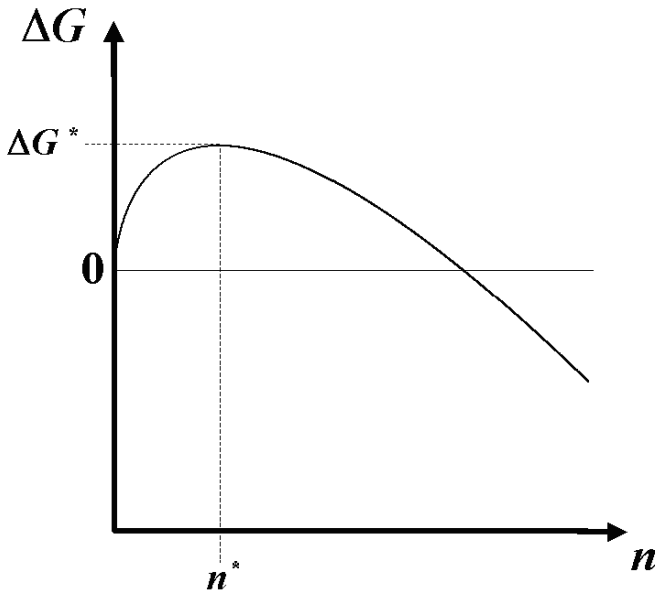

Fig. 6.1(1): development of Δ*G* a nucleus as function of its particle number *n*. A maximum Δ*G** is attained in case of the critical nucleus of *n** particles.

The concepts of nucleation are most easily understood when considering the nucleation of (liquid) droplets from a single component gaseous phase. Such a phase transition occurs spontaneously, when it leads to the reduction of the Gibbs free enthalpy *G* of the system ($\Delta G < 0$). In other words, it takes place if (on average) the chemical potential μ of a particle (e.g. an atom, when considering a monoatomic gas) is lower in the liquid state than in the gas state. The difference in chemical potential Δμ is known as *supersaturation* and it is

the driving force of first order phase transitions ($\Delta\mu = \Delta\mu_{new} - \Delta\mu_{old} < 0$). However, when a given number of particles n first adhere, i.e. a nucleus of n particles is formed, this is generally *not* energetically favourable. Fig. 6.1(1) plots schematically the development of the difference in Gibbs free enthalpy of a nucleus as a function of its particle number n.

As long as a nucleus contains fewer than n^* particles, further accretion is associated with an increase of the Gibbs free enthalpy of a system, i.e. it does not occur spontaneously and such a nucleus therefore termed a *subnucleus*. Only when the number n^* has been surpassed is accretion equivalent to a decrease of Gibbs free enthalpy and such a (spontaneously growing) nucleus is known as a *supernucleus*. A nucleus of n^* particles is a *critical nucleus* and its maximum ΔG^* represents an energy barrier for the formation of a supernucleus (*nucleation barrier*). Thus nucleation is a kinetically hindered process and is governed by the statistics of particle accretion.

Accordingly, the nucleation rate J, which gives the number of supernuclei forming per unit of time and volume, is expressed via a *Boltzmann* approach to

$$J = K_J \exp\left(\frac{-\Delta G^*}{k_B T}\right) \qquad \text{eq. 6.1(1)}$$

K_J is the kinetic prefactor and it is associated with the diffusion of material (particles) to a developing subnucleus. Hence an increase in the nucleation rate J occurs exponentially for a reduction of the nucleation energy barrier ΔG^* as depicted in fig. 6.1(2).

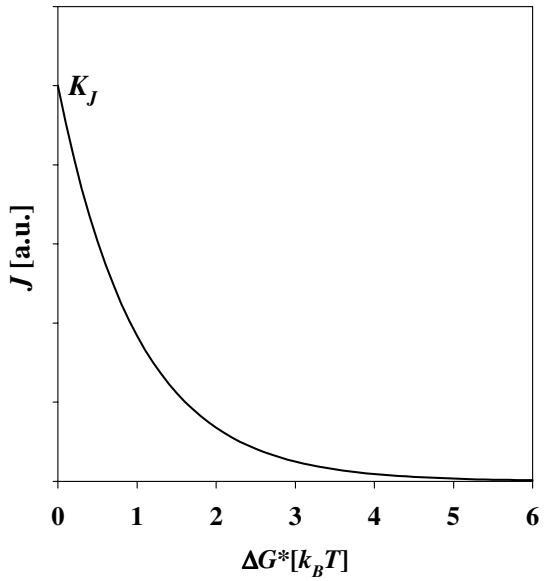

Fig. 6.1(2): evolution of the nucleation rate J as a function of the nucleation barrier ΔG^*

The form of the ΔG development in fig. 6.1(1) stems from the fact that the interface of a nucleus with the surrounding phase is energetically unfavourable, i.e. there is a surface energy σ (an energy per unit area arising from surface tension, $\sigma > 0$). Thus ΔG is the result of two opposing terms, one an expression for G reduction through transforming n particles from the old to the new phase ($\Delta\mu < 0$), the other an expression for G increase due to the formation of the nucleus interface. With the assumption of a spherical nucleus of radius r_n one obtains

$$\Delta G = n \cdot \Delta\mu + 4\pi r_n^2 \sigma \qquad \text{eq. 6.1(2)}$$

Since, the radius of a nucleus related to the particle number n via the particle volume eq. 6.1(2) can be expressed either as a function n or r_n.

In the phase transition studied, there is of course no accretion of particles when the lamellar phase nucleates. Instead a given area of bilayer surface changes topology and thus n of eq. 6.1(2) must be interpreted as a unit area of bilayer surface which results in the reduction of the system's Gibbs free enthalpy by $\Delta\mu$ when it is transformed. Furthermore, although the lamellar phase is anisotropic in nature, lamellar nuclei will be considered spherical for simplicity.

Since the basic idea of nucleation has been clarified, a closer look can now be taken at the characteristics of nucleation. If a system is perfectly pure, then nucleation will occur at random sites within the bulk of the old phase. This type of nucleation is known as *homogeneous nucleation*. In practice however, a given phase will contain many impurities, such as ions, impurity molecules, and foreign nanoparticles. Often, the nucleation barrier at the site of such an impurity is significantly lower than in the bulk phase, and accordingly *heterogeneous nucleation* occurs on these *nucleation active centres*. If the nucleation barrier of homogenous nucleation is simultaneously so high that none will take place in a realistic time frame, then heterogeneous nucleation will occur exclusively and the total number of supernuclei cannot exceed the number of active centres. In reality, it is often the case that both types of nucleation occur when observing macroscopic systems. It should be noted that nucleation at a sample's container wall is of course heterogeneous nucleation.

One can also distinguish between a *mononuclear* and a *polynuclear* mechanism. The first is generally rare, as it involves the suppression of homogeneous nucleation, while providing a single nucleation active centre. Thus the statistically relevant polynuclear mechanism is of interest in this work. If the nucleation barriers are high a considerable amount of time may pass until the first formation of a supernucleus. This time is referred to as

the onset or *onset time*. However, in this thesis supernuclei of minimal size are not detected and the term onset time will refer to the interval until a first amount of the emerging phase is registered.

6.2 The KJMA Model

This dissertation focuses in part on the sponge to lamellar phase transition and specifically on the kinetics involved. In order to investigate these kinetics, the volume fraction of the emerging phase φ (the lamellar phase) must be determined as a function of time. A theoretical model, that yields this type of description for a nucleation and growth mechanism was developed by *Kolmogorov*[76], *Johnson*, *Mehl*[77] and *Avrami*[78,79,80] (KJMA).

The KJMA model considers the growth of domains starting from infinitesimal size at time $t = 0$ and takes into account the termination of growth in regions where two domains touch and would overlap if growth would have continued. The model predicts a sigmoidal time dependence of the volume fraction of the new phase φ with an initial acceleration, due to the increase in interfacial area where the transformation occurs, and a deceleration at an advanced point in time, due to more and more domains having grown into contact. The model also considers the two cases with a fixed number of nuclei at $t = 0$ (short nucleation period) or a continuous formation of nuclei during the transformation with a constant rate (constant nucleation or long nucleation period). When there is a constant rate of nucleation, nucleation is termed 'stationary' (as opposed to its 'non-stationary' counterpart).

Furthermore, the model considers domain growth (with constant speed) in three, two or only one dimensions. Since it was initially conceived for the crystallisation of a single component system, it does not account for component information, and it is used unaltered to describe in approximation the multi-component transitions observed. The general expression of the KJMA model is

$$\varphi = 1 - \exp\left\{-(kt)^{\alpha}\right\} \qquad \text{eq. 6.2(1a)}$$

$$\alpha = n + \psi \qquad \text{eq. 6.2(1b)}$$

where the exponent α depends upon the dimensionality n of the nuclei growth (n = 1,2 or 3) and ψ designates if there is only a short nucleation period ($\psi = 0$) or if nucleation occurs continuous throughout the transition process ($\psi = 1$). The constant k is the rate constant of the

transition and it is the reciprocal of the relaxation time constant τ ($k = 1/\tau$). k contains terms describing the (constant) nucleation rate and the constant speed at which the nuclei grow, but the actual expression[81] is not necessary for this work. Domain growth is assumed to be spherical in three dimensions, as the growth speed is set identical for all directions. Also, the nuclei (both the initial ones and those of later times in case of constant nucleation) must be distributed randomly in space.

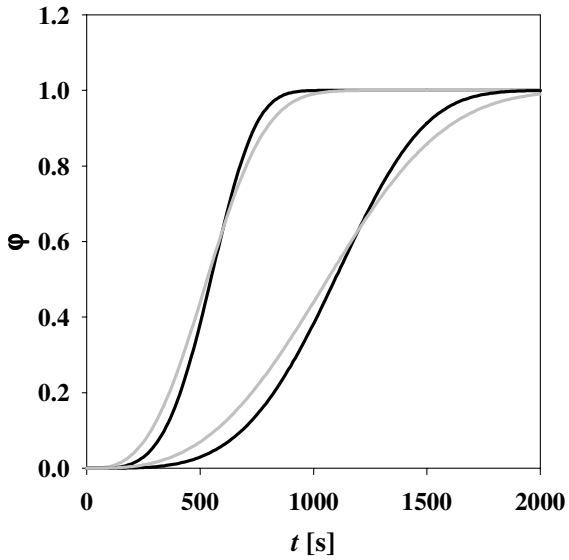

Fig. 6.2(1): results for the KJMA equation. The grey lines correspond to α=3, the black ones to α=4. τ = 600s and 1200s (visible as the points of intersection of the α=3 and α=4 curves).

Fig. 6.2(1) illustrates the development of φ calculated for two values of τ, both with an exponent α of 3 and 4, corresponding to 3D nucleation with a short and continuous nucleation period. Note that at the time $t = \tau$, the KJMA equation leads to a value independent of the exponent α, that is $\varphi = -1/e \approx 0.632$ as $k\tau = 1$, and the sigmoidal lines can be seen to cross at this point. Also note the similarity of the KJMA equation with eq. 5(1).Thus τ designates how extended or stretched the sigmoidal curve is, while α determines its steepness.

7. NMR-Spectroscopy

Nuclear magnetic resonance (NMR) is the absorption of electromagnetic radiation by an atomic nucleus with the quantum mechanical property of spin $\vec{L}$, when situated in a strong magnetic field $\vec{B}$. The absorption occurs at its resonance frequencies which are of the radiofrequency (r.f.) range and results in altering the magnetic moment $\vec{\mu}$ of the nucleus. In general, resonance is the physical phenomenon that energy is most effectively transferred to a system when the natural frequency of that system (vibrational or other) and the frequency of an oscillating energy carrier are equivalent. As interactions on the scale of atomic particles are observed, rigorous treatment of NMR requires a complex, quantum mechanical approach. However, in order to understand the simple experiments presented in this thesis a semi-classical approach using a vector formalism is generally sufficient. This is possible as an NMR sample is composed of a large number of particles, i.e. it contains a large ensemble of spins and consequently magnetic moments $\vec{\mu}$ and the vector sum of these magnetic moments is, of course, another vector $\vec{M}$. $\vec{M}$ represents the macroscopic or bulk magnetisation of the sample and it behaves in a classical manner.

As a rule, spectroscopic methods observe a physical quantity as function of frequency. In the early stages of NMR spectroscopy, this quantity was the absorption of r.f. electromagnetic radiation. Modern NMR spectroscopy, however is effectively emission spectroscopy, as the relaxation (after prior perturbation through r.f. radiation) of the sample's overall magnetisation $\vec{M}$ is monitored through registering the induction of an electromotive force in a receiver coil.

Since the 1950's, when the first commercially available spectrometers appeared, the number of NMR applications has grown far beyond the original use of structure analysis of organic compounds in solution, to expand into the most diverse fields of modern research. At present, NMR is an invaluable tool for the study of mineral and protein complexes and is even employed in the investigation of superconductors and the development of quantum computing. Even non-scientists are directly affected by the advancements in NMR. In the form of its medical application MRI (magnetic resonance imaging), it is routinely used to produce tomographic images of soft tissues in order to identify tumours, infarcts etc.

In this thesis, NMR-spectroscopy is the predominant method of investigation. It is employed to quantify the amounts of isotropic and anisotropic (sub-) domains in the temperature induced phase transition from an isotropic complex liquid (the L_3- or sponge

phase) to an anisotropic, lyotropic liquid crystal (the L_α- or lamellar phase) and *vice versa*, in a three component system consisting of water, hydrocarbon oil and nonionic surfactant. In doing so, one not only gains insight into the transition kinetics but also into the mechanisms of surfactant bilayer fusion and fission involved.

7.1 Basic Principles

This section gives a brief introduction to the physics of NMR-spectroscopy in order to understand the origins of the signals detected in the experiments of this thesis. The presented theory has been well established for many years and is based on publications of *Abragam*[82], *Atkins*[83], *Callaghan*[84], *Carrington* and *McLaugchlan*[85], *Harris*[86], and *Homans*[87]. Where a more in-depth understanding of a topic is required, specific references are given. Note that all vectorial variables are denoted with an arrow symbol ($\vec{x}$).

7.1.1 Spin Angular Momentum and Magnetic Moment

Spin or internal angular momentum $\vec{L}$ is a quantum mechanical property of many fundamental particles and it requires the theory of special relativity for full description. The magnitude of $\vec{L}$ is given by

$$\left\|\vec{L}\right\| = \hbar\left[I\left(I+1\right)\right]^{1/2} \qquad \text{eq. 7.1.1(1)}$$

where I is the so called nuclear spin quantum number, but the term ‘spin’ is often used for simplicity. It is limited to integer or half integer values. Particles with spin of the former kind are known as bosons, while those of the latter are referred to as fermions. Interestingly, all known building blocks of matter are fermions, while it is bosons that mediate the forces of interaction between them. In the quantum world, not only the magnitude of angular momentum is quantised, but additionally its orientation. This is reflected by the fact that the magnitude of the spin angular momentum with respect to an arbitrary axis in space is given by

$$\left\|\vec{L}_z\right\| = m_I\hbar \qquad \text{eq. 7.1.1(2)}$$

m_I is the magnetic quantum number and for nuclear spins possesses values of $m_I = I$, $I - 1$, …, $-I$. Thus, the vector of spin angular momentum can occupy $2I + 1$ discrete orientations in space. An atomic nucleus is composed of protons and neutrons (both particles of $I = 1/2$), which couple their spin angular momenta (also referred to simply as spins) either parallel or anti-parallel (two possible orientations each) so that only their total is observed and the nucleus can be treated as single particle. Theoretically, this coupling can lead to a variety of spin states in heavy nuclei. However, the energy difference between the ground spin state and higher states is so large (transitions between nuclear spin states involve gamma rays), that the latter may be ignored for NMR purposes. For example deuterium, the ^{2}H isotope of hydrogen, has a nucleus composed of a proton and a neutron and could therefore exhibit either a nuclear spin state of $I = 0$ or $I = 1$. But with the energy difference between the spin states amounting to ~10^{11} kJmol^{-1}, the ^{2}H nuclei are effectively only $I = 1$ particles.

A simple estimate of the nuclear spin quantum number of an element can be made, when the number of its protons and neutrons is known, as the following rules apply:

- nuclei with an even number of both protons and neutrons exhibit no spin ($I = 0$)
- nuclei with an uneven sum of protons and neutrons possess half integer spin (I = 1/2, 3/2, 5/2 …)
- nuclei with an uneven number of both protons and neutrons possess integer spin (I = 1, 2, 3…)

Note that nuclei free of spin ($I = 0$) are inactive in NMR experiments.

Charges in motion have an associated magnetic field. As such, the spin angular momentum $\vec{L}$ of an atomic nucleus is associated with a magnetic moment $\vec{\mu}$, which is correspondingly quantised in magnitude as well as orientation. The two vectors are proportional and, depending on the species of the nucleus, either parallel or anti-parallel. This later point is irrelevant for all following discussions and therefore the dominating case of parallelism will be assumed.

$$\vec{\mu} = \gamma \cdot \vec{L} \qquad \text{eq. 7.1.1(3a)}$$

$$\vec{\mu}_z = \gamma \cdot \vec{L}_z \qquad \text{eq. 7.1.1(3b)}$$

The (scalar) proportionality constant γ is referred to as the gyromagnetic ratio and depends on the type of nucleus involved.

7.1.2 The Influence of a Magnetic Field

As long as an isolated nucleus is outside of a magnetic field $\vec{B}$ (in terms of a magnetic flux density), its energy is independent of the orientation of its spin angular momentum $\vec{L}$. However, upon introducing $\vec{B}$, and therefore a preferred direction in space for the magnetic moment $\vec{\mu}$, the $2I + 1$ spin states defined by m_I (eq. 7.1.1(2)) are no longer degenerate. When defining $\vec{B}$ as being of the z-direction, the energy of a magnetic moment $\vec{\mu}$ is calculated classically by

$$E_{m_I} = -\left\|\vec{\mu}_z\right\| \cdot \left\|\vec{B}\right\| = -\gamma \cdot m_I \hbar \cdot \left\|\vec{B}\right\| \qquad \text{eq. 7.1.2(1)}$$

whereas the second part of the equation is derived using eq. 7.1.1(3b) and eq. 7.1.1(2). The energy difference between two neighbouring states ($\Delta m_I = \pm 1$, the selection rule) then calculates to

$$\Delta E_{m_I} = -\gamma \cdot (m_I + 1)\hbar \cdot \left\|\vec{B}\right\| + \gamma \cdot m_I \hbar \cdot \left\|\vec{B}\right\| = \gamma \cdot \hbar \cdot \left\|\vec{B}\right\| \qquad \text{eq. 7.1.2(2)}$$

Fig. 7.1.2(1) illustrates the energy levels, which are referred to as Zeeman energy levels, of the various spin states inside and outside a magnetic field in the case of an $I = 1/2$ and $I = 1$ nucleus.

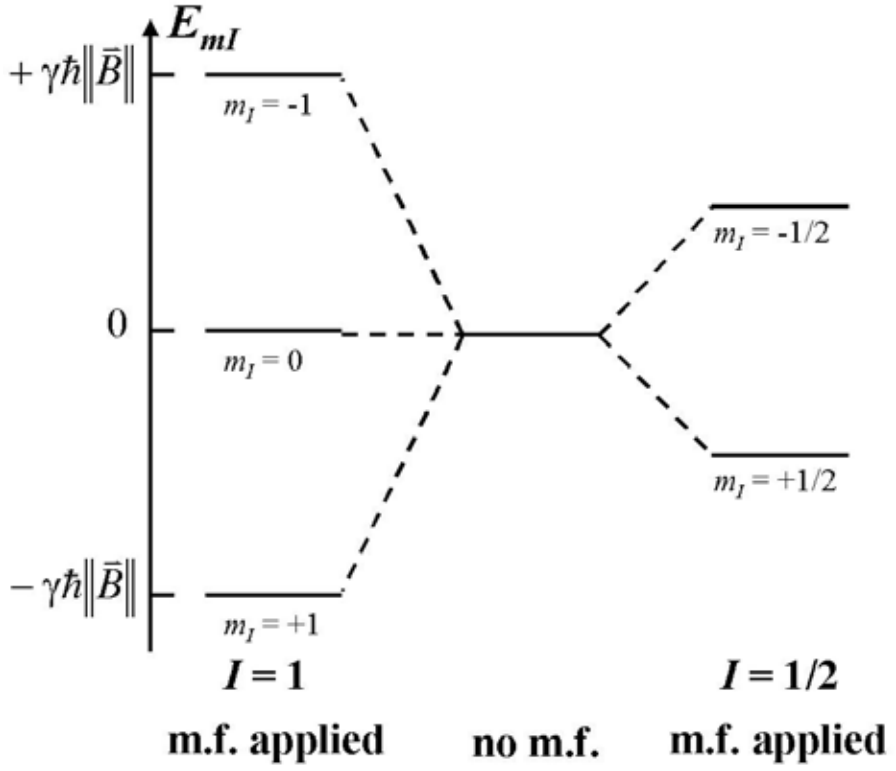

Fig. 7.1.2(1): the effect of a magnetic field (m.f.) on the Zeeman energy levels of $I = 1/2$ and $I = 1$ nuclei.

In the case of no magnetic field, i.e. degeneracy, the occupancy of each spin state is of equal probability. When this degeneracy is lost due to the introduction of a magnetic field, the occupancy of each state in *thermal equilibrium* is given by the Boltzmann distribution. In the case of $I = 1/2$ particles the two possible spin states are often referred to as α (the lower energy state) and β, so that the respective occupancy ratio is given by

$$\frac{N_\alpha}{N_\beta} = \exp\left(-\frac{\Delta E_{m_I}}{k_B T}\right) = \exp\left(-\frac{\gamma \cdot \hbar \cdot \|\vec{B}\|}{k_B T}\right) \qquad \text{eq. 7.1.2(3)}$$

It is this discrepancy in occupancy, which results in a net magnetisation $\vec{M}$ of the overall sample, which corresponds to an amount of magnetic moment per unit volume. If one considers only a single type of atomic nucleus, its magnitude corresponds to

$$\|\vec{M}\| = \frac{N \cdot \gamma^2 \hbar^2 \cdot \|\vec{B}\| \cdot I(I+1)}{3 k_B T} \qquad \text{eq. 7.1.2(4)}$$

Note, that the magnitude of magnetisation is directly proportional to the number of (specific) atomic nuclei N of the sample and therefore the signal intensity (see below) can be linked directly to concentration. The reciprocal dependency on the absolute temperature T is known as Curie's law.

The use of a vector formalism in NMR is particularly advantageous as it makes the simple visualisation of (even complex) NMR experiments possible. Assuming the most basic case of $I = 1/2$ nuclei, fig. 7.1.2(2) demonstrates the influence of a magnetic field.

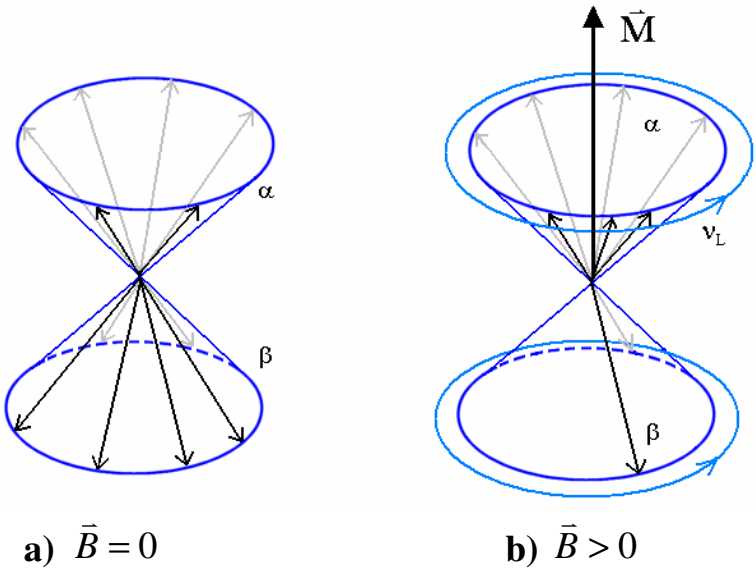

Fig. 7.1.2(2): visualisation of spin angular momenta of an ensemble of $I = 1/2$ atomic nuclei, outside (a) and inside (b) of a magnetic field in terms of the vector formalism

As stated above, in the absence of a magnetic field the α and β spin states of $I = 1/2$ nuclei are equally populated (fig. 7.1.2(2a)). Although the spin angular momentum with respect to *one* arbitrary axis in space is known exactly according to eq. 7.1.1(3b), the components of $\vec{L}$ with respect to the two perpendicular axes in space are completely unspecified. This is a direct result of Heisenberg's uncertainty principle, which prohibits the (simultaneous) exact definition of several components of the angular momentum. As such, the positions of the vectors, which at this point are thought of as stationary, on the surface of a cone are unknown. However, as there is no preferred direction in space, they are randomly, i.e. evenly, distributed. The introduction of a magnetic field, and subsequent loss of degeneracy of the energy levels, not only causes a change in the occupancy of the spin states according to eq. 7.1.2(3), but also causes a torsional moment or torque to act on the magnetic moment and the (parallel) spin angular momentum. However, as this torque can only change the component of spin angular momentum perpendicular to $\vec{B}$, the result is a precession of $\vec{L}$

around $\vec{B}$. This situation is analogous to the ensuing precession of a gyroscope, where the axis of rotation is perpendicular to the gravitational field, when said gyroscope is tipped sideways. The angular velocity (and frequency) of the precession is then given by

$$\omega_L = 2\pi \cdot \nu_L = \gamma \cdot \left\| \vec{B} \right\| \qquad \text{eq. 7.1.2(5)}$$

ν_L is known as the Larmor frequency. It is important to note, that the described precession is not real and only serves to demonstrate the energy differences of the spin states within the confines of the vector model. The magnetisation $\vec{M}$ in fig. 7.1.2(2) does not have components in the *x*- or *y*-direction, as the magnetic momenta are still evenly distributed over the surface of the two cones. Literature often does not list the gyromagnetic ratio of a nucleus type, but instead the so called *g*-factor g_I, which is directly proportional to γ but without dimension. They are related according to

$$g_I \cdot \mu_N = \gamma \hbar \qquad \text{eq. 7.1.2(6)}$$

where μ_N is the nuclear magneton, which derives directly from a proton's mass and charge.

7.1.3 The Influence of Radiofrequency Radiation

When one combines eq. 7.1.2(2) and eq. 7.1.2(5) the result is

$$\Delta E_{m_I} = \gamma \cdot \hbar \cdot \left\| \vec{B} \right\| = h \cdot \nu_L \qquad \text{eq. 7.1.3(1)}$$

Therefore, transition between two neighbouring spin energy states of a nucleus can be induced by electromagnetic radiation of the Larmor frequency, since this satisfies the Bohr frequency condition. The condition states that energy is transferred to a particle when the energy difference between two of its states is equal to $h\nu$, where ν is the frequency of the radiation. Eq. 7.1.3(1) is generally true for NMR transitions, since 'allowed' transitions follow selection rules from quantum mechanics, which state that $\Delta m_I = \pm 1$ and only one spin can be transformed per transition (single quantum transition).

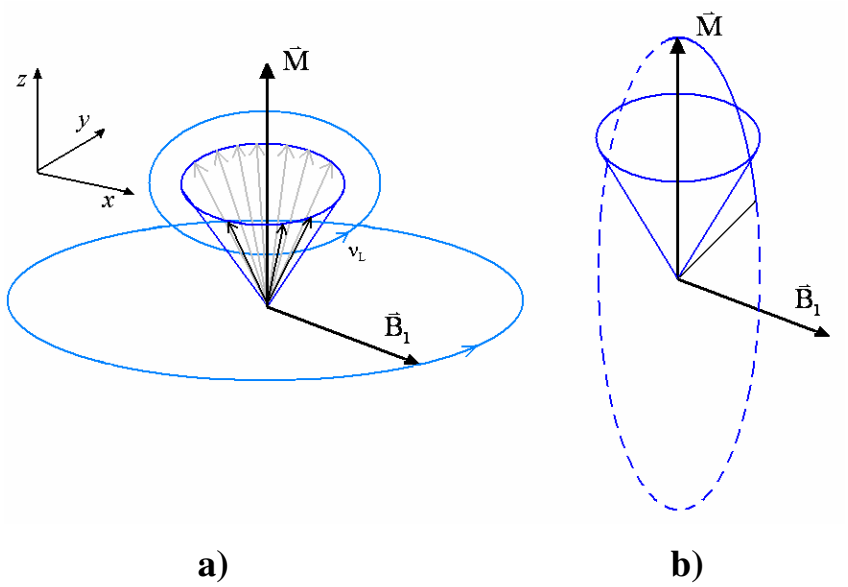

Fig. 7.1.3(1): illustration of the effect of r.f. radiation, which is polarised in the *xy*-plane and of the Larmor frequency, on an ensemble of spin angular, and thus magnetic, momenta. a) r.f. radiation rotates in the *xy*-plane resulting in $\vec{B}_1$ b) torque causes precession of $\vec{M}$

Electromagnetic radiation consists of an electric and magnetic field which are perpendicular to each other. In the case of NMR only the magnetic component must be considered. Assuming one applies a (phase-coherent) r.f. pulse, which is polarised in the *xy*-plane and of the Larmor frequency, along the *x*-axis, then this results in a magnetic field $\vec{B}_1$ rotating in said plane (fig. 7.1.3(1a)). The spin angular (and thus magnetic) momenta precessing around the *z*-axis with the same frequency experience thus a constant torque and this results in a new precession of the overall magnetisation $\vec{M}$ around $\vec{B}_1$ (fig. 7.1.3(1b)) (this situation is analogous to the one described above resulting in the precession around $\vec{B}$). Note, that the individual spin momenta are still situated on the two cones. The direction of overall magnetisation is changed, since a number of spin angular momenta is transformed into the higher energy state β *and* the distribution of the vectors over the surface of the cones is no longer even. In fact, after a pulse, they all tend towards the same position with regard to the *x*- and *y*-axes (but still precess with ν_L) and are said to be in a state of *phase coherence*, so that the $\vec{M}_x$ and $\vec{M}_y$ components of the magnetisation are then non-zero.

If the duration of the r.f. pulse, which depends upon the field strength of $\vec{B}_1$, is chosen appropriately, then a particular number of spin angular momenta are transformed from the α to the β state, so that equal populations of these two states result. The magnetisation $\vec{M}$ is shifted into the *xy*-plane in this manner, as the component of the magnetisation along the *z*-axis equals zero, and there the magnetisation then rotates with the Larmor frequency. Such a

pulse is referred to as a 90°-pulse, since the magnetisation changes direction by that angle. By using a sequence of pulses of appropriate duration, i.e. different 'angles', and different temporal spacing, complicated NMR experiments can be performed leading to a variety of information. However in this thesis, only the most basic type of pulse sequence, consisting of a single 90°-pulse, was employed (see section 10.4.2). Note that in modern NMR-spectroscopy the Larmor frequency of the target nuclei must not be known or scanned, as a broadband pulse is applied, which excites all nuclei over a broad range of frequencies.

7.1.4 Signal Detection, Free Induction Decay (FID) and Lineshape

Once the magnetisation has been shifted into the *xy*-plane, it induces an electromotive force proportional to its magnitude in a receiver coil (situated along the *y*-axis), as it rotates in said plane with ν_L. However, after the excitation of the nuclei with the 90°-pulse, the magnetisation relaxes back to its thermal equilibrium value over time. This is expressed by the phenomenologically formulated Bloch equations (that hold for ideal systems only, see section 7.1.5), which are given below for the rotating frame, i.e. the coordinate system *x*', *y*', *z* that rotates with the Larmor frequency ν_L around the *z*-axis of the previously utilized laboratory frame *x*, *y*, *z*:

$$\frac{\mathrm{d}\left\|\vec{M}_{x'}\right\|}{\mathrm{d}t} = (\omega_L - \omega)\left\|M_{y'}\right\| - \frac{\left\|\vec{M}_{x'}\right\|}{T_2} \qquad \text{eq. 7.1.4(1a)}$$

$$\frac{\mathrm{d}\left\|\vec{M}_{y'}\right\|}{\mathrm{d}t} = -(\omega_L - \omega)\left\|M_{x'}\right\| - \frac{\left\|\vec{M}_{y'}\right\|}{T_2} + \gamma \cdot \left\|\vec{B}_1\right\| \cdot \left\|\vec{M}_z\right\| \qquad \text{eq. 7.1.4(1b)}$$

$$\frac{\mathrm{d}\left\|\vec{M}_z\right\|}{\mathrm{d}t} = -\gamma \cdot \left\|\vec{B}_1\right\| \cdot \left\|\vec{M}_{y'}\right\| - \frac{\left(\left\|\vec{M}_z\right\| - \left\|\vec{M}\right\|\right)}{T_1} \qquad \text{eq. 7.1.4(1c)}$$

T_1 and T_2 are time constants which describe the relaxation in the longitudinal (*z*) and transverse (*x*, *y*) directions respectively. Modern NMR experiments monitor both the *x*- and the *y*-component of the magnetisation as a function of time with a single phase sensitive, quadrature detector along the *y*-axis. Nuclei of identical local magnetic environment lead to the induction of a signal that has the form of a damped oscillator (if one considers only one of the transverse components of the magnetisation, i.e. $\vec{M}_x$ or $\vec{M}_y$), since $\vec{M}_x$ and $\vec{M}_y$ precess

with the Larmor frequency, but grow (in the ideal case exponentially) weaker in magnitude over time due to relaxation. For the two transverse components of the magnetisation after a 90°-pulse

$$\left\|\vec{M}_x\right\| = \left\|\vec{M}\right\| \sin(\omega_L \cdot t) \cdot \exp(-t/T_2) \qquad \text{eq. 7.1.4(2a)}$$

$$\left\|\vec{M}_y\right\| = \left\|\vec{M}\right\| \cos(\omega_L \cdot t) \cdot \exp(-t/T_2) \qquad \text{eq. 7.1.4(2b)}$$

apply. In reality, the detected signal, which is known as the Free Induction Decay (FID) is a superposition of damped oscillators (an interferogram), as nuclei of different local magnetic environments (see section 7.1.6), and therefore different ν_L, contribute in intensity proportionally to their occurrence. Furthermore, it is complex in the mathematical sense, as both components of the magnetisation in the *xy*-plane must be considered and these are 90° out of phase.

$$f(t) = (\cos \omega t + \mathrm{i} \sin \omega t) \cdot \exp(-t/T_2) = \exp(\mathrm{i}\omega t) \cdot \exp(-t/T_2) \qquad \text{eq. 7.1.4(3)}$$

In order to obtain the actual NMR-spectrum, i.e. the signal in the frequency domain, the FID must be transformed from its time domain. The mathematical procedure achieving this is known as Fourier transformation.

$$f(\omega) = \int_{-\infty}^{+\infty} f(t) \exp(\mathrm{i}\omega t) \mathrm{d}t \qquad \text{eq. 7.1.4(4)}$$

The real part of an FID and its spectrum after transformation are depicted in fig. 7.1.4(1).

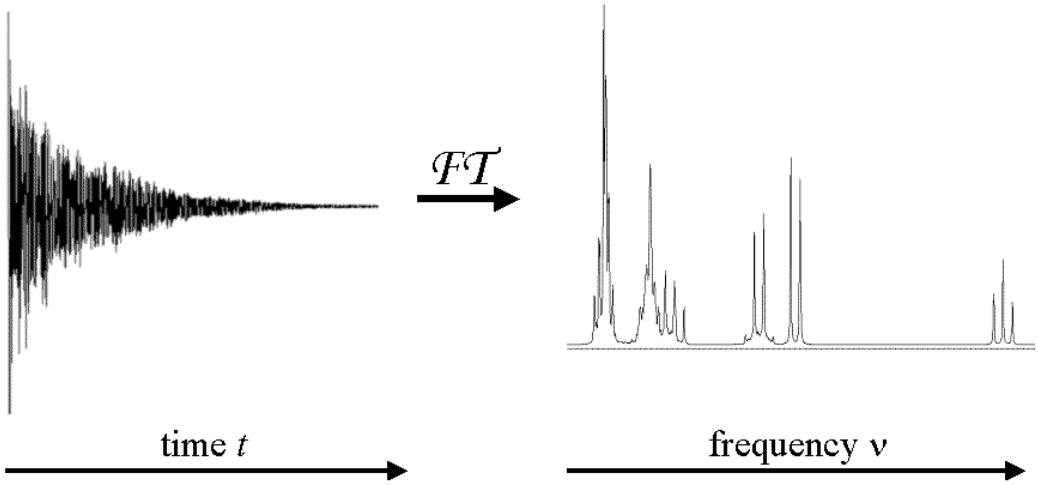

Fig. 7.1.4(1): an intricate FID (*left*) and its resulting signals in the frequency domain after Fourier transformation (*right*).

Fourier transforming a decaying exponential from the time domain, leads to a peak, a Lorentzian function, at zero frequency. One refers to this as a Lorentzian lineshape. If this decaying exponential is additionally oscillating sinusoidal or cosinusoidal, then the result is still a Lorentzian, but offset from zero by the frequency of the oscillation (in NMR experiments ν_L). A general expression for the Lorentzian function in term of the spectra's intensity $I(\nu)$ is

$$I(\nu) = \frac{I^{\max}}{1 + \left(2(\nu - \nu_L)/\Delta\nu_{1/2}\right)^2} \qquad \text{eq. 7.1.4(5)}$$

where $I^{\max}$ corresponds to the maximum intensity of the peak and $\Delta\nu_{1/2}$ to the peak width at half height. The steady state solutions (i.e. the time derivatives equal zero) of the Bloch equations are

$$\left\|\vec{M}_{x'}\right\| = \frac{\left\|\vec{M}\right\| \cdot \gamma \cdot \left\|\vec{B}_1\right\| \cdot T_2^2 (\omega_L - \omega)}{1 + T_2^2 (\omega - \omega_L)^2 + T_1 \cdot T_2 \cdot \left(\gamma \cdot \left\|\vec{B}_1\right\|\right)^2} \qquad \text{eq. 7.1.4(6a)}$$

$$\left\|\vec{M}_{y'}\right\| = \frac{\left\|\vec{M}\right\| \cdot \gamma \cdot \left\|\vec{B}_1\right\| \cdot T_2}{1 + T_2^2 (\omega - \omega_L)^2 + T_1 \cdot T_2 \cdot \left(\gamma \cdot \left\|\vec{B}_1\right\|\right)^2} \qquad \text{eq. 7.1.4(6b)}$$

respectively. Assuming that the population of the energy levels is not altered significantly by the r.f. pulse, i.e. the pulse is so weak that $\left(\gamma \cdot \left\|\vec{B}_1\right\|\right)^2 << T_1 T_2$ applies, eq. 7.1.4(6b) simplifies to

$$\left\|\vec{M}_{y'}\right\| = \frac{\left\|\vec{M}\right\| \cdot \gamma \cdot \left\|\vec{B}_1\right\| \cdot T_2}{1 + 4\pi^2 \cdot T_2^2 (\nu - \nu_L)^2} \qquad \text{eq. 7.1.4(7)}$$

Upon comparing eq. 7.1.4(7) with eq. 7.1.4(5), one sees that in the frequency domain $\left\|\vec{M}_{y'}\right\|$ describes a Lorentzian lineshape centred around ν_L, whereas

$$I^{\max} = \left\|\vec{M}\right\| \cdot \gamma \cdot \left\|\vec{B}_1\right\| \cdot T_2 \qquad \text{eq. 7.1.4(8)}$$

$$\Delta\nu_{1/2} = \frac{1}{\pi \cdot T_2} \qquad \text{eq. 7.1.4(9)}$$

$\left\|\vec{M}_{y'}\right\|$ is referred to as the absorptive component of the NMR-spectrum, while $\left\|\vec{M}_{x'}\right\|$ is known as the dispersive component. The NMR-spectrum of the frequency domain is complex, therefore

$$f(\omega) = \left\|\vec{M}_{y'}\right\| + i \cdot \left\|\vec{M}_{x'}\right\| \qquad \text{eq. 7.1.4(10)}$$

applies. However, for analysis, only the real part of the NMR-spectrum must be considered and it is this absorptive component with its Lorentzian peak(s) that is plotted. In case of multiple peaks, each has its origin in the relaxation of the $\left\|\vec{M}_{y'}\right\|$ component of the magnetisation stemming from a group of nuclei of identical local magnetic environment (see section7.1.6). There is no additional information in the dispersive component, as both components are inextricably liked, i.e. they are related by the Hilbert transform. For practical reasons it is important to be aware that a weighted combination of the absorptive and the dispersive component is detected, if the phase sensitive detector is, in terms of phase, not properly aligned along the *x*' or *y*' coordinate.

Although, $\vec{B}_1$ is in general adequately weak, so that the population of the energy levels is not significantly altered, a quick succession of excitation pulses can lead to major deviations from the thermal equilibrium distribution and even to a state known as *saturation*. This is the case, if the time between pulses is too short for the spin states to relax back to their Boltzmann distribution. Saturation is an equalisation of spin state populations, i.e. in the $I = 1/2$ case equal amounts of α and β spins are present. It is important not to confuse this situation with the one after the application of a 90°-pulse (section r.f. radia), as in case of saturation there is a complete lack of phase coherence. Consequently, the magnetisation equals zero in each of its components.

Eq. 7.1.4(8) states that the height of the Lorentzian peaks is proportional to the magnitude of the overall magnetisation of the sample and therefore, taking eq. 7.1.2(4) into account, proportional to the number of nuclei from which the signal originates. Thus, for cases in which T_2 is constant for different peaks, the height of different peaks can be directly

linked to the concentration of the nuclei from which each signal originates and the concentration ratio of those nuclei to each other. If however T_2 is variable, then the area under each peak, i.e. its integral must be considered. This is given by

$$\int_{-\infty}^{+\infty} I(\nu)\mathrm{d}\nu = 0.5 \cdot \pi \cdot I^{\max} \cdot \Delta\nu_{1/2} = 0.5 \cdot \left\|\vec{M}\right\| \cdot \gamma \cdot \left\|\vec{B}_1\right\| \qquad \text{eq. 7.1.4(11)}$$

and is independent of T_2.

7.1.5 Relaxation and Correlation Time τ_c

The relaxation of the components of the magnetisation $\vec{M}$ back to their values at thermal equilibrium, stems from thermal, i.e. random, motions of charged particles, as these motions give rise to (time dependent) magnetic fields at particular locations, where these fields interact with the quantum states of the observed nuclei. For nuclei of $I > 1/2$ electric fields may also contribute to relaxation (see section 7.1.8). The probability of spontaneous decay of an exited state in NMR is so small, that it can be neglected. The relaxation theory, for which a rough overview is given in this section, was first described by Bloembergen, Purcell and Pound[88] (BPP theory). It is only valid in the case of 'weak-collision', i.e. when for the correlation time τ_c, $\tau_c < T_2$ holds. This is the case in not too rigid materials.

The longitudinal relaxation constant T_1 describes the relaxation of the z-component of the magnetisation (eq. 7.1.4(1c)). As this magnetisation is caused by altering the occupancy of the Zeeman energy levels (fig. 7.1.3(1)), the corresponding relaxation involves energy transfer from the excited (β) spin state to the systems 'lattice', i.e. the degrees of freedom of the molecules, and the term *spin-lattice relaxation* is used. Contrariwise, the transverse relaxation is described by T_2, and as the magnetisation components of the xy-plane arise from the phase coherence of the spin angular momenta (section 7.1.3), it is consequently the loss of this coherence over time which causes relaxation. However, as opposed to the spin-lattice relaxation, energy is only transferred between spin angular momenta, i.e. via mutual spin flips, and the total Zeeman energy is unaffected. Accordingly, the term *spin-spin relaxation* is used. Note that the longitudinal relaxation (T_1) does not affect the Lorentzian lineshape (eq. 7.1.4(7)), and therefore does not affect the appearance of the NMR-spectra.

While the mechanisms of longitudinal and transverse relaxation are different, the actual processes (fluctuating electromagnetic fields) causing the relaxations are basically

identical. For instance, all processes causing longitudinal relaxation also cause transverse relaxation. The most important among these are: magnetic dipole-dipole interactions among the nuclei (modulated by molecular tumbling and translational diffusion), a variation of the magnetic shielding (section 7.1.6) in time (due to molecular reorientation due to tumbling in $\vec{B}$), interactions with magnetic fields stemming from coherent molecular rotation, time dependent spin-spin coupling (section 7.1.7), and interactions with unpaired electrons. Transverse relaxation is additionally caused by zero frequency fluctuations, i.e. differences in the local static fields (see below).

In general, relaxation is most effective when the interactions in question involve fluctuations near the Larmor frequency ν_L. Therefore rotational and diffusional motions are of prime importance (in liquids), while electronic motions and molecular vibration can normally be discounted. In order to calculate (and understand the origin of) T_1 and T_2, one needs to describe theoretically the frequency distributions of all motions relevant for the relaxation process. This is achieved using spectral density functions $J(\omega)$, which give a measure of the power at frequency ω. However to begin with, the oscillatory motions are a function of time $f(t)$. The autocorrelation function of $f(t)$ is given as

$$\rho(\tau) = \int_{-\infty}^{+\infty} f^*(t) \cdot f(t+\tau) \mathrm{d}t \qquad \text{eq. 7.1.5(1)}$$

where $f^*(t)$ represents the complex conjugate of the function $f(t)$. Eq. 7.1.5(1) describes the correlation between the value of $f(t)$ at time t and at a time differing by τ, i.e. it gives a measure of the persistence of fluctuations. Thus, $\rho(\tau)$ usually expresses high values for small τ and rapidly decays to zero as τ increases. This decay is especially swift in the case of noise (i.e. no correlation), while the autocorrelation functions of periodic functions, e.g. the sine function, do not decay and express a finite value. In many cases however, the decay is exponential with a time constant τ_c and eq. 7.1.5(1) is given as

$$\rho(\tau) = \overline{f^*(t) \cdot f(t)} \cdot \exp\left(-|\tau| / \tau_c\right) \qquad \text{eq. 7.1.5(2)}$$

where $\overline{f^*(t) \cdot f(t)}$ represents the mean square average of the two functions involved and τ_c is known as the correlation time. This condition of exponential decay of $\rho(\tau)$ holds for the description of the relaxation phenomena, as long as the involved motions are isotropic. A

perhaps better understanding of τ_c can be achieved by noting that, if a molecule exists in a given state for τ_c s, this is associated with frequency components in the region of τ_c^{-1} Hz. For small molecules (molecular mass < 100 amu) in aqueous solution of normal viscosity $\tau_c \sim 10^{-12}$ - 10^{-13}s, while macromolecules may possess τ_c around 10^{-8} s. Thus, as a rule more mobile solutions have smaller τ_c.

The Fourier transformation of an autocorrelation function is the power spectrum of the original function, and therefore the spectral density functions $J(\omega)$ can be determined using this approach. It can be shown that

$$J(\omega) = \frac{2\tau_c}{1+\omega^2\tau_c^2}\overline{f^*(t)\cdot f(t)} \qquad \text{eq. 7.1.5(3)}$$

and in particular

$$\frac{1}{T_1} = J(\omega) + J(2\omega) \qquad \text{eq. 7.1.5(4)}$$

$$\frac{1}{T_2} = J(0) + J(\omega) + J(2\omega) \qquad \text{eq. 7.1.5(5)}$$

where $J(0)$ is a measure of the aforementioned zero frequency fluctuations. For fast motions, i.e. $\omega\tau_c << 1$, $J(0)$ is small, so that $T_2 \approx T_1$. This condition is known as the *extreme narrowing limit*. In general, rapid motions give rise to Lorentzians of smaller width at half height, i.e. a narrower lineshape. On the other hand, when $\omega\tau_c >> 1$, $T_2 << T_1$ and this condition, which is known as the *spin-diffusion limit*, applies to macromolecules. Fig. 7.1.5(1) summarises the behaviour of the relaxation time constants with respect to the correlation time.

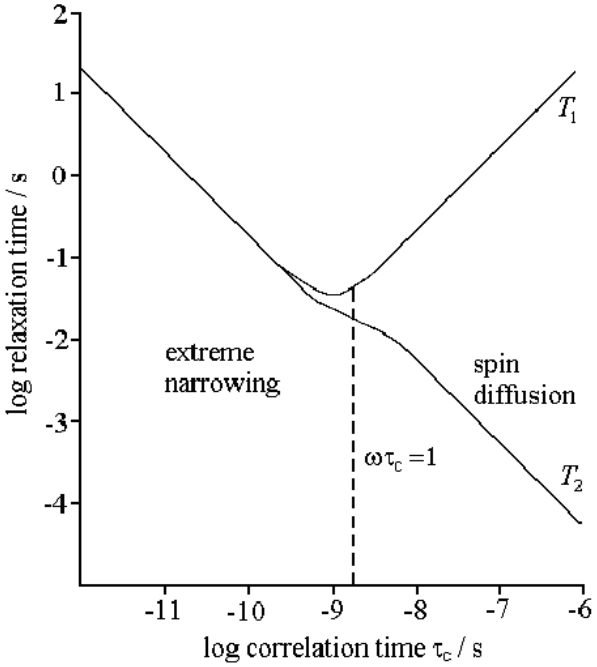

Fig. 7.1.5(1): the relaxation time T_1 and T_2 constants as function of the correlation time τ_c for (magnetic) dipole-dipole interactions of ^{1}H-nuclei at ν_L = 200MHz. Note the minimum of T_1 in the vicinity of the $\omega_L\tau_c = 1$ region and the double logarithmic scale. This figure is reproduced from ref. [87].

In liquids T_1 is on the order of 1s and T_2 slightly less or equal to this value. In fact at the T_1 minimum $T_2 = 2/3\ T_1$.

Up to this point, the presence of an ideal, i.e. perfectly constant and homogenous, magnetic field $\vec{B}$ has always been assumed. However, in reality the effective relaxation time constant T_2^* is either substantially decreased with respect to its 'true' value T_2 or even entirely dominated by a term T_2', which arises from the inhomogeneity of the magnetic field.

$$\frac{1}{T_2^*} = \frac{1}{T_2} + \frac{1}{T_2'} \qquad \text{eq. 7.1.5(6)}$$

The contribution of T_2' is sometimes referred to as inhomogeneity broadening, thus eq.7.1.4(9) must be modified accordingly. In order to minimise its effect, samples are generally spun (with the rotational axis parallel to the magnetic field) with a frequency of 15 Hz. Magnetic field inhomogeneity causes relaxation, since certain nuclei experience different field strengths and accordingly precess with different Larmor frequencies, which in turn quickens the loss of phase coherence.

The longitudinal and unmodified transverse relaxation time T_1 and T_2 can be determined experimentally. The former by what is known as the *inversion recovery sequence*, the latter by using the *Carr-Pucell-Meiboom-Gill* pulse sequence. It is important to stress, that

especially in cases where anisotropic motions are significant, i.e. in complex fluids, the autocorrelation function (eq. 7.1.5(2)) of the system studied does not necessarily decay as a single exponential or at all exponentially. As a result, T_2 is not a single value and this leads to NMR-spectra, where the peaks are of non-Lorentzian lineshape or even unsymmetrical.

7.1.6 Magnetic Shielding, Chemical Shift and Equivalent Nuclei

In an NMR-spectrum one usually plots only peaks originating from the nuclei of a single element, as the resonance frequencies ν_L of different elements lie very far apart. This is due to the differences between their gyromagnetic ratios γ (eq. 7.1.2(5)). If one considers the case of a complex organic molecule in solution (ignoring the type of solvent at this point) and focuses on the ^{1}H-nuclei, then each of the individual nuclei of a single molecule might experience a *local* magnetic environment $\vec{B}_{local}$, which differs slightly from the overall magnetic field $\vec{B}$. Consequently, all these nuclei resonate at somewhat different Larmor frequencies.

$$\nu_L = \frac{\gamma \cdot \left\| \vec{B}_{local} \right\|}{2\pi} = (1-\sigma)\frac{\gamma \cdot \left\| \vec{B} \right\|}{2\pi} \qquad \text{eq. 7.1.6(1)}$$

Usually the local magnetic field is of lesser magnitude than the overall one, so that the shielding constant σ is positive. Of course, in order to detect an NMR signal, a single molecule is far from sufficient (eq. 7.1.2(4)) and accordingly the solution must contain a multitude of molecules. However, in each of theses molecules, ^{1}H-nuclei of equivalent position will (usually) be shielded to the same degree. The reason for this is, that the shielding constant σ at given nucleus position depends upon the chemical surroundings and these are identical, *on a time scale inherent to the NMR experiment* (see section 7.1.9) for indistinguishable molecules. Thus, NMR spectra actually yield information on the local magnetic field $\vec{B}_{local}$ of ensembles of nuclei corresponding to a particular position in a molecule of a given type, as each of these ensembles leads to single peak in the spectrum. The integral under that peak is then proportional to the number of nuclei in the ensemble (eq. 7.1.4(11), eq. 7.1.2(4)). However in practice, a peak is often divided (split) into two or even more peaks, due to spin-spin interactions (section 7.1.7)

The reduction of the field strength of the magnetic field $\vec{B}$ at the site of a nucleus, i.e. the shielding, occurs due to $\vec{B}$ inducing ring currents in the electron clouds of the molecule, which in turn cause a small, additional magnetic field that opposes $\vec{B}$. In an empirical approach, one can divide the origin of the shielding constant σ into three general contributions

$$\sigma = \sigma(local) + \sigma(molecule) + \sigma(solvent) \qquad \text{eq. 7.1.6(2)}$$

σ(*local*) refers to a contribution which arises mainly due to the electrons of the atom (nuclei) in question, while σ(*molecule*) is caused by the electronic motions of the remaining atoms in the molecule and σ(*solvent*) combines interactions with the surrounding molecules. As σ(*local*) depends upon the electron density, it is very small for hydrogen and its isotopes. σ(*molecule*) varies greatly depending on the magnetic susceptibility of the surrounding (groups of) atoms, and aromatic ring systems as well as other delocalised π-electrons are exceptionally relevant. The contribution of σ(*solvent*) is of particular importance in polar solvents and when the interaction between solvent and solved molecule is strong, e.g. in the case of ionic and hydrogen bonding.

NMR spectra are often presented as a function of the chemical shift δ, which is the difference between the Larmor frequency ν_L of the detected nuclei and the Larmor frequency of nuclei of reference ($\nu_{L,0}$).

$$\delta = \frac{\nu_L - \nu_{L,0}}{\nu_{L,0}} \cdot 10^6 \qquad \text{eq. 7.1.6(3)}$$

Due to its definition, the chemical shift δ is of the unit ppm. It is important to note that the differences of the Larmor frequencies of specific nuclei (and thus δ) increase proportionally with the strength of the applied magnetic field $\vec{B}$ (eq. 7.1.6(1)). Therefore, stronger magnets lead to spectra of increased resolution.

Often nuclei at different positions in a molecule can have identical chemical surroundings due to symmetry. Such nuclei, which are said to be equivalent or isochronous, contribute of course to the same signal as they have the same chemical shift. However, if their spin-spin coupling (section 7.1.7) with another specific nucleus is different, their signal peak will be split in different manners and their peaks will ultimately appear in different locations

of the spectrum. Nuclei of this sort are considered only *chemically equivalent*, while nuclei which have the same degree of spin-spin coupling with all other atoms of their molecule are *magnetically equivalent*.

7.1.7 Spin-Spin Coupling

The local magnetic field at the site of a nucleus is also effected by the magnetic momenta of other nuclei in the molecule. However, the so called spin-spin coupling is not the *direct* dipolar coupling interaction (which generally averages to zero, section 7.1.8), but an *indirect* coupling, which is transmitted via the electrons of the system and therefore purely an intramolecular quantity. The result of this coupling is a splitting of the signal of a given nucleus, as the nucleus (or nuclei) it couples with, occupies spin states of different Zeeman energies (when considering the ensemble of molecules). The appearance of the splitting is subject to the number and the spin quantum number I of the nuclei that the nucleus in question interacts with (although *not* its own spin I), and the resulting peaks are centred upon the Larmor frequency the signal would appear in, in the absence of coupling.

Depending on the number of peaks present due to coupling, the split signal is referred to as a doublet, triplet etc. or simply a multiplet. The distance between the individual peaks of such a multiplet is constant (in terms of frequency) and quantified by a coupling constant J_{AX} (of the unit Hz), where the subscript labels the nuclei involved. J_{AX} is determined solely by the strength of the interaction, i.e. it is *independent* of the magnetic field strength $\vec{B}$. In general, it is however strongly dependent upon the distance between the nuclei in question. The multiplets of an NMR spectrum are referred to as its fine structure and it is the information given by their form and coupling constants which enables the determination of even complex structures of organic compounds and makes the identification of compounds in a mixture possible.

As a multiplet originates from a certain number of nuclei, the integral over all its peaks is identical to the value which would be determined in the case of lack of coupling. Nevertheless, the intensity distribution among the individual peaks is uneven, except in case of a doublet, but symmetric with respect to its central frequency. However, this symmetry is only existent, as long as the difference of the chemical shift of the coupling nuclei is large when compared with their coupling constant, i.e.

$$\nu_{L,0}\Delta\delta >> J \qquad \text{eq. 7.1.7(1)}$$

In cases where eq. 7.1.7(1) applies, the spectra are referred to as being of *first order* and, in the simple case where the interaction is only between two nuclei, the spin system is termed an AX-system. When the terms of eq. 7.1.7(1) are more similar, the intensity distribution becomes complex and the associated spectra of the AB-systems are known as being of *second order*. However, if the coupling occurs between two equivalent nuclei (A_2-system), i.e. $\nu_{L,0}\Delta\delta << J$, then it is ineffective, i.e. no splitting results and a singlet is detected. Generally, in terms of spin-spin coupling, a group of equivalent nuclei can be treated as a single nucleus.

In section 7.1.6 it was demonstrated that a high magnetic field strength is essential to achieving good resolution in an NMR spectrum. This is all the more the case, when considering systems, where (perhaps multiple) spin-spin coupling is present. Increasing $\vec{B}$ effectively increases the distance between multiplets (eq. 7.1.6(3)), possibly reducing spectra of second order to those of first order (eq. 7.1.7(1)).

7.1.8 Quadrupolar Interactions

Nuclei with spin quantum numbers greater than 1/2 possess an *electric* quadrupole moment, arising from the 'spatial' distribution of their positive charges. The fact that deuterium nuclei ($I = 1$) also exhibit this phenomenon, although they each contain only a single proton, is evidence for the underlying quark structure of the subatomic particles (protons and neutrons). While electric monopoles (charges) are affected by an electric potential V, electric dipoles are only influenced by a potential gradient, i.e. an electric field $\mathrm{d}V / \mathrm{d}z$. A quadrupole, however, does not interact with a homogenous electric field, since it can be considered as two dipoles back-to-back, but only with an inhomogeneous field, i.e. an electric field gradient (efg) $\mathrm{d}^2V / \mathrm{d}z^2$. It is important to note that nuclei do not posses electric dipoles.

Quadrupole moments are intrinsic properties of a given nucleus type and they are usually expressed as eQ, where e is the elementary charge and Q a quantity which is normally referred to as the electric quadrupole moment of a nucleus. Q has the dimension of a length squared and is usually given in units of *barn* ($1\mathrm{barn} = 10^{-28}\,\mathrm{m}^2$). It also possesses a sign, depending on the type of distribution of the positive charge(s) with respect to its symmetry axis, which is determined by the nuclear spin. One speaks of *prolate* and *oblate* quadrupoles, the former having a positive moment and the latter having a negative one.

A nucleus with a quadrupolar moment thus interacts with the efg of its molecule at the location of that nucleus. However, since electric influences are relatively short in range, it suffices in approximation to consider only the electrons of the nucleus in question as cause of said efg. Moreover, only cases of non-spherical distribution must be respected, i.e. all filled electron shells and *s* electrons can be discounted, as long as they are non-binding. As such, quadrupolar interactions are purely intramolecular.

The efg is represented mathematically by a tensor field of 2nd rank (often simply termed a Cartesian tensor), i.e. a 3x3 matrix. The form of this matrix can be understood when considering that the three faces of a cube-shaped infinitesimal volume are each subject to a given force. The vector components of said force are also three, due to the number of spatial dimensions. Thus, 3x3, or 9 components are required to describe the forces at this cube-shaped infinitesimal segment, which is then treated as a point.

When a nucleus in question is at a position of *axial electrical symmetry*, only a single field gradient must be considered for interaction, i.e. a single component q_{zz} of the efg tensor

$$e\left\|\vec{q}_{zz}\right\| = \frac{\partial^2 V}{\partial z^2} \qquad \text{eq. 7.1.8(1)}$$

This symmetry occurs in good approximation quite often, especially in the case of monovalent atoms (e.g. ^{2}H or ^{35}Cl), which exhibit a single bond. There, the direction of $\vec{q}_{zz}$ coincides with the direction of said bond.

In the absence of a magnetic field, the spin energy levels of a nucleus are only determined through quadrupolar interaction and are given by

$$E_{mI} = \frac{1}{4} e^2 \left\|\vec{q}_{zz}\right\| \cdot Q \cdot \left(\frac{3m_I^2 - I(I+1)}{3I^2 - I(I+1)} \right) \qquad \text{eq. 7.1.8(2)}$$

This leads to a new type of spectroscopy known as nuclear quadrupole resonance (NQR), which however is not subject of this thesis. As the magnitude of the quadrupolar moment of a nucleus type can not be determined through NQR experiments (nor NMR for that matter), constants of eq. 7.1.8(2) are often unified to the nuclear quadrupole coupling constant χ, which is of units of frequency.

$$\chi = \frac{e^2 \left\| \vec{q}_{zz} \right\| \cdot Q}{h} \qquad \text{eq. 7.1.8(3)}$$

χ is of course specific for each nucleus (even if they are of the same type) of a molecule, as the efg is location dependent.

When a nucleus of $I > 1/2$ is situated in a magnetic field, both the energy due to the nuclear Zeeman interaction (eq. 7.1.2(2)) and the energy from the quadrupolar interaction need to be considered (eq. 7.1.8(2)). In NMR experiments the magnetic field strength is so high, that the Zeeman term predominates and the energy levels are only perturbed through the quadrupolar effects

$$E_{mI} = -\gamma \cdot m_I \hbar \cdot \left\| \vec{B} \right\| + \frac{3}{8} \chi h \left[\frac{3m_I{}^2 - I(I+1)}{3I^2 - I(I+1)} \right] \left(3\cos^2 \theta - 1 \right) \qquad \text{eq. 7.1.8(4)}$$

Thus, the direction of quantisation is still given through the magnetic field, rather than the electric field. Therefore an angular dependence of the quadrupolar perturbance arises, with θ being the angle between $\vec{q}_{zz}$ and $\vec{B}$. As the selection rule $\Delta m_I = \pm 1$ is still valid, the difference between the energy levels is now given by

$$\Delta E_{m_I} = h \cdot \nu_Q = h \cdot \nu_L - \frac{3}{8} \chi h \left[\frac{3m_I{}^2 - I(I+1)}{3I^2 - I(I+1)} \right] \left(3\cos^2 \theta - 1 \right) \qquad \text{eq. 7.1.8(5)}$$

where m_I ranges from I to $-I + 1$ and ν_Q corresponds to the resonance frequency (Bohr frequency condition) of the transition. It is clear that ν_Q is a function of the magnetic quantum number of the attained energy state. In fact, the spectrum will consist of $2I$ lines, which are symmetrically distributed around ν_L, and the quadrupolar splitting $\Delta\nu_Q$ between adjacent lines is given by

$$\Delta\nu_Q = \frac{3}{4} \chi \left[\frac{1}{3I^2 - I(I+1)} \right] \left| \left(3\cos^2 \theta - 1 \right) \right| \qquad \text{eq. 7.1.8(6)}$$

It is important to note that $\Delta\nu_Q$ is independent of the magnetic field strength.

The existence of $2I$ distinct lines infers that the angle θ is constant for the entirety of quadrupolar nuclei probed in the experiment. This condition is most frequently met in a single crystal, i.e. when performing solid state NMR. However, if a powder is present, θ will vary for each of the many crystallites and the result will be a superposition of accordingly many multiplets, each given by eq. 7.1.8(5). Fig. 7.1.8(1a) illustrates the part of the function of eq. 7.1.8(5), which describes the angular dependence, and fig. 7.1.8(1b) illustrates the variation of a normalised quadrupolar splitting $\Delta\nu_Q$ as function of θ.

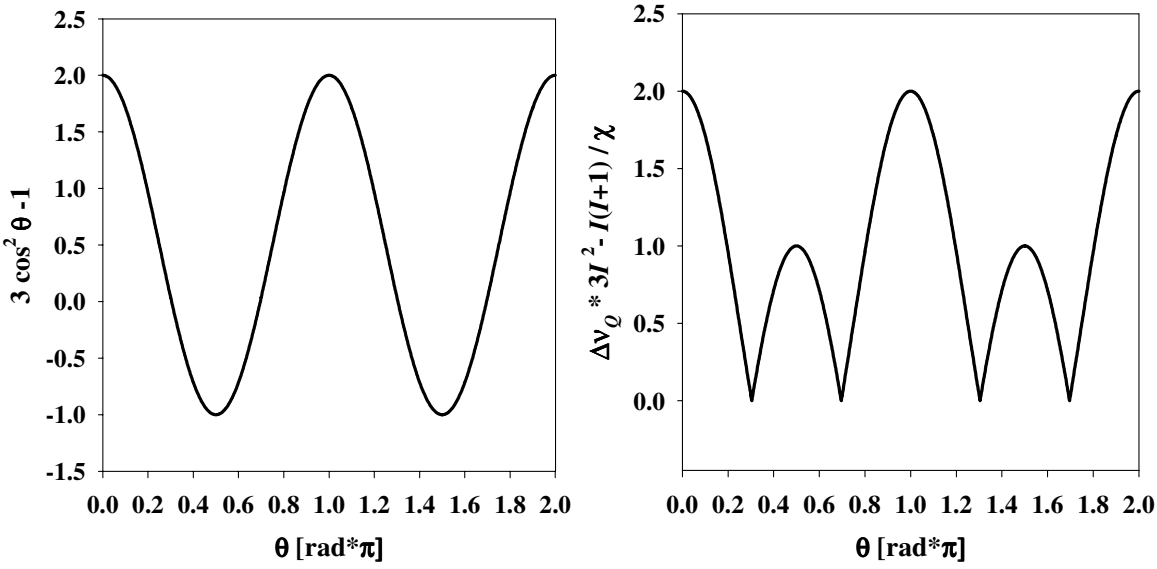

a) b)

Fig. 7.1.8(1) a) the developing of the values of the function $3\cos^2\theta - 1$ b) the evolution of a normalised quadrupolar splitting as function of θ.

Fig. 7.1.8(1b) demonstrates that the quadrupolar splitting $\Delta\nu_Q$ has a prime maximum at θ = 0° and 180° and a secondary maximum of exactly half the magnitude at θ = 90° and 270°. The quadrupolar interactions are entirely negated when θ = 54°44' (and accordingly 234°44'). This is the so called 'magic angle' and it is of principal importance in solid state NMR.

In the NMR of liquids or solutions, molecules tumble rapidly and in general isotropically, as long as they are in a truly isotropic environment. As a result, directionally dependant interactions containing the $(3\cos^2\theta - 1)$ term are negated, as the average value of said term equals zero for a random distribution of θ. Therefore neither quadrupolar interactions, nor *direct* spin-spin interactions appear in this case in the NMR spectrum. In fact only indirect scalar spin-spin coupling and scalar chemical shifts remain, i.e. the interactions which cause the structures of high-resolution NMR spectra.

In anisotropic environments of liquid crystals and complex fluids however, molecular tumbling is impeded and, as a result, rapid anisotropic reorientation incompletely averages the quadrupolar interaction, i.e. quadrupolar splitting occurs. Unfortunately, the angle θ is no longer suitable for such systems, as three frames of reference must be accounted for. These are the molecular, the liquid crystal director, and the laboratory frame. Accordingly, the definition of three angles becomes useful: θ_{qn} corresponds to the angle between the efg and the normal $\vec{n}$ of the layer which impedes molecular tumbling (e.g. water/surfactant interface), θ_{nd} is the angle between this normal and the director $\vec{d}$ of the liquid crystal and θ_{db} the angle between this director and the magnetic field $\vec{B}$. Hence eq. 7.1.8(5) is modified to

$$\Delta\nu_Q = \frac{3}{2}\chi\left[\frac{1}{3I^2 - I(I+1)}\right]\cdot\left|S_{qn}\right|\cdot\left|S_{nd}\right|\cdot\frac{1}{2}\left|\left(3\cos^2\theta_{db} - 1\right)\right| \qquad \text{eq. 7.1.8(7a)}$$

$$S_{qn} = \frac{1}{2}\overline{\left(3\cos^2\theta_{qn} - 1\right)} \qquad \text{eq. 7.1.8(7b)}$$

$$S_{nd} = \frac{1}{2}\overline{\left(3\cos^2\theta_{nd} - 1\right)} \qquad \text{eq. 7.1.8(7c)}$$

Eq. 7.1.8(7a) is derived through combining expressions of Rendell et. al.[89] and Perrson et. al.[90] The terms S_{qn} and S_{nd} are so called *order parameters*, which quantify the degree of alignment between the efg and the layer normal $\vec{n}$ and $\vec{n}$ and the phase director $\vec{d}$ respectively. S_{qn} is small for liquid crystals and S_{nd} is constant for a given liquid crystal structure, e.g. $S_{nd} = 1$ in the case of a lamellar structure ($\theta_{nd} = 0°$), $S_{nd} = 1/2$ in case of a hexagonal one ($\theta_{nd} = 90°$), whilst $S_{nd} \equiv 0$ in case of a bicontinuous or cubic structure (actually, as there is no director the averaging of an angle θ_{nb} must be considered, see section 7.2.4). And indeed, the quadrupolar splitting of a hexagonal phase is only half as large as that of a respective lamellar one, while cubic and bicontinuous phases do not exhibit a splitting at all[34]. However, eq. 7.1.8(7b,c) only apply in the case of a *fast exchange* between the involved angles, with respect to an NMR timescale (see section 7.1.9). Thus, the term including θ_{db} is not converted into another order parameter, as a distribution of this angle (as in a powder sample) does not lead to an averaged signal, but rather a superposition of signals (multiplets), where each splitting is defined for a single crystallite and given by eq. 7.1.8(7a).

As mentioned in section 7.1.5, quadrupolar interactions lead to relaxation and this is true even in the case of isotropic molecular tumbling. Relaxation can be thought of as arising from insufficiently effective averaging leading to broader signals, but the cause of it is essentially a local change of the efg, brought about by rotational and vibrational motions (the efg is part of the molecular frame and when a molecule tumbles the quadrupolar energy is altered constantly). Quadrupole relaxation is the only relaxation which depends on electrical interactions and is purely intramolecular. In *mobile isotropic fluids* the longitudinal T_{1Q} and transverse T_{2Q} time constants of this process are equal:

$$\frac{1}{T_{2Q}} = \frac{1}{T_{1Q}} = \frac{3}{10}\pi^2 \frac{2I+3}{I^2(2I-1)}\chi^2\tau_c \qquad \text{eq. 7.1.8(8)}$$

Eq. 7.1.8(8) is only true for the extreme narrowing condition (section 7.1.5) and a term containing the so-called asymmetry parameter (which is needed when the efg cannot be described by a single parameter $\vec{q}_{zz}$) has been omitted. The correlation time τ_c corresponds to the process of molecular tumbling and therefore increases with increasing viscosity and decreasing temperature. For most $I > 1/2$ nuclei, quadrupolar relaxation dominates the relaxation process, and thus even inhomogeneity broadening (section 7.1.5), so that eq. 7.1.8(8) corresponds directly to the width $\Delta\nu_{1/2}$ of the detected signal.

7.1.9 NMR Experiment Time Scale and Chemical Exchange

The fact that *rapid* molecular tumbling leads to an averaging of the geometrical factor of eq. 7.1.8(6), implies that there is an intrinsic time scale to NMR experiments. This time scale generally encompasses lifetimes of a given state of 1s to 10^{-6}s and accordingly correlation times τ_c from 1Hz to 1MHz. The 1s limit originates from the time necessary to record a FID (~1s).

A distinction can be readily made between to extremes. The *slow-exchange regime* refers to the case when lifetimes are considerably greater than the NMR timescale and the *fast-exchange regime* to the case where the opposite is true. In the former situation, the NMR spectra consists of the superposition of the sub-spectra of all existing states, while in the latter an average spectrum is recorded, to which each state contributes proportionally according to its population and lifetime.

The exchange of states can occur both *inter-* and *intramolecularly*. An example of intramolecular exchange is internal rotation, i.e. the transition between different rotamers, while intermolecular exchange involves the breaking of chemical bonds, as for instance in the exchange of OH and NH protons in aqueous solution. In the theory of NMR, the dynamic exchange between states is termed *chemical exchange*. If the exchange between two states is truly rapid, then the detected signal is correspondingly sharp. This fact can be understood by considering that an exchange process changes the frequency of a recorded FID, if it occurs in the time T_2^*. Then, if this exchange occurs in an amount of time which is small when *compared to the difference between the two frequencies*, the FID will be identical to the one of a system which leads to a signal at the average frequency. Therefore, the time scale of an NMR experiment must always be seen relative to the shift in resonance frequency between existing states.

Hence, sample spinning along an axis parallel to the magnetic field with 15Hz effectively reduces line broadening due to magnetic field inhomogeneities, if these inhomogeneities cause deviations from the ideal frequency, which are considerably smaller than 15Hz. Likewise for solid state NMR, as samples can only be spun with a maximum rate of ~5KHz at the 'magic angle' $\theta = 54°44'$ (section 7.1.8) with respect to the magnetic field, only direct spin-spin interactions and quadrupolar interactions can be averaged effectively, which would lead to a splitting of a considerably smaller value. From the above description, it is now obvious that vibrational ($\tau_c \sim 10^{12}$ - 10^{14} Hz) and rotational motions ($\tau_c \sim 10^{-12}$ - 10^{-13}s for molecules <100 amu , $\tau_c \sim 10^{-10}$s for >500 amu and macromolecules may possess τ_c around 10^{-8} s) cause transitions between states that are averaged according to the fast-exchange principle.

If the exchange between states is neither slow nor rapid, but rather of an *intermediate* nature, spectra appearance becomes more complex. The simplest case to consider is a situation with two states, which are uncoupled and equally populated. The first condition ensures that in the limit of slow exchange only two singlets are observed, one at each Larmor frequency associated with the respective state. The second condition states that the intensities and integrals of the two peaks are identical, i.e. that the spectra are symmetrical. In the limit of fast exchange, of course, only a single singlet is registered and its integral is identical to the sum of the integrals of the slow exchange singlets. An approach by McConnell[91] describes the lineshape for the whole range from slow to fast exchange theoretically

$$I(\omega) \propto \frac{1}{2} \cdot \frac{P \cdot (\Delta\omega_Q)^2}{\left[(\omega - \omega_0)^2 - (\Delta\omega_Q)^2 / 4\right]^2 + 4 \cdot P^2 \cdot (\omega - \omega_0)^2} \qquad \text{eq. 7.1.9(1)}$$

The intensity of the spectrum $I(\omega)$ is given as a function of the angular velocity ω. It can be converted with eq. 7.1.2(5) to $I(\nu)$. ω_0 corresponds to the position of singlet in the limit of fast exchange, $\Delta\omega_Q$ to the maximum splitting in limit of slow exchange and P is the parameter representing the probability of exchange, i.e. the rate of conversion between the two states. Note that eq. 7.1.9(1). does not account for a natural linewidth, i.e. $1/T_2^* = 0$ and this leads to peaks of infinite intensity, i.e. their width approach zero, in the limit of fast and slow exchange. Fig. 7.1.9(1) illustrates the lineshapes calculated with eq. 7.1.9(1) for variations of P (for a constant value of $\Delta\omega_Q$).

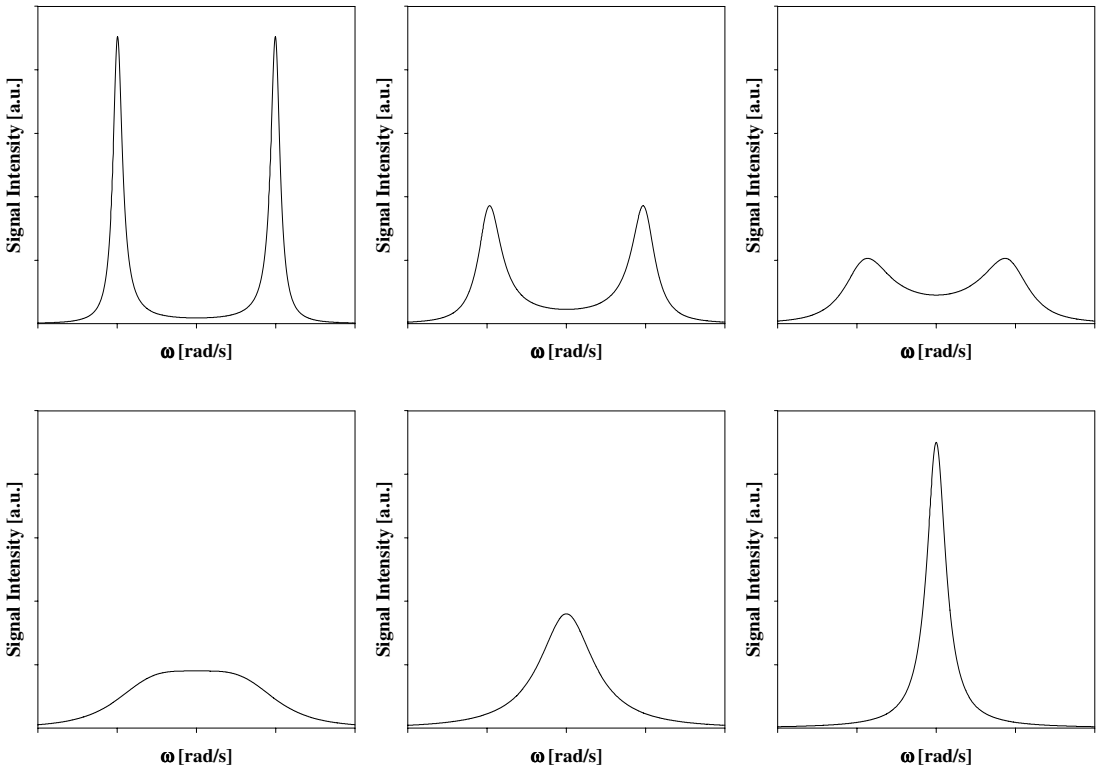

Fig. 7.1.9(1): lineshapes according to the McConnell equation (eq. 7.1.9(1)). Spectra are calculated with multiples of the ratio $P/\Delta\omega_Q$=1/(2*2^0.5), the value at which coalescence occurs. From top left to right and top to bottom, these multiples correspond to 0.1, 0.25, 0.5, 1, 2 and 5.

Fig. 7.1.9(1) shows that as P increases, the doublet peaks lose in intensity but gain in width. Also, the splitting between them decreases until coalescence is reached. Beyond that point, the obtained singlet becomes more and more defined as P continues to rise. It is however nonsensical to give concrete values of P, as it is the ratio $P/\Delta\omega_Q$ which ultimately determines the lineshape, e.g. coalescence occurs for $P/\Delta\omega_Q$=1/(2*2^0.5).

7.2 The NMR Experiments

Nuclear magnetic resonance is employed to monitor temperature induced phase transitions from the L_3- or sponge phase to the L_α- or lamellar phase (and *vice versa*) in a three component system consisting of heavy water (D_2O), *n*-decane and the nonionic surfactant *n*-dodecylpentaoxyethylene ($C_{12}E_5$). The quadrupolar ^{2}H-nuclei act as a non-invasive probe of the system, yielding information on the isotropy of the surroundings through the quadrupolar splitting phenomenon (section 7.1.8). Two distinctly different signals are detected in the two phases in question, and through their quantisation one not only gains information regarding the transition kinetics, but also about the mechanisms involved.

This section begins with a description of the D_2O molecule from a ^{2}H-NMR perspective and a derivation of how its quadrupolar splitting can be calculated in the event of anisotropic surroundings. It continues with an explanation of the so called *two-sites model* and why this model must be taken into account in the complex fluids studied. Then the effects of non-averaged *direct* dipole-dipole interactions (section 7.1.8) are considered. Finally, the steady state ^{2}H-NMR spectra of the L_3- and L_α-phase can be understood and the chapter can proceed with the presentation of the various phase transition experiments.

7.2.1 D_2O, the Probe Molecule

The NMR experiments presented in this thesis focus on the resonance frequencies of the hydrogen isotope deuterium ^{2}H (D) and were conducted using fully deuterated water (99.8 wt. % D_2O). Samples containing exclusively D_2O of this concentration, lead only to a singlet, i.e. a single Lorentzian peak is observed in the NMR spectrum. The reason for this simplicity and the lack of fine structure (section 7.1.7) is elucidated in the following paragraph.

Molecules of HDO type, which lead to a different ^{2}H signal (a doublet), are not present in relevant concentration. Due to the symmetry and simplicity of the D_2O molecule, its two ^{2}H-nuclei are not only isochronous, but also magnetically equivalent (section 7.1.6). Thus, they can be considered a single nucleus with respect to indirect spin-spin interactions (section 7.1.7) and the coupling between them has no effect on the spectrum. In addition, the D_2O molecule contains one oxygen atom. The ^{16}O nucleus is inactive in NMR experiments as $I = 0$ (section 7.1.1), while the ^{17}O isotope is active, as $I = 5/2$. However, the latter occurs naturally only with 0.037% probability and therefore the result of indirect spin-spin coupling between the deuterium nuclei and the few present ^{17}O nuclei does not appear in the spectrum

(as the respective magnetisation is negligibly small, eq. 7.1.2(4)). Finally, the intermolecular exchange of the deuterons is very rapid, so that an average resonance frequency results for the detected signal (see fast exchange, section 7.1.9).

The three Zeeman energy levels (m_I = -1, 0 and +1) of ^{2}H-nuclei (I = 1) can be calculated using eq. 7.1.2(1). However, since ^{2}H-nuclei posses a quadrupole moment, perturbations of these spin energy levels must be accounted for in anisotropic environments and in those cases eq. 7.1.8(4) applies. This equation reduces to

$$E_{mI} = -\gamma \cdot m_I \hbar \cdot \left\|\vec{B}\right\| + \frac{3}{8}\chi h \cdot \left(3m_I^{\,2} - 2\right) \cdot \left(3\cos^2\theta - 1\right) \qquad \text{eq. 7.2.1(1)}$$

for I = 1. Fig. 7.2.1(1) illustrates the energy levels with and without perturbation through quadrupolar interactions.

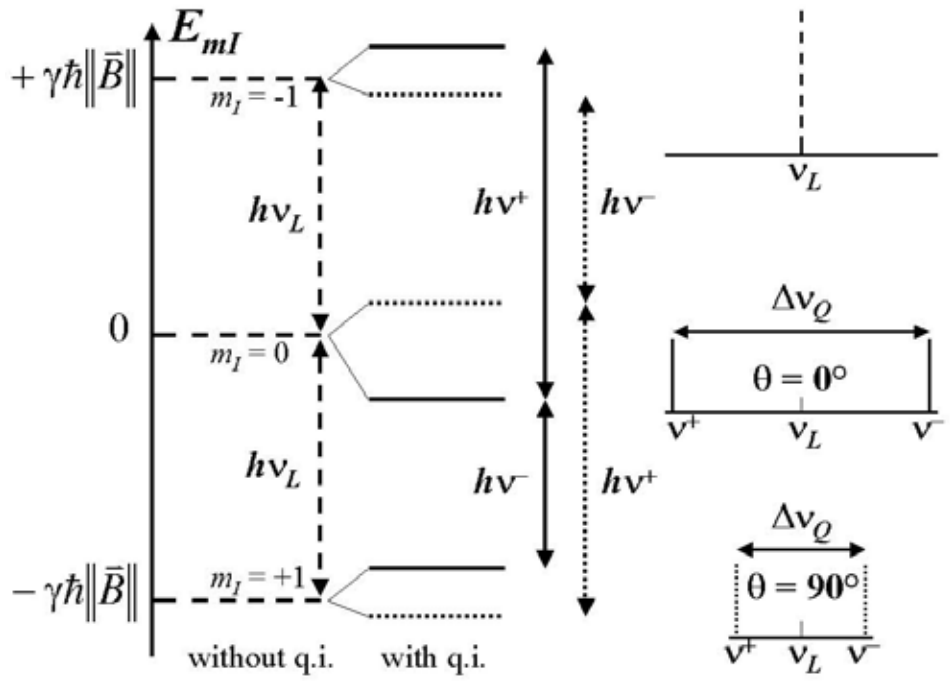

Fig. 7.2.1(1): the Zeeman energy levels of an I = 1 nucleus with and without perturbation due to quadrupolar interactions (q.i.) and a schematic representation of the respective NMR spectra to which they lead. The position of the perturbed energy levels assumes a positive nuclear quadrupole coupling constant χ (eq. 7.1.8(3)) and the perturbation effects are greatly exaggerated with respect to the energy scale. The non-perturbed case (dashed lines) leads to a signal at ν_L, while in the perturbed case a doublet with a quadrupolar splitting $\Delta\nu_Q$ results. The magnitude of the splitting, is strongly dependent on θ. θ = 0° (solid lines) and 90°(dotted lines).

As long as isotropic conditions prevail, i.e. unimpeded molecular tumbling can occur as in pure D_2O, the quadrupolar interactions are averaged to zero and the non-perturbed Zeeman energy levels are present (see section 7.1.8). As these levels are equidistant and

selection rules apply, which state that $\Delta m_I = \pm 1$ and only one spin can be transformed per transition (single quantum transition), the $m_I = +1 \rightarrow 0$ and $m_I = 0 \rightarrow -1$ transition both contribute (equally) to a signal detected at the Larmor frequency ν_L.

In anisotropic conditions, where the angle θ between the principal component of the efg tensor (field) $\vec{q}_{zz}$ and the magnetic field $\vec{B}$ is constant (e.g. in a single crystal), the singlet is split into a doublet due to the quadrupolar interactions and the two signals of half the previous intensity now appear at ν^+ and ν^- centred around ν_L. The value of the quadrupolar moment of deuterium is $Q = 2.8 \cdot 10^{-3}$ barn and it is of positive sign, as the positive charge distribution is prolate relative to the nuclear spin. Respectively, the nuclear quadrupole coupling constant χ is also positive (eq. 7.1.8(3)) and quadrupolar interactions cause an increase in energy E_{mI} for non-zero m_I in the $\theta = 0°$ case.

The magnitude of the quadrupolar splitting $\Delta\nu_Q$ is decisively influenced by the value of θ (see fig. 7.1.8(1)). Fig. 7.2.1(1) plots the spin energy levels for the two cases, where $\Delta\nu_Q$ attains a maximum, i.e. for $\theta = 0°$ and 90°. Notably, the splitting in case of perpendicular orientation is only half as large as for the parallel condition. As the perturbation of the energy levels is small when compared to their spacing, the $m_I = +1 \rightarrow 0$ and $m_I = 0 \rightarrow -1$ transitions are still equally likely and accordingly the peaks of the doublet are of the same intensity.

When accounting for $I = 1$ and the respective m_I, it becomes clear from eq. 7.2.1(1) that the resonance frequencies $\nu^{\pm}$ of the quadrupolar doublet are given by

$$\nu^{\pm} = \nu_L \pm \frac{3}{8}\chi\left|\left(3\cos^2\theta - 1\right)\right| \qquad \text{eq. 7.2.1(2)}$$

Eq. 7.2.1(2) shows that the doublet is centred on the Larmor frequency ν_L and its splitting is easily calculated via

$$\Delta\nu_Q = \frac{3}{4}\chi\left|\left(3\cos^2\theta - 1\right)\right| \qquad \text{eq. 7.2.1(3)}$$

Eq. 7.2.1(3) also results when accounting for $I = 1$ in eq. 7.1.8(6). However, as stated in section 7.1.8, θ is not convenient to describe the angular dependency of the quadrupolar splitting in liquid crystals and accordingly eq. 7.1.8(7) will be used which for $I = 1$ reduces to

$$\Delta\nu_Q = \frac{3}{2}\chi \cdot \left|S_{qn}\right| \cdot \left|S_{nd}\right| \cdot \frac{1}{2}\left|\left(3\cos^2\theta_{db} - 1\right)\right| \qquad \text{eq. 7.2.1(4)}$$

It is important to note that the quadrupolar coupling constant χ is identical for both deuterium nuclei of the D_2O molecule, as they have identical electrical surroundings and hence experience the same efg. Furthermore, since the order parameter $\left|S_{qn}\right|$ is the result of averaging (eq. 7.1.8(7b)), and therefore independent of an 'initial' θ_{qn}-value, it is also the same for both nuclei and as a result both nuclei contribute to the same signal.

From eq. 7.2.1(4) it is immediately obvious that no quadrupolar splitting is expected for the macroscopically isotropic L_3-phase (since $S_{nd} \equiv 0$, section 7.1.8), even though molecular tumbling is not expected to be isotropic for small time increments (see spectrum of the L_3-phase below). On the other hand, the splitting of the lamellar phase seems to depend solely on the orientation of the lamellar with respect to the magnetic field, i.e. θ_{db}, as $S_{nd} = 1$ (section 7.1.8) and S_{qn} is constant for all D_2O molecules (see two site model below).

7.2.2 The Two-Sites Model

Up to this point it was assumed that for a given phase, all D_2O molecules have the same properties and that their ^2H-nuclei correspondingly lead to the same NMR signal. However, when one considers the dilute lamellar phases studied, there is an evident disparity regarding the amount of perturbation to isotropic molecular tumbling, with respect to D_2O molecules which are distant to the surfactant film and those which are in its immediate proximity. This degree of hindrance is essentially expressed by the order parameter S_{qn} (eq. 7.2.1(4) and 7.1.8(7b)) and sites of differing S_{qn} accordingly lead to different quadrupolar splittings. Assuming *fast exchange* of the molecules containing nuclei of $I > 1/2$ to occur between different sites of more or less perturbed or even unperturbed tumbling (varying S_{qn}), the resulting, i.e. *averaged*, quadrupolar splitting can be calculated as a weighted sum of the splittings $\Delta\nu_{Q,i}$ at each of the sites

$$\Delta\nu_Q = \sum_i p_i \cdot \Delta\nu_{Q,i} \qquad \text{eq. 7.2.2(1)}$$

where p_i is the fraction of quadrupolar nuclei at site i and each $\Delta\nu_{Q,i}$ is calculated via eq. 7.2.1(4). To comprehend the validity of this equation, one must understand the following

concept contained within the idea of *fast exchange*. During the time scale of the NMR experiment, *each and every* molecule containing the quadrupolar nucleus will be at *each and every* site many times over. Each site leads to a specific value of $\Delta\nu_{Q,i}$ and thus the *time-averaged* value of $\Delta\nu_Q$ depends upon the fraction of time spent at each site. This time fraction is however assumed to be directly proportional to the number of molecules that can occupy a given site and that is exactly what eq. 7.2.2(1) states.

As a simple approximation for the system at hand, *three* sites should initially be considered. Firstly, there is the hydration water of the five ethylene oxide groups of the surfactant films, which is most effectively perturbed and accordingly the primary cause of the splitting. This water is often referred to as 'bound' to the surfactant film, but this term is misleading as fast exchange occurs between the different sites and therefore mobile, through adsorption partially aligned[92] (MAPA) D_2O will be spoken of instead. Secondly, there is the large amount of 'bulk' D_2O (as very dilute systems were studied), which one would expect to experience very little or no hindrance in its isotropic tumbling. Finally, one should not forget to consider the terminal hydroxyl group of the $C_{12}E_5$ molecules themselves.

Rapid intermolecular exchange of the deuterons among the D_2O molecules, is a property of heavy water. A somewhat slower, but with respect to the presented studies still very rapid exchange exist for hydroxyl group protons next to primary carbons. Of course, the hydroxyl hydrogen of $C_{12}E_5$, will not (significantly) exchange among the surfactant molecules themselves, but mainly with the overwhelmingly large amount of present deuterium. Actually, the hydrogen-atoms become evenly distributed among all the sites that exchange ^1H or ^2H soon after the preparation of the samples. Fortunately, the molar ratio of surfactant to D_2O is very low (< 2‰), so that there is no significant contamination with hydrogen and HDO molecules are still sufficiently rare as not to add their undesired doublet signal to the spectrum.

How strongly the deuterium of the hydroxyl-group contributes to the detected quadrupolar splitting depends on the relative amount present (i.e. p_i) and its order parameter S_{qn}. *Rendall* and *Tiddy*[93] show that both of theses numbers are low. In fact, it is thought that significant contribution to a quadrupolar splitting comes only from hydration water of the first and perhaps second ethylene oxide group next to the polar/apolar interface, because the freedom of movement of further groups is so great that the S_{qn} of their respective hydration water approaches zero. Accordingly, the same is expected for the deuterium of the hydroxyl group. Furthermore, there is experimental evidence that the OD-group contribution is irrelevant, as NMR experiments of lamellar phases comprised of D_2O – $C_{12}E_4$ and D_2O –

$C_{12}E_4OCH_3$ show that both yield the same splitting. Analogue to this reasoning, S_{qn} of bulk D_2O must be so close to zero, that no contribution to the splitting is thought to come from it, and indeed it has been shown experimentally that this is true[90]. Thus, the simple two-sites model describes the situation at hand well. Indeed, the two-sites model was already used to describe water binding in lyotropic mesophases in 1975[94]. Accordingly, the quadrupolar splitting in the lamellar phase can now be calculated via

$$\Delta\nu_Q = p_x \cdot \frac{3}{4}\chi \cdot \left|S_{qn}\right| \cdot \left|\left(3\cos^2\theta_{db} - 1\right)\right| \qquad \text{eq. 7.2.2(2)}$$

where p_x represents the mole fraction of MAPA D_2O.

7.2.3 Direct Dipole-Dipole Interactions

Similar to the quadrupolar interactions of section 7.1.8, the direct magnetic dipole-dipole interactions of NMR active nuclei do not average to zero in case of anisotropic molecular tumbling. Thus, the question arises as to how these interactions influence the spectra of the experiments at hand. The dipolar coupling constant R between two nuclei can easily be calculated using

$$R = \frac{\mu_0}{4\pi} \cdot \frac{\hbar}{2\pi} \cdot r^{-3} \cdot \gamma_1\gamma_2 \qquad \text{eq. 7.2.3(1)}$$

where μ_0 is the permeability of a vacuum, r the distance between the coupling nuclei and γ their respective gyromagnetic ratios. Similar to χ, R is of frequency units. However, due to the relatively low γ-value of the deuterium nucleus, the dipolar coupling constant of the deuterium nuclei of the D_2O molecule calculates to only R_{DD} (D_2O) = 0.717 kHz. As a means of comparison, R_{HH} (H_2O) = 46 kHz. For a homonuclear pair of nuclei, the splitting caused by direct dipole-dipole interactions are given by

$$\Delta\nu_{dd} = \frac{3}{2}R\left|3\cos^2\theta - 1\right| \qquad \text{eq. 7.2.3(2)}$$

where θ is the angle between the vector connecting the interacting nuclei and the magnetic field $\vec{B}$. When considering that the coupling constant of the quadrupolar splitting for liquid heavy water $\chi(D_2O) = 255$ kHz[95] and assuming that the order parameter S_{qn} is identical in both cases, then the magnitude of $\Delta\nu_{dd}$ is expected to be only ~0.6% of the quadrupolar splitting. Since, the experiments typical yield splitting values of ~10-16Hz, contributions due to direct dipole-dipole interactions can be neglected. In fact, even their effect on peak width is insignificant, as the best peak resolutions achieved correspond to $\Delta\nu_{1/2} \sim 1.5$ Hz.

7.2.4 NMR Signal of the Steady State Isotropic L_3-Phase

Fig. 7.2.4(1) displays the ^{2}H-NMR singlet recorded in the steady L_3-state. Eq. 7.2.1(4) expresses that no bicontinous phase or phase of cubic symmetry will lead to the detection of a quadrupolar splitting, as $S_{nd} \equiv 0$ in these cases. However, since an isotropic phase has no definite director, what is actually meant is that the angle between the surface normal and the magnetic field θ_{nb} must be considered. Its geometric term $(3\cos^2 \theta_{nb} - 1)$ only averages to zero as long as all θ_{nb} are equally likely to occur and there is fast exchange between them. Changes of θ_{nb} are probed by the molecule containing the quadrupolar nuclei, i.e. in this case through the diffusion of D_2O.

The *fast exchange* condition of the two-sites model states that there can be no distinction between MAPA and bulk D_2O on the time scale of the NMR experiment, i.e. each and every D_2O molecule will switch frequently between the two sites. However, in the isotropic L_3-phase the term *two* sites is misleading, as MAPA D_2O at different positions on bilayer would theoretically lead to different $\Delta\nu_{Q,i}$, since θ_{nb} varies at each position. Thus the MAPA site must essentially be subdivided into many sites of its own. Over the NMR time scale, a D_2O molecule will still spend time proportional to the fraction of bulk D_2O at the bulk site, but the remaining time proportional to the fraction of MAPA D_2O is spent at a multitude of different MAPA subsites. Due to the random nature of diffusion and the isotropic distribution of the bilayers, the many different θ_{nb} experienced at those subsites will effectively cancel each other out, i.e. average to zero. Accordingly, there is no splitting arising from time spent at MAPA sites and a singlet is detected.

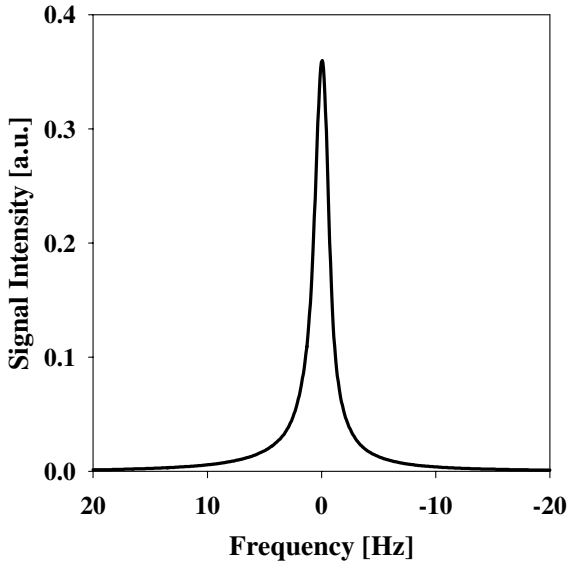

Fig. 7.2.4(1): the NMR signal for a typical L_3-phase studied.

7.2.5 NMR Signal of the Steady State Anisotropic L_α-Phase

Interestingly, only a simple doublet arising from quadrupolar interactions is detected for all lamellar phases studied, i.e. there is no single peak from isotropic D_2O nor is there an obvious superposition of doublets corresponding to a powder pattern (fig. 7.2.5(1a,b)). The first observation entails that the exchange between the two sites of MAPA D_2O and bulk D_2O is indeed rapid. In fact, the detected peaks are generally well separated and of Lorentzian form, thus eliminating the possibility of the systems being in a region of *intermediate* exchange rates (see section 7.1.9).

According to the second observation, θ_{db} is constant (eq. 7.2.1(4)) and therefore *all* lamellae are oriented in identical manner *with respect to the magnetic field* $\vec{B}$. This is true if either all lamellae are essentially parallel to each other, i.e. a single 'crystal' is present, or if there exists a macroscopic alignment between a multitude of 'crystallites'. That is to say, instead of a three dimensional (3D-) 'powder' a two dimensional (2D-) 'powder' is present, where the lamellae are all parallel to the magnetic field (z-axis), but each individual 'crystallite' is orientated randomly in the xy-plane (fig. 7.2.5(1c)). The single crystal explanation can be easily discounted, since in the course of this thesis it will be shown that the L_α-phase is formed through a nucleation and growth process when it originates from the L_3-phase (see section 7.4.5.1). Thus, for all studied samples $\theta_{db} = 90°$ and the equation describing the quadrupolar splitting (eq. 7.2.2(2)) can be reduced one last time to

$$\Delta\nu_Q = p_x \cdot \frac{3}{4}\chi \cdot \left|S_{qn}\right| \qquad \text{eq. 7.2.5(1)}$$

The cause of the lamellar orientation and further implication on the spectrum will be discussed in section 7.4.2. Although χ does vary somewhat for D_2O in the gaseous or solid state, it can be considered constant if in its liquid form, as neither strong changes of temperature nor the addition of electrolytes effects its value[96]. Thus for all discussions of $\Delta\nu_Q$ only p_x and S_{qn} must be considered.

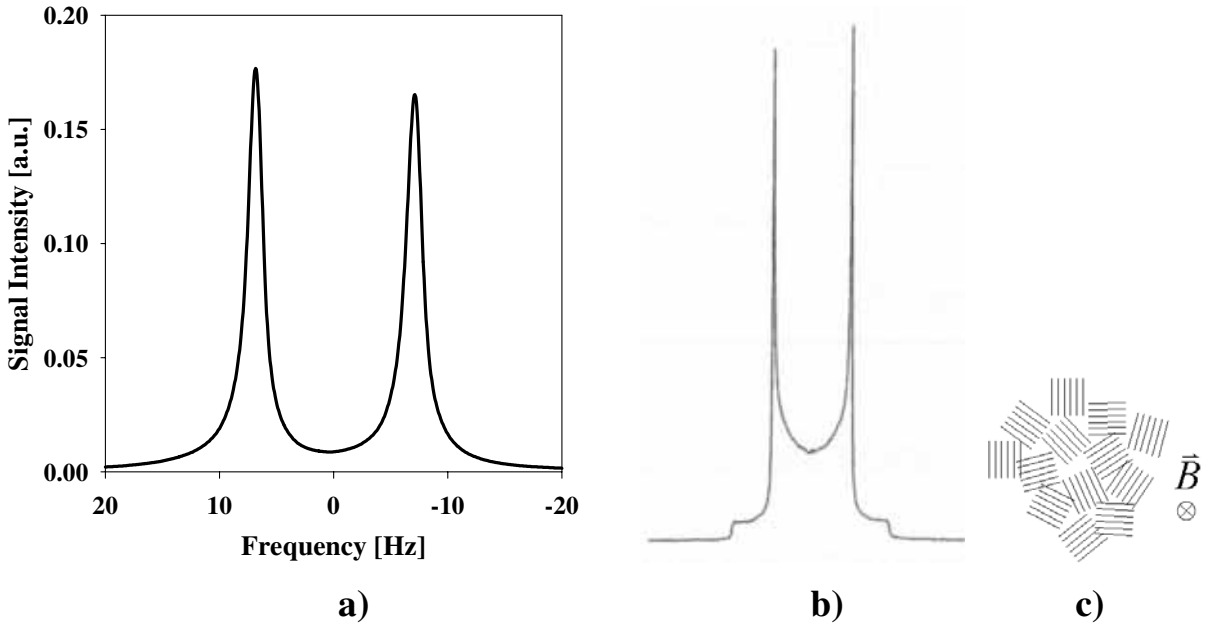

Fig. 7.2.5(1): a) the typical NMR signal of a studied lamellar phase. The slight asymmetry results from imperfect shimming and phasing of the spectrum. b) a typical 3D-powder pattern resulting from the superposition of many doublets with varying $\Delta\nu_Q$. c) schematic representation of a 2D-lamellar powder, when viewed in line with the magnetic field

7.2.6 L_3/L_α Transition Experiments

The ^{2}H-NMR investigations were performed on two different occasions at the University of Lund, Sweden. Preliminary experiments were carried out on a Bruker DMX-200 spectrometer ($\nu_L(^2H) = 30.7$ MHz) at the Department of Physical Chemistry 1. These proofed the feasibility of the experiments and gave evidence that the L_3-to-L_α phase transition and the reverse process have different underlying mechanisms. Further, more established, experiments were executed at a later date on a Varian 360 spectrometer ($\nu_L(^2H) = 55.2$ MHz) of the Department of Biophysical Chemistry. The results of the initial study are detailed in a publication[97], but will be presented again below and then later reanalysed in the light of the insights gained from the second, more detailed and comprehensive set of experiments (section 7.3.1.2 et sqq.). The results of these investigations are at present given exclusively in this thesis, but are also being considered for publication.

7.2.6.1 Experimental Procedure

Samples were flame sealed in 8mm and 10mm tubes and introduced into a spectrometer of appropriate temperature for the desired initial state, i.e. either L_3 or L_α. The sponge phase steady state serves as the point of reference for the magnitude of the performed temperature jumps ΔT and corresponds to a point just above (~0.1°C) the L_3/L_α phase boundary. After thermal equilibration, the initial steady state spectrum was recorded using a pulse sequence containing a single 90°-pulse. The temperature of the spectrometer was then reduced (for sponge to lamellar transitions) or raised (for lamellar to sponge transitions, see phase diagrams section 2.), thus causing a phase transition. Throughout this thesis, the former action is referred to as a *negative temperature jump*, the latter as a *positive temperature jump* (*T*-jump). Spectra were recorded consecutively after initiation of a *T*-jump until the transition was completed. The same pulse sequence as for the steady state spectra was employed in each case. Generally, the success of a transition was verified visually, after removing the samples from the spectrometer. In order to identify the L_α-phase, crossed polarisers were used. Experiments were carried out with varying bilayer volume fraction ϕ_{B+C}, viscosity η, and magnitudes of the *T*-jump ΔT. Unless noted otherwise, the water component of the samples consists only of D_2O (η_0=1.251 cP) and thus is of 'standard' viscosity, i.e. there is no addition of sucrose (see section 10.2).

The experiments were performed on stationary, i.e. non-spinning, samples. The time necessary for the acquisition of a spectrum is very short compared to the transition speeds, i.e. the spectra represent 'snap-shots' of the transition states. The samples were thermally equilibrated inside the magnet through an air flow. It was ensured, that the rate of temperature equilibration was fast compared to the transition kinetics observed. This rate was determined in separate experiments, for both cooling and heating, using a thermocouple (fig 7.2.6(1)). Temperature equilibration times are on the order of 200s and this represents the time resolution for the phase transition kinetics, using the described simple temperature variation procedure.

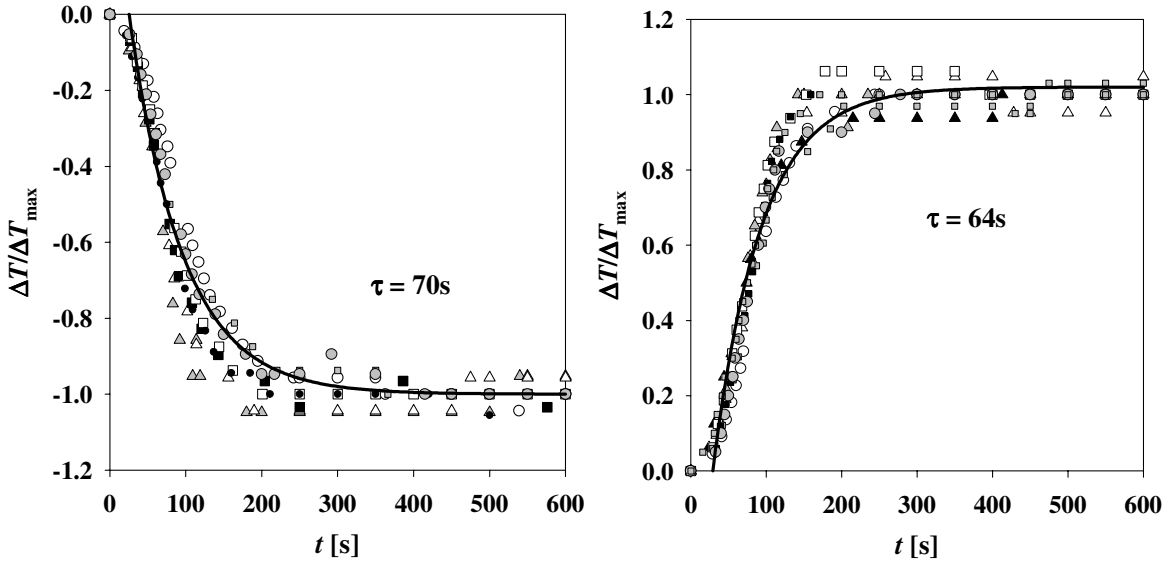

Fig. 7.2.6(1): cooling (*left*) and heating (*right*) kinetics for *T*-jumps of varying Δ*T*, normalised by dividing each value by of the final (maximum) absolute value of the appropriate curve. The figures include the heating/cooling time constant τ (details in section 10.4.4).

For elaborations on the information given above, the reader is referred to section 10.4. Experimental particulars concerning technical information, experimental setup, the utilised pulsed sequence and data processing are addressed there in detail.

7.2.6.2 L_3 to L_α Transitions

The general peak evolution occurring in sponge to lamellar phase transitions is similar for all the performed experiments, i.e. irrespective of changes of the three studied parameters (Δ*T*, ϕ_{B+C} and η). It will be described via the exemplary transition of a ϕ_{B+C}= 0.06 sample, which underwent a *T*-jump of Δ*T* = -1.5°C and was monitored on the Varian 360 spectrometer (fig.7.2.6(2) *top*, 3D-depiction and *bottom*, 2D-depiction).

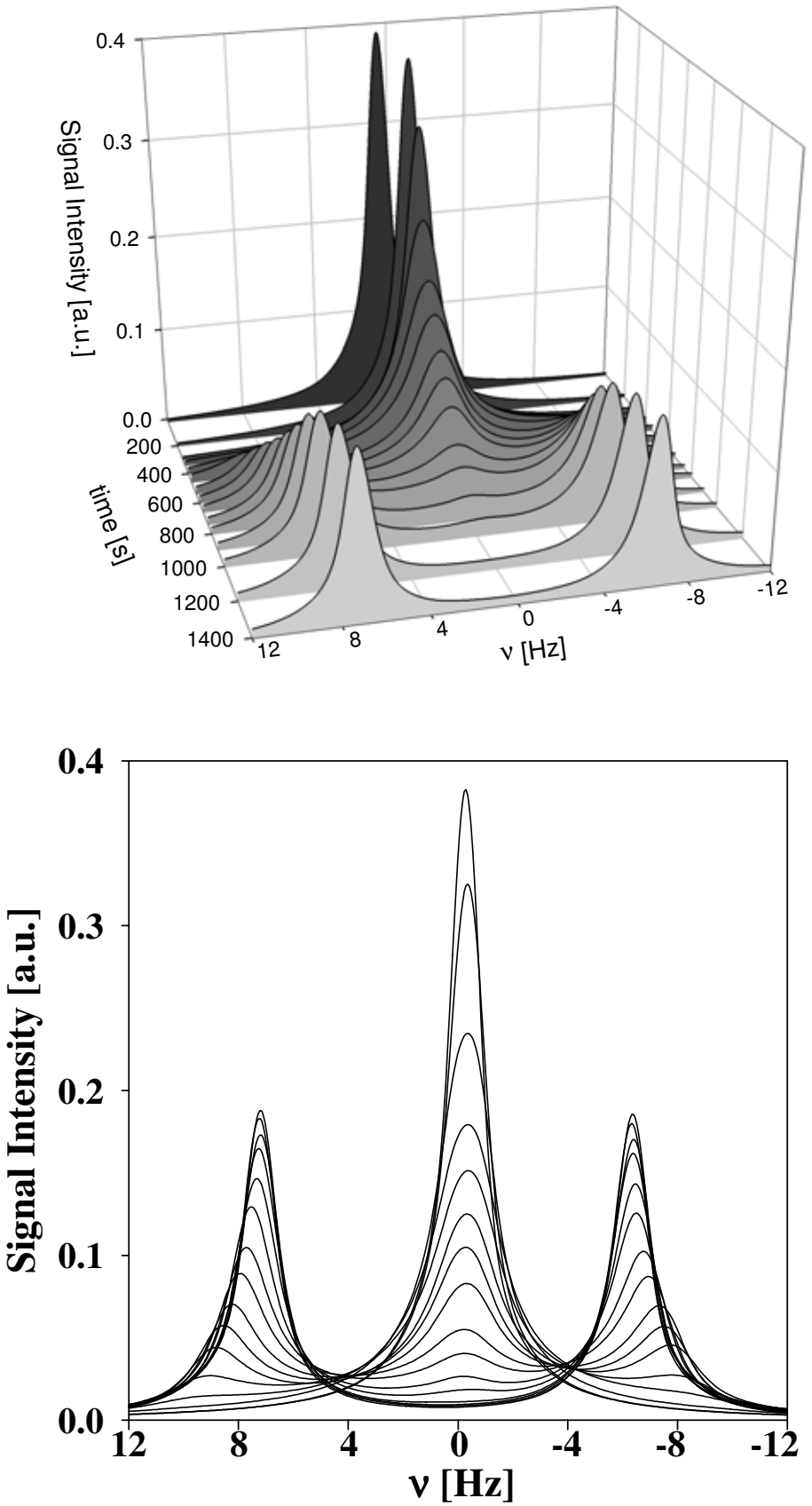

Fig. 7.2.6(2): experiment FT_24, ϕ_{B+C}=0.06, ΔT=-1.5°C, Varian 360 *top*: temporally subsequent ^{2}H-NMR spectra stacked in a 3D-plot to visualise peak evolution. *bottom*: superposition of the ^{2}H-NMR spectra displayed above, eliminating the time axis. Two isosbestic points are clearly visible. The initial L_3-peak has been omitted for clarity.

Initially, the spectrum consists only of the singlet originating from the isotropic L_3-phase. As time progresses, the L_α-doublet appears and subsequently grows in intensity, while simultaneously the central L_3-peak diminishes, until it vanishes completely and only the doublet of the steady L_α-state remains. Thus, during the transition three peaks are present concurrently, indicating the coexistence of a lamellar and sponge phase. All through the phase transition the peak positions remain roughly constant (see below).

In fig. 7.2.6(2) *bottom* the spectra are superimposed, thereby eliminating the time axis. Two frequencies are clearly visible, one on each side of the singlet maximum, where the intensity remains essentially constant throughout the transformation process. The existence of these isosbestic points indicates that the spectra recorded at intermediate times can be seen as the weighted sums of two constant subspectra, in this case the L_3-singlet and the L_α-doublet. Furthermore, the difference in frequency of the two L_α-peaks, i.e. the quadrupolar splitting $\Delta\nu_Q$, is somewhat larger when these first appear and decreases continuously until the minimal value of the steady lamellar state is attained. In addition, the lamellar peaks sharpen over time, that is their width at half height $\Delta\nu_{1/2}$ decreases. Finally, the opposite is true for the central L_3-peak, i.e. its $\Delta\nu_{1/2}$ value appears to increase as the transition progresses. Note, that the first spectrum, the L_3 steady state singlet, is omitted in fig. 7.2.6(2) bottom for clarity, since there is a slight but characteristic shift of the L_3-peak position to lower frequencies at the start of each transition. This first singlet is only given in fig. 7.2.6(9).

Fig. 7.2.6(3) to (11) demonstrate the peak evolution for various typical phase transition experiments in both two and three dimensions. In all cases the frequency range observed is 40Hz to facilitate comparisons between the different figures. Fig. (3) to (6) show the result of increasing the bilayer volume fraction ϕ_{B+C} from 0.05 to 0.08 and fig. (7) to fig. (10) illustrate the effect of increasing the magnitude of ΔT. Finally, fig. (11) is a transition of a sample with increased viscosity. The figure captions state on which spectrometer the respective experiment was performed. Note that only established experiments on the Varian 360 spectrometer are identified with a name (in the form FT_xx).

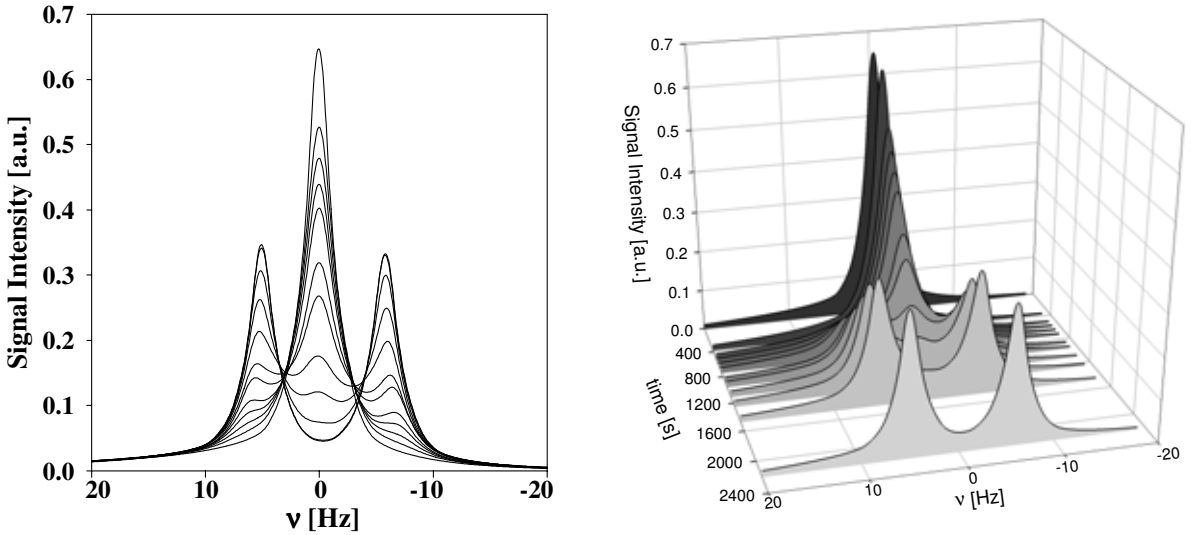

Fig. 7.2.6(3): ϕ_{B+C}=0.05, ΔT=-1.5°C, Bruker DMX-200

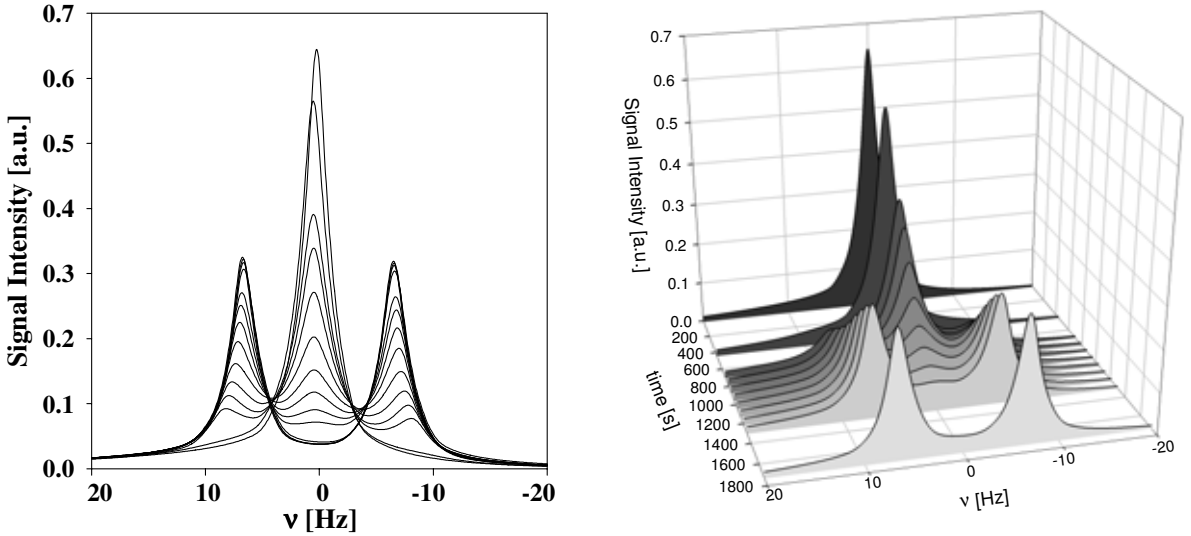

Fig. 7.2.6(4): ϕ_{B+C}=0.06, ΔT=-1.5°C, Bruker DMX-200

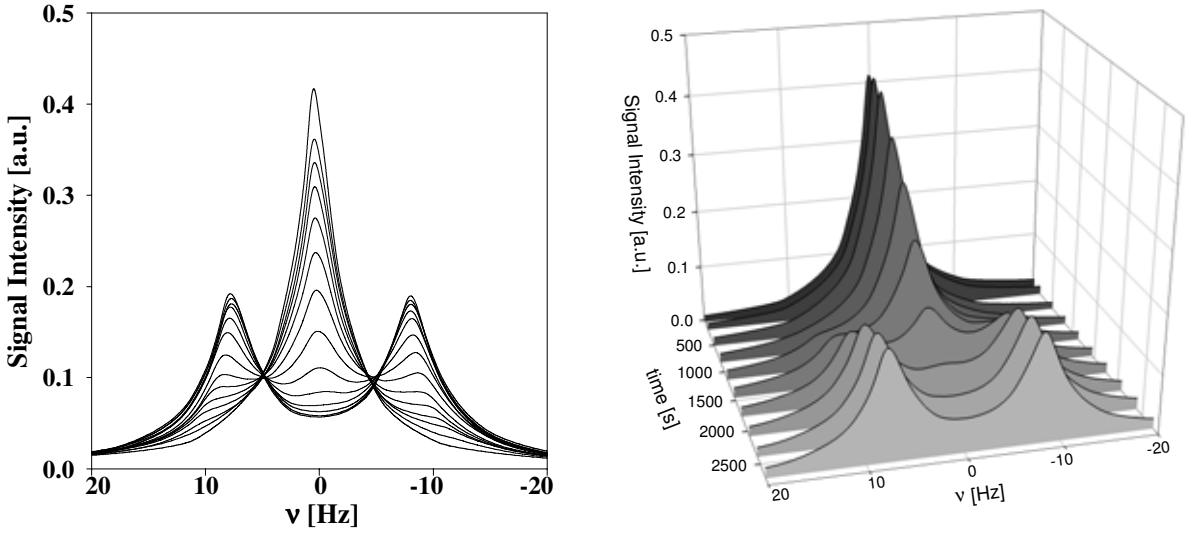

Fig. 7.2.6(5): ϕ_{B+C}=0.07, ΔT=-1.0°C, Bruker DMX-200

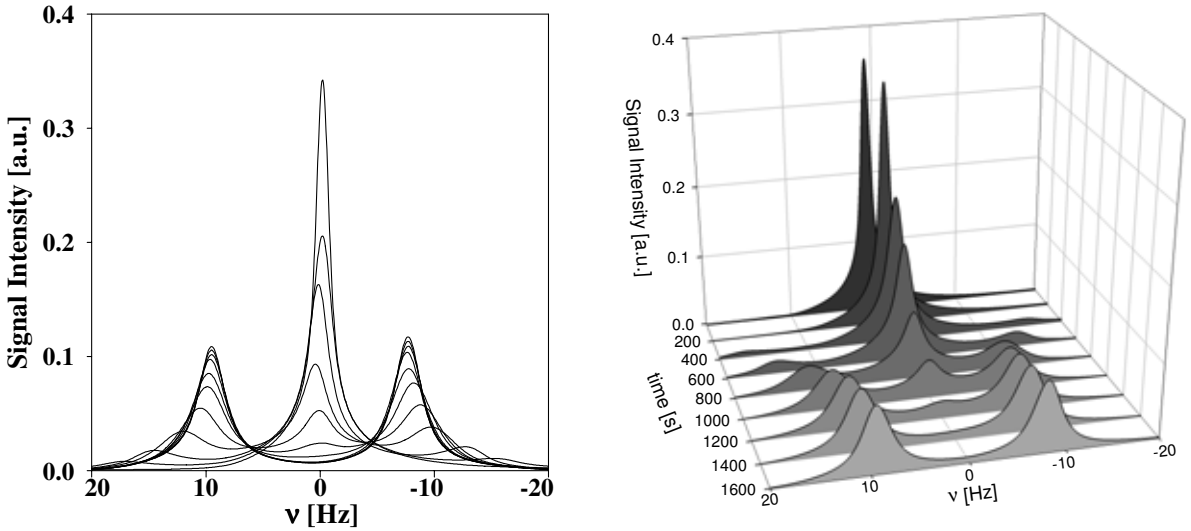

Fig. 7.2.6(6): experiment FT_75, ϕ_{B+C}=0.08, ΔT=-1.3°C, Varian 360

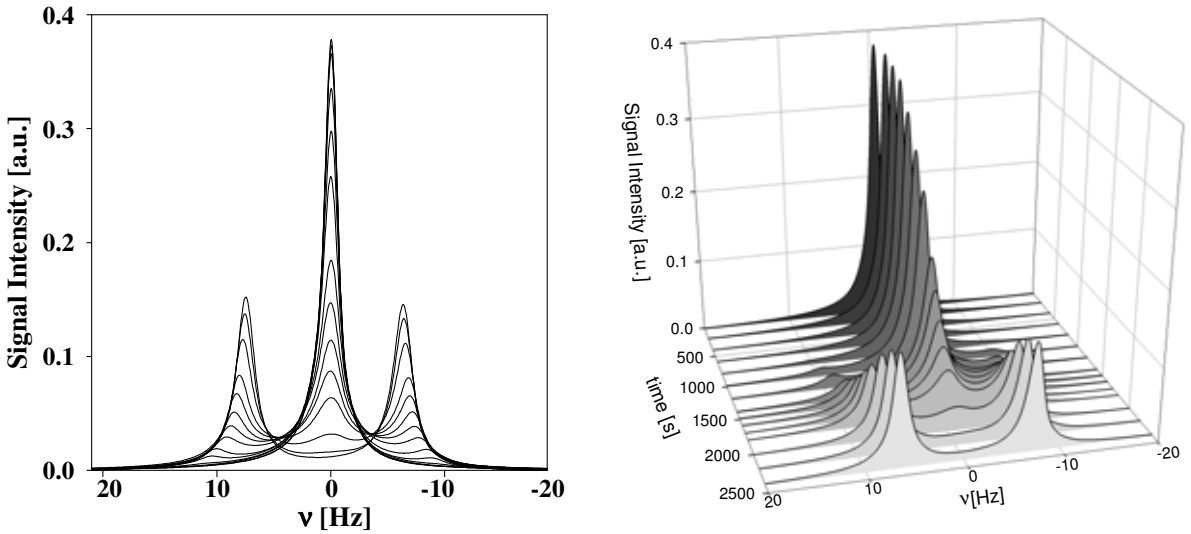

Fig. 7.2.6(7): experiment FT_32, ϕ_{B+C}=0.06, ΔT=-1.0°C, Varian 360

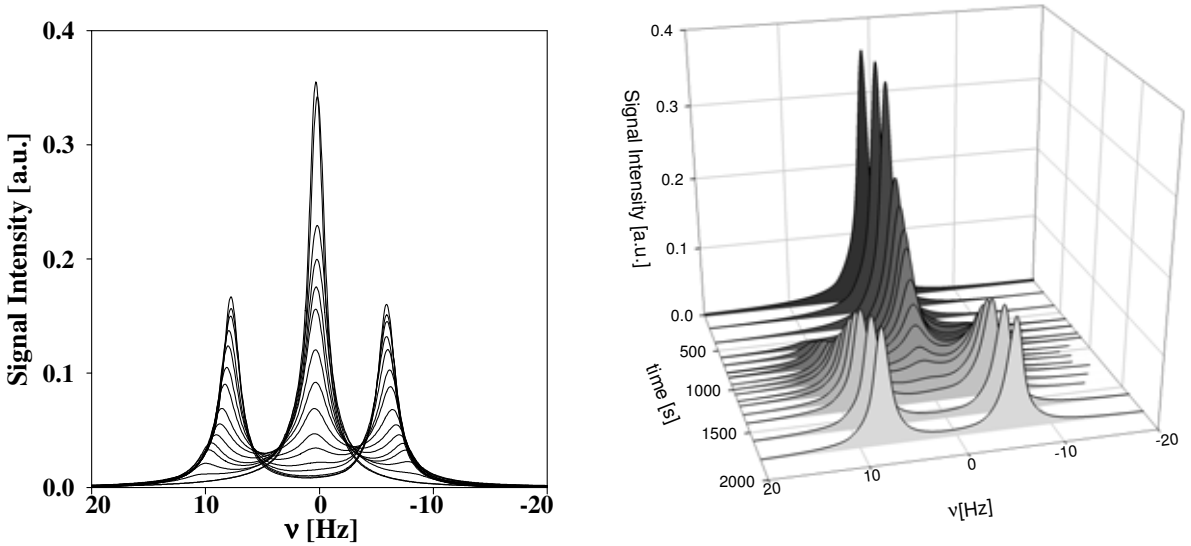

Fig. 7.2.6(8): experiment FT_20, ϕ_{B+C}=0.06, ΔT=-1.3°C, Varian 360

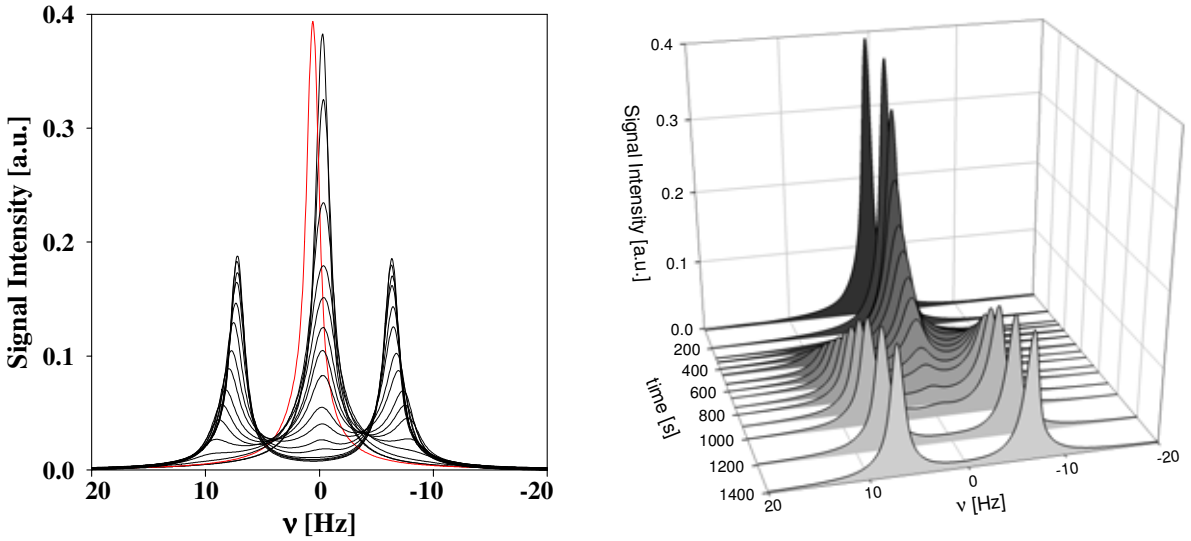

Fig. 7.2.6(9): experiment FT_24, ϕ_{B+C}=0.06, ΔT=-1.5°C, Varian 360. The two images are those of fig. 7.2.6(2) top and bottom with the frequency range extended to 40Hz for comparison. The plot of superimposed spectra includes the initial L_3 steady state singlet (grey) and demonstrates the characteristic shift to lower frequencies at the start of the transitions.

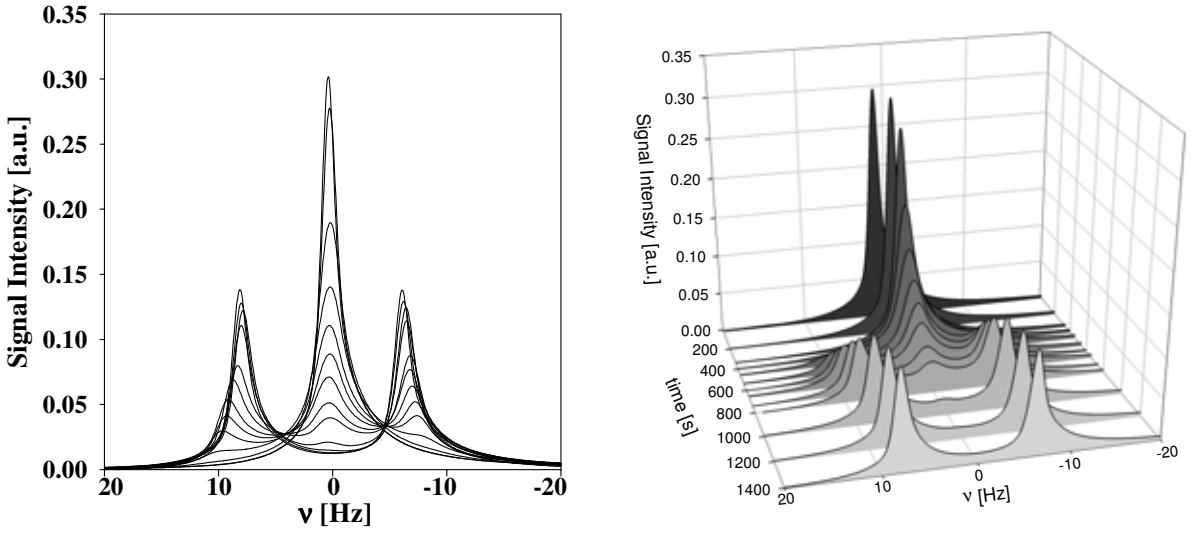

Fig. 7.2.6(10): experiment FT_03, ϕ_{B+C}=0.06, ΔT=-1.7°C, Varian 360

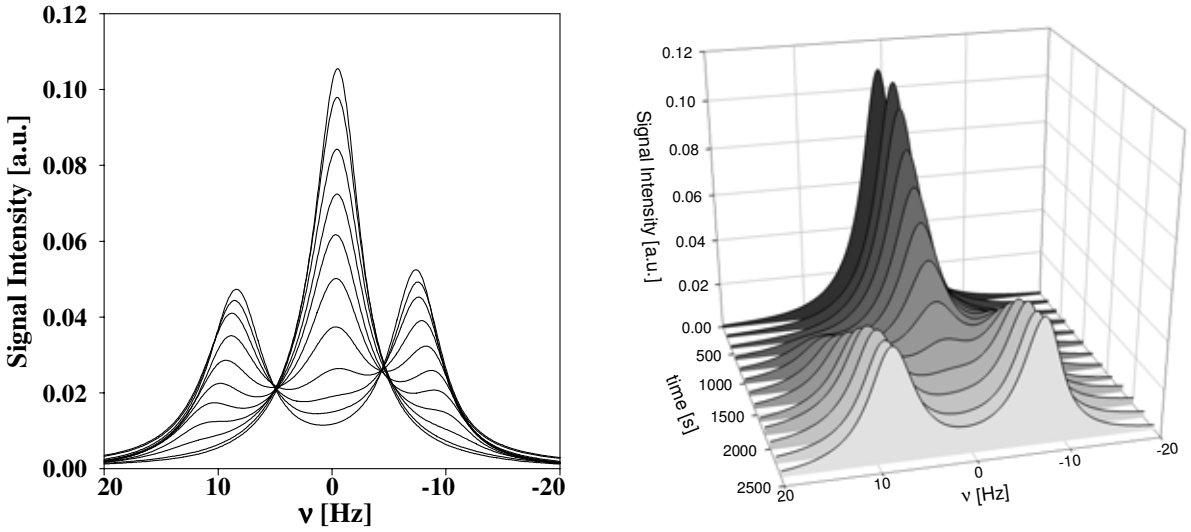

Fig. 7.2.6(11): experiment FT_78, ϕ_{B+C}=0.06, ΔT=-1.9°C, $\eta_{D2O/S} = \eta_0 \cdot 2.261$, Varian 360

Comparison of fig. (3) to (6) shows plainly that the quadrupolar splitting $\Delta\nu_Q$ of the final spectrum, i.e. that of the equilibrium lamellar phase, increases steadily with an increase of bilayer volume fraction ϕ_{B+C}. Also, when comparing the initial splitting, i.e. when the lamellar peaks first appear, with this final splitting in each experiment, one sees that the difference is quite large for the ϕ_{B+C}=0.08 sample (fig. (6)), while for the ϕ_{B+C}=0.05 sample (fig. (3)) the L_α-peaks shift only very slightly in frequency over the course of the transition. For the ϕ_{B+C}=0.06 sample (fig. (4)) an intermediate of these extremes is true, while in case of the ϕ_{B+C}=0.07 sample (fig. (5)), this phenomenon cannot be judged as all the peaks are rather wide, due to poor shimming in this preliminary experiment. Finally, when comparing the peak width $\Delta\nu_{1/2}$ of the initial L_3-peak with $\Delta\nu_{1/2}$ of the final L_α-peaks in each experiment, the L_α-peaks at higher bilayer volume fractions do not seem to sharpen as much as those of lower ϕ_{B+C}. This is most readily visible by noting the ratio of the *intensities* of the peaks in question.

In case of varying ΔT at constant ϕ_{B+C} (fig. (7) to (10)), differences in the graphs of superimposed spectra are not discernable. On the other hand, the 3D depictions demonstrate that the sponge to lamellar transition process occurs faster with increasing magnitude of ΔT. However, the kinetics of the transition will be analysed in detail for all of the varied parameters (ΔT, ϕ_{B+C} and η) in section 7.3.1.

Fig. (4) and fig. (9) represent in principle the same experiment, since in each case a ϕ_{B+C}=0.06 sample was subjected to a T-jump of ΔT=-1.5°C. Yet, the experiments were performed at different times on different spectrometers. The general peak morphology and their evolution, visible in the 2D-graphs, are very similar. However, the peaks of fig. (9) are notably sharper, due to superior shimming that is distinctive for the more established experiments conducted on the Varian 360 spectrometer. With regard to the time scale of the transition process, the two experiments are alike as well. While the transition of fig. (4) is completed at ~1500s, the one of fig. (9) is finished at ~1100s. In essence, the two graphs demonstrate the good reproducibility of the experiments.

In fig. (11) the transition process of a sample with increased viscosity is depicted. Evidently the peaks are very wide. This could be the result of poor shimming as was the case in fig. (5), but a more probable cause will be discussed in section 7.4.5.4. Also, the splitting of the steady state lamellar phase is notably larger, than in the case of the other samples where ϕ_{B+C}=0.06. Finally, although a large T-jump of ΔT=-1.9°C was carried out, the transition process is quite slow, i.e. it is completed at ~2000s.

Fig. 7.2.6(12) illustrates a further phenomenon that appears only when very fast transitions are observed, i.e. *T*-jumps with a high magnitude of ΔT are conducted. In those cases, as the L_3-peak declines in intensity, it appears that this central 'peak' is actually comprised of a doublet of small separation (<5Hz), one that is close to the limit of resolution. This additional splitting does not seem to be an artefact as it could be detected in all very fast transitions, regardless of sample composition and the actual ΔT values. The apparent asymmetry of the 'L_3' doublet is not a transition phenomenon in itself. NMR spectra often show deviations from ideal, Lorentzian lineshapes. These artefacts can result for example from the spectra acquisitioning process or from processing of the FID

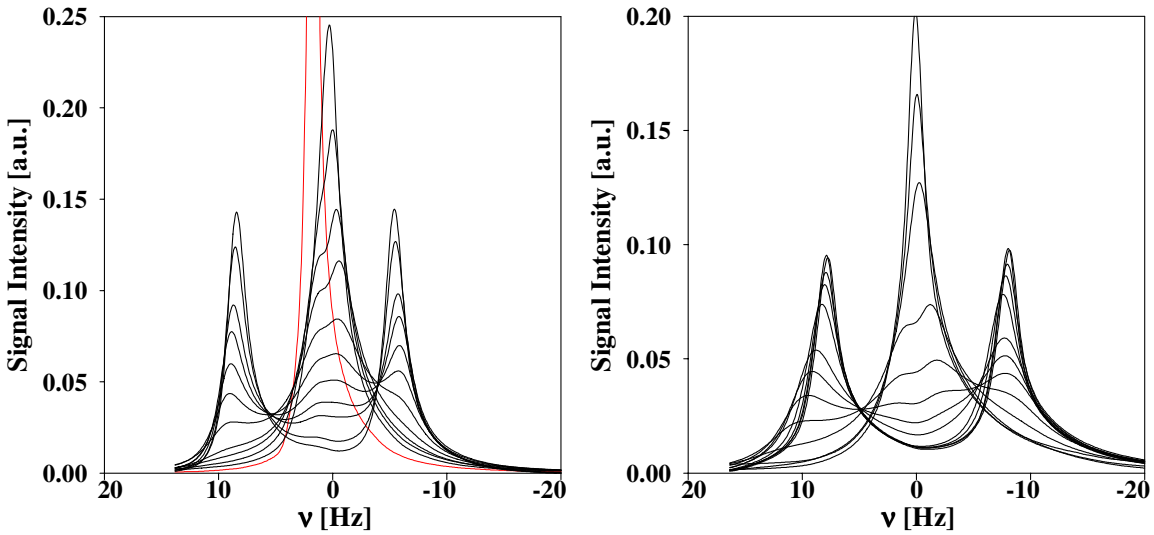

Fig. 7.2.6(12): *left*: experiment FT_06, ϕ_{B+C}=0.06, ΔT=-2.0°C, Varian 360. *right*: experiment FT_69, ϕ_{B+C}=0.07, ΔT=-3.9°C, Varian 360. In both graphs, several of the first and final spectra have been omitted for clarity.

7.2.6.3 L_α to L_3 Transitions

The general peak evolution occurring in lamellar to sponge phase transitions is similar for all the performed experiments, i.e. irrespective of changes of the three studied parameters (ΔT, ϕ_{B+C} and η). It will be described via the exemplary transition of a ϕ_{B+C}= 0.06 sample, which underwent a *T*-jump of $\Delta T = +1.5°C$ and was monitored on the Varian 360 spectrometer (fig. 7.2.6(13) top, 3D-depiction and bottom, 2D-depiction).

Initially, the spectrum consists only of a doublet originating from the anisotropic L_α-phase. As time progresses, the quadrupolar splitting $\Delta\nu_Q$ of this doublet decreases steadily, i.e. the two peaks converge, up to the point where they coalesce and thus form a central singlet. At the same time, the intensity of the peaks decreases and their width at half height increases. Contrariwise, the formed singlet subsequently grows in intensity and simultaneously decreases in width, until the typical singlet of a steady state sponge phase is attained. Therefore, and in contrast to the sponge to lamellar transitions, there is no simultaneous existence of an L_α-doublet and an L_3-singlet and accordingly there is no coexistence of a conventional lamellar and sponge phase during the transition process. Note, that the first spectrum, the L_α steady state doublet, is omitted in fig. 7.2.6(13) *bottom* for clarity, since there is a slight but characteristic shift of the doublet position to higher frequencies at the start of each transition. This first doublet is given for reference only in fig. 7.2.6(15).

Fig. 7.2.6(14) to (19) demonstrate the peak evolution for various typical phase transition experiments in both two and three dimensions. In all cases the frequency range observed is 40Hz to facilitate comparisons between the different figures. As opposed to the sponge to lamellar transition, there is no essential difference between transitions of samples with different bilayer volume fraction ϕ_{B+C}, nor does a variation of ΔT or η have any discernible effect. In fact, even the time scales of the transition processes are comparable, as all seem to be completed within ~600s. Actually, only differences that are not directly related to the transition processes can be determined. For instance, the initial, steady L_α-state quadrupolar splitting of course varies with ϕ_{B+C} as described previously (section 7.2.6.2). Also, the peaks of the transitions with samples of increased viscosity (fig. 7.2.6(19)) are once again rather wide. This issue will be addressed in section 7.4.5.4.

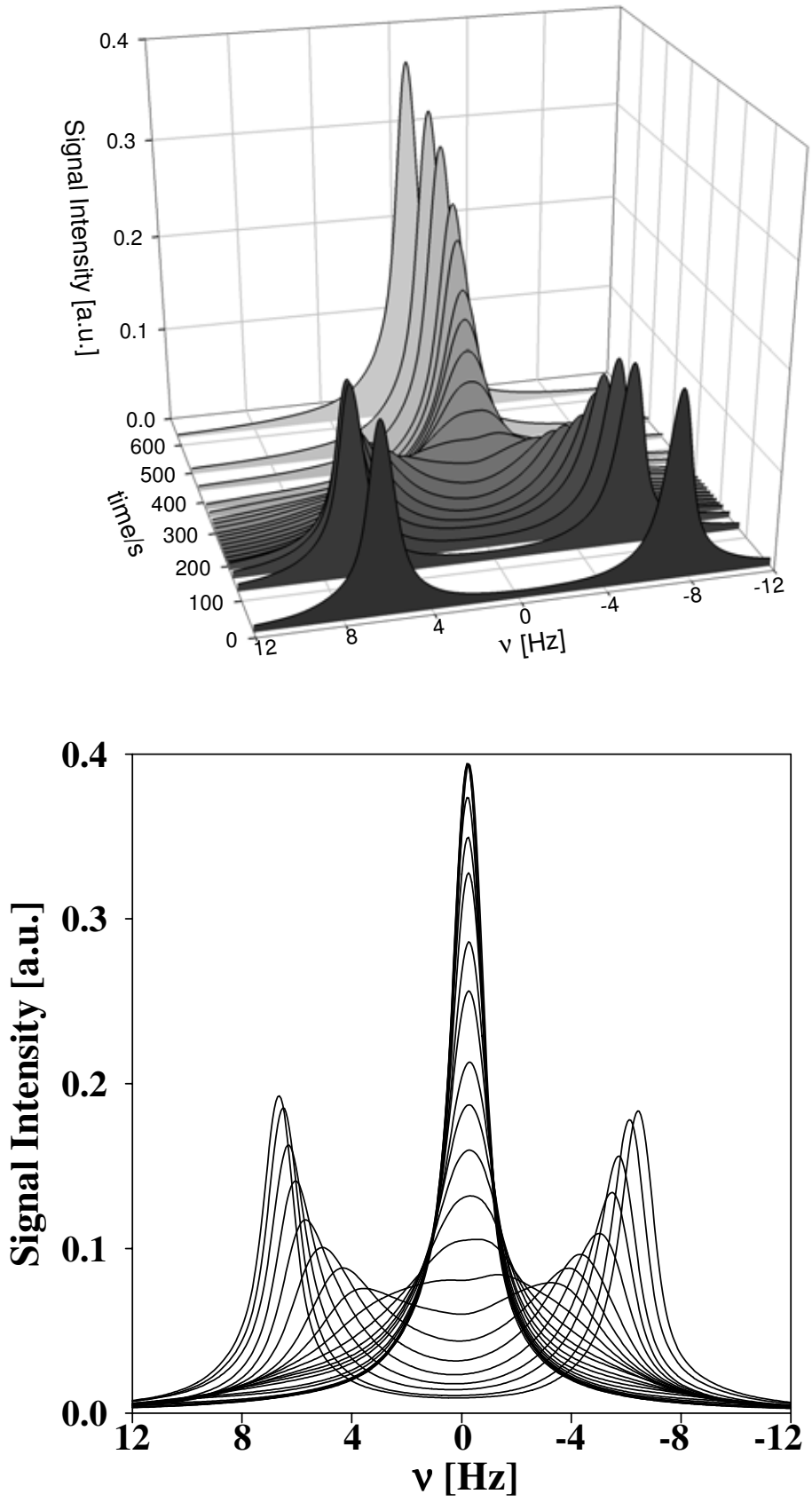

Fig. 7.2.6(13): experiment FT_25, ϕ_{B+C}=0.06, ΔT=+1.5°C, Varian 360 *top*: temporally subsequent ^{2}H-NMR spectra stacked in a 3D-plot to visualise peak evolution. *bottom*: superposition of the ^{2}H-NMR spectra displayed above, eliminating the time axis. In contrast to the sponge to lamellar transitions, the simultaneous existence of three peaks is not visible. Instead the lamellar doublets converge and finally coalesce to form the singlet of the sponge phase. The initial L_α-doublet has been omitted for clarity.

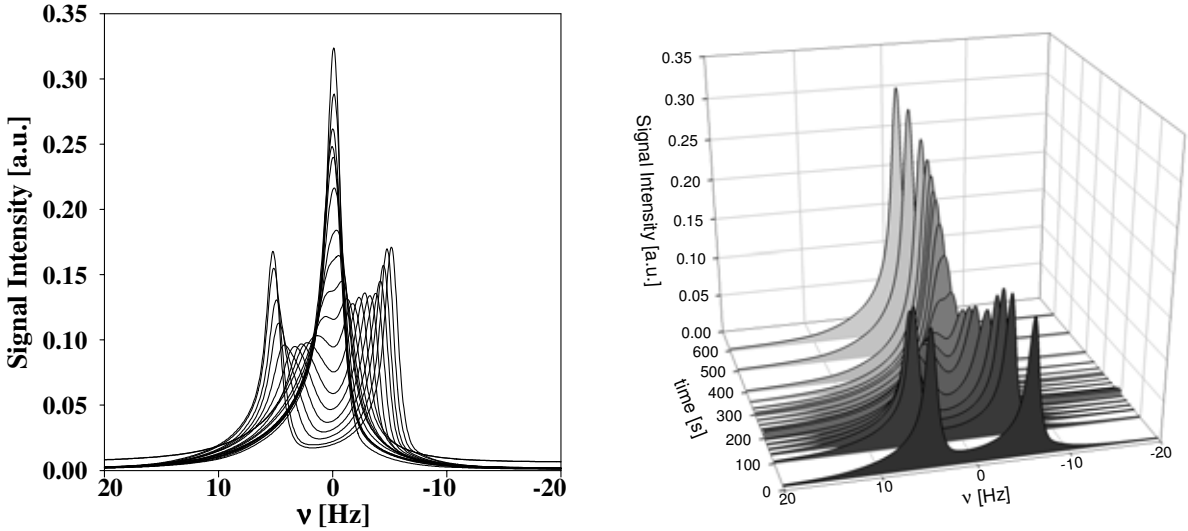

Fig. 7.2.6(14): experiment FT_55, ϕ_{B+C}=0.05, ΔT=+1.5°C, Varian 360

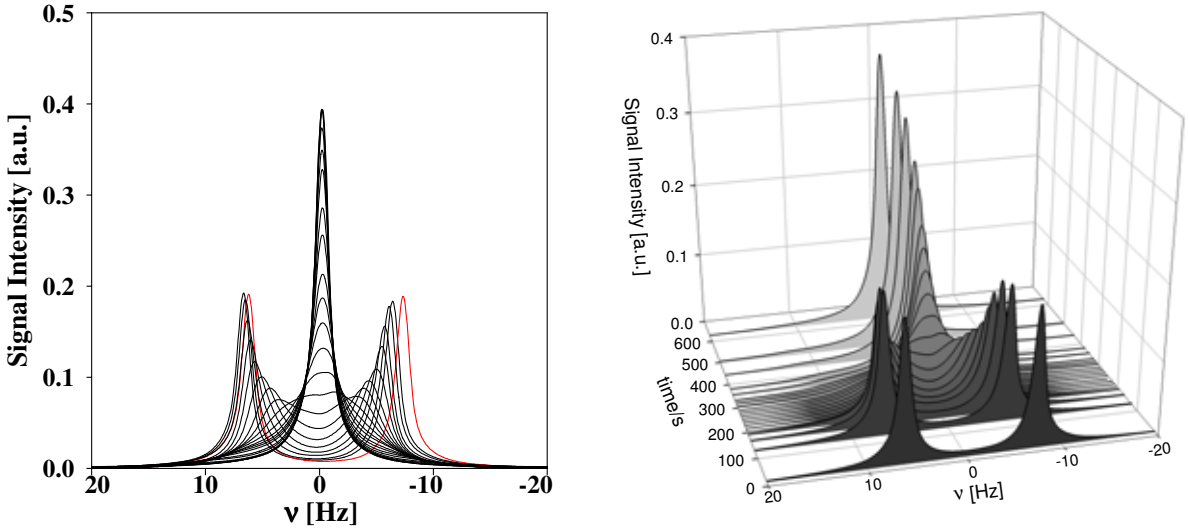

Fig. 7.2.6(15): experiment FT_25, ϕ_{B+C}=0.06, ΔT=+1.5°C, Varian 360 The plot of superimposed spectra includes the initial L_α steady state doublet (grey) and demonstrates the characteristic shift to higher frequencies at the start of the transitions.

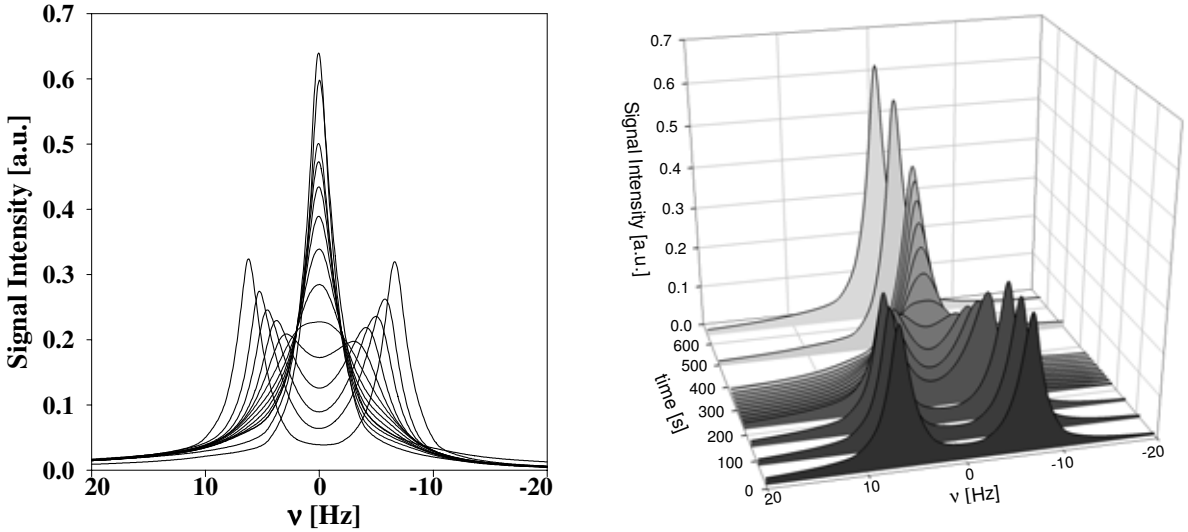

Fig. 7.2.6(16): ϕ_{B+C}=0.06, ΔT=+1.5°C, Bruker DMX-200

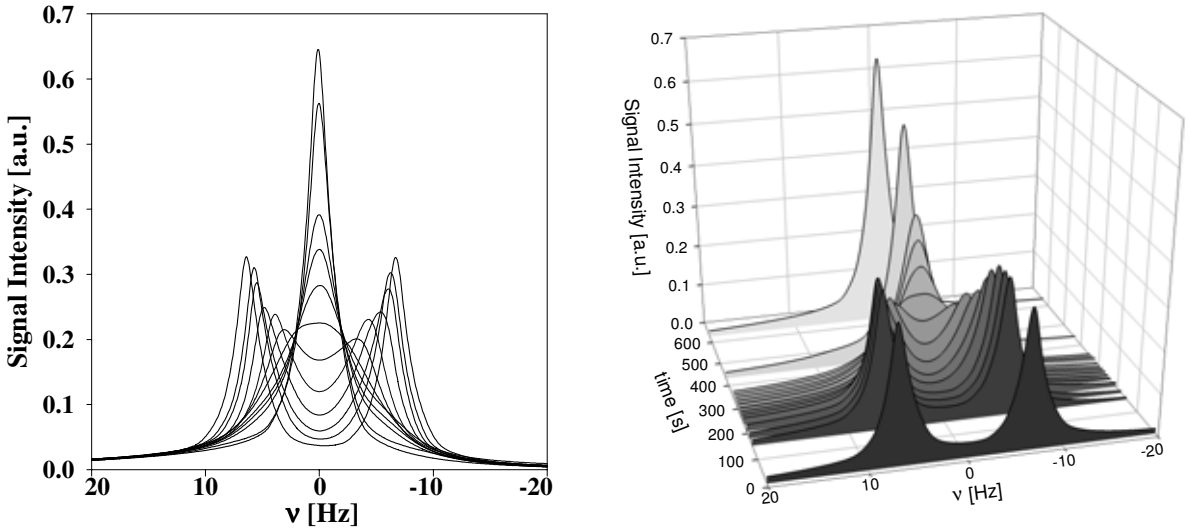

Fig. 7.2.6(17): ϕ_{B+C}=0.06, ΔT=+2.0°C, Bruker DMX-200

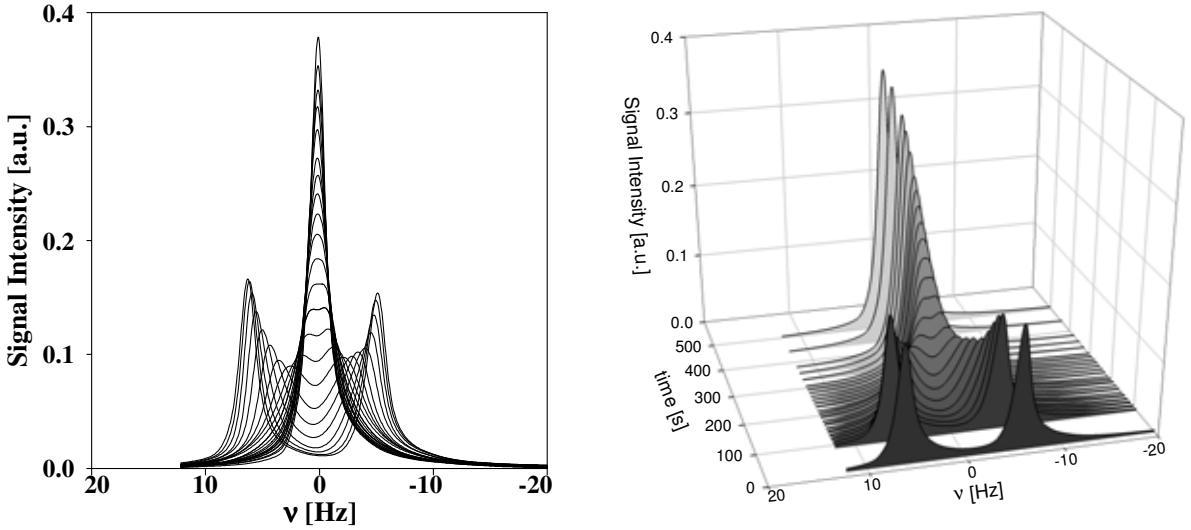

Fig. 7.2.6(18): experiment FT_14, ϕ_{B+C}=0.06, ΔT=+0.9°C, Varian 360 The two images are those of fig. 7.2.6(13) top and bottom with the frequency range extended to 40Hz for comparison.

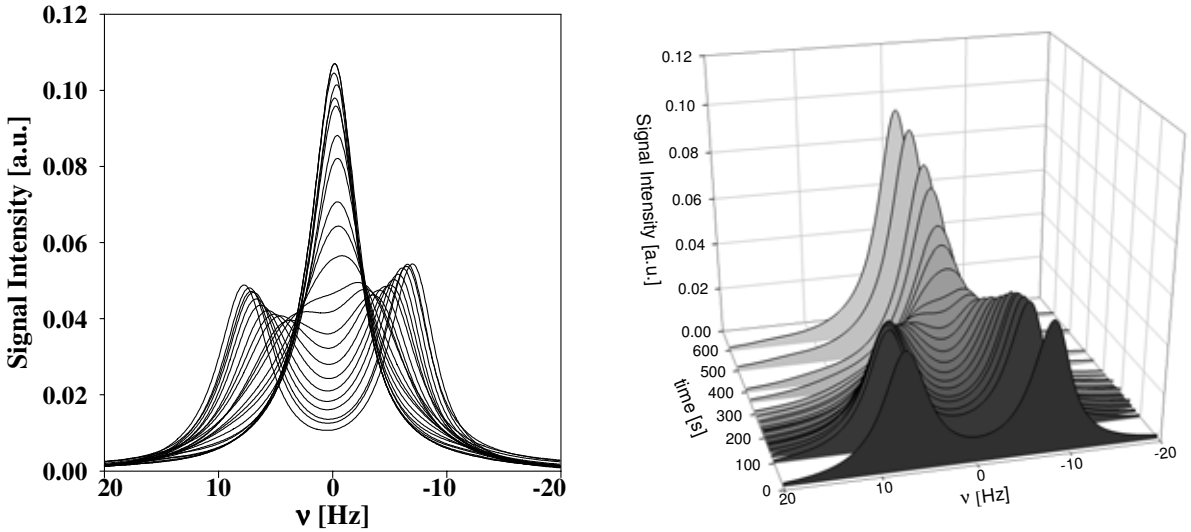

Fig. 7.2.6(19): experiment FT_83, ϕ_{B+C}=0.06, ΔT=+1.5°C, $\eta_{D2O/S} = \eta_0 \cdot 2.261$, Varian 360

On a different note, fig. 7.2.6(15) and (16). serve to demonstrate reproducibility, as these graphs represent in principle the same experiment. In each case a sample of 'standard' viscosity and ϕ_{B+C}=0.06 was subjected to a *T*-jump of ΔT=+1.5°C, but the transitions were monitored on separate spectrometers. Nevertheless, the two cases yield very similar results, apart for the fact that improved shimming on the Varian 360 spectrometer leads to more defined peaks. The deviations form the general peak shape in fig. 7.2.6(14) are not transition phenomena, but serve to demonstrate possible artefacts, which can result from problems in spectra acquisitioning and/or processing of the FID.

7.2.6.4 Additional Experiments

In separate experiments on the Varian 360 spectrometer, the reversibility of the phase transitions was investigated. To this purpose, a $\phi_{B+C} = 0.05$ sample in the lamellar state was subjected to a positive temperature jump, causing a lamellar to sponge phase transition to occur. This transition was however stopped and reversed by performing a $\Delta T = -1.0$°C jump, as the lamellar peaks were still moving towards coalescence. Fig. 7.2.6(20) displays the result of this experiment from two perspectives. The negative temperature jump was initiated at $t = 60$s, just as the 6^{th} spectrum (counting from $t = 0$, fig (20) *left*) was being recorded. Peak convergence continues for a while and coalescence actually occurs, as the temperature change is not instantaneous, but already at $t = 100$s the first lamellar peaks are visible. The transformation to the steady state lamellar phase then proceeds normally, i.e. the intensity of the lamellar doublet increases steadily as its splitting decreases and simultaneously the sponge peak diminishes and grows broader.

In fig 7.2.6(21), the reversal of a sponge to lamellar transition is portrayed. At $t = 2517$s of a $\phi_{B+C} = 0.05$, $\Delta T = -1.0$°C phase transition experiment, temperature was changed back to the value of the steady state L_3-phase via $\Delta T = +1.0$°C. This point in time equals $t = 17$s in the plot. The lamellar peaks, which exist at the time can be seen to converge normally, while the present L_3-peak remains unchanged. (It can be seen increasing in intensity at ~150s, this however is a result of the superposition with the lamellar peaks, which are beginning to notably reduce their splitting and increase their width $\Delta\nu_{1/2}$ at this point in time.) On the whole, a standard lamellar to sponge transition is witnessed, with the exception that a constant L_3-peak is present at all times.

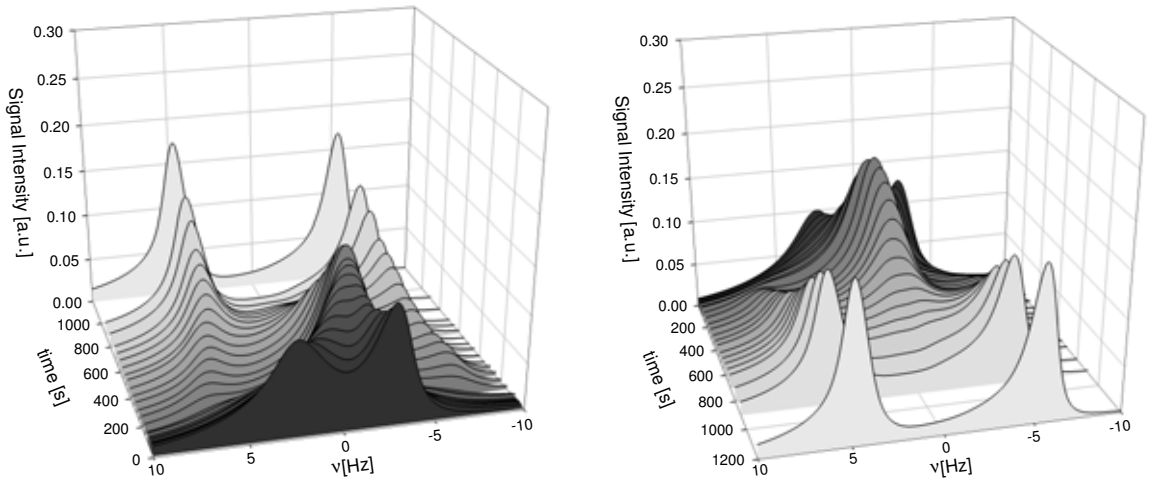

Fig. 7.2.6(20): experiment FT_67, $\phi_{B+C} = 0.05$, Varian 360. A lamellar to sponge phase transition is reversed by performing a *T*-jump of $\Delta T = -1.0°C$ before peak coalescence is attained. The *left* and *right* serve to show different perspectives of the same plot.

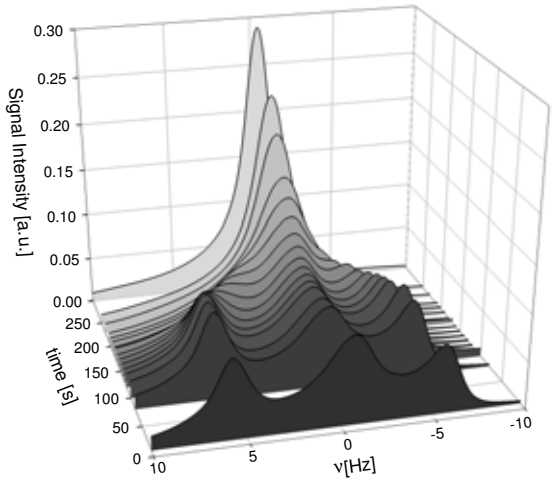

Fig. 7.2.6(21): experiment FT_66, $\phi_{B+C} = 0.05$, Varian 360. Reversal of a sponge to lamellar phase transition experiment, by increasing temperature by ΔT=+1.0°C back to the value of the steady state L_3-phase.

Finally, a completely new type of phase transition was monitored, the transition from the micellar to the L_α-phase. A $\phi_{B+C} = 0.06$ sample which was in equilibrium at room temperature ($RT \approx 19°C$) was introduced into the spectrometer, in which the airflow temperature corresponded to the temperature of the steady state sponge phase. Therefore a *T*-jump of $\Delta T \approx +18°C$ was performed. The result of the experiment is illustrated in fig. 7.2.6(22).

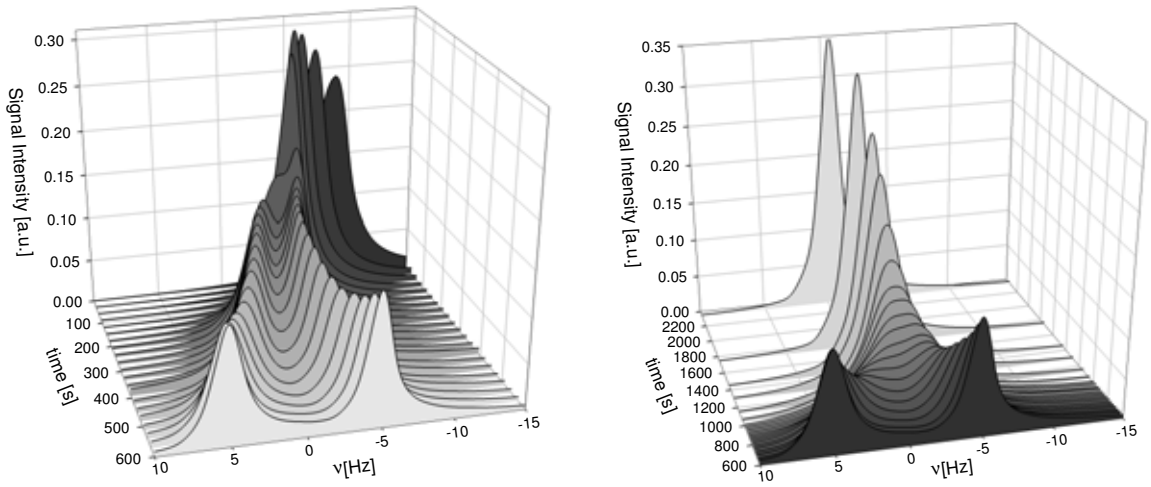

Fig. 7.2.6(22): experiment FT_19, $\phi_{B+C} = 0.06$. Varian 360. Phase transition from the micellar L_1-phase to the lamellar phase (*left*) and onwards to the L_3-phase (*right*). $\Delta T \approx +18°C$.

The isotropic micellar or L_1 phase causes the detection of a broad singlet ($t = 0$, *left* plot). The peak sharpens quickly until a maximum intensity is attained. Afterwards, the intensity decreases again as the peak gets broader. However, it is clear that the cause of this broadening is actually the development of a doublet, which continues to increase its splitting. The beginning of the transition is also marked by a strong shift of the peak position (or central position, when the doublet is formed) to higher frequency. The spectra attain a constant position after ~450s. After 600s, the maximum $\Delta\nu_Q$ value of this transition is reached, and the transformation continues in the standard fashion to the L_3-phase (*right* plot). Notably, the first part of the transition, i.e. the L_1 to L_α transition, is similar to the L_α to L_3 transition when viewed backwards in time.

Note that all of the experiments described in this section were performed at least twice, and that in each case similar results were obtained.

7.3 Analysis of the Experimental Findings

One of the primary goals of this thesis, is to investigate the kinetics of L_3/L_α phase transitions. In this context, the acquired NMR spectra yield several parameters, which can be examined as a function of time. In case of the sponge to lamellar transition, the analysis procedure is more straight forward, since the three detected peaks do not shift greatly in frequency, are reasonably separated, and are essentially of Lorentzian lineshape. Accordingly, the peak intensities and their width at half height $\Delta\nu_{1/2}$, as well as the quadrupolar splitting $\Delta\nu_Q$ between the L_α-peaks are obvious parameters to follow. These same parameters are also of importance for the lamellar to sponge transition, but they can only be monitored for maximum two peaks, since the detected doublets converge and become one peak after the occurrence of coalescence. In addition, the observed behaviour is reminiscent of the lineshapes which appear when there is an exchange of intermediate rates between two distinct states (see section 7.1.9, fig. 7.1.9(1)). Thus a supplementary evaluation procedure with parameters akin to those of the McConnell equation (eq. 7.1.9(1)) appeared appropriate.

7.3.1 L_3 to L_α Transitions

Before undertaking any analysis of the sponge L_3 to lamellar L_α transitions, it is important to recognise, that at *any* stage of the conversion the detected doublet arises from D_2O in an L_α-phase, while the singlet stems from D_2O in a sponge phase. This is a sensible hypothesis because the peak evolution is continuous in terms of the signal intensities and integrals, and furthermore because the frequencies at which these single peaks appear are (approximately) constant. Therefore a *nucleation and growth* type process is observed, i.e. the L_α-phase nucleates in the L_3-phase and the formed domains subsequently grow at the expense of their sponge phase surroundings until all of the initial phase is converted. Furthermore, since two separate signal types are detected, the exchange of probe molecules, i.e. the D_2O, between the lamellar and the sponge phases is slow on the NMR timescale (section 7.1.9).

Section 7.2.5 explains the origin of the doublet for the steady state lamellar phase and, with the aid of eq. 7.2.5(1), states that the magnitude of its quadrupolar splitting $\Delta\nu_Q$ is only a function of the mole fraction of MAPA D_2O p_x and the order parameter S_{qn}. For ideal one-dimensional swelling (see section 2), water addition to a lamellar phase only increase the amount of bulk water. Therefore p_x corresponds to the number of MAPA D_2O molecules n per

surfactant molecule times the mole ratio of surfactant x_C to heavy water x_A[90] and eq. 7.2.5(1) transforms to

$$\Delta\nu_Q = \frac{n \cdot x_C}{x_A} \cdot \frac{3}{4}\chi \cdot \left|S_{qn}\right| \qquad \text{eq. 7.3.1(1)}$$

The mole ratio can be expressed as a volume ratio when accounting for the appropriate densities ρ and molar masses *M*. Thus,

$$\Delta\nu_Q = \frac{n \cdot V_C}{V_A} \cdot \frac{\rho_C \cdot M_A}{\rho_A \cdot M_C} \cdot \frac{3}{4}\chi \cdot \left|S_{qn}\right| \qquad \text{eq. 7.3.1(2)}$$

and the volume ratio can in turn be expressed as the ratio of volume fractions, where the volume fraction of water ϕ_A equals $(1-\phi_{B+C})$ and $\phi_C = \phi_{B+C} \cdot \omega_b$. Therefore,

$$\Delta\nu_Q = n \cdot \omega_b \cdot \frac{\phi_{B+C}}{1-\phi_{B+C}} \cdot \frac{\rho_C \cdot M_A}{\rho_A \cdot M_C} \cdot \frac{3}{4}\chi \cdot \left|S_{qn}\right| \qquad \text{eq. 7.3.1(3)}$$

Already the preliminary NMR experiments showed that the quadrupolar splitting of the steady state lamellar phase (from now on termed $\Delta\nu_{Q,L}$ to differentiate between equilibrium and non-equilibrium splittings) is directly proportional to the ratio $\phi_{B+C}/(1-\phi_{B+C})$ (fig. 7.3.1(1)), so that eq. 7.3.1(3) is verified.

From this it follows that $n\left|S_{qn}\right|$ is constant over the observed concentration and temperature range (no trends for $\Delta\nu_{Q,L}$ are discernible for the varying magnitudes of the temperature jump for a given sample). Thus the increased values of $\Delta\nu_Q$ at the beginning of the L_3 to L_α transitions must stem from lamellar domains with an appropriately higher bilayer volume fraction.

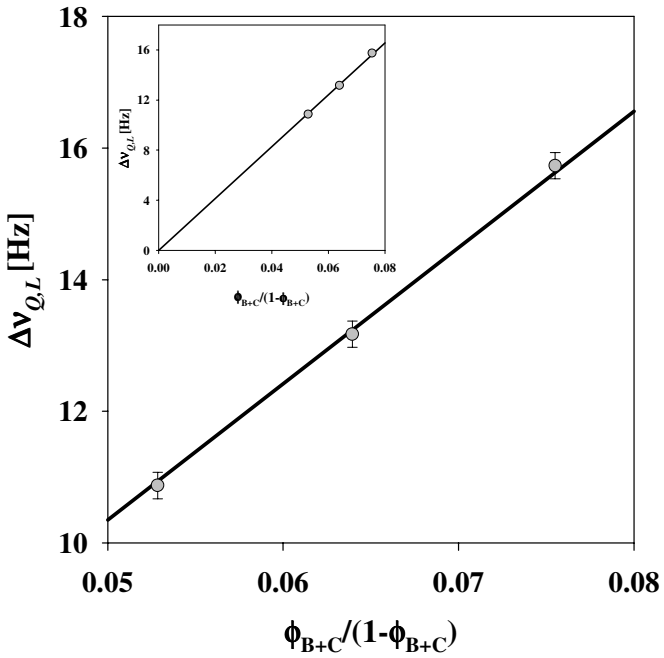

Fig. 7.3.1(1): the quadrupolar splitting within the steady state lamellar phases for samples of varying bilayer volume fraction (ϕ_{B+C} ~ 0.05, 0.06 and 0.07) as determined by the preliminary experiments. The linear regression passes through the origin (*insert*).

In section 7.1.4 it is shown, that when one compares the integral values of different Lorentzian lineshapes, one directly compares the number of nuclei from which these signals originate. During the L_3 to L_α transitions, the singlet of the sponge phase and the doublet of the lamellar phase coexist. Thus, by determining the integrals of these two signal types for each spectrum, one obtains the evolution of their ratio, i.e. the mole ratio of D_2O in the sponge to D_2O in the lamellar phase (fig. 7.3.1(2)).

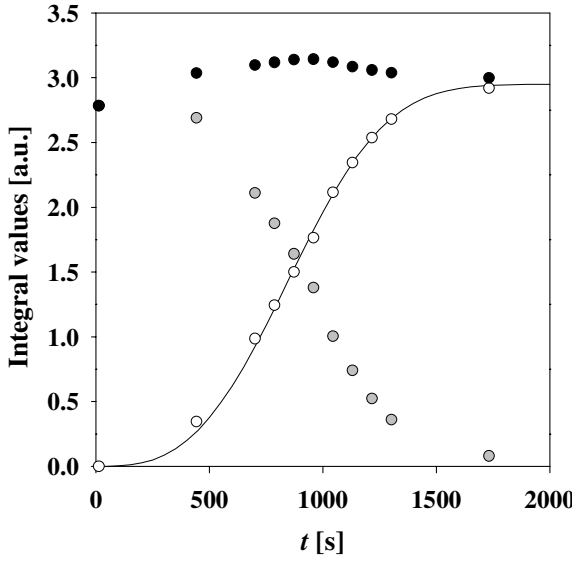

Fig. 7.3.1(2): ϕ_{B+C}=0.06, ΔT=-1.5°C, Bruker DMX-200 (compare fig. 7.2.6(4)). Integral development as a function of time. The empty symbols depict the sum of the integrals of the two lamellar peaks, the grey symbols the integral over the L_3-peak and the dark symbols the sum over all integrals.

These mole ratios directly correspond to the volume ratios of the two phases as long as their bilayer volume fractions are identical. However, this condition is not met as was shown above. Then again, even in cases of the most extreme deviations from the equilibrium bilayer volume fraction, which occur at the beginning of the transitions, the higher ϕ_{B+C} values generally cause the volume fraction of the L_α-phase to be underestimated by less than 2%. An underestimate of ~7% occurs only for the very large splittings initially detected for the $\phi_{B+C} = 0.08$ sample. Thus, when neglecting these small deviations, the doublet integral can indeed be identified as the lamellar phase volume fraction φ.

Unfortunately, the determination of the signal integrals is not trivial. An inherent problem of the integral analysis is that the individual peaks are not well separated, i.e. there is significant overlap between the resonances. Therefore, the integrals of the each peak cannot be determined directly. Instead, the NMR spectra are fitted with the sum of a number of Lorentzian curves corresponding to the number of visible peaks. The lineshape of a single Lorentzian is given by eq. 7.1.4(5) and its integral is calculated via eq. 7.1.4(11). Thus there are nine parameters which need to be determined for each fit, i.e. height, width and location of each peak. Peak location can generally be estimated well, since the types of overlaps encountered lead to only slight shifts in frequency. Peak intensity is also straight forward. The fitting procedure is more problematic for the width at half height $\Delta\nu_{1/2}$, especially when the respective peak is obscured beyond that point (fig. 7.3.1(3)). Note that altering even a single parameter affects all others.

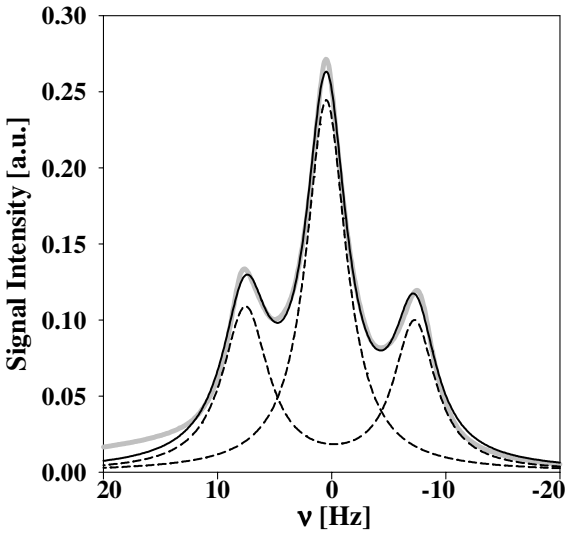

Fig. 7.3.1(3): spectrum (fig. 7.2.6(4), t = 873s) during a sponge to lamellar transition (grey) automatically fitted with the sum of three Lorentzians (solid line). The width $\Delta\nu_{1/2}$ of the lamellar peaks is not directly observable. To visualise the integrals associated with the L_α and L_3-phase, the lineshape of the lamellar doublet of the fit (which itself is the sum of two Lorentzians) and the L_3 singlet are given (dashed lines).

The L_3 to L_α transition spectra (detailed e.g. in fig. 7.2.6(4)) were fitted automatically by software which had first to be written in the SigmaPlot program (see section 10.4.5). The fit is performed according to the least squares method. It is in this manner that the data points of fig. 7.3.1(2) were derived. The integrals of the lamellar peaks, that is the values of φ, evolve as a rule in a sigmoidal form, i.e. initially slow then accelerating and finally decelerating again before completion. A theoretical model, that yields this type of description for a nucleation and growth mechanism was developed by *Kolmogorov*[76], *Johnson*, *Mehl*[77] and *Avrami*[78,79,80] (KJMA). It is described in section 6.2.

7.3.1.1 Kinetic Analysis and Re-Evaluation of the Preliminary Experiments

The first set of experiments which were conducted on the Bruker DMX-200 spectrometer, were initially analysed by using the automated fitting procedure described above. Once the integrals were determined, the L_α-doublet integral values were normalised to the integral value of the steady state lamellar phase, i.e. the final spectrum. The results of these investigations have been published[97]. However, after the second set of experiments using the Varian 360 spectrometer, this approach was reconsidered for several reasons. Firstly, the total integral is not constant over time (fig. 7.3.1(2)) as would be expected in case of perfect spectra of Lorentzian lineshape. Hence, normalisation on the steady state lamellar phase can lead to distortions in the φ-value. Instead, it is advantageous to normalise on the total integral (the sum of the lamellar and sponge signal) at each point in time, i.e. at a constant value of *t*. Then, if there are abnormalities during the transition, such as strong asymmetry or simply deviations from the Lorentzian lineshape, the new type of normalisation still compares integrals acquired at the same conditions. Finally, if a steady state L_α-spectrum is unavailable due to file corruption or premature termination of the transition process, the experiment can be yet evaluated normally.

Apart from improving the normalisation procedure, further development of the method of determining the integral became also necessary in the light of the established experiments. It turned out, that the automated fitting procedure leads to imprecise results, especially if the spectra are not particularly symmetric. This is partly due to the fact that the fitting program does not discriminate between fit deviations from the data that occur far away from a peak and those at the site of a peak, i.e. it does not realise in what part of the spectrum a close fit is more important. Also, negative and positive deviations cancel each other out, since the integral of the fit attempts to match the one of the data. Although this may at first seem

desirable, it is not, because it is the integral ratio of the L_3-peak and the L_α-peaks underlying the fit, which is the objective, and a positive deviation in one part of the spectrum and a negative one in another can severely compromise the result. Thus, in order to increase precision, the parameters acquired after an automated fit were subsequently optimised manually.

Fig. 7.3.1(4) a-d present spectra (grey lines) at various stages of a preliminary experiment and as stated above, the results obtained using the original evaluation procedure have been published[97]. The dashed lines correspond to the original fits acquired using only the automated procedure, while the solid ones indicate the result after manual optimisation. Thus the solid lines represent simulations of the spectra, as their data points no longer correspond to a mathematical fit according to the least squares method.

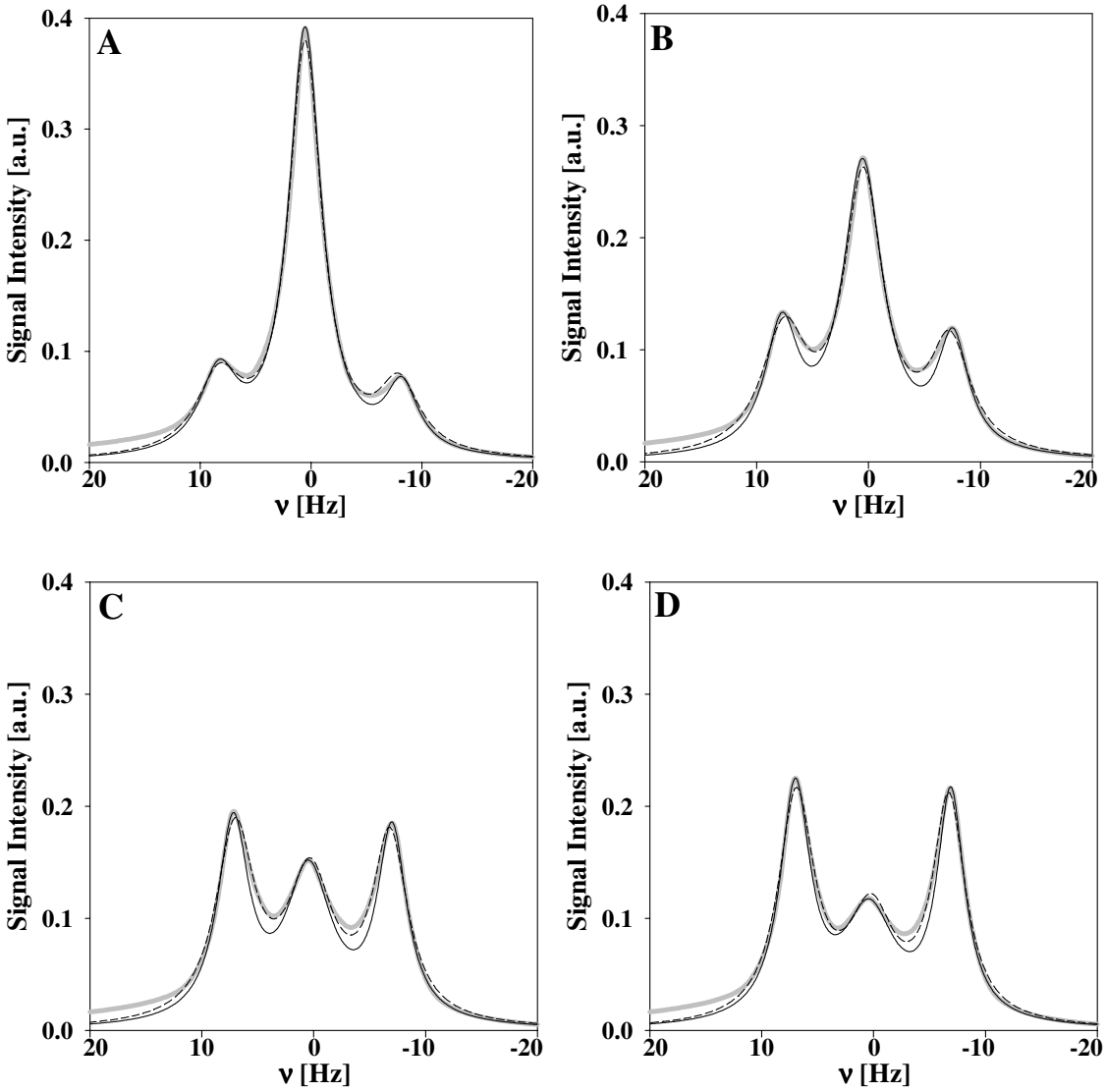

Fig. 7.3.1(4): ϕ_{B+C}=0.06, ΔT=-1.5°C, Bruker DMX-200 (fig. 7.2.6(4)) The presented spectra (grey lines) A-D were taken at time from t = 701, 873, 1045 and 1131s The dashed lines correspond to the automated least squares fit, the solid lines represent an optimised simulation.

At first glance, it appears that the automated fits (dashed lines) lead to superior results when compared to the simulations (solid lines). Note however, that the simulations match the experimental data especially at the peak maxima and thus give an accurate value for the quadrupolar splitting $\Delta\nu_Q$. Also, the simulations were chosen to equal the data particularly on the outside of the lamellar peaks. These two measures lead to pronounced deviations from the spectra in the regions between the central L_3-peak and the lamellar peaks. However, the evaluation another experiment further below will show, that this type of deviation is unavoidable, since the high intensities between the lamellar peaks and the sponge phase peak stem from the fact that the registered signals are not of true Lorentzian form (see section 7.4.4).

The integrals derived from the spectra A-D, as well as others, enable to plot the lamellar phase volume fraction φ as a function of time (fig. 7.3.1(5)).

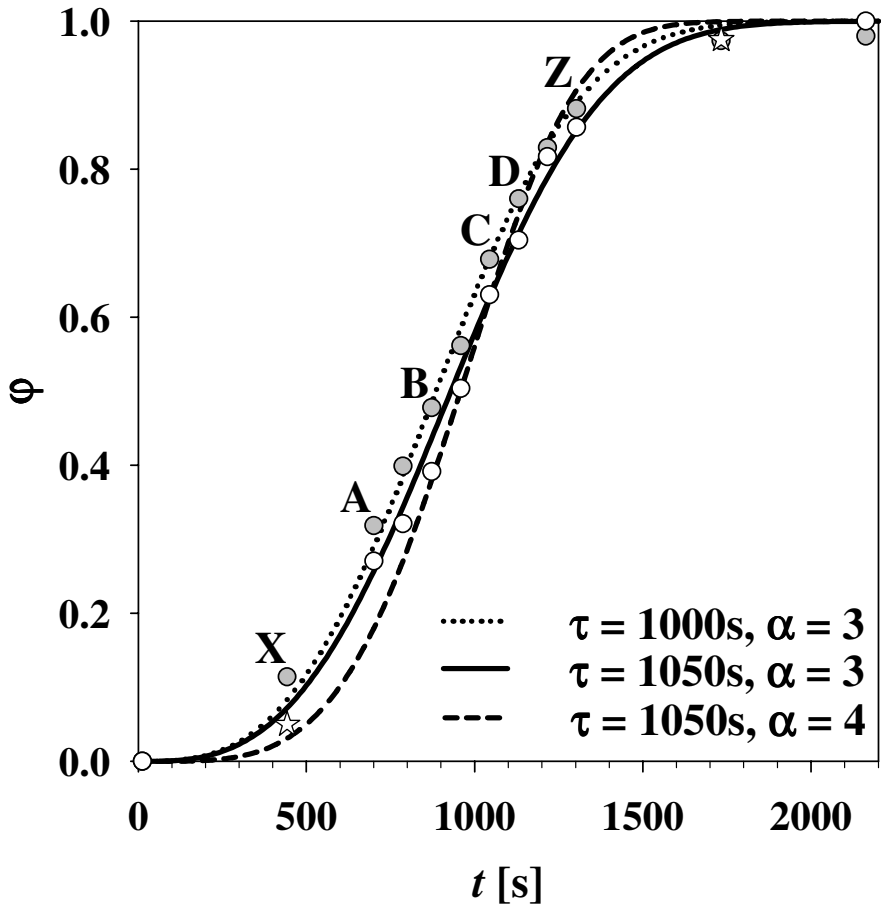

Fig. 7.3.1(5): ϕ_{B+C}=0.06, ΔT=-1.5°C, Bruker DMX-200 The development of the lamellar phase volume fraction φ. The grey data points result from the automated fitting procedure and from normalising on the steady state lamellar phase integral, while the white ones result from the optimised simulation and normalisation at each point in time. The stars indicate estimates where the integral values are difficult to determine, i.e. the error is high. Three fits using the KJMA equation are indicated by different line types.

Regardless of the type of fitting and normalisation method used, φ clearly develops in a sigmoidal manner and accordingly simulations of the KJMA eq. are included in the plot. Interestingly, the data acquired using the automated fits, where normalisation occurred using the steady state lamellar integral value (grey circles), does not differ significantly from the one resulting from the simulation, where normalisation was done at each point in time (white circles). Therefore the parameters of their respective simulations using the KJMA equation (eq. 6.2(1)) are almost identical. The grey data is simulated with the dotted line, the white data with the solid line. Furthermore, the dashed line indicates that, although the relaxation time constant τ of the transition can be estimated well, the value of the exponent α is inexplicit to the extend that the type of nucleation described by the constant ψ can not be determined in this experiment. The dimensionality of the growth can however be ascertained to $n = 3$.

The difficulty in determining α, i.e. the steepness of the sigmoidal curve, stems from the fact that for low values of τ, the course of the curve is quite insensitive to changes in α. This is visible in fig. 6.2(1), which also demonstrates that with increasing τ values this insensitivity is increasingly lost. Thus experiments which yield exceptionally high values of τ are required to identify the exponent with accuracy. The differences of an $\alpha = 3$ or 4 curve are however most pronounced towards the beginning and the end of a transition process. Unfortunately, it is just in these regions that the error of integral determining is high.

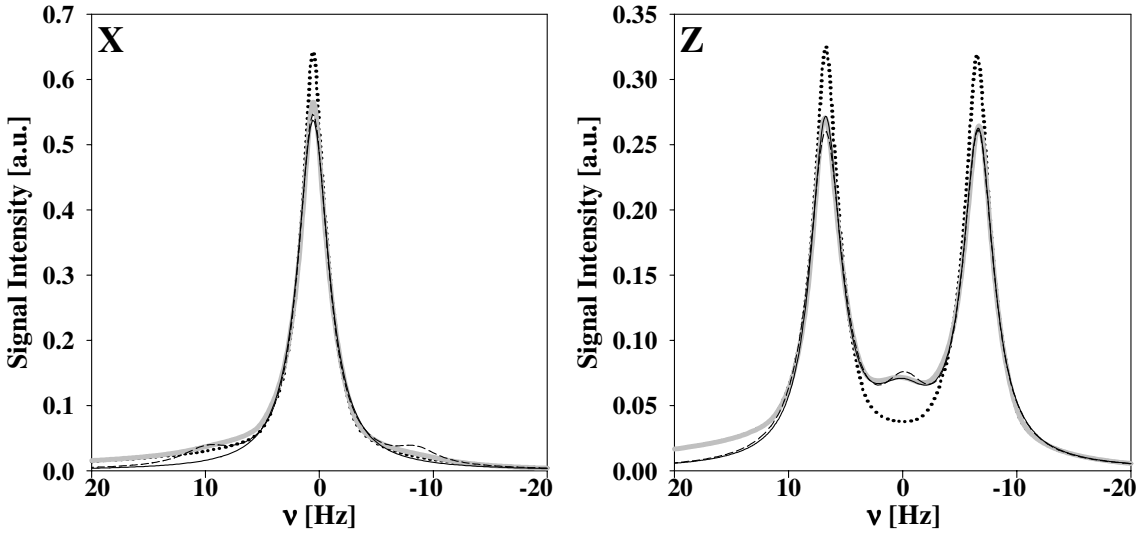

Fig. 7.3.1(6): ϕ_{B+C}=0.06, ΔT=-1.5°C, Bruker DMX-200. The spectra (grey lines) corresponding to point X and Z in fig. 7.3.1(5). Dashed lines correspond to the automated fit, solid ones to the optimised simulation. The dotted line indicates the spectrum of the steady state L_3-phase (left) or the steady state L_α-phase (right).

Fig. 7.3.1(6) shows the spectra (grey lines) corresponding to the points X and Z in fig. 7.3.1(5). The automated fits (dashed lines) in these regions need to governed by so many 'constraints', i.e. the fit parameters are restricted to certain ranges of values (see section

10.4.5), that a transition to simulation is essentially attained. In the figure X it is clear that the transition has commenced (the dotted line indicates the spectrum of the L_3 steady state), however the integral chosen for the lamellar phase using the dashed fit is most likely to high (grey circles fig. 7.3.1(5)). Then again, the solid line of a single Lorentzian emphasises the fact that the lamellar integral should be non-zero at this point. Thus a value of φ=0.05 is chosen to indicate that the transition process has started, but is not advanced enough to form distinct lamellar peaks (fig. 7.3.1(5), star symbol).

In the figure marked Z, the central L_3-peak is just barely visible between the lamellar doublet. The dotted line indicates the steady state lamellar doublet that will be the result of the experiment. Clearly though, a significant fraction of the total integral is still contributed through the L_3-phase and the fit and simulation (dashed and solid line) lead to a similar result. Beyond this point in time however the L_3-peak is totally obscured through the L_α-peaks and any fitting must be done manually, which is very time consuming and prone to considerable error. Thus only a point in time (t=1733s), where the transition is deemed to be just incomplete is marked by φ=0.975 (fig. 7.3.1(5) star symbol).

The experiment above was presented to demonstrate that the published results are still valid, although the procedure of integral determining and normalisation has been changed. Furthermore, it was shown that it can be difficult to distinguish between an α-value of 3 or 4. In the publication[97] the φ development of all experiments was described using $\alpha = 3$. The following section will demonstrate that $\alpha = 4$ is much more likely and that the lower value in the preliminary experiments probably resulted from inaccuracies due to suboptimal shimming, i.e. overly wide peaks.

7.3.1.2 Kinetic Analysis of the Established Experiments

In fig. 7.3.1(7) [1a to 120a] the well resolved and symmetric spectra (grey lines) of an L_3 to L_α phase transition experiment (experiment FT_32, ϕ_{B+C}=0.06, ΔT = -1.0°C, Varian 360, see fig. 7.2.6(7)) are presented. The plots will clarify why the automated fitting procedure is insufficiently accurate in case of well-defined peaks and that an α-value of 4 appears highly likely. Furthermore, it is shown that the width at half height $\Delta\nu_{1/2}$ of all the peaks is *not* constant during the transition and that φ can thus be determined only via the complex integral analysis employed and not simply by comparing the peak intensities.

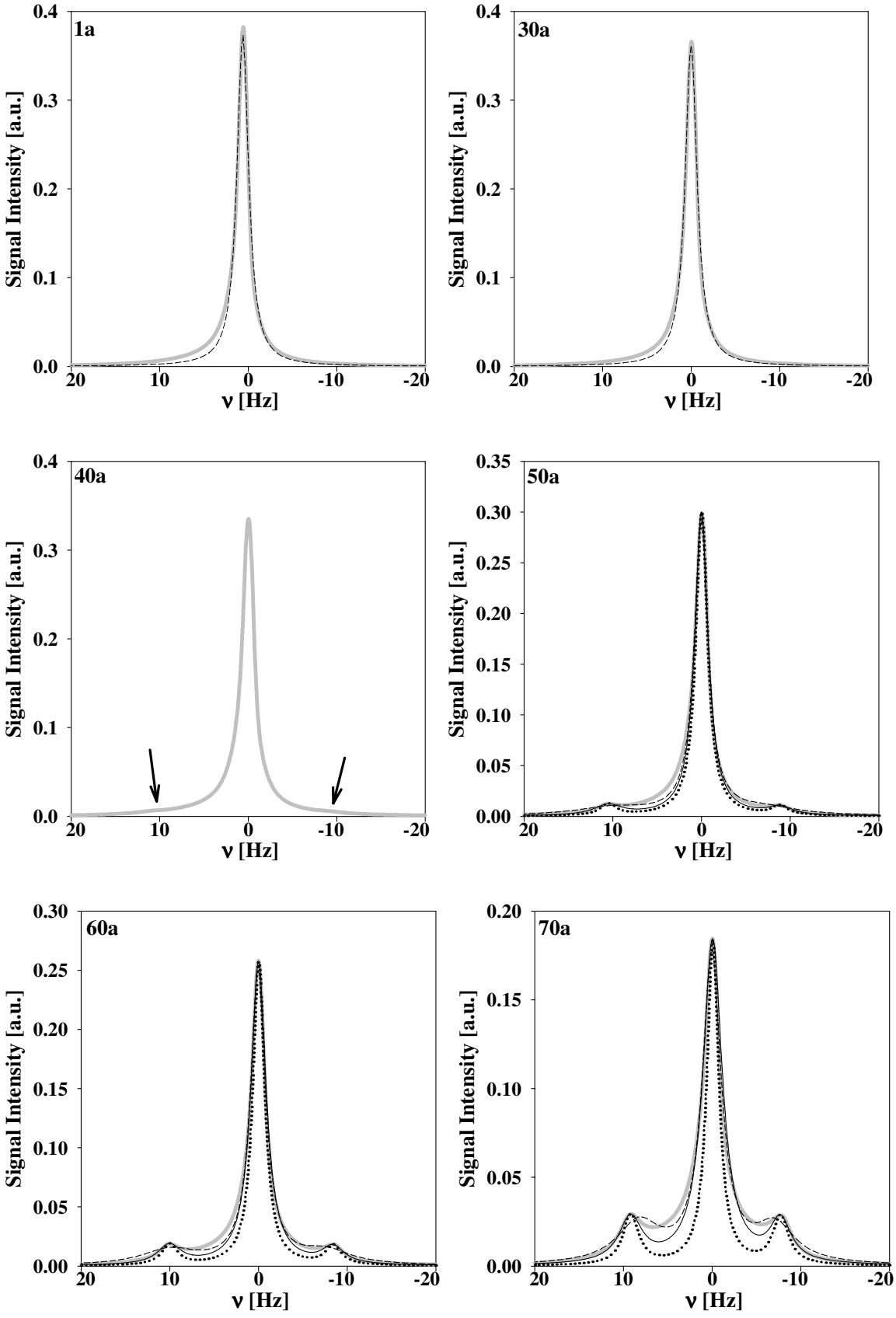
1a
30a
40a
50a
60a
70a
Signal Intensity [a.u.]
ν [Hz]

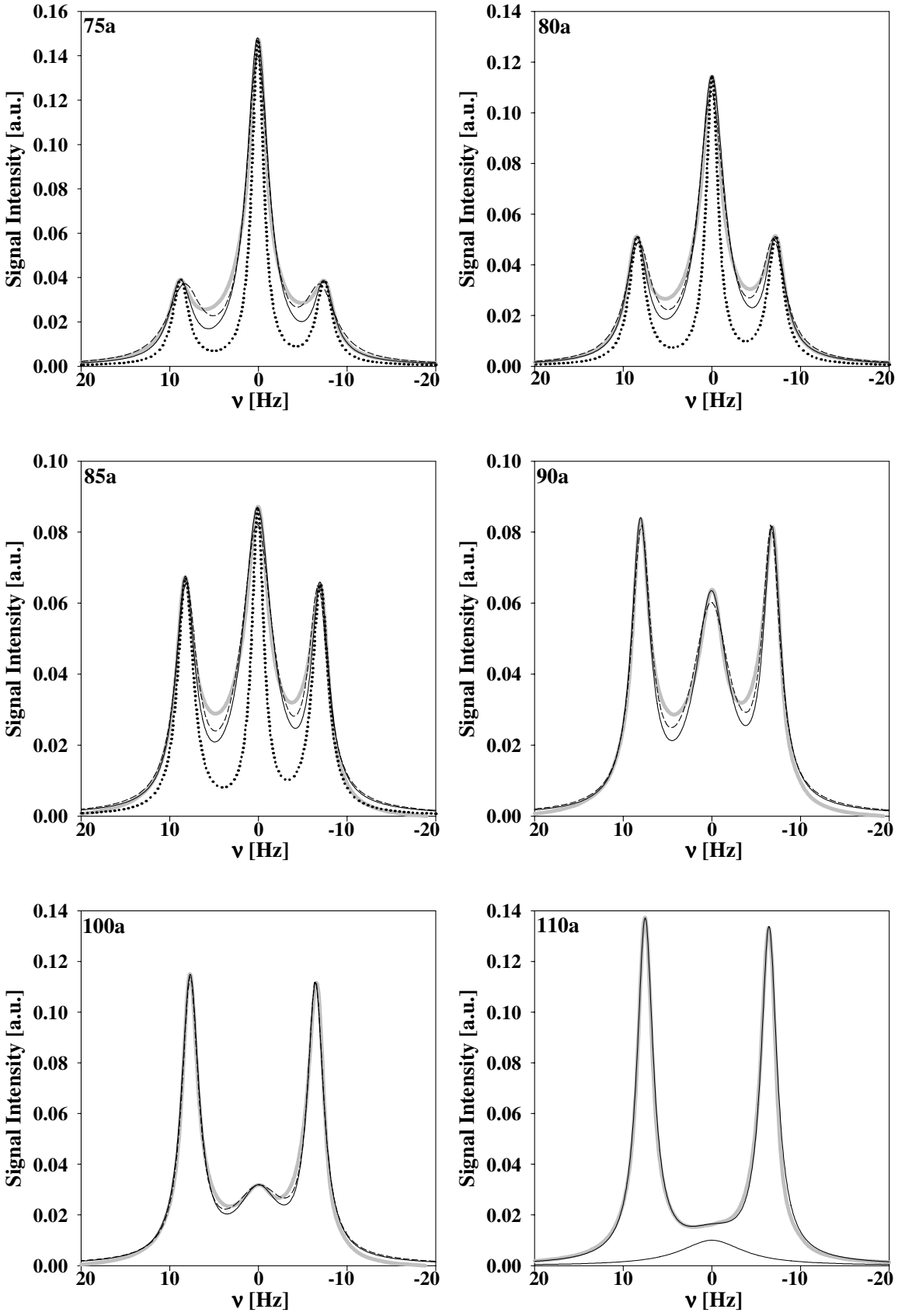
75a
80a
85a
90a
100a
110a
Signal Intensity [a.u.]
ν [Hz]
20
10
0
-10
-20

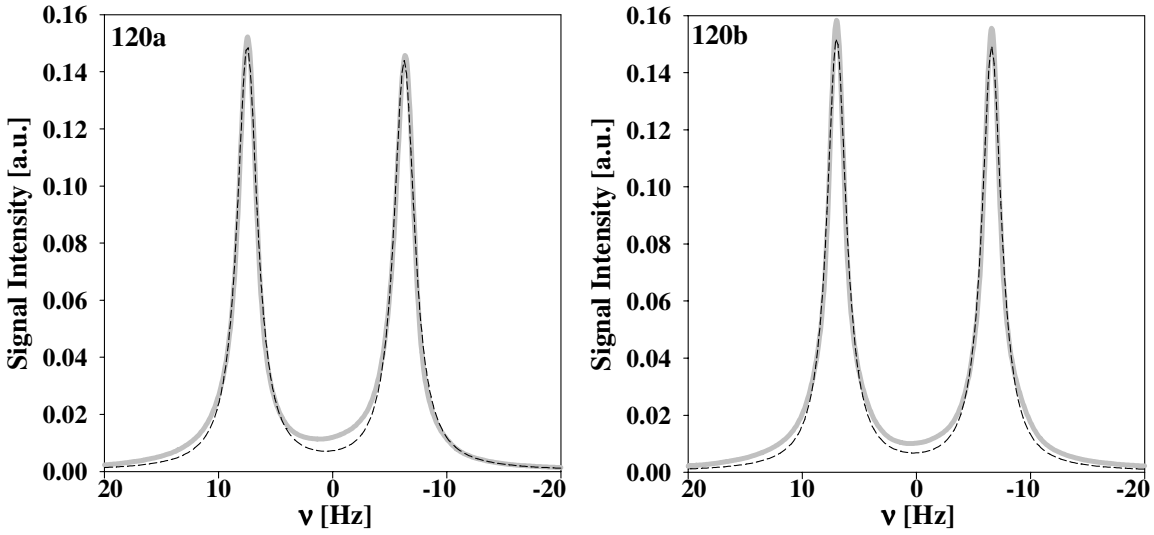

Fig. 7.3.1(7): experiment FT_32, ϕ_{B+C}=0.06, ΔT=-1.0°C, Varian 360 Spectra (grey) at various stages of the phase transition (1a to 120a). Dashed lines correspond to automated fits using one (1a, 30a) two (120a) or three Lorentzians (50a to 100a). Solid lines correspond to simulations. Plot 120b is the steady state lamellar phase of a different experiment (FT_16) and serves for comparison.

Until the appearance of the lamellar peaks (spectrum 40a, peaks indicated by arrows), all spectra are fitted with a *single* Lorentzian line and the value of φ thus considered zero. As soon as the L_α-doublet is more define (50a) fitting can commence. The dashed line corresponds to the automated fit, while the solid one represents the simulation. The dotted line is calculated using the identical parameters of the simulation with the exception of the peak width at half height $\Delta\nu_{1/2}$. For these, the steady state value of the L_3-peak and the L_α-peaks are used and set constant for the respective peaks for the entire transition. Spectra 70a through 85a clearly show that that the dotted fit (constant width) is unsatisfactory and thus that $\Delta\nu_{1/2}$ must be variable during the transition. Spectra 80a to 90a show that the automated fit fails in matching the data in the two regions between the lamellar peaks and the L_3-peak, just like the solid line of the simulation (where the deviation is even greater).

This is a most important finding, because it demonstrates that the experimental data cannot be fitted with Lorentzians in this region. In other words, there is 'added' intensity (when compared to the Lorentzian lineshape) on the 'inside' slope of the lamellar peaks and/or on both slopes of the L_3-peak (in both cases close to the base of the peaks, i.e. somewhat removed from the peak centres). In fact, these types of deviations are already visible for the sponge peak in spectrum 1a. Also, the inability of the Lorentzian functions to equal the data between the peaks causes the lamellar peaks of the automated fit (dashed line) to move in position towards the L_3-peak in order to compensate for the shortcomings (spectra 70a and 75a). It is because of these results that the choice to simulate the data (solid lines)

was made in the first place. The peak positions as well as the peak widths are well visible since the shimming procedure was very successful (the latter only in the cases where a peak is uncovered for at least half its intensity), but only the simulation method accounts for this, i.e. matches these parameters accurately.

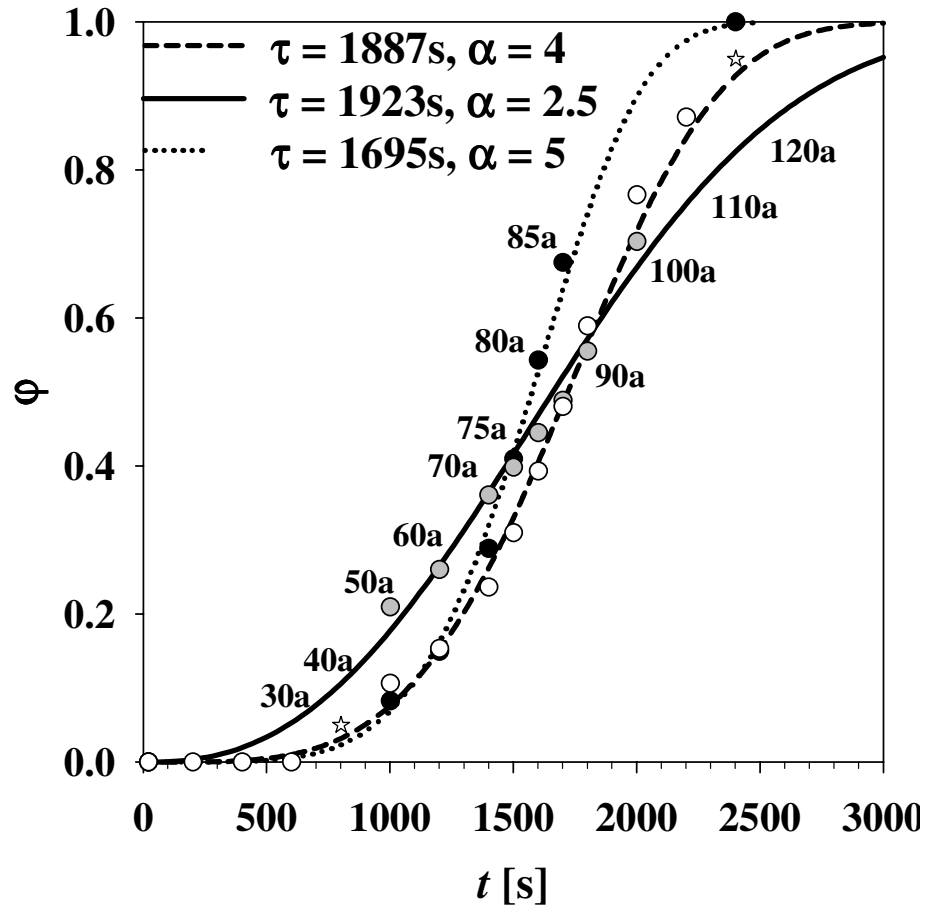

Fig. 7.3.1(8): experiment FT_32, ϕ_{B+C}=0.06, ΔT=-1.0°C, Varian 360. The development of the lamellar phase volume fraction φ as determined by different fitting procedures (fig. 7.3.1(7) 1a to 120a). Grey dots represent the results from the automated fitting procedure, white dots the results of the simulations and black dots the results when the minimum L_3 and L_α-peak widths of the steady state sponge and lamellar phases were used as constants for the simulations of all the spectra. The respective KJMA fits are given by a solid, dashed and dotted line.

In fig. 7.3.1(8) the lamellar phase volume fractions φ of the different fitting procedures presented in fig. 7.3.1(7) [1a-120a] are plotted as a function of time. Grey symbols are the results of the automated fitting procedure, white symbols the result of the simulation and black symbols the result of the simulations when $\Delta\nu_{1/2}$ is kept constant at the minimum values. Again it is clear that the latter method fails, since the corresponding KJMA fit to the black symbols (dotted line) results in an α-value of 5, for which there is no physical explanation. The KJMA fit to φ derived from the automated fits (grey symbols, solid line), leads to α = 2.5 and this non-integer result is also not satisfactory. In addition, automated fits without a great number of constraints to the variables only succeed when used for spectra

acquired in the middle of the transition process. The fit to the results of the simulation however (dashed line), leads to an $\alpha = 4$, even when ignoring data from spectra where the integral determination is difficult and its error is accordingly high (spectra 50a to70a and 100a to 120a).

For the plot 110a the volume fraction $\varphi = 0.87$ was determined by including an L_3-peak of $\Delta\nu_{1/2}$ = 8.6 Hz as part of the three peak fit. That L_3-peak is shown individually the plot. In plot 120a an automated fit using only two Lorentzians (dashed line) was included. Due to the deviations between the spectrum and the fit in the area between the doublet, it was deemed that this plot does not yet represent the steady lamellar phase, i.e. since this is the last acquired spectrum, the experiment was terminated prematurely. This point is made clear, when comparing 120a with a steady state L_α-spectrum from a similar experiment of similar shimming quality (120b, experiment FT_16, ϕ_{B+C}=0.06, ΔT=-1.1°C, Varian 360), where the difference between the spectrum and a fit consisting of two Lorentzian is notably less. Accordingly, a value of $\varphi = 0.95$ was assigned to the time of spectrum 120a and the associated data point is represented by a star symbol in fig. 7.3.1(8). Similarly a value of $\varphi = 0.05$ was assigned to the spectrum 40a to indicate that the transition process has begun and that φ must be non-zero at this point in time (also indicated by a start symbol).

Note that due to the normalisation procedure very different fits can lead to similar results in φ (plot 75a, automated fit and simulation with minimum width). Note also, that although the procedure of automated fitting and the spectra simulations lead to different values of α, the resulting relaxation time constants τ are essentially the same for both cases. This fact inspires confidence in the τ-values determined for this thesis, because it shows that there is a certain independence between the integral determining process and the acquired relaxation time constants and accordingly, that said process allows for errors (systematic or otherwise).

Fig. 7.3.1(9) shows that for the currently considered phase transition, an α-value of four (dashed line) is indeed more likely than one of three (solid line), when assuming a relaxation time constant of τ = 1887s. This is true even if the error of integral determining and thus of φ would be so great in the middle of the transition process, that a distinction between an $\alpha = 4$ and an $\alpha = 3$ KJMA fit would be nonsensical, or even if the systematic shift of the data in fig. 7.3.1(9) to the $\alpha = 4$ fit could be attributed to bias simulations on part of the author. The fact remains that spectra 110a and 120a would require considerably lower φ-values and thus an even larger L_3-peak integral. A larger L_3-peak integral can however only

be attained through increasing peak width (and this does not seem plausible, see section 7.3.1.6), since increases in intensity would cause a singlet to be discernible. Additionally, spectra 30a and 40a would require higher values of φ than currently assumed (zero and 0.05 respectively). This alternative is also not believable.

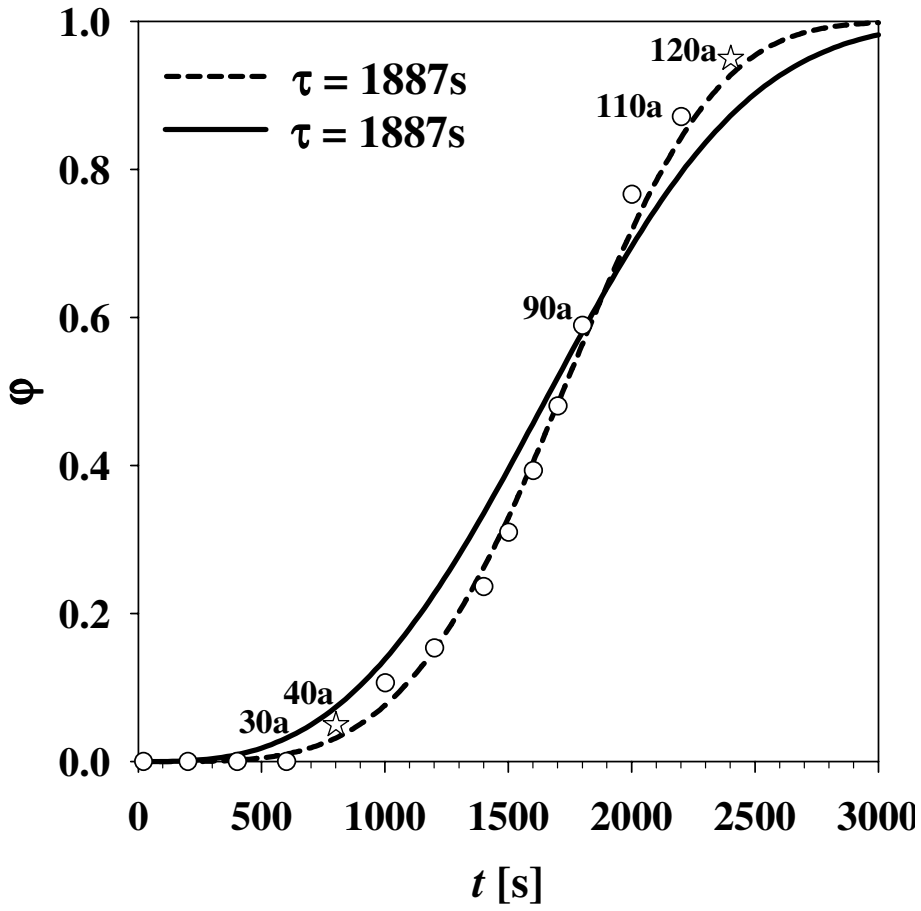

Fig. 7.3.1(9): experiment FT_32, ϕ_{B+C}=0.06, ΔT = -1.0°C, Varian 360. KJMA fits of $\alpha = 4$ (dashed line) and $\alpha = 3$ (solid line) to the data of fig. 7.3.1(7).

The $\alpha = 4$ scenario, and thus 3D nucleation with a constant nucleation rate, is not an exception but the rule when analysing well shimmed spectra of slow sponge to lamellar phase transitions. To demonstrate this, the detailed evaluation of the first and last spectra of another experiment (which is this case definitely attained the lamellar steady state) is presented below. Fig. 7.3.1(10) shows the φ-development of FT_16 (ϕ_{B+C}=0.06, ΔT=-1.1°C, Varian 360) derived from spectra simulations. The KJMA fits are given for the $\alpha = 4$ and $\alpha = 3$ case (dashed and solid lines).

Fig 7.3.1(11), plot 90a shows that at this point in time the transition process is already complete, as comparison with the final spectrum 120a (solid line) shows no difference in intensity between the doublet (the peaks themselves, do continue to sharpen after this

spectrum). The dashed line indicates the deviation to a fit with only two Lorentzians. On the other hand, plot 80a shows that there is still an L_3-peak present, although it is of course obscured by the doublet, because there is a small but distinct difference in intensity between the spectrum (grey line) and the 120a steady state spectrum (solid line) in the area between the peaks. In order to match the KJMA $\alpha = 4$ fit at this point, a φ-value of ~0.975 is necessary and this appears to be indeed reasonable.

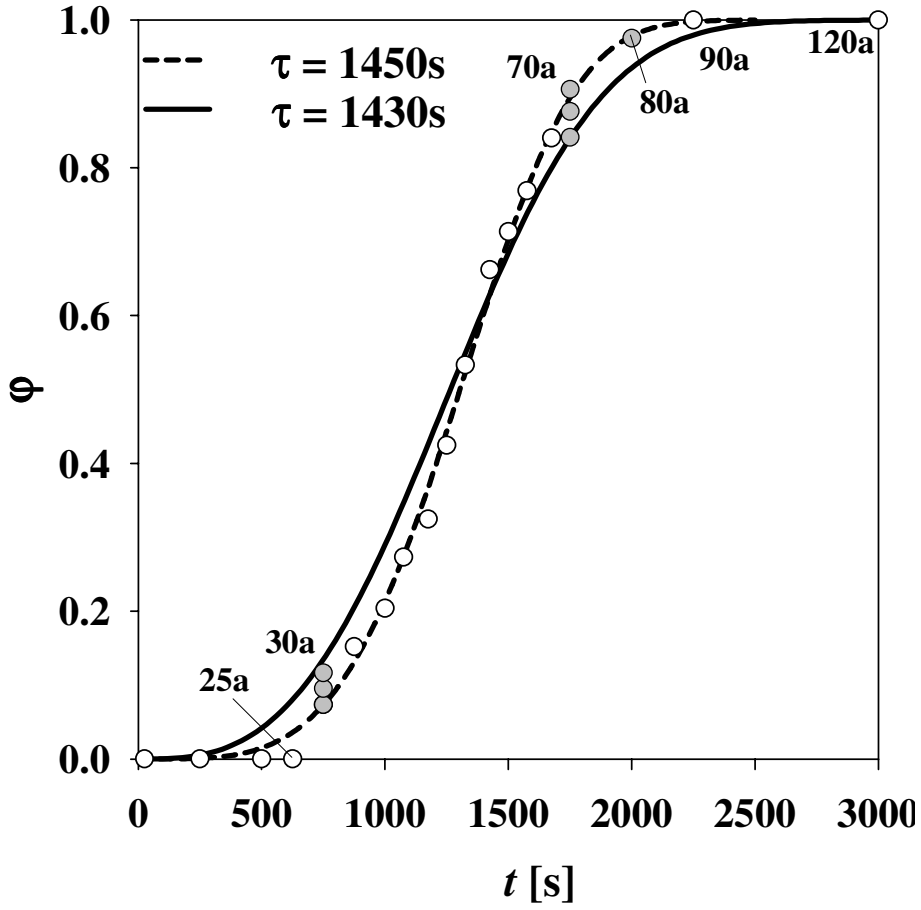

Fig. 7.3.1(10): experiment FT_16, ϕ_{B+C}=0.06, ΔT=-1.1°C, Varian 360 The development of the lamellar phase volume fraction φ with KJMA fits, $\alpha = 4$ dashed line and $\alpha = 3$ solid line.

In plot 25a no lamellar peaks are seen and accordingly the spectrum is fitted with a single Lorentzian (dashed line) and φ = 0. In plot 30a however small but distinct lamellar peaks are visible (*insert*). These are fitted with three different peak widths $\Delta\nu_{1/2}$ = 3, 4 and 5 Hz (enlargement) leading to the three different values of φ plotted in fig. 7.3.1(10). In a similar manner an enlargement of plot 70a is shown, where the width of the obscured L_3-peak was varied ($\Delta\nu_{1/2}$ = 6, 8 and 10.4 Hz) and the three corresponding values of φ are again given in fig. (10). In order to judge the size and integral of the sponge peak, its Lorentzian is plotted

separately for the three cases. Also, a fit with only two Lorentzians (as one needs for the steady state lamellar phase), dotted line, emphasises the amount of intensity still present between the peaks.

The strongest argument here (as in all of the evaluations) for the validity of the $\alpha = 4$ KJMA behaviour is the differences in the spectra 25a and 30a as well as 70a, 80a and 90a. The point in time at which the transition begins, i.e. lamellar peaks are detected, and is completed can be determined quite well. The $\alpha = 3$ case would require extraordinarily wide lamellar and L_3-peaks and the start at the end of the transition. Moreover, for plot 25a a $\varphi \approx 0.10$ is required although no lamellar peaks are visible. Finally, although the wider lamellar peaks in 30a fit the data (grey) better, a non-lorentzian lineshape of the L_3-peak at this point could easily account for the differences (section 7.4.4).

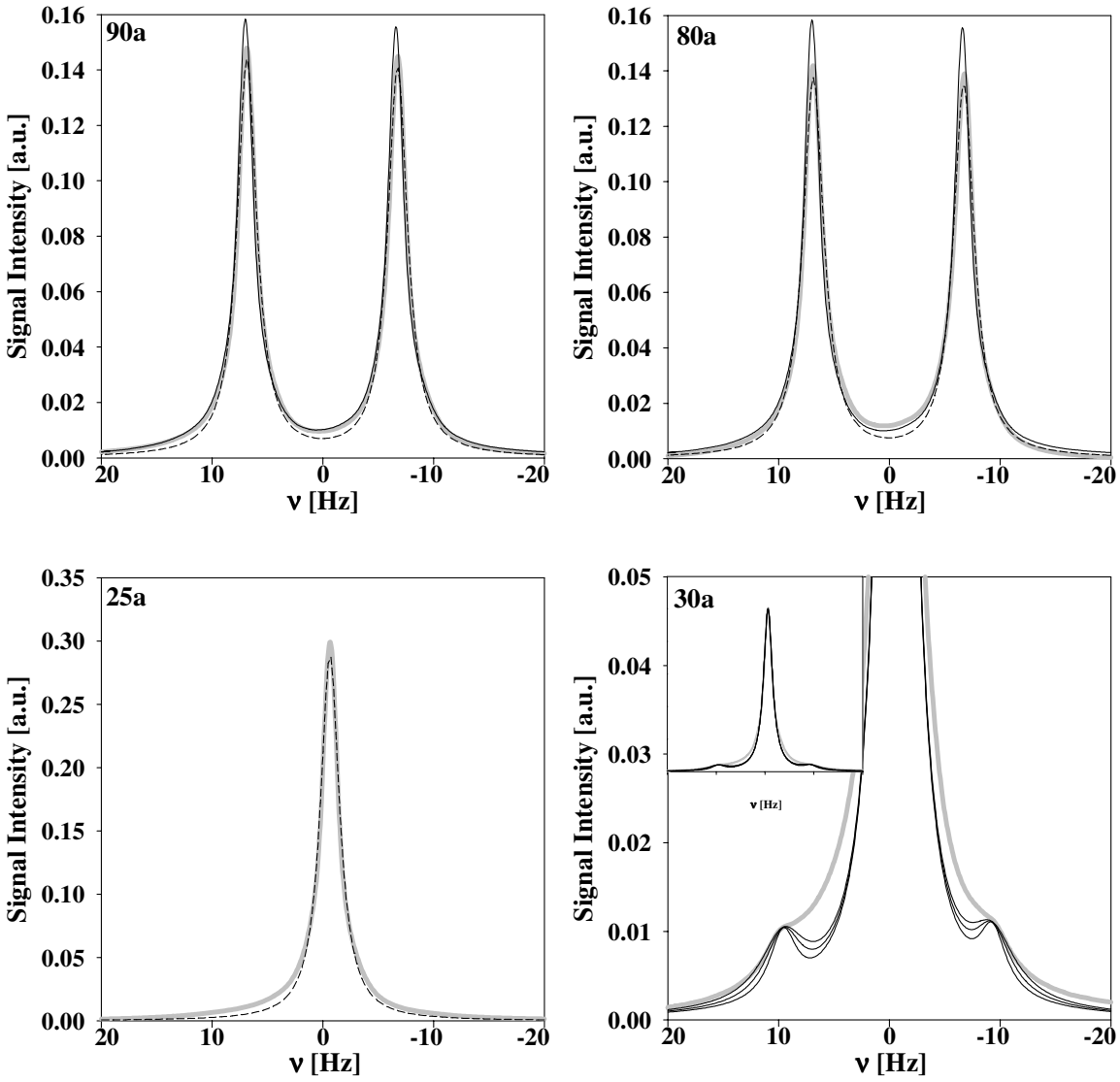

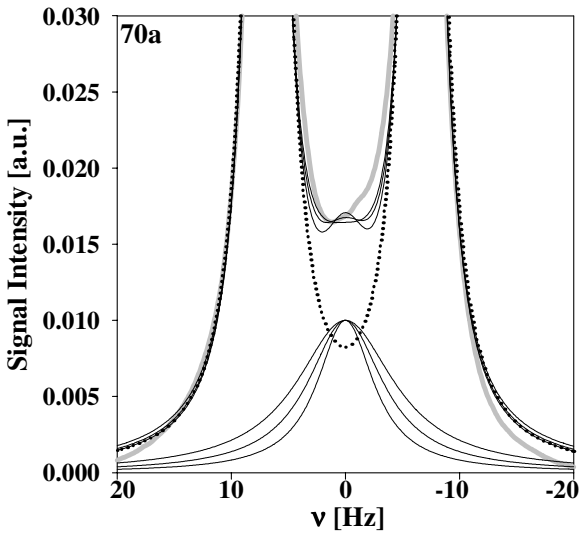

Fig. 7.3.1(11): experiment FT_16, ϕ_{B+C}=0.06, ΔT=-1.1°C, Varian 360, spectra for fig 7.3.1(10). Dashed lines correspond to automated fits with one (25a) or two (90a and 80a) Lorentzians. Solid lines in 90a and 80a represent the steady state lamellar phase spectrum 120a. In 30a and 70a three Lorentzian simulations with varying lamellar and sponge peaks are shown (solid lines). In 70a the isolated L_3-peaks are additionally shown, the dotted line represents a fit without any L_3-peak.

7.3.1.3 Trends in the Development of the L_α-Phase Volume Fraction φ

Fig. 7.3.1(12) – (15). show the φ development for all the experiments presented in section 7.2.6.2, unless already presented above. By and large, φ rises in a sigmoidal manner, exceptions will be discussed below. All data points result from simulations and normalising at each point in time. Each plot is fitted with two lines corresponding to KJMA fits of $\alpha = 4$ and $\alpha = 3$ (dashed and solid lines respectively). Stars in the plots represent estimates of φ, often simply indicating that the lamellar or sponge phase volume fraction must be non-zero at the given point in time. The data is presented in order from the slowest to the fastest transition. Note the different time scales.

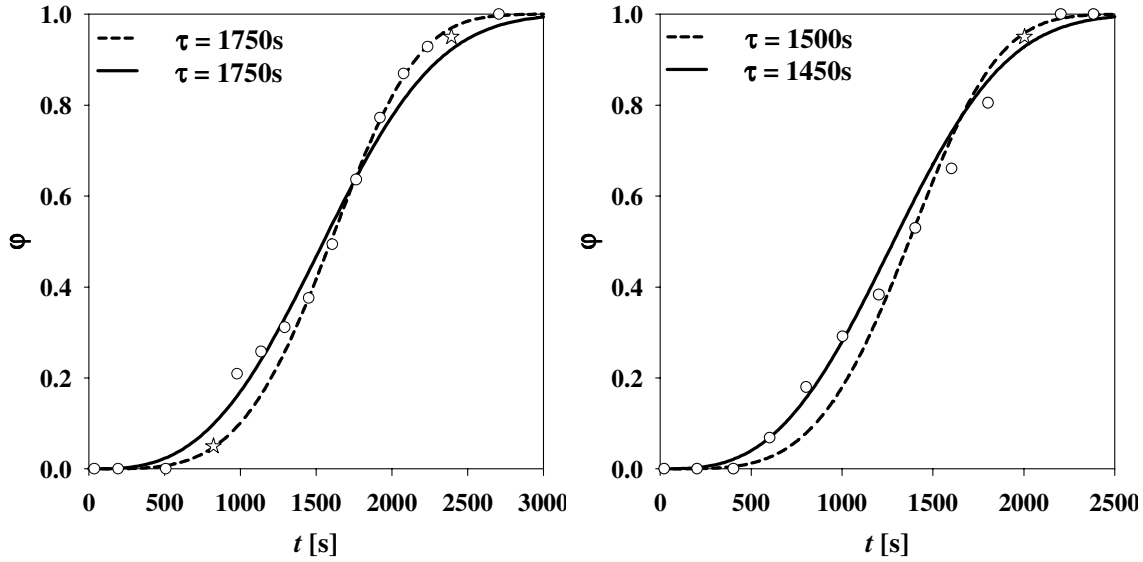

Fig. 7.3.1(12):, *left*: ϕ_{B+C}=0.07, ΔT=-1.0°C, Bruker DMX-200; *right*: FT_78 ϕ_{B+C}=0.06, ΔT=-1.9°C, $\eta_{D2O/S} = \eta_0 \cdot 2.261$,Varian 360

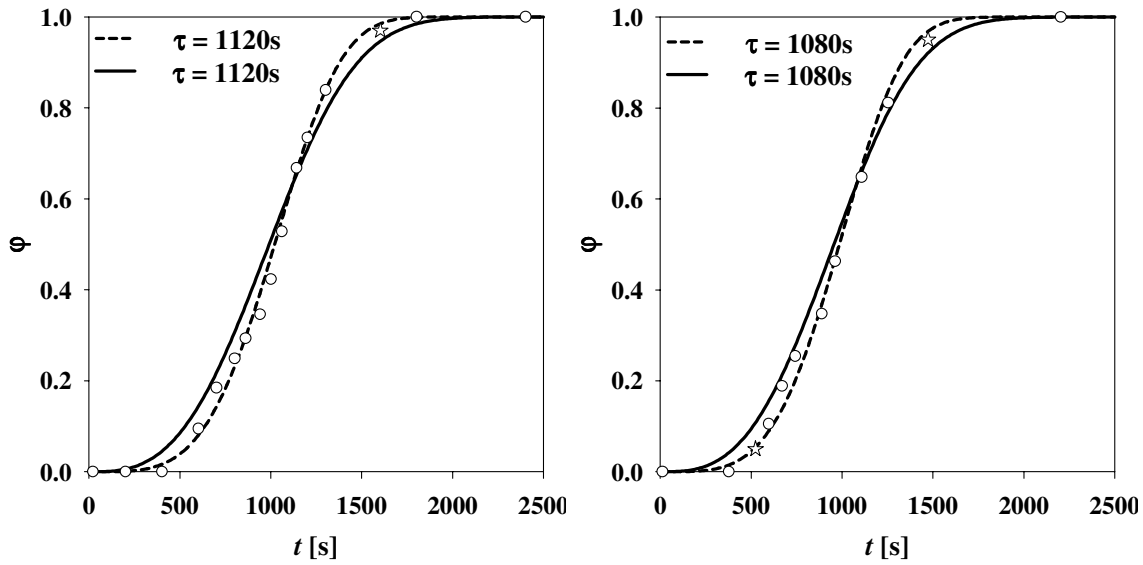

Fig. 7.3.1(13): *left*: FT_20 ϕ_{B+C}=0.06, ΔT=-1.3°C,Varian 360; *right*: ϕ_{B+C}=0.05, ΔT=-1.5°C, Bruker DMX-200

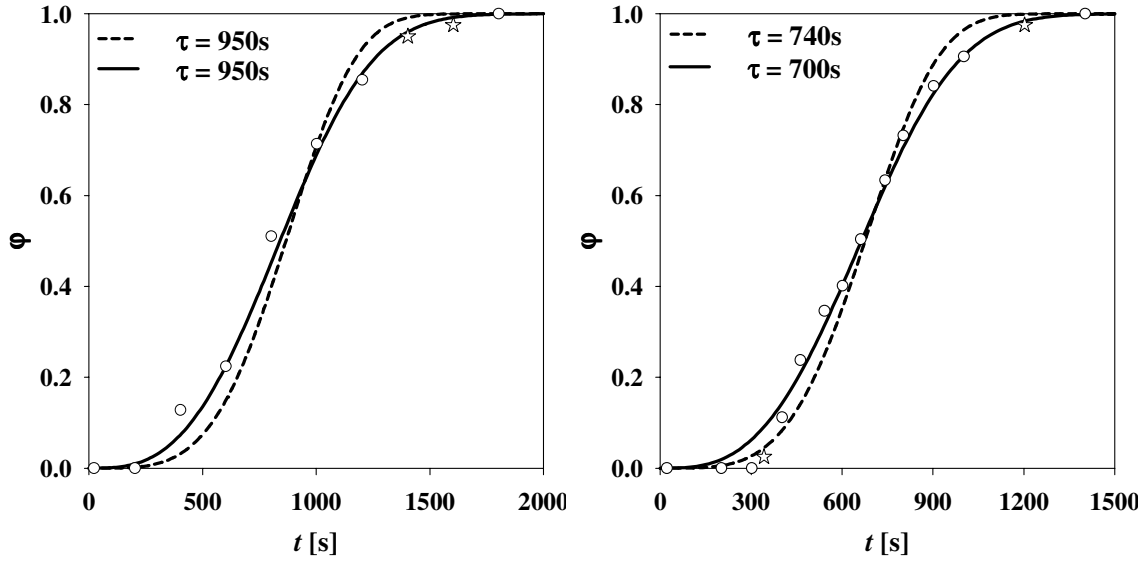

Fig. 7.3.1(14): *left*: FT_75 ϕ_{B+C}=0.08, ΔT=-1.3°C,Varian 360; *right*: FT_24 ϕ_{B+C}=0.06, ΔT=-1.5°C

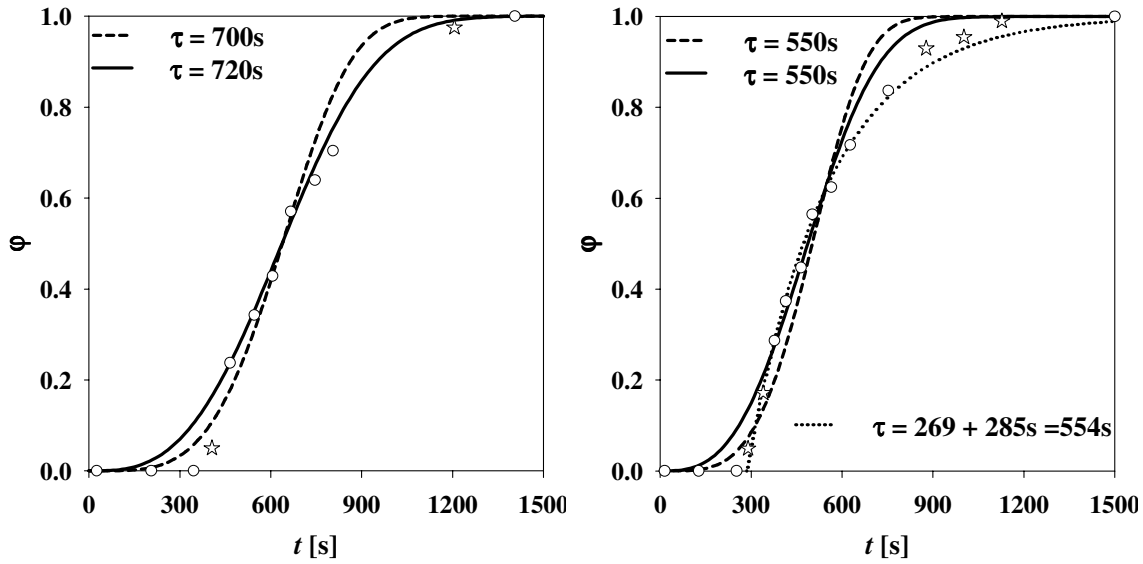

Fig. 7.3.1(15): *left*: FT_03 ϕ_{B+C}=0.06, ΔT=-1.7°C,Varian 360; *right*: FT_04 ϕ_{B+C}=0.06, ΔT=-1.7°C

In case of slow sponge to lamellar transition kinetics ($\tau > 1000$s) the development of φ can generally be described by the KJMA equation using $\alpha = 4$. Fig. 7.3.1(12) left and right represent the *worst case* scenario, where α is not definite, as neither a value of three nor four describes the data well. However, analysis of these two experiments was difficult, due to the extreme wideness of the peaks and the large amount of overlap which that entails. Fig (13) left and right represent experiments which were considerably slower. For the experiment FT_20 $\alpha = 4$ appears to be the most likely result, while for the preliminary experiment of $\tau = 1080$s a distinction between the two values is already difficult, due to the speed of the transition.

The experiment FT_75 with the $\phi_{B+C} = 0.08$ sample of fig. (14) shows somewhat atypical behaviour with a deviation to high values of φ at ~400s. However, one has to consider that the initial lamellar peaks were of extreme width (fig. 7.2.6(6)) and this could have led to an overestimation of φ. The end of the transition is seemingly characterised by $\alpha = 3$. This is a general phenomenon of fast transitions ($\tau < 1000$s) as is shown in experiment FT_20 and fig. (15) left and right. Although integral determining in these regions is often difficult (star symbols), comparison with the steady state lamellar spectra do show that sponge integral is still present (spectra not shown) and an $\alpha = 4$ behaviour therefore precluded. However, the initial rise of φ is still steep, and an α-value of four or even higher is appropriate in this region. This can cause the development of φ in very fast transitions to take the form akin to a simple exponential rise (fig. (15), right), and therefore a respective fit was added to the spectrum (dotted line). The time constant of this fit is $\tau = 269$s, but in order to compare this value with the time constant of the KJMA equation, the offset time from the beginning of the experiment ($t = 0$) must be added ($t_{offset} = 285$s). The result is a time constant, which is virtually identical to those determined with eq. 6.2(1) (KJMA).

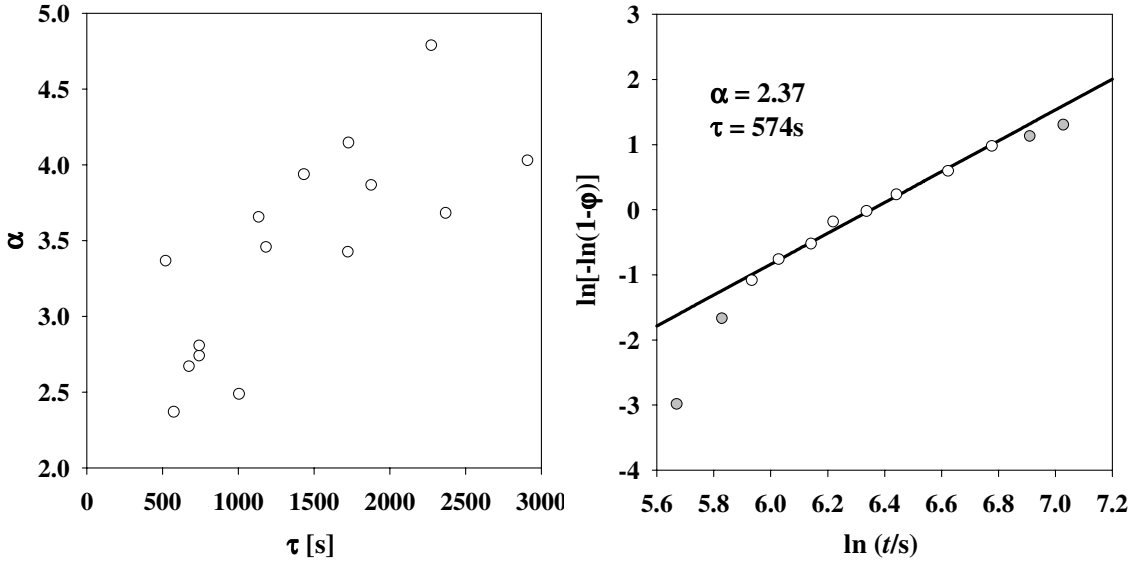

Fig. 7.3.1(16) *left*: The KJMA exponent α as function of τ, derived from least square fits to the data in the manner shown on the *right*. Shown are the results from the analysis of the established experiments using the $\phi_{B+C} = 0.06$ sample. *right*: determining of α and τ for the very fast transition observed in experiment FT_04 (fig. 7.3.1(15, right)). The linear fit was applied to white data, the deviations (grey data) were not accounted for.

The following trends can be summarised for the development of φ. For slow transition kinetics ($\tau > 1000$s) the data can be described well with the KJMA equation using $\alpha = 4$. Faster transitions still begin with a strong rise of φ, and thus $\alpha = 4$ appears to be appropriate to describe said rise. These transitions terminate however with a form better described by

$\alpha = 3$, and this feature becomes more pronounced the slower a transition is. That this is true is shown more formally in fig. 7.3.1(16 *left*).

The KJMA equation can be transformed into

$$\ln\left[-\ln(1-\varphi)\right] = \alpha \cdot \ln t - \alpha \cdot \ln \tau \qquad \text{eq. 7.3.1(4)}$$

and thus by plotting ln[-ln(1-φ)] vs. ln *t*, one gains the values of both the exponent α and the relaxation time constant τ, through a linear fit. Note that α corresponds directly to the slope of the straight line. In fig. 7.3.1(16 *left*) α is plotted as a function of τ acquired from such fits, which in turn stem from the detailed analysis of established experiments with the $\phi_{B+C} = 0.06$ sample. As stated, $\alpha \approx 4$ for slow transitions, while $\alpha \approx 3$ for the faster ones.

In fig. (16 *right*), the KJMA analysis plot is given for the extreme case of experiment FT_04 (ϕ_{B+C}=0.06, ΔT=-1.7°C), whose unusual φ-development has been presented in fig. 7.3.1(15, *right*). The slope of the linear fit to the white data corresponds merely to $\alpha = 2.37$. However, at low *t* there is a strong deviation to lower values of φ and the slope of a linear fit to the first three data points is 7.3 (fit not shown), i.e. the volume fraction of the lamellar phase increases very rapidly in this region. On the other hand, towards the end of the transition φ increases so slowly that even a slope of 2.37 overestimates φ. Note that the time constant τ, derived from the linear fit is almost identical to one of the simulated KJMA fit of fig. 7.3.1(15 *right*) and this is true for all the experiments analysed in this manner (see tab. T13, section 11).

An additional characteristic of the sigmoidal φ-development, which must be considered is the 'onset time'. Generally, the onset time of a nucleation and growth process is the time from when system parameters are changed so that a there is a state of *supersaturation* up until the first supernuclei are formed (see section 6.1). In plots akin to those of figure 7.3.1(12) to (15) this time will be identified as the interval from the start of the experiment ($t = 0$), up to when φ is first non-zero. The true onset time is shorter than this, as the sensitivity of the NMR experiment only allows to observe the lamellar phase, if a considerable volume fraction of this phase has already formed. Nevertheless, the defined interval serves as an estimate. Note, that in fig. 7.3.1(9) and (10) the onset time is > 600s and that its value decreases continuously as the relaxation time constant τ decreases. In fig (15), its value has decreases to ~300s.

The characteristic that $\alpha \approx 3$ towards the end of fast transitions, and the fact that suboptimal shimming led to wide peaks, were the cause of initially describing the preliminary experiments with a KJMA fit of $\alpha = 3$ [97]. Of great significance is that the determined time constants τ are basically independent of the exponent α used in the KJMA fits, as expected according to eq. 6.2(1), and even the use of a simple exponential rise fit (fig. 7.3.1(15 *right*)) suffices to determine τ in case of fast transition. This coupled with the independence of τ from the type of integral determination process described above, gives great confidence in the acquired relaxation time constants.

7.3.1.4 General Kinetic Behaviour

The type of analysis present above is very laborious and time consuming. Since the overall trends (more of which will be presented in sections 7.3.1.5 and 7.3.16 below) of the transition process have been discovered by evaluating experiments varying in ϕ_{B+C}, ΔT and η. Thus there is no further gain in continuing in this detail, i.e. from the sizeable number of experiments rigorously analysed, it can be gauged that further experiments differ only in the time scales involved. Therefore a method to quickly determine relaxation time constants would be very advantageous. Fortunately, such a possibility exists.

From eq. 6.2(1) and fig. 6.2(1) it is clear that φ is independent of the exponent α at the characteristic time $t = \tau$ as in this case the product $kt = 1$. The value calculated for φ at this point in time has been shown in the section '*The KJMA model*' to equal $1\text{-}1/e \approx 0.632$. A characteristic point that can be determined with good accuracy during the sponge to lamellar transitions, is when the intensities of the three coexisting peaks are equal. If the peak widths at this point would also be equivalent, then φ would take the value of 2/3, as there are two L_α peaks as opposed the single L_3 peak. However from figure 7.3.1(4c) and fig. 7.3.1(7, 85a, 90a) it is evident that the sponge peak is somewhat wider that the corresponding lamellar peaks. Therefore, the integral of the singlet is accordingly larger and φ smaller than the 'ideal' value. Hence, the 'equal peak moment' (EPM) occurs sooner than τ. However, at this phase of the transition the slope of the sigmoidal curve is steep (especially in predominant number of cases where $\alpha = 4$), so that the difference between the two times should not be dramatic.

That this is indeed true is shown in tab. T12 (section 11), where τ and the EMP times are compared for established experiments of $\phi_{B+C} = 0.05$ and 0.06. The ratio of τ of the detailed evaluation to the EMP calculates to 1.063±0.026 (error by standard deviation). Thus a good estimate of τ can be gained quickly by determining the EMP. Another advantage of

this method is, that it is even successful in the case of badly shimmed spectra, i.e. were the peaks are wide, distorted or the lamellar doublet even asymmetric.

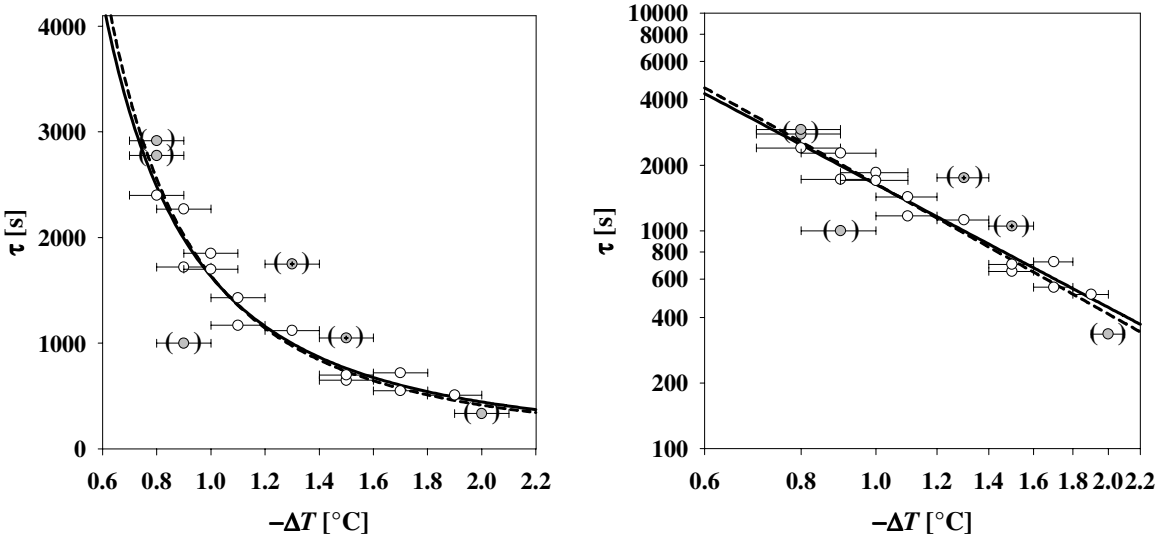

Fig. 7.3.1(17): the relaxation time constants τ of ϕ_{B+C}=0.06 experiments in linear and double logarithmic depiction. Results from preliminary experiments are denoted with a cross. Included are power law fits with m = -1.88, b = 3.21 and m = -1.98, b = 3.22 (solid and dashed lines).

Fig. 7.3.1(17) summarises the relaxation time constants τ of various $\phi_{B+C} = 0.06$ experiments thereby showing its dependence on Δ*T*. Note that negative temperature jumps are described, and the abscissa is given as -Δ*T* for convenience. Preliminary experiments are denoted with a cross. An inherent problem of the NMR experiments is the temperature stability of the spectrometers. From the experience of many hours of conducting experiments, where at times shifts of the phase behaviour could be observed for samples within the spectrometers, the author comes to the conclusion that an error of ±0.1°C must be considered for Δ*T*. As stated above, the τ values are confidently determined, so that their error is estimated to within ±50s, i.e. approximately the extend of the data symbols. The data can be fitted according to a power law

$$\tau = b \cdot \Delta T^{m} \qquad \text{eq. 7.3.1(5a)}$$

$$\log(\tau) = m \cdot \log(\Delta T) + \log(b) \qquad \text{eq. 7.3.1(5b)}$$

which corresponds to a straight line on a double logarithmic scale. The data in parenthesis were excluded from the fit (solid line), where m = -1.88. The data at -Δ*T* = 0.9°C was excluded due to its outlier characteristic, while the high τ values at -Δ*T* = 0.8°C were ignored, since the highest was the yield from an experiment which terminated in the lamellar and sponge coexistence region of the phase diagram. The data from the preliminary experiments

was not considered, since especially the data at $-\Delta T$ = 1.3°C deviates from the other findings. Finally the data at $-\Delta T$ = 2.0°C was ignored, due to its deviation visible in the double logarithmic plot and the fact that this is the only τ value of the plot determined by the EPM time multiplied by 1.063. If this last point is included in the power law fit, then it yields m = -1.98 (dashed line).

Fig. 7.3.1(18) summarises experiments with samples of ϕ_{B+C} = 0.05 in the exact same manner as shown above. The ordinates and abscissas are of the same scaling for comparison. The power law fit yields a considerably stronger ΔT dependency than in the ϕ_{B+C} = 0.06 case, as m = -2.63. That the difference is indeed relevant, is emphasised in the *right* part of the graph, where the dashed line corresponds to m = -2.0. The data at $-\Delta T$ = 0.9°C was excluded due to supposed temperature stability problems in the experiment and also the value of the preliminary experiment at $-\Delta T$ = 1.0°C, due to the deviations from the results of the established experiments. However, both extremely high τ times are right in line with the power law fit. In general, the results of the preliminary experiments and those of the established ones match well.

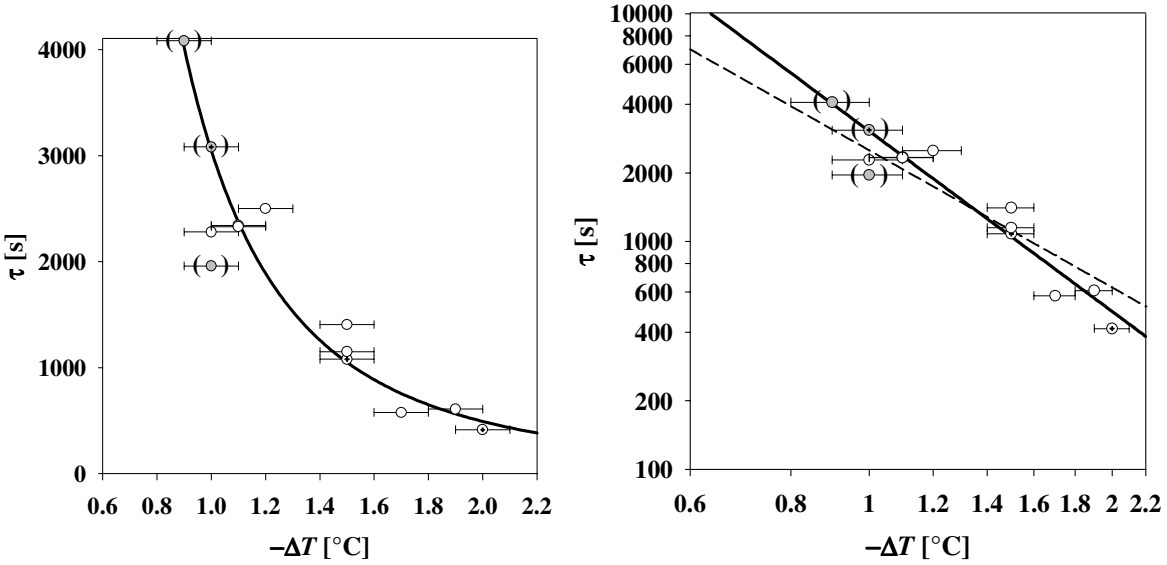

Fig. 7.3.1(18): the relaxation time constants τ of ϕ_{B+C}=0.05 experiments in linear and double logarithmic depiction. Results from preliminary experiments are denoted with a cross. Included is a power law fit with m = -2.63, b = 3.49 (solid line) and m = -2.0, b = 3.4 (dashed line).

Fig. 7.3.1(19) summarises the relaxation time constants derived from the experiments using a sample of ϕ_{B+C} = 0.06 of increased viscosity ($\eta_{D2O/S} = \eta_0 \cdot 2.261$). The data point at $-\Delta T$ = 1.1°C stems from an extrapolation and has to be considered a rough estimate ($\Delta\tau = \pm 1000$s, see below). If this point is included in the power law fit m = -2.73 (solid line), if not, then m = -2.97.

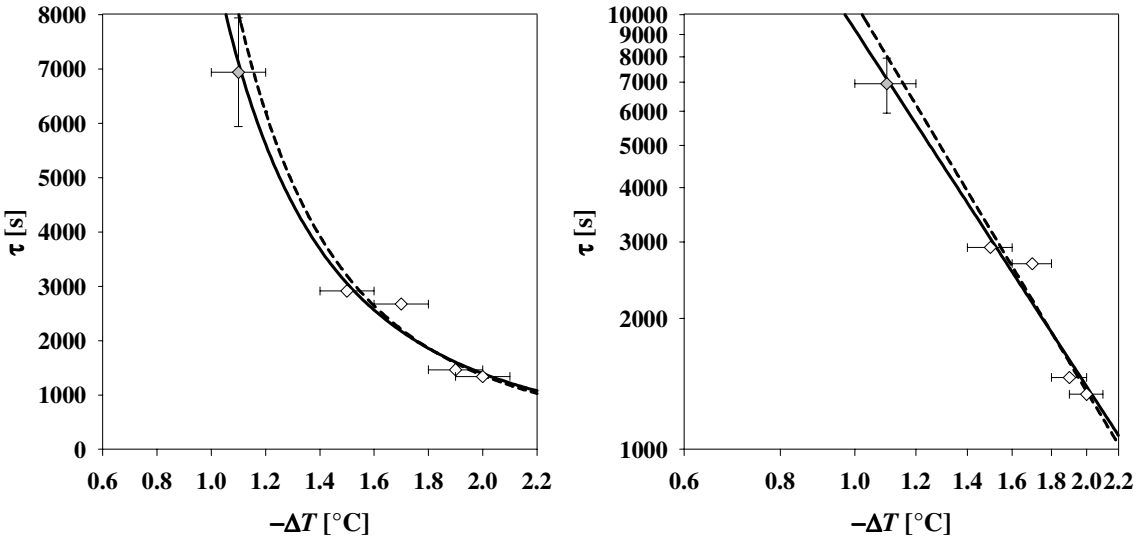

Fig. 7.3.1(19): the relaxation time constants τ of experiments with the ϕ_{B+C}=0.06 sample of increased viscosity ($\eta_{D2O/S} = \eta_0 \cdot 2.261$) in linear and double logarithmic depiction. Included are power law fits with m = -2.73, b = 3.97 and m = -2.97, b = 4.03 (solid and dashed lines).

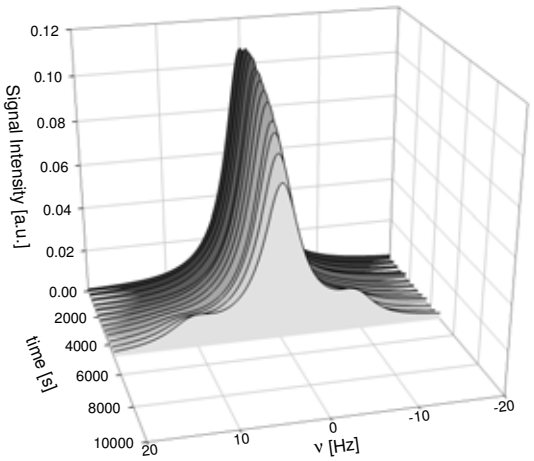

Fig. 7.3.1(20): 3D depiction of the NMR spectra development for a ϕ_{B+C}=0.06 sample of increased viscosity ($\eta_{D2O/S} = \eta_0 \cdot 2.261$) in an experiment with $-\Delta T$ = 1.1°C. The EPM is estimated to 6900±1000s.

The experiment at $-\Delta T$ = 1.1°C was terminated prematurely (fig. 7.3.1(20)). However, up to this point normal transition behaviour is detected. Through visual comparison of fig. 7.3.1(20) and the corresponding plots of the four other experiments, the EPM is estimated to 6900±1000s. The likeness of the solid and dashed fits of fig. 7.3.1(19) gives confidence in this estimate.

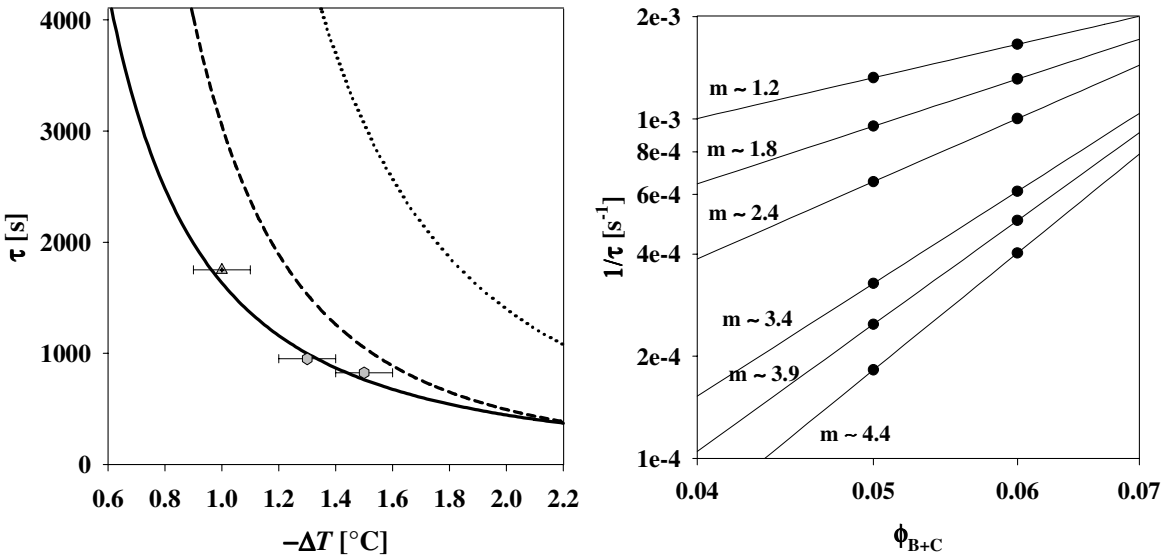

Fig. 7.3.1(21): *left*: the primary power law fits of the dependence of τ on the magnitude of the negative temperature jumps of the experiments with $\phi_{B+C} = 0.06$ (solid line) 0.05 (dashed line) and 0.06 ($\eta_{D2O/S} = \eta_0 \cdot 2.261$; dotted line). Results of individual experiments with $\phi_{B+C} = 0.07$ and 0.08 are represented by triangles and hexagons. *right*: determining of the exponent m of a hypothetical power law describing the dependence of $1/\tau$ on ϕ_{B+C} at constant ΔT. From top to bottom: with $-\Delta T$ = 1.7, 1.5, 1.3, 1.0, 0.9, 0.8 °C.

In order to describe the ϕ_{B+C} dependence of τ at a constant value of ΔT, the power law fits from fig. 7.3.1(17) (m = -1.88) and fig. 7.3.1(18) (m = -2.63) are shown in the same graph (fig. 7.3.1(21) left, solid and dashed line). In addition, the fit of fig. 7.3.1(19) (m = -2.73) is given for comparison (dotted line). The results of the three experiments performed with samples of higher bilayer volume fraction are also included ($\phi_{B+C} = 0.07$ and 0.08, triangle and hexagons). These however, do *not* show that ΔT dependence decreases with increasing ϕ_{B+C}. Then again, the significance of these experiments is in question simply because of their low number. In addition, their analysis proved difficult due to suboptimal shimming and asymmetric spectra. Finally, the detailed analysis of a $\phi_{B+C} = 0.08$ experiment showed an atypical development of φ (fig. 7.3.1(14 *left*)).

Thus if one chooses to ignore the results of these three experiments, accepts the validity of the power law fits and assumes that the relaxation kinetics follow a power law dependence in ϕ_{B+C}, then the exponent m for that dependence can be calculated for various values of ΔT (fig. 7.3.1(21, *right*)). The assumption of a power law dependence in ϕ_{B+C}, is not absurd as such a dependence has been found for the relaxation kinetics within the L_3-phase, where $1/\tau \propto \phi_{B+C}^3$ in the dilute region[46] (see section 5). For the investigations at hand, one finds for $1/\tau \propto \phi_{B+C}^m$, for m to vary between values of 1.2 and 4.4 for the temperature range investigated. The direct comparison of the two power laws derived from fig. 7.3.1(17) and (18), and thus the ΔT values, however requires that the initial sample states are analogues and

that the absolute temperature of the experiments is not dominantly important. The former condition is met as the experiments commence at a temperature just above the L_3/L_α phase boundary and the latter also, since the slant of the L_3-channel is small (see fig. 2.3(1)) and differences in temperature are marginal.

7.3.1.5 Splitting Development

The quadrupolar splitting $\Delta\nu_Q$ at any given point of the transitions, i.e. the frequency difference of the positions of the two lamellar peaks, can be determined well. The differences between the values gained from the spectra simulations and the distances between the actual spectra maxima of concern is marginal and thus the former values are discussed. When one plots $\Delta\nu_Q$ as a function of time (fig. 7.3.1(22) to (27)), the decay of said parameter appears of exponential form (if one ignores some initial values at small *t*, see below), regardless of the magnitude of the temperature jump performed or the type of sample studied. Therefore the data is fitted using the least squares method and a three parameter exponential function

$$y = y_0 + a\left(1 - e^{-bx}\right) \qquad \text{eq. 7.3.1(6)}$$

where y and x correspond $\Delta\nu_Q$ and t respectively and y_0, a and b are constants. Furthermore, the conditions $y_0 + a = \Delta\nu_{Q,L}$ ($\Delta\nu_{Q,L}$ corresponds to the final, steady state L_α-splitting) and $a < 0$ apply. For the time constants derived from eq. 7.3.1(6) $\tau_s = 1/b$ is true.

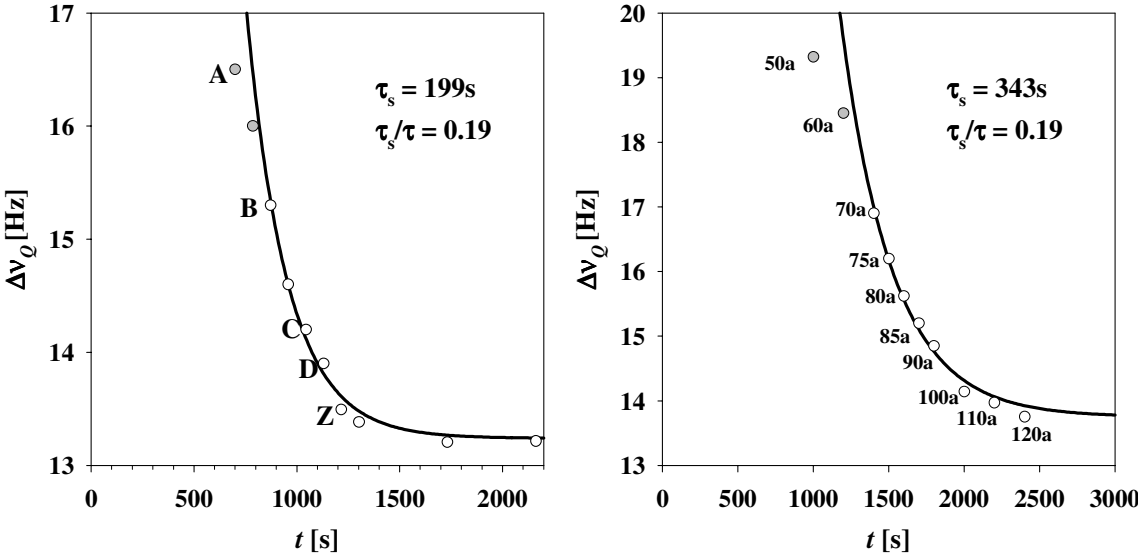

Fig. 7.3.1(22): *left*: ϕ_{B+C}=0.06, ΔT=-1.5°C, Bruker DMX-200, *right*: FT_32 ϕ_{B+C}=0.06, ΔT=-1.0°C, Varian 360

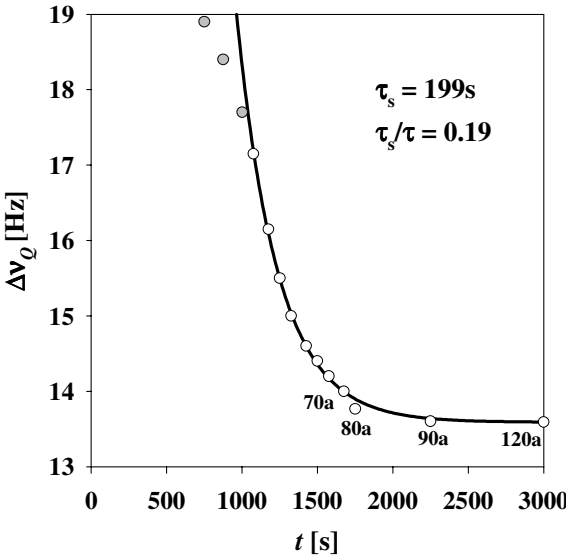

Fig. 7.3.1(23): FT_16 ϕ_{B+C}=0.06, ΔT=-1.1°C, Varian 360

Fig. (22) and (23) illustrate the development of $\Delta\nu_Q$ of the experiments for which a detailed analysis of the φ development was presented in section 7.3.1.1 and 7.3.1.2. The data corresponding to the grey symbols was not included to determine the fits presented (solid lines). These deviations to lower values of $\Delta\nu_Q$ infer that the true course of $\Delta\nu_Q$ is more of a sigmoidal form. Note that exp FT_32 (22 *right*) was deemed incomplete and this hypothesis is further supported by the course of the plotted splitting. Interestingly, the determined ratios of the time constant of the splitting development and the φ-development are constant for the three experiments as $\tau_s/\tau = 0.19$. Fig. (24) to (27) illustrate the development of $\Delta\nu_Q$ of all the experiments presented in section 7.3.1.3 and the order of appearing is kept to simplify comparisons.

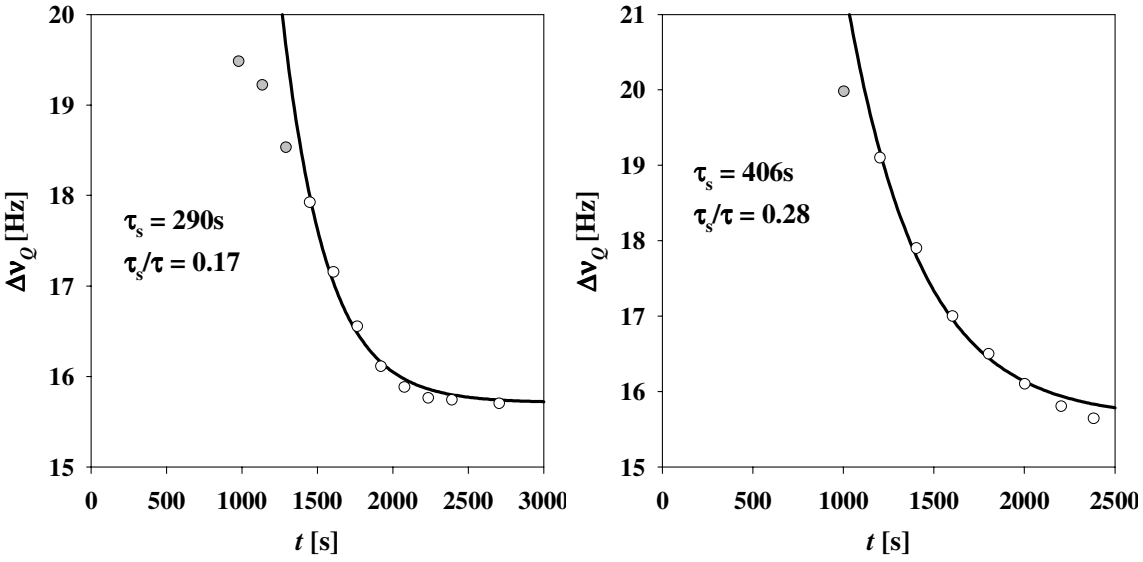

Fig. 7.3.1(24): *left*: ϕ_{B+C}=0.07, ΔT=-1.0°C, Bruker DMX-200; *right*: FT_78 ϕ_{B+C}=0.06, ΔT=-1.9°C, $\eta_{D2O/S} = \eta_0 \cdot 2.261$,Varian 360

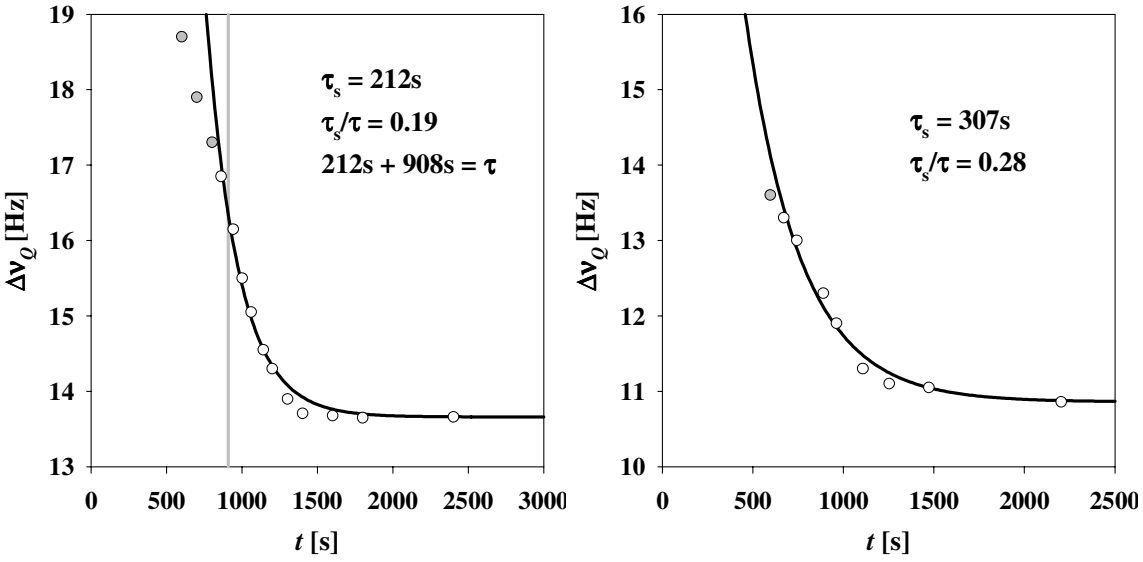

Fig. 7.3.1(25): *left*: FT_20 ϕ_{B+C}=0.06, ΔT=-1.3°C,Varian 360; *right*: ϕ_{B+C}=0.05, ΔT=-1.5°C, Bruker DMX-200

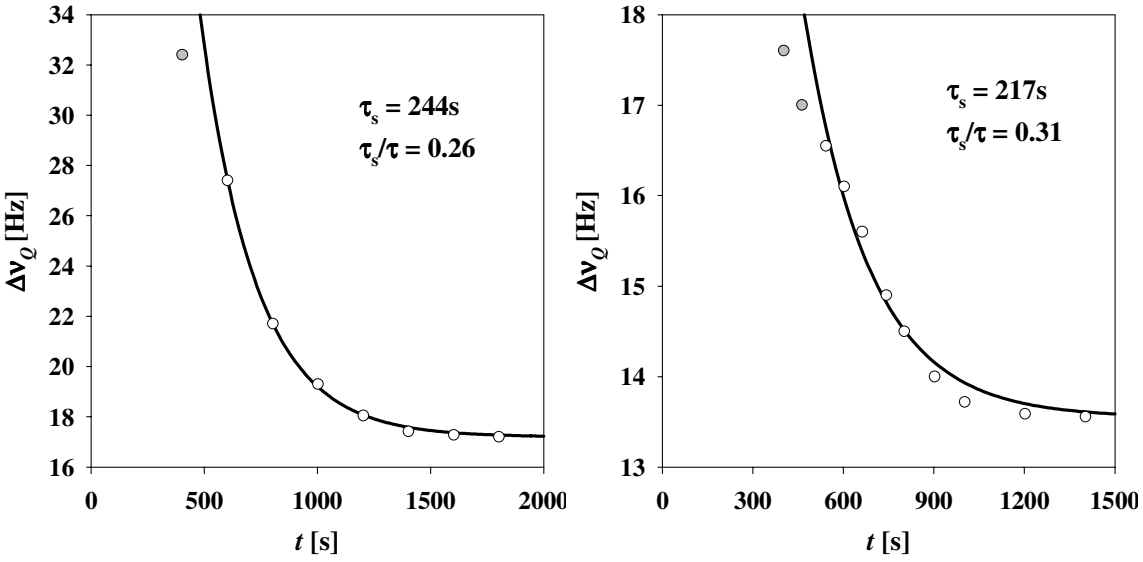

Fig. 7.3.1(26): *left*: FT_75 ϕ_{B+C}=0.08, ΔT=-1.3°C,Varian 360; *right*: FT_24 ϕ_{B+C}=0.06, ΔT=-1.5°C

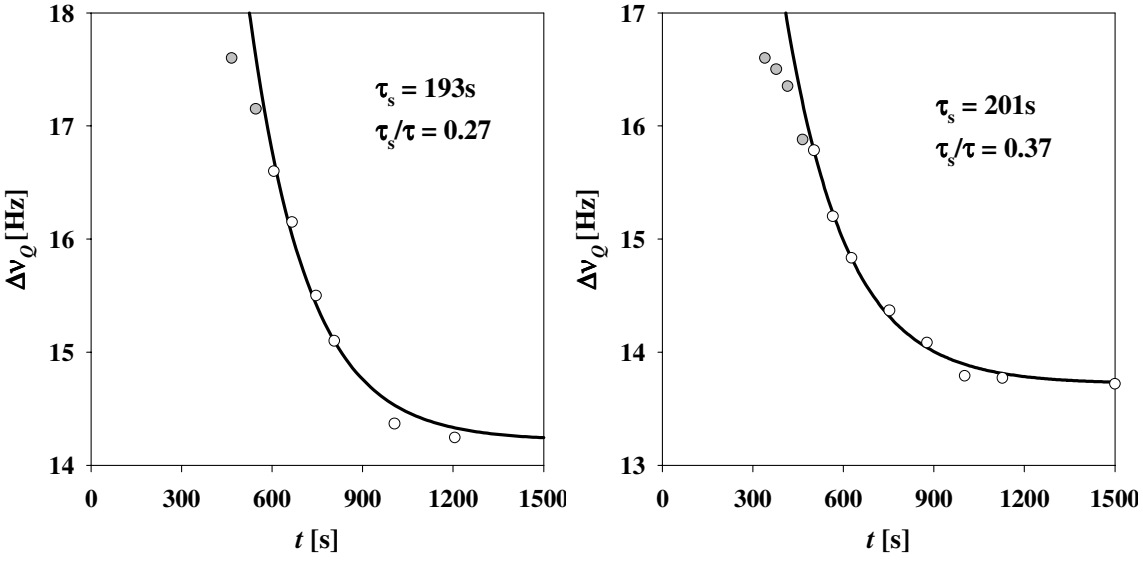

Fig. 7.3.1(27): *left*: FT_03 ϕ_{B+C}=0.06, ΔT=-1.7°C,Varian 360; *right*: FT_04 ϕ_{B+C}=0.06, ΔT=-1.7°C

The plots of above show the same characteristics as the ones presented previously. When determining the ratio τ_s/τ two types of values are found, ~0.19 and ~0.30. If one ignores the fast transitions of experiment FT_03 and FT_04 (which have atypical φ–development), then it appears that the low 0.19 value results in plots which show a clear deviation of the initial $\Delta\nu_Q$ values from the fit, thereby giving the course of $\Delta\nu_Q$ a sigmoidal appearance. The 0.30 value results when the deviation is not so great.

It could not be found that τ_s and τ are identical, in the sense as it was shown for the KJMA time constants and the time constant of the exponential rise (dotted line) in fig. 7.3.1(15, *right*). That is to say, adding an offset time to τ_s to equate it to τ, generally showed that this offset time would have to be too large, i.e. it signifies a point in time where the decline of $\Delta\nu_Q$ is already advanced. This is illustrated in fig. 7.3.1(25, *left*), where the hypothetical offset time is denoted by the grey line. However, the constant ratios do imply some sort of correlation between τ and τ_s. They are summarised in tables T9.

Fig. 7.3.1(28) plots the average quadrupolar splitting of the steady state lamellar phase $\Delta\nu_{Q,L}$ of all samples studied akin to fig. 7.3.1(1). The errors for $\Delta\nu_{Q,L}$ of the established experiments of the ϕ_{B+C}=0.05 and 0.06 samples were calculated as standard deviations, as these experiments were great in number. All other errors were estimated to ±0.2 Hz from the spread of results. Note, that the final value of $\Delta\nu_{Q,L}$ determined from the experiment FT_03 (fig. 7.3.1(27, *left*)) is unusually high (for a sample of ϕ_{B+C} = 0.06) and it was therefore not include in calculating the respective average. Generally one would expect to detect higher $\Delta\nu_{Q,L}$ values in the event of (mistakenly) jumping into the L_3/L_α coexistence region. This however seems impossible, due to the speed of the transition and the fact that a ΔT = -1.7°C jump was performed.

The results of the preliminary (white) and established (grey) experiments are very similar, with the exception of the ϕ_{B+C}=0.06 case, where the grey symbol shows deviation to slightly higher values with respect to the linear regression (solid line). Similarly, the result from the ϕ_{B+C}=0.08 sample is lower than would be expected. Nevertheless, a linear development of $\Delta\nu_{Q,L}$ is clearly visible and thus its direct proportionality to the ratio $\phi_{B+C}/(1-\phi_{B+C})$ is yet again confirmed and eq. 7.3.1(3) therefore true.

The average splitting from the sample of increased viscosity (ϕ_{B+C}=0.06, $\eta_{D2O/S} = \eta_0 \cdot 2.261$, black square) however, is clearly higher than would be expected from its bilayer volume fraction. As indicated by the parenthesis, it was not used to calculate the linear regression. This deviation is discussed in section 7.4.5.2.

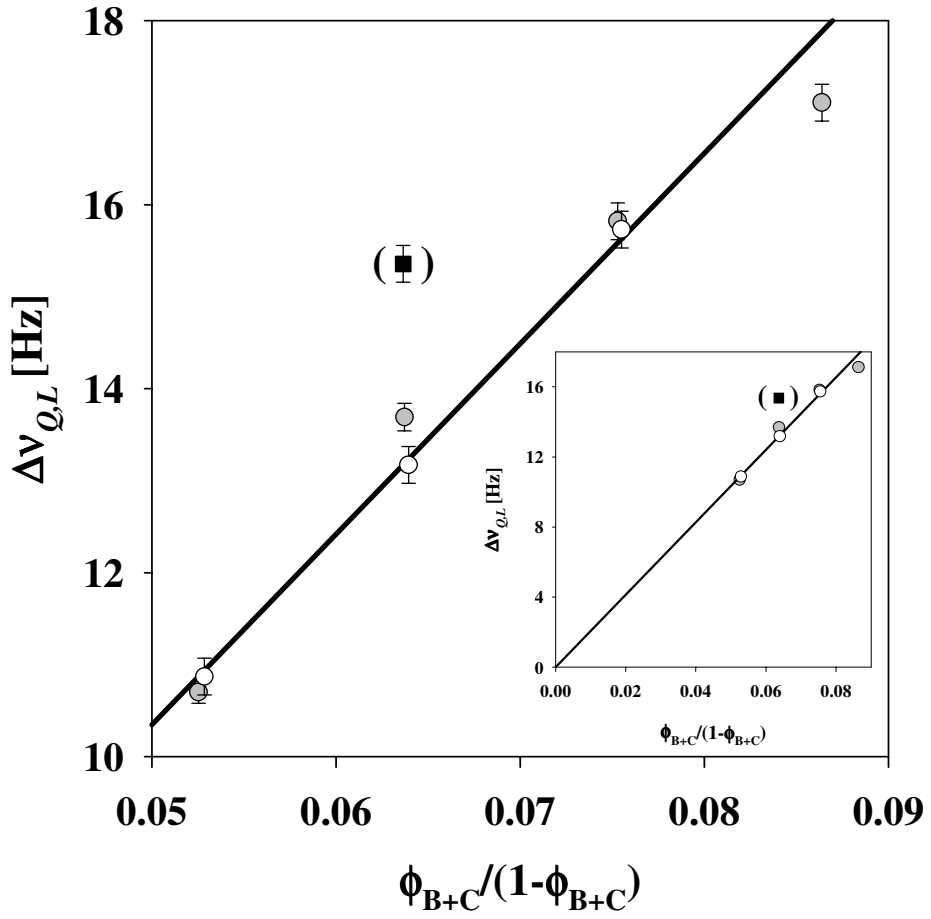

Fig. 7.3.1(28): the average quadrupolar splitting within the steady state lamellar phases for samples of varying bilayer volume fraction (ϕ_{B+C} ~ 0.05, 0.06, 0.07 and 0.08) as determined by the preliminary (white) and established (grey) experiments. The linear regression passes through the origin (insert). The result from the sample of increased viscosity (ϕ_{B+C}=0.06, $\eta_{D2O/S} = \eta_0 \cdot 2.261$, black square) shows a clear deviation from the expected value.

7.3.1.6 Sponge and Lamellar Peak Width Development

Another parameter to follow is the peak width at half height $\Delta\nu_{1/2}$, for the L_3-peak and the two lamellar peaks. In general, $\Delta\nu_{1/2}$ of the lamellar peaks is very similar at a given point in time, but in cases of asymmetric spectra the values can vary considerably and thus their arithmetic mean value is always investigated. Note that $\Delta\nu_{1/2}$ is directly related to the (effective) time constant of the transversal relaxation T_2^* (eq. 7.1.5(6)). Fig. 7.3.1(29) to (31) plot the development of the sponge (*left*) and average lamellar peak width (*right*), for the three experiments that have been presented above in most detail. The L_3-peak data is fitted as three parameter exponential growth

$$y = y_0 + a \cdot e^{bx} \qquad \text{eq. 7.3.1(7)}$$

while for the L_α-peak data eq. 7.3.1(6) is used. As before, data represented by grey symbols is not included in the fits. The determined time constants $\tau = 1/b$ are given in the respective graphs.

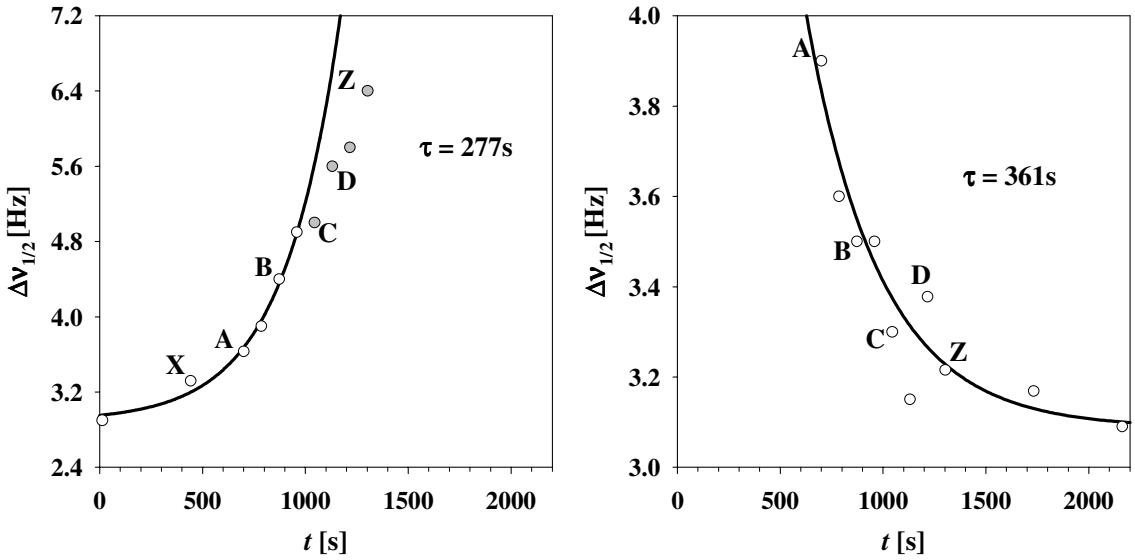

Fig. 7.3.1(29): ϕ_{B+C}=0.06, ΔT=-1.5°C, Bruker DMX-200

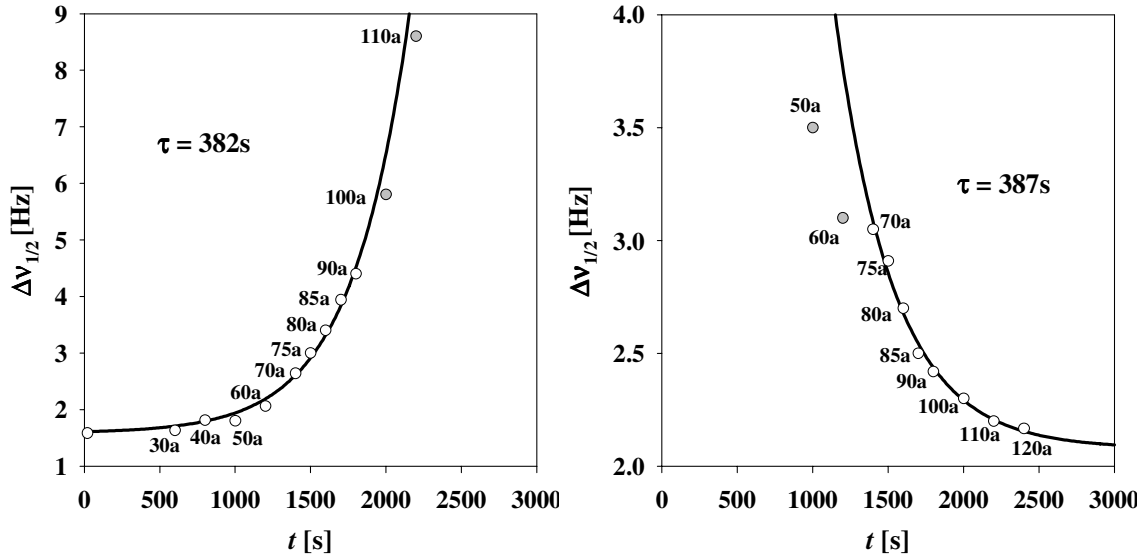

Fig. 7.3.1(30): experiment FT_32 ϕ_{B+C}=0.06, ΔT=-1.0°C, Varian 360. Note that at data 120a a steady state lamellar phase has not yet been attained.

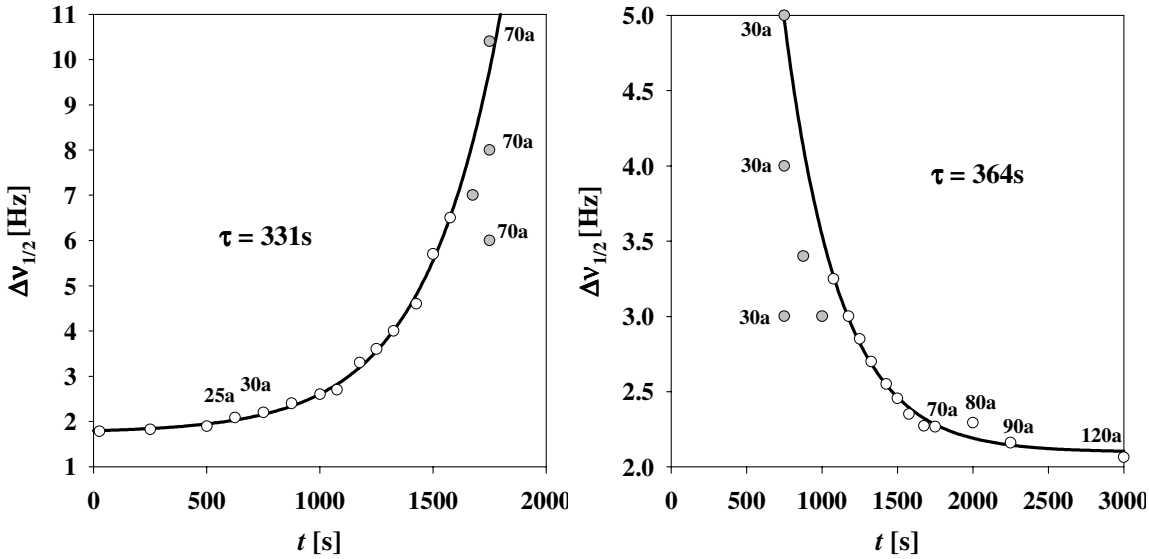

Fig. 7.3.1(31): experiment FT_16 ϕ_{B+C}=0.06, ΔT=-1.1°C, Varian 360

As a rule, an exponential growth of the L_3-peak width and an exponential decay of the lamellar peak width are observed in the L_3 to L_α transition experiments. Note that the time constants τ are somewhat higher than those found in the development of the splittings. In the plots marked 30a and 70a of fig. 7.3.1(11), the effect of varying $\Delta\nu_{1/2}$ was explored for the simulation of the NMR spectra and in fig. 7.3.1(10), the result for the lamellar phase volume fraction φ was illustrated respectively. The plots of fig. 7.3.1(31), left and right now show these $\Delta\nu_{1/2}$ values in the context of preceding and subsequent values. The good likelihood of a steep φ-development (described by an $\alpha = 4$ in the KJMA equation) was elucidated in section 7.3.2.1. This type of development requires the widths of the L_3 (70a) and L_α peaks (30a) to adopt values well below those predicted by the fits of fig. 7.3.1(31), i.e. to deviate towards an overall sigmoidal form.

Deviations towards such a sigmoidal form are sometimes already found for spectra where the L_3-peaks are still well visible or the lamellar peaks already well pronounced, e.g. plot C and D of fig. 7.3.1(4) and plot 60a of fig 7.3.1(7). However, the $\Delta\nu_{1/2}$ values of the lamellar peaks for 100a and 110a (fig. 7.3.1(7)) do not follow this trend (fig. 7.3.1(30 *left*)). Then again, the error of any values in the early or late stages of a transition is high and these findings represent exceptions. The fact remains, that for most of the transitions studied the discussed deviation to lower values is needed for an $\alpha = 4$ course of φ. The sigmoidal deviations found in the development of the quadrupolar splitting (7.3.1(22) to (27)) are reassuring, as they are irrelevant for, i.e. independent of, the development of φ, and thus give credibility to the deviations observed here.

In tables T9 the steady state widths of the sponge and lamellar phases are given for the performed experiments with ϕ_{B+C} = 0.05 and 0.06 as well as the associated T_2^* values. Note that T_2^* of the sponge peak is approximately 10% to 30% larger than the value for the lamellar peaks, and they are accordingly more defined.

7.3.2 L_α to L_3 Transitions

The straight forward method to analyse the lamellar to sponge phase transition experiments is to fit the spectra using two Lorentzians up to the point of coalescence and then a single Lorentzian until completion. Thus the actual evaluation method is very similar to the automated fitting procedure used to investigate the sponge to lamellar transitions of section 7.3.1. The plots below will show that this type of least squares fit is adequate. However, a lamellar phase volume fraction φ cannot be determined, as there is no coexistence of sponge and lamellar phase.

7.3.2.1 The Two States Model and the McConnell Equation

As was stated in the introduction of this chapter, the observed lineshape development is similar to what is found in the event of a certain type of *chemical exchange*, i.e. an exchange of intermediate rates between two distinct states (section 7.1.9). The McConnell equation (eq. 7.1.9(1)) describes those lineshapes as a function of the position of singlet in the limit of fast exchange ω_0, the maximum splitting in limit of slow exchange $\Delta\omega_Q$, and a parameter P representing the probability of exchange, i.e. the rate of conversion between the two states. However, the spectra cannot be fitted with the McConnell equation, since it does not account for a linewidth caused by transversal relaxation. *H. Wennerström*[98] extended the equation to account for this and the result is

$$I(\omega) \propto \frac{(\omega-\omega_0)^2 \cdot 1/T_2^* + \left[(1/T_2^*)^2 + (2P/T_2^*) + (\Delta\omega_Q/2)^2\right] \cdot (1/T_2^* + 2P)}{\left[(\omega-\omega_0)^2 - (1/T_2^*)^2 - (2P/T_2^*) - (\Delta\omega_Q/2)^2\right]^2 + 4\cdot(\omega-\omega_0)^2 \cdot (1/T_2^* + P)^2}$$

eq. 7.3.2(1)

Before this equation can be used to fit the NMR spectra of section 7.2.6.3 it needs to be converted to be a direct function frequency ν using the relation $\omega=2\pi\nu$. The result is

$$I(\nu) \propto \frac{[2\pi(\nu-\nu_0)]^2 \cdot 1/T_2^* + \left[(1/T_2^*)^2 + (2P/T_2^*) + (\pi \cdot \Delta\nu_{Q,L})^2\right] \cdot (1/T_2^* + 2P)}{\left[[2\pi(\nu-\nu_0)]^2 - (1/T_2^*)^2 - (2P/T_2^*) - (\pi \cdot \Delta\nu_{Q,L})^2\right]^2 + 4 \cdot [2\pi(\nu-\nu_0)]^2 \cdot (1/T_2^* + P)^2}$$

eq. 7.3.2(2)

In the limit of $1/T_2^* = 0$ this equation corresponds to the McConnell equation, while for $P = 0$ it corresponds to two identical Lorentzian functions of $\Delta\nu_{1/2} = 1/(\pi T_2^*)$, which are separated by $\Delta\nu_{Q,L}$ and centred on ν_0. Note that ν_0 is constant for all probabilities of exchange and this corresponds to a constant central position of the observed transition. Note also that $\Delta\nu_{Q,L}$ corresponds to $\Delta\omega_Q$ of eq. 7.3.2(1) and that, for the task at hand, it is the quadrupolar splitting detected for the steady state lamellar phase doublet. Furthermore, the variation of lineshape from two singlets to one singlet is achieved with a constant value of $\Delta\omega_Q$ in section 7.1.9. Now, the spectra are fitted with eq. 7.3.2(2) (multiplied with an intensity factor) according to the least squares method. An algorithm (given in section 10.4.5) was written in the SigmaPlot program to achieve this.

It is nonsensical to describe the situation of exchange simply with a value of P, as it is the ratio $P/\Delta\omega_Q$ which ultimately determines lineshape. In the case of $1/T_2^* = 0$, coalescence occurs at $P/\Delta\omega_Q$=1/(2*2^0.5). Thus, in order to compare transition situations of experiments with varying values of $\Delta\nu_{Q,L}$ the coalescence parameter χ_P is introduced

$$\chi_P = \frac{P\sqrt{2}}{\pi \cdot \Delta\nu_{Q,L}}$$

eq. 7.3.2(3)

For $\chi_P < 1$ the spectra show a splitting, coalescence occurs at $\chi_P = 1$ and when $\chi_P > 1$, there is a single peak.

The splitting at any moment in time $\Delta\nu_Q$ as function of P (and any given but constant value of $\Delta\nu_{Q,L}$) can be calculated for the McConnell equation via

$$\Delta\nu_Q = \frac{\sqrt{(2\pi \cdot \Delta\nu_{Q,L})^2 - 8P^2}}{2\pi}$$

eq. 7.3.2(4)

A plot of this equation for $\Delta\nu_{Q,L}$ = 14Hz is given in fig. 7.3.2(1, *left*) as a function of the normalisation parameter χ_P (solid line). In order to examine how the introduction of an intrinsic linewidth via T_2^* influences the development of the splitting (and thus lineshape development), spectra with $\Delta\nu_{Q,L}$ = 14Hz were simulated for three values of T_2^* (0.2, 0.1 and 0.05s) at different χ_P. The splitting of these spectra was determined manually, i.e. by determining the distance between peak maxima. The results are included in fig. 7.3.2(1, *left*). Note that the data points at $\Delta\nu_Q = 0$ are not at the minimum possible χ_P, that is to, say $\Delta\nu_Q = 0$ might already exist at lower values of χ_P. Furthermore, 14Hz is close to the $\Delta\nu_{Q,L}$ value of the ϕ_{B+C}=0.06 samples and T_2^* values of the established experiments range from approximately 0.15 to 0.2s for samples of standard viscosity.

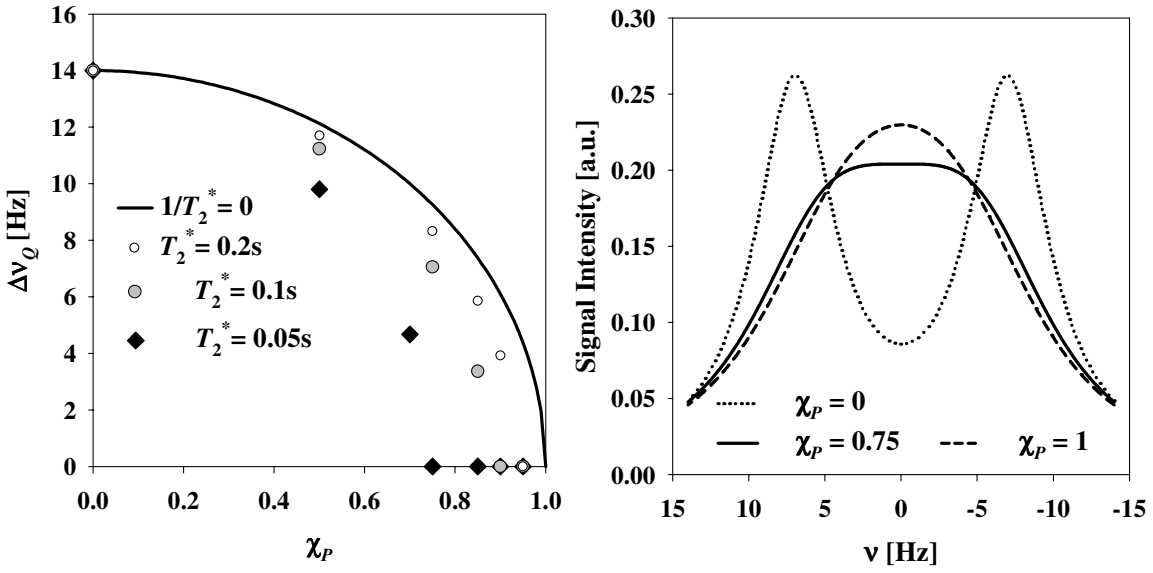

Fig. 7.3.2(1): *left*: the splitting during intermediate exchange for different values of T_2^* normalised by χ_P. *right*: Simulated lineshapes when T_2^* = 0.05s for different values of χ_P.

It is clear that the splitting of spectra with wider initial peaks (low T_2^* values) decreases sooner than those with more defined ones and accordingly the point of coalescence occurs sooner (fig. 7.3.2(1, *right*)). However, at $\chi_P = 1$ they are not truly closer to the fast exchange limit than those spectra where T_2^* is high. In fact it takes several tens of multiples of χ_P to reach a linewidth reminiscent of this limit (where the width of the single peak is $\Delta\nu_{1/2} = 1/(\pi T_2^*)$). Thus, even though spectra of varying T_2^* do not have identical lineshape at a given χ_P, the normalisation with χ_P is valid nevertheless.

7.3.2.2 Failure of the Two States Model

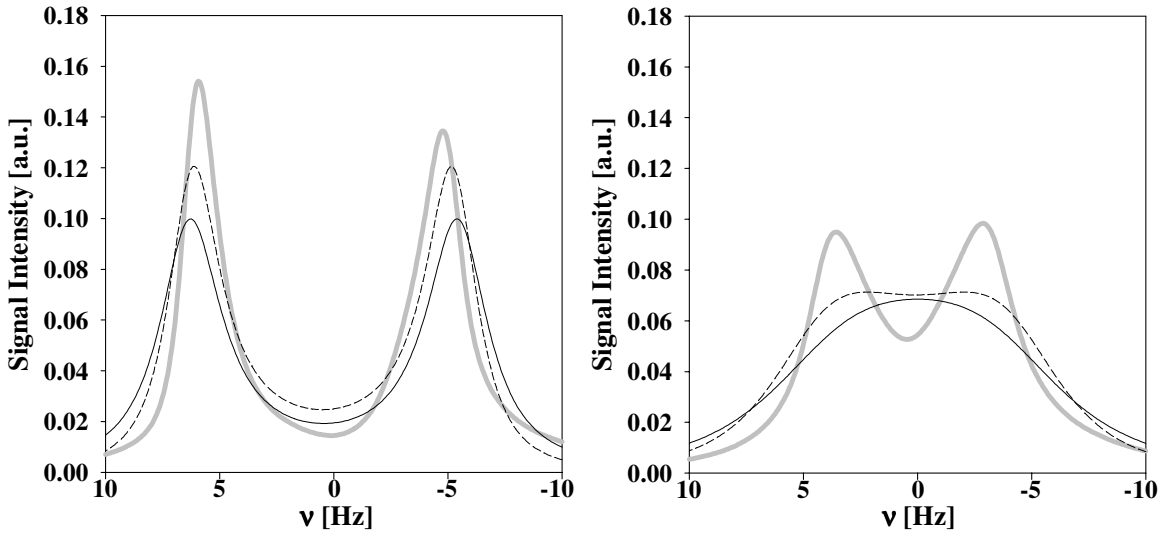

Fig. 7.3.2(2): the fitting of two spectra (grey lines) before the point of coalescence using the modified McConnell equation and the value of $\Delta\nu_{Q,L}$ (eq. 7.3.2(2)). The fits fail, both for the case of an unrestricted T_2^* (dashed line) and the case where T_2^* is set constant to the T_2^* value of the steady state lamellar peaks (solid line). The coalescence parameters of the fits are *left*: χ_P = 0.33 (dashed) and 0.16 (solid line) and *right*: χ_P = 0.94 (dashed) and 1.04 (solid line).

Fig. 7.3.2(2), left and right shows two spectra (grey lines) of a lamellar to sponge transition experiment before the point of coalescence. Fitting of the spectra was attempted using eq. 7.3.2(2) and the initial splitting value $\Delta\nu_{Q,L}$. If T_2^* is an unrestricted parameter, then the result is the dashed line. It is clear that the fit fails. In addition, the fitted T_2^* is so high that $1/T_2^*$ is essentially zero and the original McConnell equation might as well have been used. On the other hand, if T_2^* is set constant to the T_2^* value determined from $\Delta\nu_{1/2}$ of the steady state lamellar peaks, then the result is the solid line. Obviously the fit fails even more drastically.

Therefore, the essential result of evaluating the lamellar to sponge phase transitions is, that the model of exchange between two states *cannot* describe the transitions (using the modified McConnell equation). However, it is shown in the spectra below that if $\Delta\nu_{Q,L}$ is allowed to be a fit parameter, i.e. non-constant throughout a transition, then good fitting is indeed achieved.

7.3.2.3 Spectra Fitting

Fig. 7.3.2(3) to (7) display spectra of experiment FT_25 (ϕ_{B+C}=0.06, ΔT=+1.5°C) in chronological order. The plots on the left always show an automated fit using the sum of two

Lorentzians (solid line), while the ones on the right include a fit using the modified McConnell equation (dashed line). The McConnell fits are performed with a constant value of T_2^* and, as stated, $\Delta\nu_{Q,L}$ is a fit parameter. This T_2^* value is determined by fitting the modified McConnell equation to the steady state lamellar phase spectrum (fig. 7.3.2(3, *right*)), and for the experiment at hand T_2^*=0.1977s. Notably, the value of P resulting from this fit is zero (and thus $\chi_P = 0$), as the peaks are well separated and of Lorentzian form. This is true not only for the displayed experiment, but for all analysed experiments. The general peak evolution of the experiment in question was demonstrated in detail in both two and three dimensions in fig. 7.2.6(13).

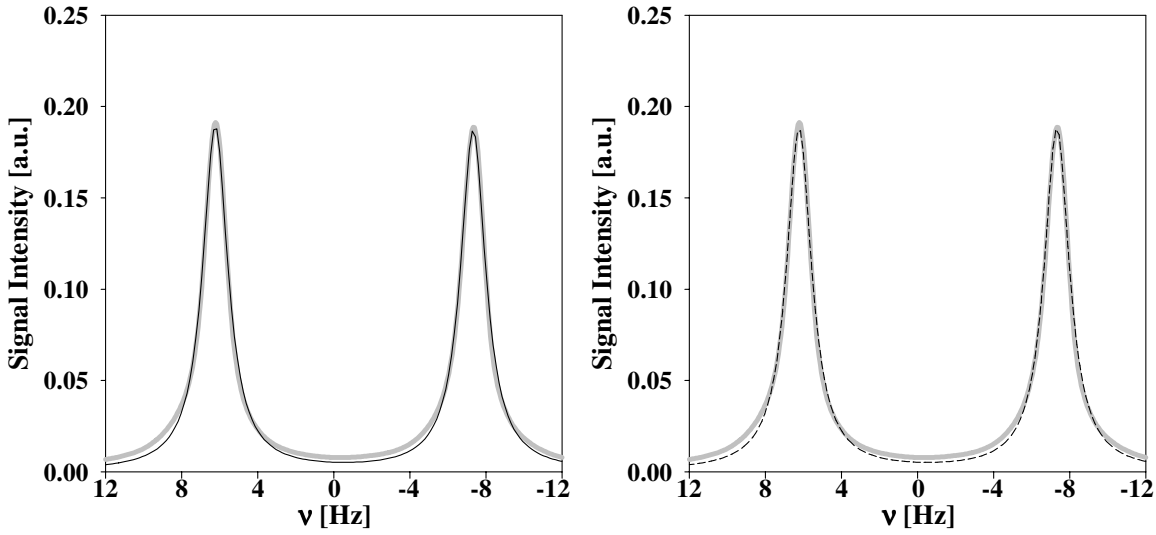

Fig. 7.3.2(3): FT_25 ϕ_{B+C}=0.06, ΔT=+1.5°C, Varian 360, t = 15s. The spectra are of the steady state lamellar phase.

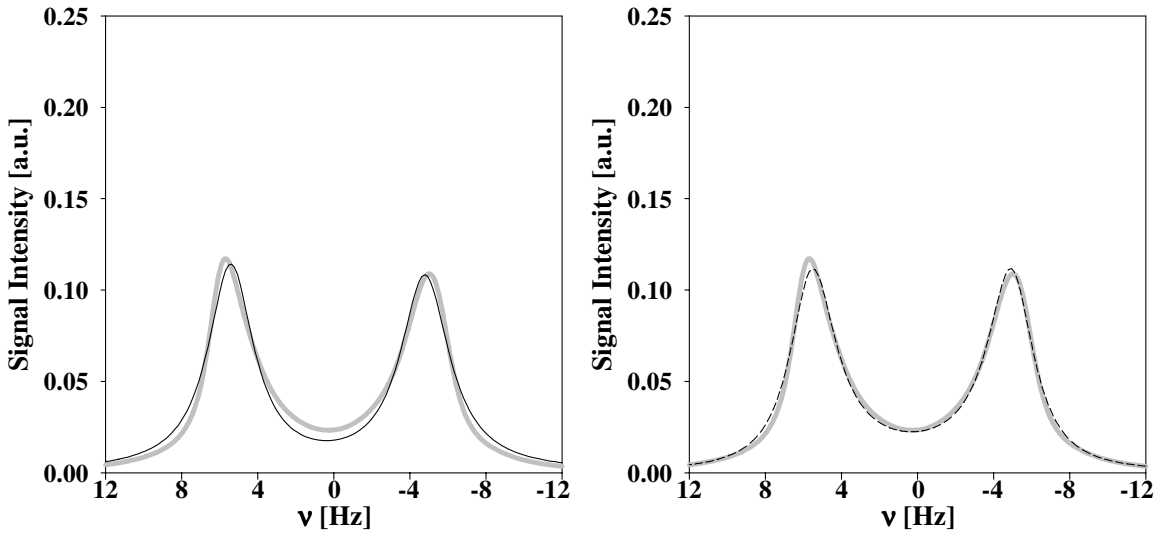

Fig. 7.3.2(4): FT_25 ϕ_{B+C}=0.06, ΔT=+1.5°C, Varian 360, t = 215s.

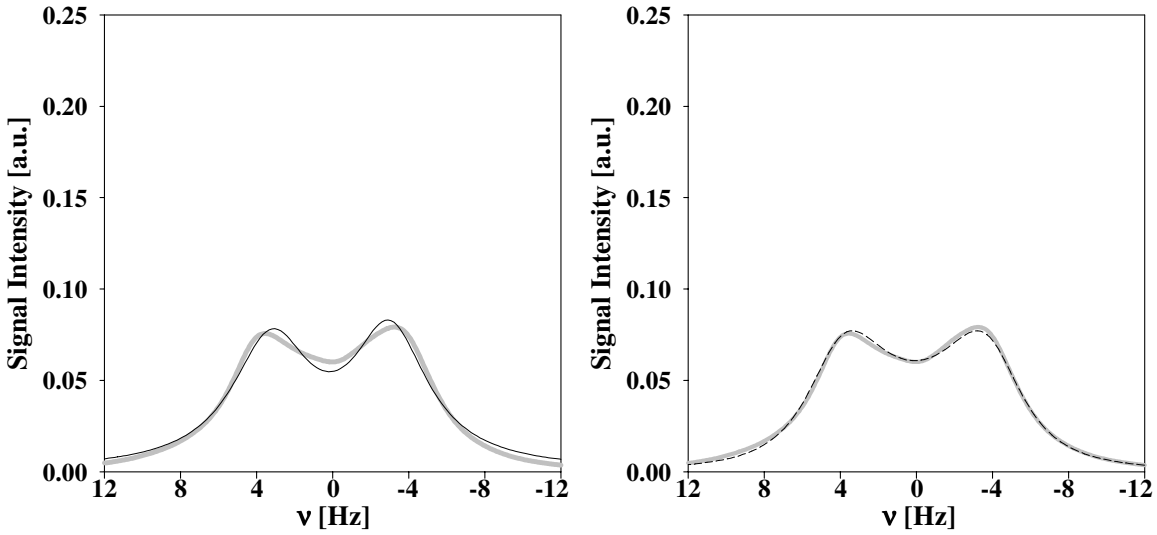

Fig. 7.3.2(5): FT_25 ϕ_{B+C}=0.06, ΔT=+1.5°C, Varian 360, t = 252s

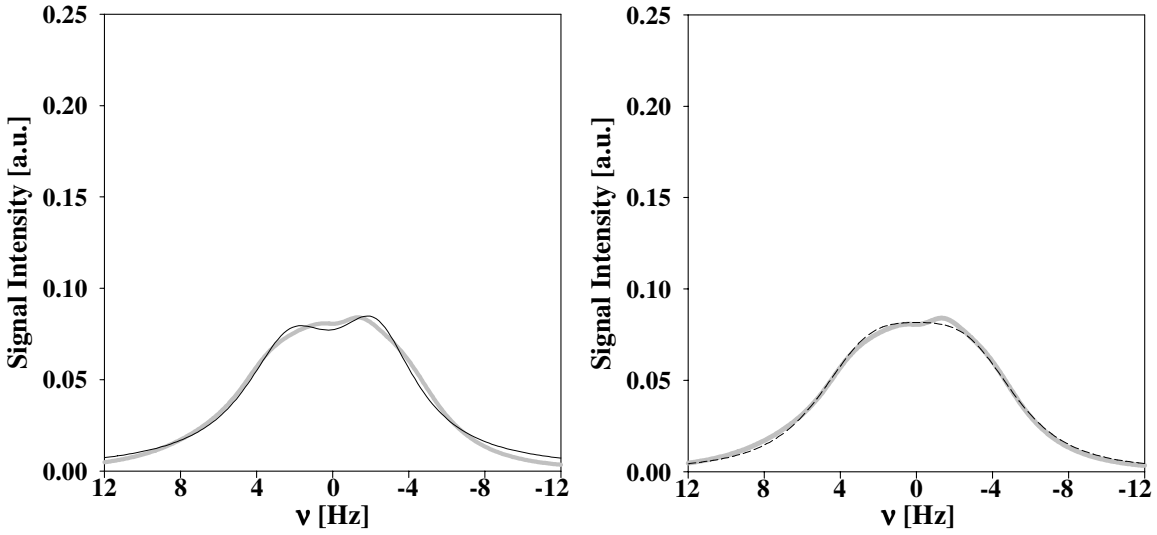

Fig. 7.3.2(6): FT_25 ϕ_{B+C}=0.06, ΔT=+1.5°C, Varian 360, t = 265s

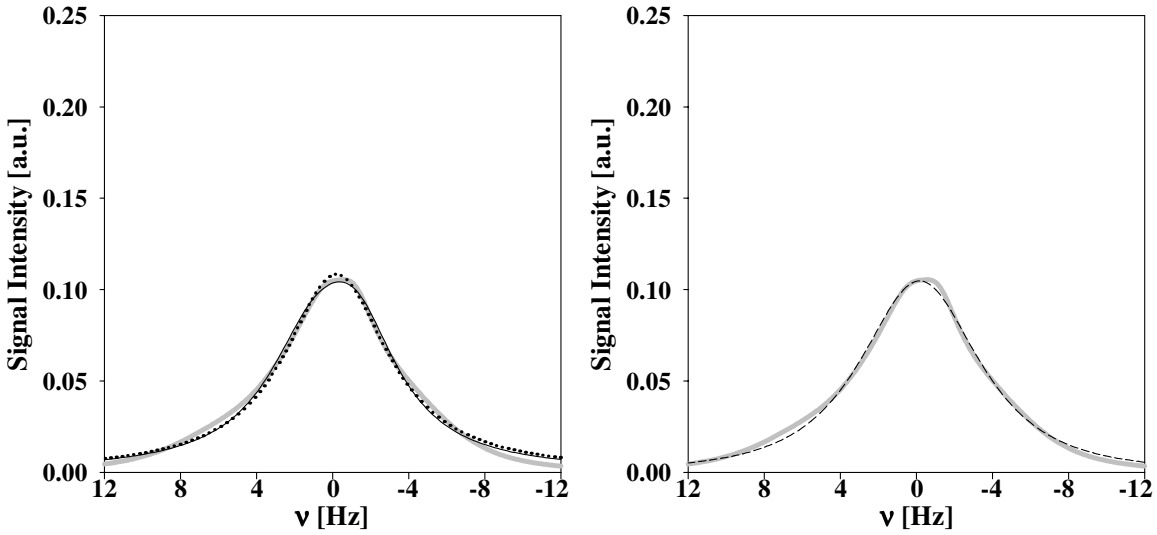

Fig. 7.3.2(7): FT_25 ϕ_{B+C}=0.06, ΔT=+1.5°C, Varian 360, t = 277s. A fit using a single Lorentzian is included in the left spectrum (dotted line).

Fig. 7.3.2(3) to (7) show that although the fits using the sum of two Lorentzians (solid lines) describe the spectra in first approximation, there are characteristic deviations. These

become pronounced as the peaks get close to the point of coalescence. In fig. (4) (t = 215s) and (5) (t = 252s) one sees that, the intensity between the two peaks is too low in the fit. The fit attempts to compensated for this through a reduced splitting $\Delta\nu_Q$. The fact that the spectra show more intensity between the peaks than can be achieved through addition of two Lorentzians is an important finding.

On the other hand, the fits using the modified McConnell equation (dashed lines), do not show the deviation from the data and thus the observed splitting is described much more accurately. However, this type of fit cannot compensate for dissimilarities in the two lamellar peaks of the spectrum, as it intrinsically results in two identical peaks (there is an axis of reflection at ν_0). Thus only experiments which yield spectra of highly similar lamellar peaks can be analysed with this procedure in the first place.

When the spectra are very close to coalescence, the limit of both types of fits is reached. In the spectrum of fig. 7.3.2(6) (t = 265s) a slight splitting is still visible in the data. However, the fit of two Lorentzians results in a much higher splitting, while the McConnell fit already shows coalescence. Once the actual point of coalescence is surpassed (fig (7), t = 277s), both fits work well. However, instead of two Lorentzians one might as well use a single one (dotted line) and a McConnell fit yields no information.

The second statement is true, because for lineshapes past coalescence $\Delta\nu_{Q,L}$ can be arbitrarily high (the fitting program chooses the highest value permissible in the constraints) and an associated P value is always determined, so that the data is well described. Unfortunately, the ratio of $P/\Delta\nu_{Q,L}$ and thus χ_P is *not* constant for different $\Delta\nu_{Q,L}$. In other words, a given lineshape can be fitted with an arbitrarily high value of χ_P, while the fits themselves are identical nevertheless. Thus, analysis of the lineshape using the modified McConnell equation was not pursued past coalescence. Instead, spectra are simply fitted using a single Lorentzian and fig. 7.3.2(8) left and right shows that this leads to satisfactory results (dotted lines).

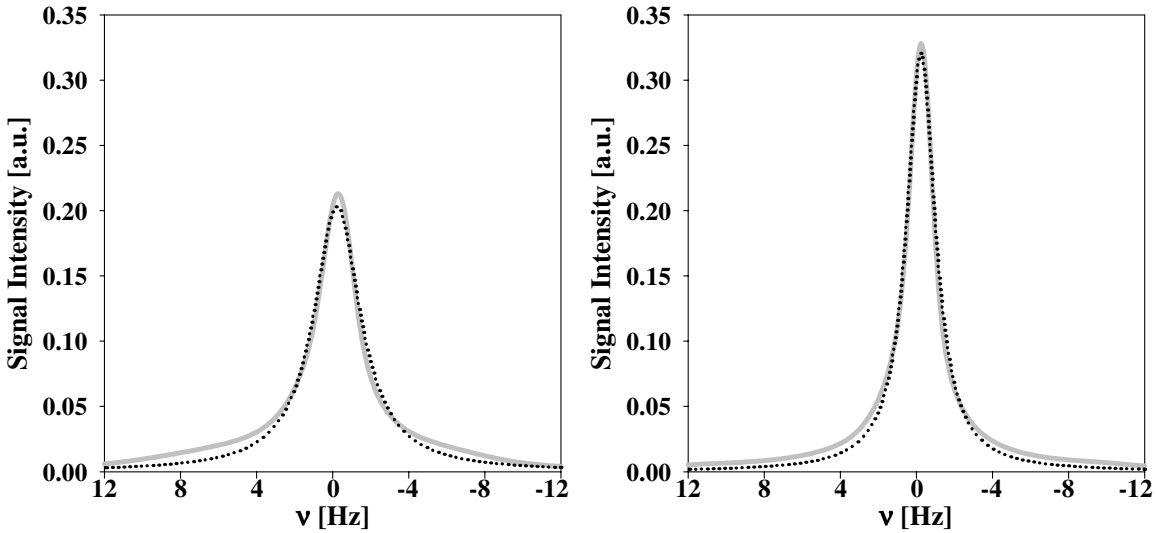

Fig. 7.3.2(8): FT_25 ϕ_{B+C}=0.06, ΔT=+1.5°C, Varian 360, *left:* t = 327s, *right:* t = 440s. Fits (dotted lines) consist of a single Lorentzian.

Already in fig. (6) (t = 265s) it was shown that the McConnell fit leads to a lineshape of or past coalescence, even though a splitting is still visible. This is even more obvious in an experiment (FT_14, ϕ_{B+C}=0.06, ΔT=+0.9°C), where because of superb shimming the existence of a doublet could be observed for a very long time (see fig. 7.2.6(18) for peak development in 2D and 3D). Fig. 7.3.2(9) shows the spectrum at t = 190s, where the peaks are still clearly separated, but the McConnell fit shows a spectrum past coalescence (solid line). A splitting in the fit can only be introduced artificially, i.e. by abandoning the least squares condition, through setting $\Delta\nu_{Q,L}$ to a lower value (dashed line). Resulting parameters from this type of simulation will be represented by diamond symbols in the graphs below.

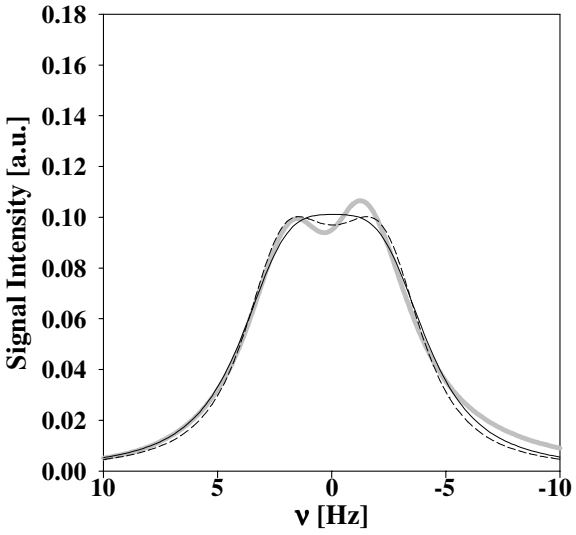

Fig. 7.3.2(9): experiment FT_14, ϕ_{B+C}=0.06, ΔT=+0.9°C, Varian 360. Shown is a McConnell fit (solid line) and a simulation, where the McConnell parameter $\Delta\nu_{Q,L}$ is set to a lower value.

7.3.2.4. Trends in the Development of the Fitting Parameters

Fig. 7.3.2(10) and (11). display the development of parameters for the FT_25 experiment (ϕ_{B+C}=0.06, ΔT=+1.5°C), gained from the fitting procedures described above. Fig. (10) *left* shows the width of the peaks at half height $\Delta\nu_{1/2}$ attained from the fits using first two Lorentzians (up to the point of coalescence, grey data) and then a single Lorentzian (white data). The increase of width is essentially linear, while the decrease is somewhat slower and has a form which is well described through *double* exponential decay.

$$y = y_0 + a \cdot e^{-bx} + c \cdot e^{-dx} \qquad \text{eq. 7.3.2(5)}$$

$\Delta\nu_{1/2}$ first decreases quickly, but towards the end of the transition the decrease is much slower than in the case of a single exponential description, i.e. there is continuous but very slow peak sharpening. Thus two time constants are needed to describe the course of the data and they calculate to 1/b = τ_1 = 35s and 1/d = τ_2 = 210s. The line parallel to the *x*-axis represents the $\Delta\nu_{1/2}$ value of the last acquired spectrum at t = 1500s. This type of progressive peak sharpening is always observed at the end of a transition, even for the lamellar peaks after L_3 to L_α transition experiments (data not shown), but it is best observed for the L_3-peak. Note that irrespective of peak sharpening, the steady state lamellar peaks are always somewhat wider than their L_3-peaks counterparts.

Fig. 7.3.2(10,*right*) shows the development of the actual splitting determined manually by measuring the distance between peak maxima (white data), $\Delta\nu_Q$ according to the fit using two Lorentzians (black data) and $\Delta\nu_{Q,L}$, which has to be a *variable* parameter in the modified McConnell equation (grey data). The course of all three data points is similar, i.e. an exponential decay from a maximum is seen. However, the black data is generally above the white, due to the splitting being reduced in the fit of two Lorentzians in order to compensate for the low intensity between the peaks (see above). On the other hand, the grey data is above the white, since the increase of P in the McConnell equation does cause the splitting to be somewhat reduced, but this decrease is far too little and so $\Delta\nu_{Q,L}$ decreases almost as quickly as the actual splitting. Only as the point of coalescence is approached, does the decrease stop and $\Delta\nu_{Q,L}$ levels off.

In fig. 7.3.2(11) the development of the coalescence parameter χ_P is plotted. It can be described as an exponential growth, akin to the increase of the L_3-peak width (eq. 7.3.1(7)) However the increase is very quick and the determined time constant is similar to that of τ_1.

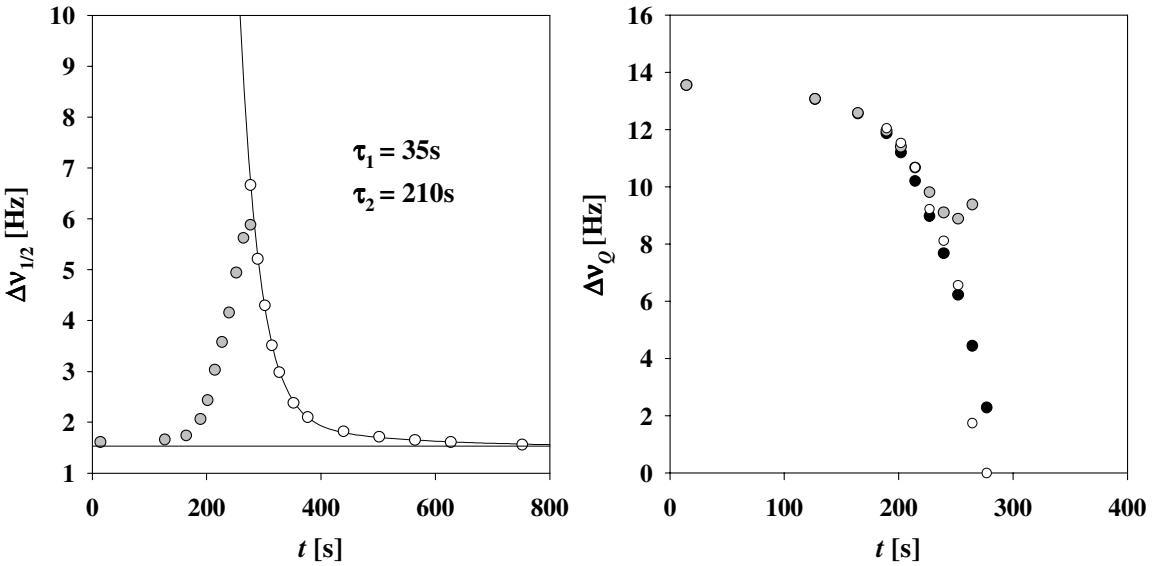

Fig. 7.3.2(10): FT_25 ϕ_{B+C}=0.06, ΔT=+1.5°C, Varian 360. *left*: increase of the peak width of the lamellar doublet until coalescence (grey data) and decrease of the peak width of a single Lorentzian after coalescence. Note that at one point a spectrum was fitted with both methods (t = 277s, see 7.3.2(7, *left*)). *right*: decrease of the splitting with time. Symbol definition is given in the text.

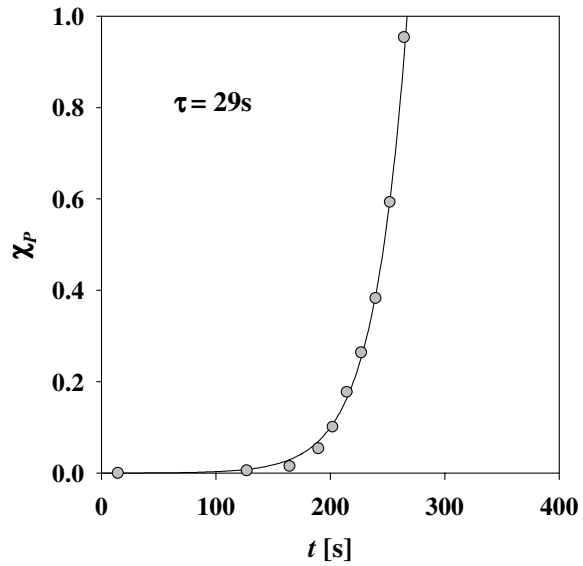

Fig. 7.3.2(11): FT_25 ϕ_{B+C}=0.06, ΔT=+1.5°C, Varian 360. The development of the coalescence parameter χ_P is well described through exponential growth.

Fig. 7.3.2(12) to (17) depict the same plots as given above, but for experiments of varied ΔT and viscosity. They serve to show that the described trends are found in all of the conducted experiments. Note that the scaling is identical for easy comparison. Each of the analysed experiments has its peak development illustrated in 2D and 3D plots in section

7.2.6.2. The diamond symbols in the plots of the McConnell parameters result from artificially reducing the value of $\Delta\nu_{Q,L}$ in order to force the existence of a splitting (see above). Note that in case of exp FT_14 the initial splitting is unusually small for a sample of ϕ_{B+C}=0.06 (so small in fact that it was considered an outlier and not used to calculate the average splitting value). Also, the decline of the L_3-peak width in fig. 7.3.2(16) is only described using a single exponential, because no spectra were taken at an advanced point in time and peak sharpening therefore was not observed.

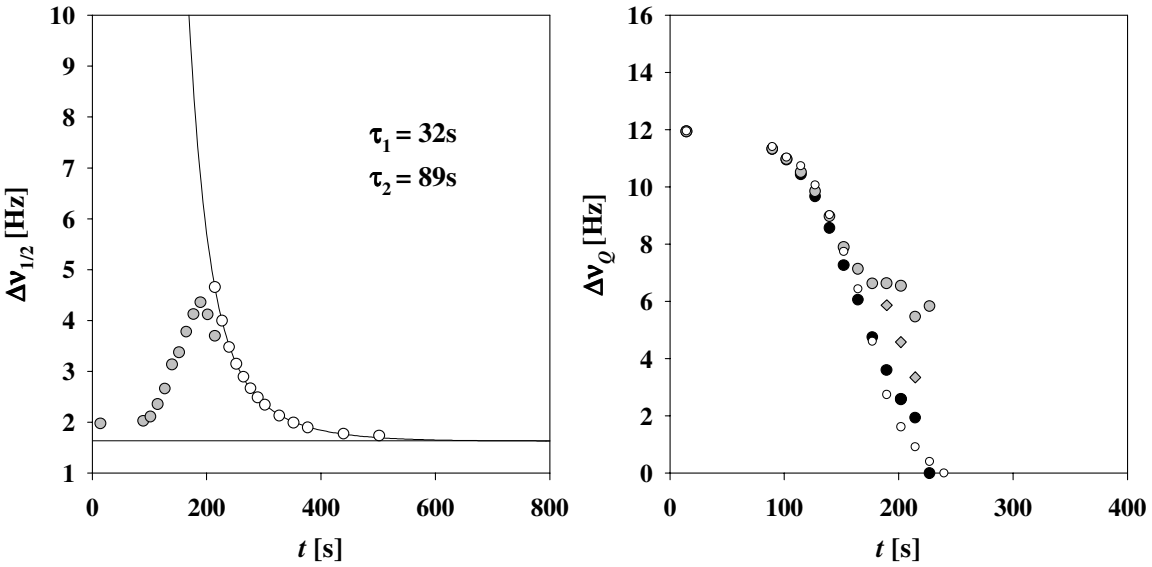

Fig. 7.3.2(12): experiment FT_14, ϕ_{B+C}=0.06, ΔT=+0.9°C, Varian 360. Symbols are analogous to those in fig. 7.3.2(10). The grey diamonds, represent fits where $\Delta\nu_{Q,L}$ was reduced in order to force the existence of a splitting.

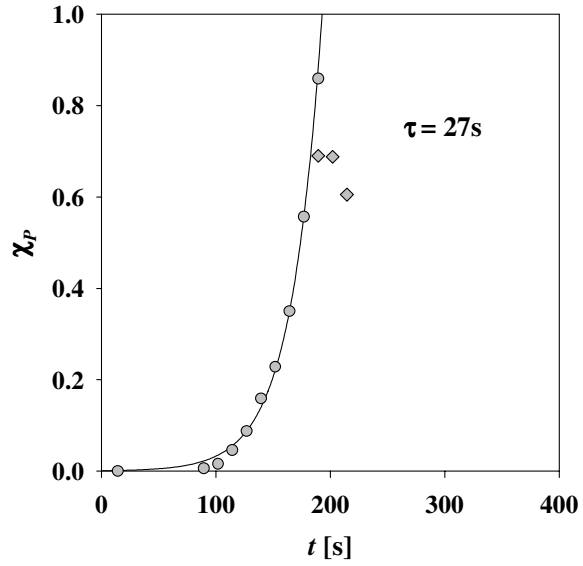

Fig. 7.3.2(13): experiment FT_14, ϕ_{B+C}=0.06, ΔT=+0.9°C, Varian 360. Symbols are analogous to those in fig. 7.3.2(11). The grey diamonds, represent fits where $\Delta\nu_{Q,L}$ was reduced in order to force the existence of a splitting.

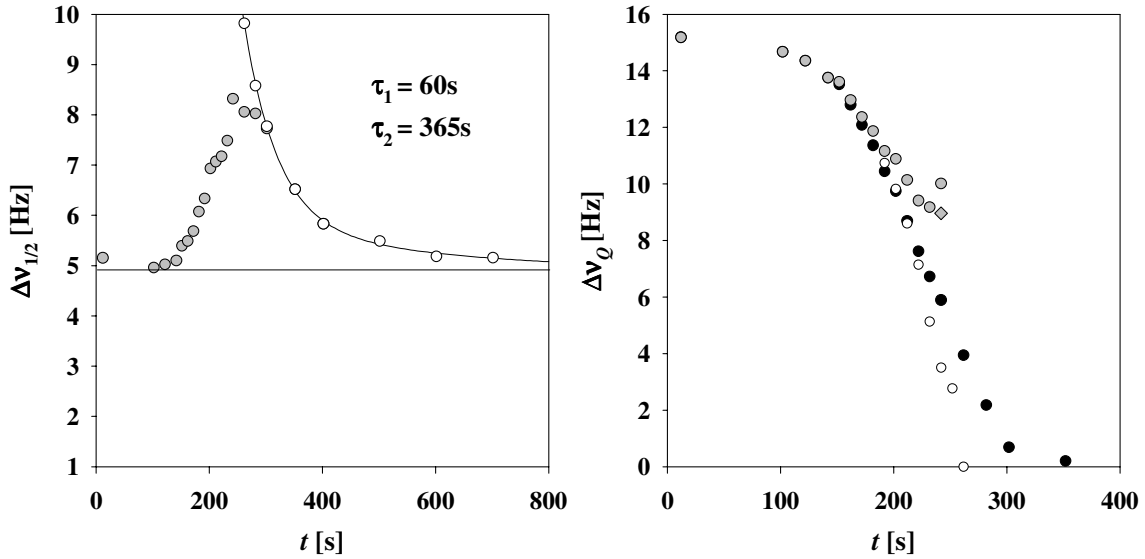

Fig. 7.3.2(14): experiment FT_83, ϕ_{B+C}=0.06, ΔT=+1.5°C, $\eta_{D2O/S} = \eta_0 \cdot 2.261$, Varian 360

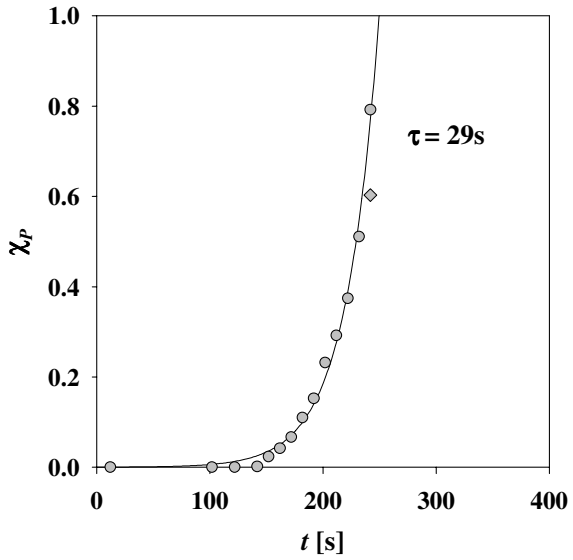

Fig. 7.3.2(15): experiment FT_83, ϕ_{B+C}=0.06, ΔT=+1.5°C, $\eta_{D2O/S} = \eta_0 \cdot 2.261$, Varian 360

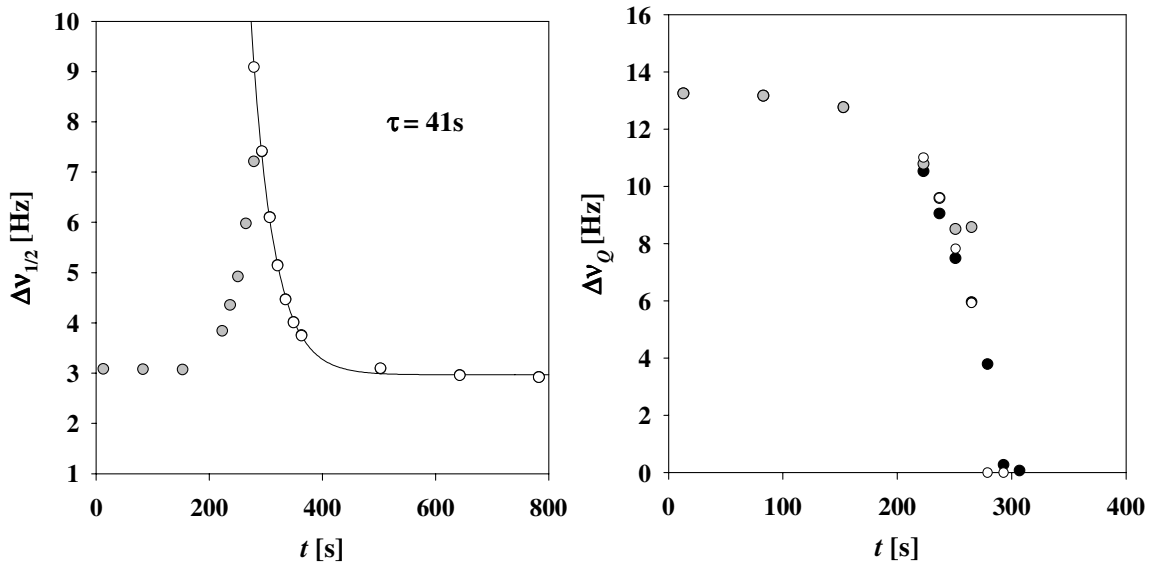

Fig. 7.3.2(16): ϕ_{B+C}=0.06, ΔT=+2.0°C, Bruker DMX-200

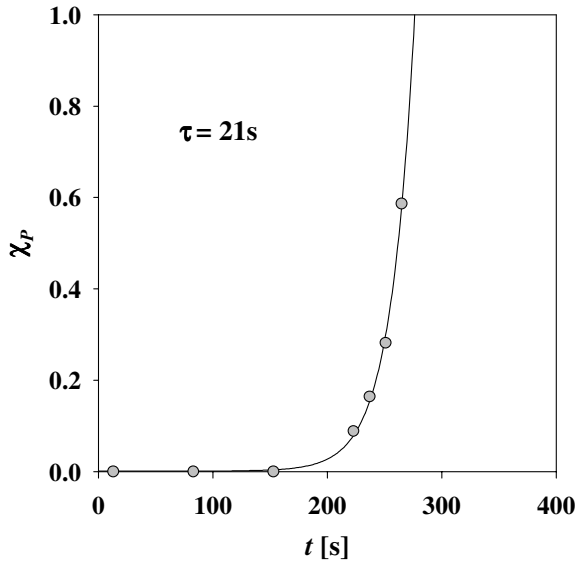

Fig. 7.3.2(17): ϕ_{B+C}=0.06, ΔT=+2.0°C, Bruker DMX-200

Unfortunately, the kinetics of the lamellar to sponge transition experiments cannot be described directly, as a working model is presently unavailable. Nor is there even a parameter which can be monitored continuously from the beginning to the end of the phase transition process. However, the characteristic point of coalescence can serve to compare the transition speeds of the various experiments. The point in time at which coalescence occurs can generally be determined to within ±10s (depending on the speed at which NMR spectra were taken). This is even the case when spectra are of poor quality, i.e. the peaks are wide due to suboptimal shimming or asymmetric due to errors in phasing. Fig. 7.3.2(18) illustrates the coalescence times for a variety of experiments. White symbols represent times acquired from

studying samples of ϕ_{B+C}=0.05, while grey symbols denote those of ϕ_{B+C}=0.06. Diamonds are used in the case of increased viscosity ($\eta_{D2O/S}$ =η_0·2.261) and results from preliminary experiments are as always denoted by a cross.

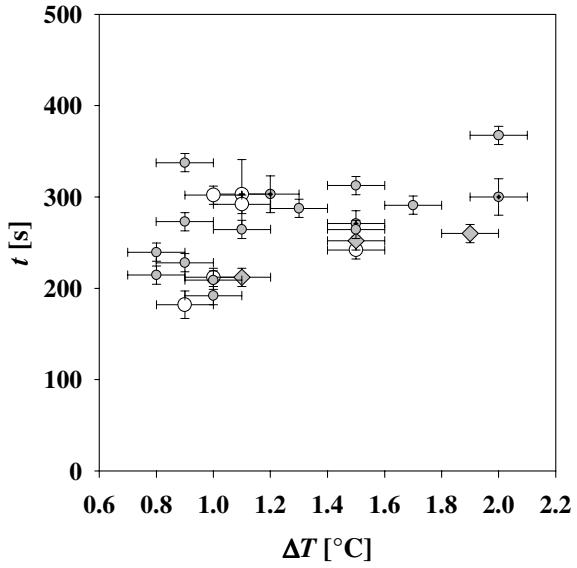

Fig. 7.3.2(18): time until coalescence of the peak doublet in lamellar to sponge transitions as a function of the magnitude of the temperature jump Δ*T*. The different symbols denote samples of varying composition (description given in text).

Notably, and in contrast to the sponge to lamellar transition experiments, a trend for the transition kinetics is not detectable. This is true both in terms of sample bilayer volume fraction as well as viscosity. Especially the latter finding is of interest, since increasing viscosity has such a profound effect on the sponge to lamellar transition experiments. Finally, when considering the distribution of values and the low number of experiments at high Δ*T*, changes in the magnitude of the temperature jump do not influence transition speeds either.

7.3.3 Kinetics of the 'Additional Experiments'

The three types of experiments presented in section 7.2.6.4, were not analysed in detail, as it is the general development of their peak positions which is of interest. The experiments are however part of the discussion of section 7.4.7. Nevertheless, in light of the insights gained from the kinetic evaluation of the normal temperature jump experiments (presented above), a few comments regarding the kinetics involved will be made.

In the reversed lamellar to sponge transition of fig. 7.2.6(20), it takes ~1100s from the first appearance of the lamellar doublet to the formation of the L_α steady state. Although this is somewhat faster than the ~1500s seen for the development of similar peak shapes in a

comparable standard experiment ($\phi_{B+C} = 0.05$, $\Delta T = -1.0°C$), it is not an extraordinarily difference (data not shown). What is remarkable however, is the very short time needed for the appearance of quite well defined lamellar peaks of a large splitting (present at the $t = 200s$ mark, i.e. ~140s after reversal of the temperature). For the appearance of similar lamellar peaks a standard experiment requires ~1200s (data not shown). Thus the onset time is minimal if not non-existent in the reversal experiment.

The reversing of a sponge to lamellar phase transition experiment, which was presented in fig. 7.2.6(22), does not show any peculiarities with respect to the kinetics. The coalescence of the lamellar doublet occurs at ~250s. Since the temperature was reversed at $t = 17s$, the time needed until coalescence is ~230s and this is an average value with respect to the standard L_α to L_3 transition experiments (fig. 7.3.2(18)).

The micellar to lamellar phase transition of fig. 7.2.6(22, *left*), is not analysed in terms of kinetics as this transition is not the object of this thesis and too few experiments were performed to obtain significant results. However, the ensuing lamellar to sponge transition (fig. 7.2.6(22, *right*)) is examined. Firstly, although the time up to peak coalescence is quite long (~330s, when considering the $t = 600s$ moment as the initial lamellar phase) it is still within the range of detected values when observing 'standard' experiments (fig. 7.3.2(18)). However, the maximum splitting detected at $t = 600s$, is with $\Delta\nu_Q = 10.1$ Hz small, when compared to the average value of the steady state lamellar phase of $\phi_{B+C} = 0.06$ samples ($\Delta\nu_{Q,L} = 13.7$ Hz). Then again, it is important to be aware that at $t = 600s$, the lamellar phase is not in a steady state, since the system temperature is of the value of the sponge phase and the transition from the micellar phase might not even be completed.

7.3.4 Experiments Separating Nucleation from Growth

In order to gain further information on the mechanism which governs the sponge to lamellar phase transitions, i.e. the nucleation and growth process, additional experiments were performed on the Varian 360 spectrometer with the aim of separating the nucleation from the growth phase. For this purpose, a $\phi_{B+C} = 0.06$ sample was subjected to temperature jumps of $\Delta T = -1.0°C$. However, the sample liquid was cooled below the target temperature for a brief period of time, before said target condition was actually reached. Thus, initial nucleation occurs at a state of lower temperature, while the lamellar domain growth and possibly further nucleation (in case of a progressive nucleation, i.e. $\alpha = 4.$) occurs at a higher temperature. A schematic profile of the temperature development during the experiments in question is displayed in fig. 7.3.4(1). It is divided into segments which will be detailed in the following paragraph.

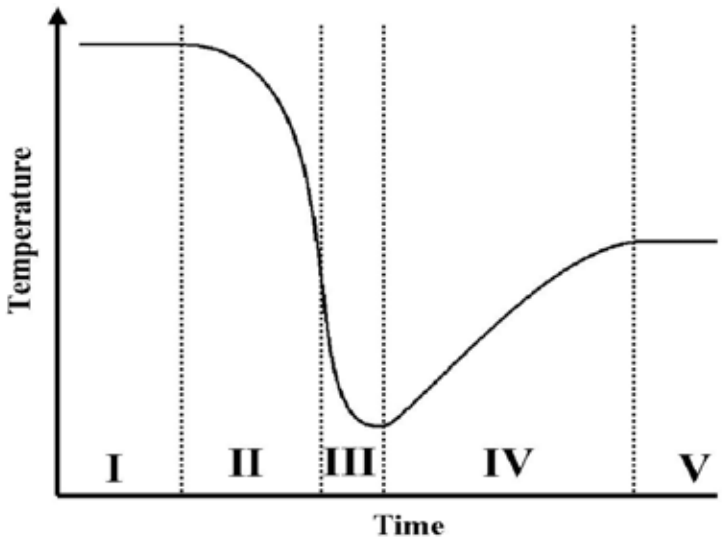

Fig. 7.3.4(1): schematic temperature profile of the sample liquid during L_3-to-L_α phase transition experiments. The transition begins at the steady state and accordingly at L_3-temperature (segment I). A minimum is traversed at the boundary of segment III and IV, before the L_α target temperature is reached at the end of segment IV. It is important to note that the total time of phases II, III and IV is short when compared with the one of the overall phase transition.

In segment I, the sample is located inside the spectrometer, where it resides in its equilibrium L_3-state. In segment II, the sample is swiftly removed and, for the time being, simply left hanging in air of room temperature (~19°C), which initiates an intense temperature decrease. By placing the sample within a heating block in segment III, referred to as the 'cold block', the temperature drop is quenched and the minimum temperature achieved. In segment IV, the sample is promptly transferred to an adjacent heating block (the 'hot block'), where

the target temperature of the transition is attained quickly. This target temperature is one, where the lamellar phase is in equilibrium. Finally, in segment V the sample is returned to the spectrometer, which by this time is of the target temperature (the spectrometer airflow temperature is changed to the target value as soon as segment II commences) and the ongoing sponge to lamellar transition is monitored normally by the acquisition of subsequent spectra. The longest time necessary to reach segment V was 240s and thus the period of temperature alteration is still short when compared to the time of the phase transition process (see below). For further details regarding the experimental procedures see 10.4.4.

Although the method of temperature alteration is primitive and likely associated with significant errors, meaningful results could be achieved nonetheless. Fig. 7.3.4(2, *left*) illustrates the φ-development of two standard ΔT = -1.0°C experiments (white symbols), two where the minimum of fig. 7.3.4(1) corresponds to –1.5°C (light grey symbols) and two where said minimum is –2.0°C (dark grey symbols). In *all* cases the target temperature amounted to ΔT = -1.0°C. The figure on the *right* depicts the relaxation time constants τ of the respective experiments with respect to the temperature dependence of τ derived for ϕ_{B+C} = 0.06 samples (solid line, taken from fig. 7.3.1(17)).

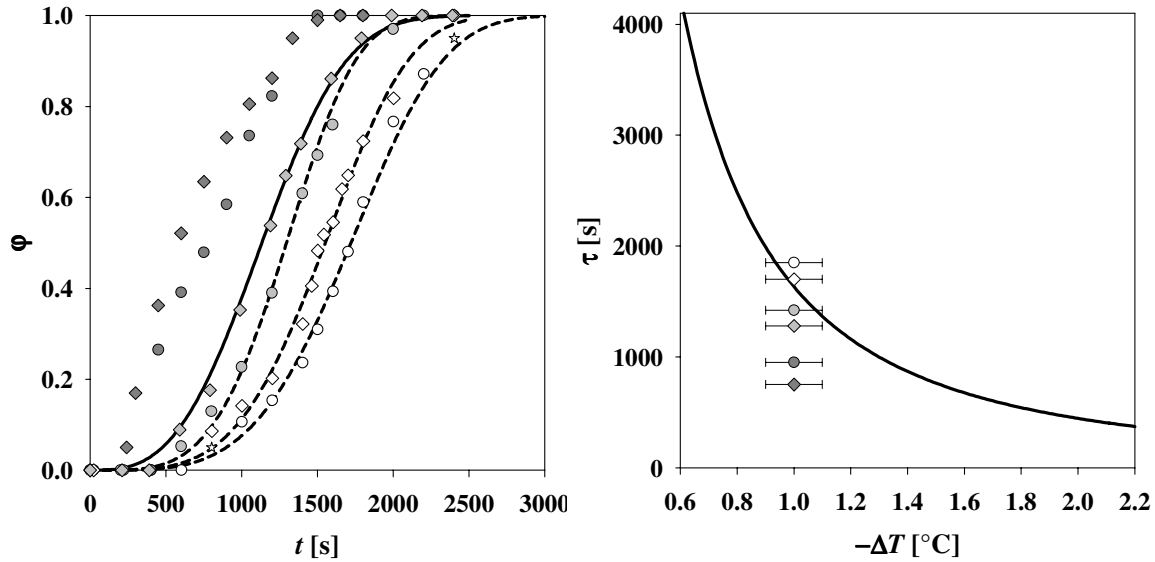

Fig. 7.3.4(2) *left*: φ-development of standard ϕ_{B+C} = 0.06, ΔT = -1.0°C experiments (white symbols), and experiments, where a minimum temperature was traversed before the target temperature of ΔT = -1.0°C (light grey symbols, ΔT_{min} = -1.5°C and dark grey symbols, ΔT_{min} = -2.0°C). Where possible the data is fitted according to the Avrami equation (dashed lines α = 4, solid line α = 3). *right*: τ times of the depicted experiments in relation to the τ as function of ΔT behaviour observed for ϕ_{B+C} = 0.06 samples (solid line).

Although the target temperature is surpassed only for a short time, this overcooling profoundly increases the speed of the transition kinetics. In addition, the shape of the φ-development is affected similarly, as when faster transitions are induced in the standard experiments through increasing the magnitude of ΔT (section 7.3.1.3), i.e. the fast transitions

still show a steep increase of φ at the beginning of the process, but towards the end this increase slows down continuously and φ can no longer be described by $\alpha = 4$ (or even $\alpha = 3$, dark grey symbols). However, it must be kept in mind that towards the conclusion of the transitions $\Delta T = -1.0°C$ and that for these cases (standard experiments) φ increases slowly even for $\alpha = 4$. This is not obvious in the graphs of section 7.3.1.3, since the time scale of these experiments is large due to the large τ times involved. Thus the slow increase in fig. 7.3.4(2, *left*) (dark grey symbols) is actually comparable to the increase found in standard $\Delta T = -1.0°C$ experiments, and this is seen if the φ-development of the latter experiments is shifted to lower *t* (not illustrated). Finally, fig. 7.3.4(2, *left*) shows that the onset time decreases as overcooling is increases and for the fastest case (dark grey diamonds) a minimum onset time of ~200s is detected.

7.4 Interpretations of the Experimental Findings

7.4.1 The Driving Force of the L_3/L_α Phase Transition

It has been stated in section 3.2 that, according to *Morse*[59], the boundary of stability between the lamellar and sponge phase can be expressed via

$$\ln \phi_C = \frac{6\pi}{5}\left(\frac{\bar{\kappa}}{k_B T}\right) \qquad \text{eq. 3.2(3)}$$

with the L_α-phase becoming instable compared to the L_3-phase (or vice versa) in case of $\bar{\kappa}(\xi) = 0$[99]. Hence the saddle splay modulus $\bar{\kappa}$ is the key parameter determining L_α/L_3 phase stability. *Porte*[57] stated that $\bar{\kappa}$ of a bilayer structure can be calculated according to

$$\bar{\kappa}_{bi} = 2\bar{\kappa}_{mono} - 4\varepsilon c_{0,mono}\kappa_{mono} \qquad \text{eq. 7.4.1(1)}$$

Since κ_{mono} and $\bar{\kappa}_{mono}$ are constant for a given system around the phase inversion temperature $\bar{T}$, in fact *Uhrmeister*[46] determined them to

$$\kappa_{mono} = 1.24 k_B T$$
$$\bar{\kappa}_{mono} = -0.75 k_B T$$

for the system H_2O/NaCl – *n*-decane – $C_{12}E_5$ (0.1M NaCl solution), and ε is constant for a given value of ω_b, $\bar{\kappa}_{bi}$ is only a function of the spontaneous curvature of the monolayers $c_{0,mono}$. It can be assumed that $c_{0,mono}$ varies with temperature similarly to c_1 and c_2 (fig. 3.1(1)) so that

$$c_{0,mono} = c\left(\bar{T} - T\right) \qquad \text{eq. 7.4.1(2)}$$

applies. The constant c varies with ω_b and for the composition of interest (ω_b=0.45) calculates to $0.977 \cdot 10^{-3}$ Å^{-1}K^{-1}, while $\bar{T}$ =38.24°C [46]. Thus $\bar{\kappa}_{bi}$ is simply a function of temperature T and since $\bar{\kappa}_{mono} < 0$ and κ_{mono} and $\varepsilon > 0$ (eq. 7.4.1(1)), $\bar{\kappa}_{bi}$ grows increasingly negative towards

lower values of *T*. In section 3.2, it is stated that due to the scaling invariance, $\bar{\kappa}$ necessarily grows more negative with dilution. This has direct impact on the phase behaviour, inasmuch as the L_3-phase is accordingly stable at lower temperatures in that region (see phase diagrams section 2).

The elastic energy of a flexible surface was derived by *Helfrich*[51] and given in eq. 3.2(1). This equation considers the properties of a monolayer, but can be adapted for bilayers as well. It is sensible to assume that the spontaneous curvature of the bilayer(s) $c_{0,bi}$ within both the lamellar and sponge phases is zero. This permits a reduction of eq. 3.2(1) to

$$E = \int \mathrm{d}A \cdot \left[\frac{\kappa_{bi}}{2} (c_{1,bi} + c_{2,bi})^2 + \bar{\kappa}_{bi} c_{1,bi} c_{2,bi} \right] \qquad \text{eq. 7.4.1(3)}$$

For the lamellar phase $c_{1,bi}=c_{2,bi}=0$, while for the sponge phase $c_{1,bi} = -c_{2,bi}$. Thus only the right sum of eq. 7.4.1(3) must be considered and it becomes clear why a change of temperature is the driving force of L_3/L_α transitions. For L_3 to L_α transition, i.e. upon lowering *T*, $c_{0,mono}$ becomes less negative or more positive and respectively $\bar{\kappa}_{bi}$ become more negative. This increases the bending energy *E* of the L_3-structure as $c_{1,bi}$ and $c_{2,bi}$ remain constant for the time being and $c_{1,bi} \cdot c_{2,bi} < 0$. *E* can only be minimised by reducing the magnitude of the $c_{1,bi} \cdot c_{2,bi}$ term and accordingly planar structures are formed. For the L_α to L_3 transition, $\bar{\kappa}_{bi}$ becomes less negative and for $\bar{\kappa}_{bi} > 0$ saddle splay topology ($c_{1,bi} \cdot c_{2,bi} < 0$) becomes energetically favourable. However, in practice $\bar{\kappa}_{bi}$ does not become positive for the system at hand[46], but the formation of saddle splay topology is less costly nevertheless. In addition, entropic fluctuations must be considered[27].

7.4.2 Influence of the Magnetic Field

It is well known that magnetic fields can be used to control the alignment of liquid crystals, even though the interaction between the molecules and the magnetic field is generally weak[100]. It will in fact be shown in section 7.4.5.1 that alignment also occurs in the highly dilute, lyotropic liquid crystal, which is the lamellar phase of the studied samples, and that the angle between the bilayer normals and the magnetic field θ_{nb} is 90° (as proposed in section 7.2.5). The cause of the alignment is a negative anisotropy of the surfactant molecules' diamagnetic susceptibility, orienting the longitudinal axis of the $C_{12}E_5$ molecules

perpendicular to the magnetic field[34]. Accordingly however, there is a magnetic contribution g_H to a sample's free energy density

$$g_H = \frac{1}{2}\gamma_a \left\|\vec{H}\right\|^2 \qquad \text{eq. 7.4.2(1)}$$

where γ_a is the diamagnetic susceptibility and $\left\|\vec{H}\right\|^2$ the magnitude of the magnetic field strength and this can cause a shift in the phase transition temperatures[101]. Shifts to both higher and lower temperatures are known and the magnitude of shift can be calculated by comparing the magnetic energy with the transition enthalpy. For the established experiments (at ~8.5T, section appendix) only a slight shift of 0.8°C to lower temperatures was registered, while for the few preliminary experiments conducted (at ~4.7T) no shift of phase behaviour was noticed (however, it is not unlikely that the absolute calibration of the thermocouple used for externally testing spectrometer temperature was off and a shift of 0.25°C therefore not observed).

Thus, in case of the NMR investigations, the phase transitions were not truly studied in the absence of an outside, vectored force (excluding gravity of course), although the effect cannot be compared to shearing experiments. Nevertheless, it is conceivable that the magnetic field could influence bilayer undulations und accordingly the kinetics of the observed phase transitions (see section 7.4.5.5 below). However, in the study, where a sponge to lamellar phase transition was also monitored via NMR[35], any possible effects of the magnetic field were simply ignored and since the interaction between the magnetic field and the surfactant is weak (see above), especially when seen per unit volume at the respective dilution, the same will be done here.

7.4.3 Shift of Resonance Frequency

As stated in section 7.2.6 (e.g. fig. 7.2.6(9)), a small but characteristic shift of the resonance frequency ν_Q is detected at the beginning of each *T*-jump experiment. The cause of this shift is the variation of absolute temperature itself. For negative *T*-jumps resonance is moved to lower frequencies, while for positive *T*-jumps the opposite is true. The amount of shift is proportional to the temperature variation, and for small variations behaves linearly

(fig. 7.4.3(1)). For the large magnitude of ΔT, used to initiate the $L_1 \rightarrow L_\alpha \rightarrow L_3$ transition (section 7.2.6.4), the resonance shift deviates to a lower value.

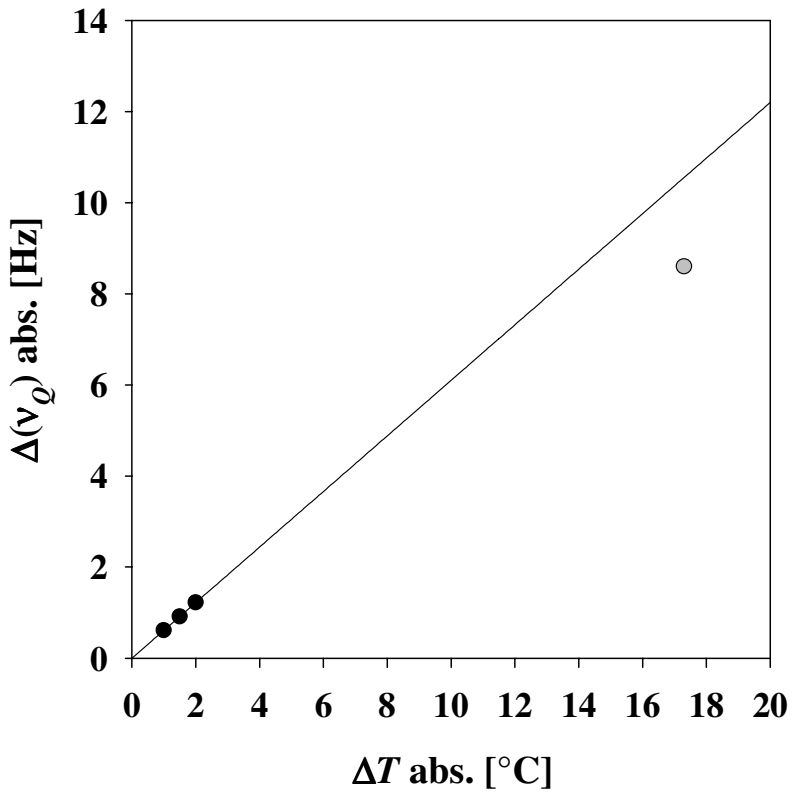

Fig. 7.4.3(1): absolute value of the shift of resonance frequency ν_Q as function of the absolute value of the temperature jump. Black symbols result from the negative *T*-jumps FT_32, FT_24 and FT_06 (section 7.2.6.2), the grey one from the positive *T*-jump FT_19 (section 7.2.6.4).

7.4.4. Experimental Data vs. Fits and Simulation

Section 7.1.4 details that a Fourier transformation of a FID leads to a signal of Lorentzian lineshape. This is however strictly true only as long as the decay of the components of the transverse magnetisation occurs exponentially. This was elucidated in section 7.1.5., where the exponential decay of the autocorrelation function $\rho(\tau)$ of oscillatory motions of a particle ensemble was associated with the correlation time τ_c. But rotational and diffusional motions in an anisotropic environment, e.g. in a complex fluid, can lead to relaxation, which can not be expressed in terms of a single exponential.[86] This in turn can lead to deviations from the Lorentzian lineshape. A detailed discussion of non-exponential/multi-exponential relaxation is however beyond the scope of this thesis.

Although generally the spectra of the L_3 to L_α transitions in section 7.3.1 were fitted/simulated well using one, or the sum of two or three Lorentzians, there nevertheless remain certain deviations from the experimental data which require closer inspection. This is

most obvious in fig. 7.3.1(7) 70a to 100a, where the intensity between the central L_3-peak and the surrounding L_α-peaks is considerably higher (grey line) than the simulated fit (solid line). Also, even the steady state spectra 1a and 120b show distinct differences between data and simulation, though these are noticeably smaller than in the previous case. Due to the overall symmetry of the spectra and low values of the peak width $\Delta\nu_{1/2}$, it seems unlikely that the differences result from abnormalities/artefacts caused by technical problems in data acquisition and processing (such as appear for example in Fig. 7.2.6(14)) Therefore, it is plausible that non-exponential relaxation occurs to a minor degree.

For the lamellar to sponge phase transition experiments, the deviations from the data, for fits using the sum of two Lorentzians or the modified McConnell equation (eq. 7.3.2(2)), have already been reported in section 7.3.2.3. At long and medium times to coalescence, eq. 7.3.2(2) describes the non-Lorentzian spectra lineshapes very well, but fails close to coalescence if the peaks are well separated due to good shimming (fig. 7.3.2(9)). However, since it is the model that fails to describe the complex lineshapes (the data does not correspond to a superposition of two Lorentzians), it is futile to speculate on the reasons of the deviations. Thus a different model is needed (see section 7.4.6 below). After coalescence the lineshapes resemble those of a single Lorentzian and the same minor deviations that were discussed for the L_3 to L_α transitions above are observed.

7.4.5 L_3 to L_α Transitions

7.4.5.1 Characteristics of the Nucleation and Growth Mechanism

In section 7.3.1 is argued that a *nucleation and growth* process is witnessed for the sponge to lamellar transition. From the fact that a simply, well resolved doublet is detected in the lamellar phase, it is additionally clear that there is macroscopic order in the orientation of the bilayers, i.e. that the angle θ_{db} between the phase director and the magnetic field is constant (section 7.2.5). At first glance, this could lead to the impression that perhaps a *mononuclear* mechanism governs the L_3 to L_α phase transition, i.e. that the growth of a single 'crystal' is witnessed. However, to achieve this type of crystallisation on macroscopic scales (the NMR experiment examines a few millilitres of sample) generally requires a great deal of effort and very controlled environments (e.g. high system purity, no disturbances, a low supersaturation and the introduction of a nucleation-active centre). More importantly, the acquired data clearly show that this mechanism can be discounted for the experiments at hand, since the onset times and relaxation time constants τ are reproducible for a given set of

temperature jump conditions. Therefore a statistical, *polynuclear* mechanism must be considered and discussed and θ_{db}=90° (section 7.2.5).

The constant value of θ_{db} may at first seem remarkable, however it is well known that high magnetic fields have orienting effects on amphiphilic bilayers in solution[102,103,104]. In fact, the magnetically induced order is proportional to the square of the applied field strength[105]. However, the viscosity of the complex fluid is also significant, so that for the viscous hexagonal phase in the D_2O - $C_{12}E_6$ system (ϕ_C=0.43 to 0.58) full orientation (θ_{db}=0°, see section 7.1.8) could not always be achieved even at very high field strength (~14.1T)[106], while for the lamellar phase of the same system (ϕ_C=0.63 to 0.82) isoorientation occurred at ~14.1T, partial orientation at ~4.7T and no orientation at ~1.9T.[107] The phases in these studies were created by cooling from the isotropic, micellar L_1 phase. In the light of these results it is not surprising that total orientation occurred in the investigations of this thesis, since very dilute (and accordingly highly fluid) systems were subjected to magnetic flux densities of ~4.7T or ~8.5T (see section 10.4). Even the sample of increased viscosity ($\eta_{D2O/S} = \eta_0 \cdot 2.261$, ~8.5T only) does not show any line shape characteristics of a 3D-powder spectrum (fig. 7.2.4(2)).

Since it has been established that polynuclear nucleation is observed, it is now necessary to determine whether the process is of a *homogeneous* or *heterogeneous* nature. In homogeneous nucleation, a supernucleus (section 6) can be formed anywhere in the supersaturated medium (here the L_3-phase), while in heterogeneous nucleation, these nuclei develop on nucleation-active centres, which in comparison lower the energy of the nucleation barrier[74,75]. These active centres can be ions, impurity molecules, or foreign nanoparticles in the solution bulk, or of course impurities on a macroscopic substrate (the glass of the sample tubes) or even the unevenness of said substrate. Therefore in practice, it is usually difficult to observe homogeneous nucleation exclusively, as this requires very pure media.

For the experiments at hand however, it is not so much of a question whether nucleation in the bulk occurs on active centres or homogeneously, but rather if it occurs in the bulk at all. For it may at first seem plausible, that nucleation takes place predominantly on the glass with the lamellar domain(s) subsequently growing towards the centre. This would result in a single crystal like structure, where the lamellae are parallel to the glass wall (due to the hydrophilicity of the material), thus forming concentric circles in the circular test tubes. Therefore, the orientation of the bilayers with respect to the magnetic field would actually result from interactions with the glass and not the field itself. Since θ_{db}=90°, the NMR signal

of this type of bilayer arrangement would be indistinguishable from the one of a '2D-powder', i.e. a well defined doublet (steady state La phase).

This seeming possibility can be discounted however for several reasons. Firstly it has been shown previously, that nucleation of the lamellar phase from the isotropic L_1 phase in a macroscopic sample tube via cooling outside of a strong magnetic field does result in a mosaic state, i.e. a '3D-powder' (D_2O - $C_{12}E_6$ system)[107]. Furthermore, a study of the H_2O - $C_{12}E_5$ system showed that bulk nucleation of the L_α-phase within the L_3-phase upon temperature quench can only be *prevented*, by combining extreme spatial confinement between two glass plates with slow cooling rates[33]. Thus for a sample of ϕ_C=0.095 a gap of ~100µm (!) is necessary at a cooling rate of 1K/min. For samples of lower concentration even smaller gaps or cooling rates are needed. However, nucleation does occur first on the glass in all cases, and this is surely also true for the experiments of this thesis, especially since upon temperature reduction the thermal energy is removed from the glass first (cooling via air stream).

Finally, an increase of the magnitude of the negative temperature jump causes an increase in the speed of the phase transitions (fig. 7.3.1(21)). However the experiments decoupling the nucleation period from the growth period (section 7.3.4) show that transition speeds are increased considerably even if a minimum temperature (ΔT_{min} = -1.5 or -2.0°C) exists only for a short period of time (<240s), before a temperature is attained, at which transitions usually occur more slowly (ΔT = -1.0°C) (fig. 7.3.4(1)). The higher temperature is present for the vast majority of the overall transition time (>1150s) and represents the 'growth phase' of initially formed nuclei. Even if more nuclei are formed during this growth phase (constant nucleation, see below), the rate of formation will be constant for the six experiments (fig. 7.3.4(2)) within this time. Therefore, the occurrences at the minimum temperature determine the transition speeds decisively. If one excludes the hypothetical possibility of very low nucleation rates coupled with excessively high growth speeds (that is to say standard nucleation and growth behaviour is observed[74], where the amount of nuclei present dominate the rate of transition and not the growth speed of said nuclei), the only conclusion can be that in that first time period an increase in the magnitude of the temperature jump leads to a (considerable) increase in the number of initially formed nuclei, i.e. the nucleation rate *J*. This corresponds well with the concept that a larger *T*-jump is associated with a higher supersaturation $\Delta\mu$ and thus a lowering of the nucleation energy barrier (see section 7.4.5.5).

If however, all these additional nuclei would only form on the glass an increase in transition speed would not be noticeable. Thus with regards to the above explanations, it is

clear that almost exclusively bulk nucleation is observed in the 8mm and 10mm NMR tubes and that in the absence of a magnetic field a '3D-powder' structure would result. As a result, the KJMA nucleation model is in principle applicable as long as the assumptions made in section 6.2 are true.

In section 7.3.1, it was detailed why the method chosen for determining the lamellar phase volume fraction φ (i.e. the integral determining procedure) is deemed necessary and that based on this a KJMA exponent of α=4 is found for slow transitions (τ>1000s). This implies, that nuclei grow in three dimensions and that nucleation occurs continuously throughout the transition process (long nucleation period) in these cases (n=3, ψ=1, eq. 6.2(1b)). For jumps of greater magnitude and accordingly faster transition times, it was found however that, towards completion of the transitions, α is reduced in value to three or even below (fig. 7.3.1(16)).

There are two possible explanations for this within the KJMA model. Either nucleation remains to be continuous but nuclei growth only proceeds in two dimensions (n=2, ψ=1), or there is suspension of continuous nucleation and growth remains three dimensional (n=3, ψ=0). The discussions below will show that the latter case appears to be the more probable cause, based on both experimental evidence and theoretical considerations. However it must be kept in mind that the KJMA model greatly simplifies physical reality (both the nucleation rate and the growth rate must be constant throughout a transition and growth speed must be independent of direction, i.e. spherical growth is postulated to occur even though the 'crystallites' are anisotropic in nature) so that a n=2, ψ=1 situation cannot be ruled out nor that a moderate combination of the two possibilities takes place. In fact, since for a fast transition a greater number density of nuclei is expected (see above), the volume where the different nuclei of the '2D-powder' come into contact is forced to accommodate a greater number of different bilayer orientations. Due to the need of having continuous bilayers in the final steady state (i.e. no exposed edges), it is likely that this disorder could slow down a transition process. Despite all these considerations however, the fact remains that the KJMA model generally describes the φ development well.

7.4.5.2 Quadrupolar Splitting of the Steady State Lamellar Phase

In section 7.3.1 the quadrupolar splitting $\Delta\nu_Q$ is clearly correlated with the bilayer volume fraction ϕ_{B+C} via eq. 7.3.1(3).

$$\Delta\nu_Q = n \cdot \omega_b \cdot \frac{\phi_{B+C}}{1-\phi_{B+C}} \cdot \frac{\rho_C \cdot M_A}{\rho_A \cdot M_C} \cdot \frac{3}{4}\chi \cdot \left|S_{qn}\right| \qquad \text{eq. 7.3.1(3)}$$

and the direct proportionality of $\Delta\nu_Q$ to the ϕ_{B+C} term for lamellar phases in equilibrium was demonstrated for samples of 'standard' composition, i.e. those where the water phase does not contain any sucrose, in fig. 7.3.1(28). From eq. 7.3.1(3) the constant $n \cdot S_{qn}$ can be calculated for each sample using χ=255kHz[95] and its average value corresponds to ~0.056. This value matches well with those of several D_2O surfactant/co-surfactant mixtures studied by *Persson* and *Lindman*, where $0.04<n \cdot S_{qn}<0.12$ for lamellar phases[90]. Also, if the number of MAPA D_2O molecules per molecule of surfactant is known, then the order parameter S_{qn} and a theoretical, maximum quadrupolar splitting ($\Delta\nu_Q$(max)) can be calculated. $\Delta\nu_Q$(max) is the value that would be detected if a sample consisted only of MAPA D_2O. With n=5.75[93], the average values of the samples studied correspond to $\Delta\nu_Q$(max)=1860Hz and S_{qn}=0.0097. $\Delta\nu_Q$ values of 1900-2350Hz were detected previously for highly concentrated lamellar phases of the D_2O – $C_{12}E_5$ system[93]. The results obtained for the individual samples here are given in tabular form in tab. T15.

Fig. 7.3.1(28). shows, that for the sample of increased viscosity ($\eta_{D2O/S} = \eta_0 \cdot 2.261$) a notably higher $\Delta\nu_Q$-value (2.2Hz deviation from the linear regression) is detected, than one would expect according to its ϕ_{B+C} = 0.06 composition. The cause of this increase is probably directly linked to the addition of sucrose. Sucrose has eight hydroxyl protons which will be exchanged with deuterons upon sample preparation similar to the hydroxyl proton of the surfactant (see section 7.2.2). Thus the sucrose molecules, which are present at a mole fraction of x=0.0172 (with respect to D_2O only), represent another site of a particular quadrupolar splitting $\Delta\nu_{Q,i}$. As there is fast exchange of the deuterons between all the sites, this splitting must be incorporated in eq. 7.2.2(1). The order parameter and accordingly $\Delta\nu_{Q,i}$ of the large sucrose molecule will however be significantly greater than for a D_2O molecule, as its rotational motion is slower and its averaging of θ_{db} therefore less efficient. Thus the detected splitting is expected to increase according to the statistical weight of the sucrose molecules. Since the difference in absolute temperature to a standard sample is relatively small (-8.4°C see fig. 2.3(2)) the rotational motion of the D_2O molecules is hardly reduced and $\Delta\nu_Q$ therefore not affected. Similarly, the increase of macroscopic viscosity itself is irrelevant.

7.4.5.3 Significances of the Quadrupolar Splitting Development

In section 7.3.1.5 it was demonstrated that $\Delta\nu_Q$ experiences an exponential decay with time, but is most likely to be of sigmoidal shape. Thus a key result of the sponge to lamellar phase transitions is the fact that the bilayer volume fraction ϕ_{B+C} of at least the initial nuclei is significantly greater than the equilibrium concentration. Since ϕ_{B+C} is a conserved parameter however, the average ϕ_{B+C}-value for the lamellar 'crystallites' has to approach the equilibrium concentration, as a transition nears completion. This poses the question whether nuclei that *appear* close to completion (continuous nucleation case, ψ=1) are of higher bilayer volume fraction or not. If they are, then this would result in a wider lamellar peak at that point in time, as a superposition of different lamellar doublets of different $\Delta\nu_Q$ would be witnessed. In fact, the peaks would be more intense on their *outside*, i.e. the side opposite from the L_3-singlet, since doublets of increased $\Delta\nu_Q$ are added. Fig. 7.4.5(1) gives a detailed view of the 2D-depiction of the evolution of a lamellar peak (akin to fig. 7.2.6(2)) for the $\phi_{B+C} = 0.06$ sample experiencing a negative temperature jump of ΔT=-1.1 (*left*) and ΔT=-1.5 (*right*).

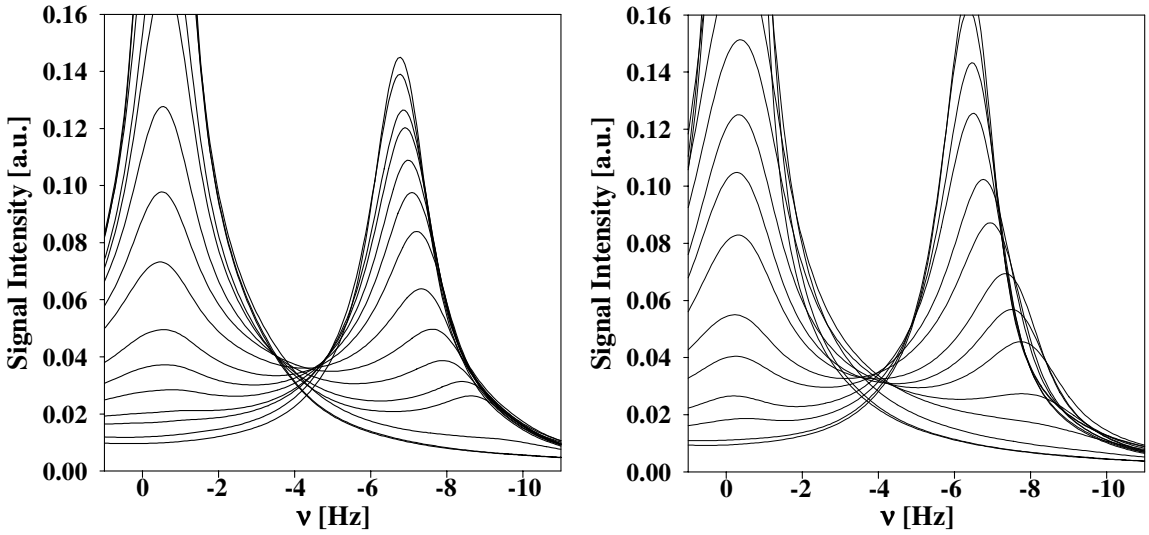

Fig. 7.4.5(1): detail of the L_α-peak evolution for an experiment exhibiting continuous nucleation (FT_16, *left*) and for one where nucleation is suspended towards completion of the transition (FT_24, *right*). ϕ_{B+C}=0.06, ΔT = -1.1°C and –1.5°C respectively

The φ-development of the ΔT=-1.1°C jump (*left*) shows the typical behaviour of a slow transition, i.e. α=4 and thus continuous nucleation occurs (FT_16, fig 7.3.1(10)). On the other hand the ΔT=-1.5°C jump (*right*) clearly develops with α=3 towards the end of the transition (FT_24, fig 7.3.1(14, *right*)) and so it can be assumed that continuous nucleation is suspended at least in that time increment. Thus the lamellar peaks at that time are expected to

be more defined, i.e. be of less intensity on their outside. This is exactly what fig. 7.4.5(1) shows and hence this is direct experimental evidence that continuous nucleation does occur in slow transitions, while it is suspended (towards completion) in the fast ones, *and* that nuclei are as a matter of principle formed at higher bilayer concentrations regardless of the progress of a transition.

The different developments of fig. 7.4.5(1) are no coincidence and all the more significant as the splitting declines more slowly for experiment FT_24 than for FT_16 (τ_s/τ = 0.19 and 0.31, respectively). Furthermore, the outside of lamellar peaks of slow (α=4) transition generally show good overlap (see section 7.2.6.2 fig. (3), (5), (7), (8), (11)), while fast transitions (α=3, towards termination) show stepping. ((6) and (10)). The mentioned figures include all the experiments which have both their 2D peak evolution and their φ-development plotted. The extreme stepping in case of FT_75 (fig. 7.2.6(6)) is of course nicely visible due to magnification because of the unusually wide primary splittings.

The Effects of Initial Nuclei Orientation on Lineshape

A further factor which influences peak shape and thus the appearance of peak evolution is a distribution of the θ_{db} angles. Up to this point it was shown that θ_{db}=90°. Yet, this is only true for the steady state lamellar phase and even then there is of course a slight distribution of angles present. However, when the lamellar phase nucleates the orientation of a given nucleus will at first be random (if the possibility of the magnetic field strongly influencing the actual nucleation process is ruled out). Thus there will be a superposition of doublets again (see above), but this time the splitting will generally be smaller than in the θ_{db}=90° case and accordingly the peaks will be more intense on their *inside*. (The 90° orientation represents a (local) maximum in eq. 7.2.1(4) and most orientations lead to smaller values, see fig. 7.1.8(1). Additionally, those orientations that lead to a larger splitting are centred on θ_{db}=0° and crystallites of this sort will be turned towards the equilibrium orientation most strongly.)

In fig. 7.4.5(1) it can be seen that the first lamellar peaks are drawn-out on their inside and that this progressively decreases with time (one must imagine the peaks to be of equal intensity). Of course one does not see the pure lamellar peak but a superposition with the L_3-singlet and its contribution must be subtracted, the effect is however there nevertheless (best visible in the *right* figure, where no superposition from new nuclei appear towards the end). The two types of superpositioning in fact may well account for the lamellar peak width

to initially appear large and then decreases with progress of the transition (section 7.3.1.6). Potential further causes will be discussed below when the development of $\Delta\nu_{1/2}$ is analysed. One might assume that the afore mentioned deviations between spectra simulation and data (section 7.4.4) in fig. 7.3.1(7) 70a to 100a stem from the spread of θ_{db}. However, the deviations persist up to an advanced point in time and are found in the vicinity of the isosbestic points and these are found at quite a distance from the lamellar peaks. Nevertheless the spread of θ_{db} possibility cannot be discounted.

It seems reasonable to assume that in case of higher nucleation rates (coupled with faster transitions) the lamellar phase at the end of a transition would be more disordered, i.e. consist of a larger distribution in θ_{db}, than in case of a low rate. One would intuitively suspect the same in case of experiments where the viscosity was increased. However, comparison of steady state spectra shows no increase of intensity on the inside of the peaks for the potentially more disordered states (data not shown). In fact, in no case are there particular deviations from the fit using two Lorentzians on the inside of the peaks. On the other hand, if data is collected far past the point in time, where the equilibrium state is deemed to have been attained (+30min), the lamellar peaks do continue to sharpen ever so slightly and this is most likely associated with the annihilation of defects and a development towards a single crystal like state. A reduction of the distribution in inter lamellar spacing could of course also contribute to this peak sharpening (especially in the case of continuous nucleation), although this should happen rather quickly through the diffusion of D_2O.

Splitting Development: Comparisons at Varying Amplitude of the T-Jump

Figure 7.4.5(2) depicts a trend in the development of the quadrupolar splitting not discussed previously.

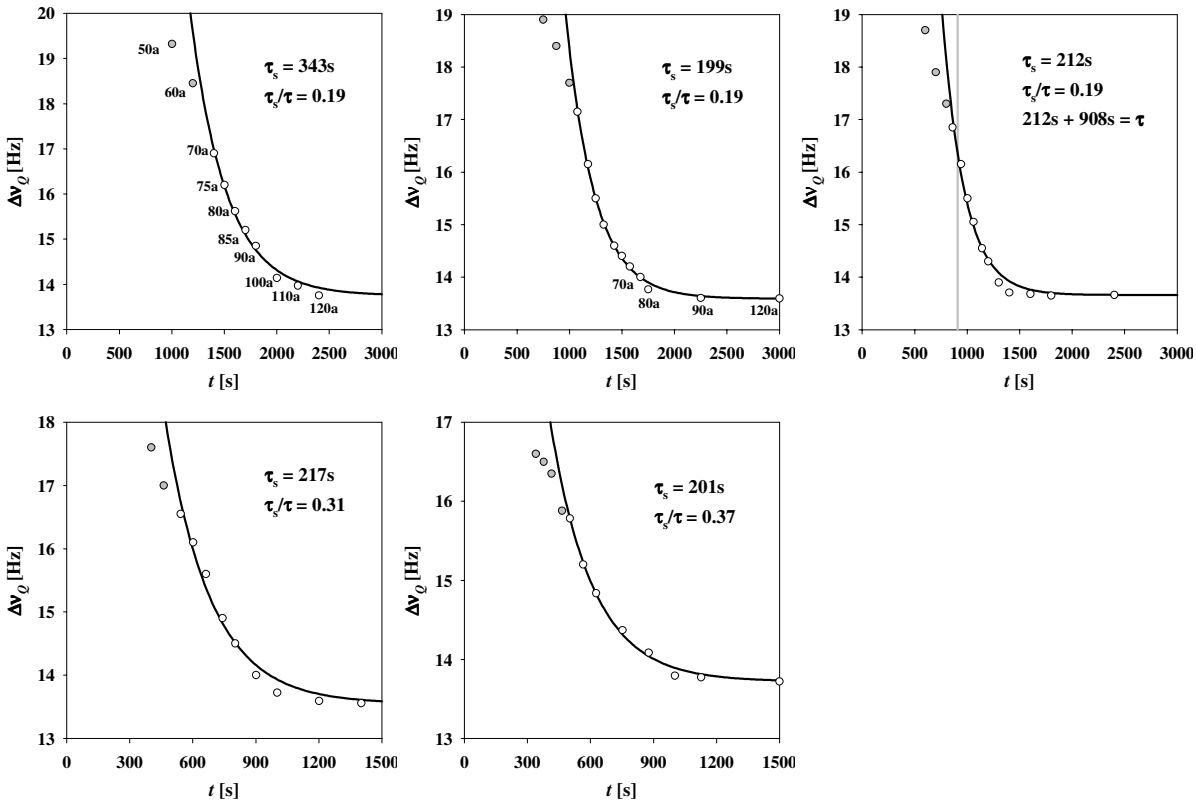

Fig. 7.4.5(2): development of the quadrupolar splitting for $\phi_{B+C} = 0.06$ as function of the magnitude of the temperature jump. Top left to bottom right: FT_32 ΔT=–1.0°C, FT_16 ΔT=-1.1°C, FT_20 ΔT=–1.3°C, FT_24 ΔT=–1.5°C, FT_04 ΔT=–1.7°C

From fig. 7.4.5(1) it is clear that the splitting for the steady state lamellar phase is roughly constant for the experiments with the $\phi_{B+C} = 0.06$ sample presented here. (Note the varying time and splitting scales). Note also that the 'onset time', here the time until the first lamellar peaks are seen, decreases steadily with increase in absolute ΔT as previously reported. What is striking however, is that the difference between value of the splitting when lamellar peaks are first noted and the steady state value decreases continuously with the magnitude of the *T*-jump. This trend continuous for experiment FT_06 (ΔT=-2.0°C), in which case the doublet seems to rise at almost constant splitting (no detailed evaluation was performed for the experiment, so note fig. 7.2.6(12, *left*). This is a possible indication that at the beginning of a transition there is indeed a great distribution of crystallite orientations as previously suspected (see above). For fast transitions φ rises quickly and so lamellar peaks are detected at a time when the distribution of θ_{db} is still great and the splitting therefore somewhat smaller.

There exists however another, perhaps more intriguing, explanation for the identified phenomenon. It seems clear that the initial high concentration of bilayer in the nuclei must result from D_2O diffusing out of the formation area (while possibly a little bilayer volume

actually diffuses towards it). The question that arises is of course, why supernuclei form at this concentration in the first place. Although it cannot be shown directly via Classical Nucleation Theory (see section 7.4.5.5 below) that the nucleation barrier of a more concentrated nucleus is reduced, reflections in view of the passage destruction mechanism clarify that nucleation should be facilitated in this case (see below). If this is indeed the case, then nucleation occurring at a *lower* value of ϕ_{B+C} must coincide with a greater supersaturation $\Delta\mu$, since the transitions at larger ΔT occur faster, i.e. the nucleation rate J is increased. In other words, the subnuclei of a lamellar phase 'crystallite' depend less on the diffusion of D_2O to lower the bilayer concentration in the area of their expansion, when a large T-jump is conducted. Thus fig. 7.4.5(2) could display direct experimental evidence of increasing supersaturation with increase of the magnitude of the temperature jump ΔT. A detailed description of the interaction of the parameters ϕ_{B+C}, ΔT and $\Delta\mu$ will be presented below (section 7.4.5.5), on the basis of CNT.

Diffusion and the Dilution Effect

It was just mentioned that the formation of young supernuclei is facilitated at higher bilayer volume fraction. This explains why nuclei are detected at increased ϕ_{B+C}, but not what actually causes this increase of concentration. The phenomenon is connected with the properties of the metastable sponge phase surroundings. If temperature would be reduced only far enough to reach the two phase region (fig. 7.4.5(3)), then in equilibrium the lamellar phase bilayer volume fraction would be higher than the average composition $\phi_\alpha' > \phi_0$ and the sponge phase of a lower ($\phi_3' < \phi_0$). The composition of each of the phases is given by the respective phase boundaries at the temperature in question as indicated, while the amount of substance of each phase is determined by the Lever law of phase diagrams[83]. (This is true only in first approximation, since a three component system is present, and therefore is based on the assumption that ω_b remains constant in both phases.)

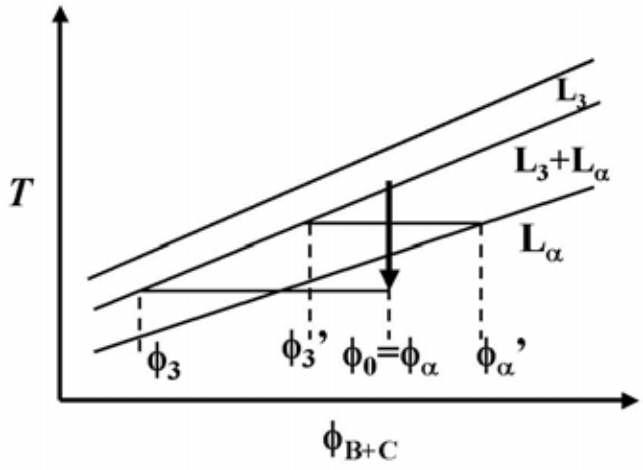

Fig. 7.4.5(3): schematic phase diagram, illustrating the equilibrium bilayer concentration of coexisting phases (ϕ_3',ϕ_α'). In case of a jump leading directly into the one phase L_α-region (arrow) the equilibrium concentration of the lamellar phase will correspond to ϕ_0. Before equilibrium is reached the L_3 phase will strive towards ϕ_3.

With the *T*-jump however resulting in an equilibrium condition, at which only the lamellar phase exists, it seems likely that the sponge phase (during non-equilibrium) strives towards a bilayer volume fraction at which it would be stable at said temperature, i.e. $\phi_3 << \phi_0$. Thus there results an 'osmotic pressure' which transports D_2O away from the emerging L_α domains and possibly some bilayer volume towards them. On the other hand, there should be no resistance from the lamellar phase against reducing its water content or receiving bilayer volume, since at the given temperature L_α is stable up to the highest of concentrations (see phase diagrams Section 2). However, as the phase transition draws towards completion it is clear that the bilayer concentration of the L_α-phase must approach the overall concentration, i.e $\phi_\alpha \rightarrow \phi_0$. From this concept it becomes apparent that the speed of a phase transition process might increase with increasing magnitude of ΔT, due to an increase of said 'osmotic pressure' (since lower temperatures require a more dilute L_3-phase, fig. 7.4.5(3)), which in turn aids in nuclei attaining higher concentrations. This is in accordance with the experimental results (section 7.3). Also, the transport of D_2O and bilayer volume will occur via diffusion and it is therefore probable that this process can become a limiting factor regarding the phase transition speed. And indeed, with increase of viscosity, the experiments show a strong decrease of said speed (fig. 7.3.1(19)).

Since a growing nucleus gains its increased bilayer volume through expelling D_2O, the sponge phase in its vicinity will experience dilution (this phenomena will be referred to as the dilution effect). This in turn is identical to an increase in the bilayer distance d_3 in that area and section 7.4.5.5 (below) will demonstrate that this condition inhibits nucleation. This is a final argument for bulk nucleation, since nuclei will only appear at a given distance from each

other. More importantly though, it provides an impressive explanation for the experimental results of the φ–development attained for large ΔT. Fig. 7.4.5(1) demonstrated that suspension of continuous nucleation is a likely cause for an α=3 KJMA exponent towards the conclusion of fast phase transitions. Fast transitions are however equivalent with a large nucleation rate, i.e. many nuclei expel their D_2O into the surrounding medium. Thus at an advanced point, dilution in the sponge phase will have increased to such an extend that further nucleation is not possible. In experiments with a slower nucleation rate continuous nucleation is not suspended, since the surface area of the (fewer and larger) nuclei is smaller and with it the overall volume of the 'dilution zones' surrounding them. Also, it is possible that older nuclei strive towards the equilibrium bilayer concentration.

From the just stated explanations, one might assume that the decrease in the difference of initial and final quadrupolar splitting with increase of the magnitude of ΔT (fig. 7.4.5(2)) is not a result of increased supersaturation, but rather stems from many nuclei diluting the sponge phase, so that an individual nucleus is not able to attain such high concentration. This view on the matter can however be discounted, since at the time of the initial splitting φ still increases steeply, i.e. further nucleation occurs (in the bulk). In other words, the areas of diluted sponge phase surrounding the nuclei do not overlap at this time (of course a dilution zone is not static around a nucleus but will grow in extension over time while decreasing in intensity) and accordingly the nuclei should be able to increase in bilayer concentration similar to those formed for small *T*-jumps. It is however likely, that also the growth speeds of nuclei increase in case of a large *T*-jump. This could result in diffusion simply not being able to extract water fast enough from a speedily growing supernucleus, leading to a smaller initial splitting. This view however seems to be equivalent with the hypothesis of increased supersaturation, since the nuclei simply do not require high bilayer concentrations to grow quickly.

From the phase behaviour however (fig. 7.4.5(3)) one would at first glance expect larger *T*-jumps to result in an increased initial splitting, since the sponge phase is then stable at lower concentrations. Then again, the L_3-phase cannot be diluted *ad infinitum* and most likely disintegrates well before the critical micellar concentration. To the knowledge of the author, the L_3-phase of the system at hand has in fact not been found below $\phi_{B+C} = 0.04$ (see section 2.2). Since the measurements of fig. 7.4.5(2) were performed on the already very dilute $\phi_{B+C} = 0.06$ sample, it is well possible that the *T*-jumps led to conditions, where the sponge phase is not stable at *any* concentration and dilution advanced towards the same maximum in all five experiments. This in turn would indicate though, that the above

mentioned increase of 'osmotic pressure' with increasing magnitude of ΔT would not apply in the $\phi_{B+C} = 0.06$ case. The concept should hold however for higher concentrations.

As it is the diffusion and tumbling of the D_2O probe molecule which leads to information in the NMR experiments, the observation of a quadrupolar splitting allows one to estimate a minimum lateral extension of the bilayers in the emerging lamellar domains. The fact that one obtains separate signals from the sponge and lamellar domains implies that the lifetime τ_1 of D_2O molecules within the lamellar domains is greater than the inverse of the quadrupolar splitting, e.g. 19.4 Hz (FT_32, fig. 7.4.5(2)). While the bilayers represent a barrier for the diffusion of the water molecules, water is essentially free to diffuse parallel to the bilayers, with a two dimensional mean-square displacement given by

$$\left\langle r^2 \right\rangle = 4Dt \qquad \text{eq. 7.4.5(1)}$$

where D is the diffusion coefficient and t is the time. With $t = \tau_1 \approx 1/(2\pi 19.4)$s and assuming free two-dimensional diffusion of water with $D \approx 2\ 10^{-9} m^2 s^{-1}$, one obtains with eq. 7.4.5(1) a root mean square displacement of ~8µm. Thus, when one observe a quadrupolar splitting after ~1000s, it comes from lamellar domains where the bilayers are larger than approx. 8.1µm. This value is about 40 times the structural length scale of the equilibrium sponge-like structure of the L_3-phase d_3, which at $\phi_{B+C} = 0.06$ was determined by SANS measurements to be d_3=0.185µm (see tab. T18). Even the domains of a lamellar phase with an initial splitting of 13.6Hz (the equilibrium splitting value for $\phi_{B+C} = 0.06$ *and* the initial splitting of a $\phi_{B+C} = 0.05$, ΔT=-1.5 experiment see fig. 7.4.5(4) below) would be of comparative size (9.6µm), while the extreme value of ~33Hz detected for the $\phi_{B+C} = 0.08$ sample (FT_75) corresponds to an expansion of 6.2µm.

Splitting Development: Comparisons at Varying Concentration

In the previous paragraph the initial size of crystallites of bilayer volume fractions other than $\phi_{B+C} = 0.06$ were estimated and so it is only consequential to look at the decline of the quadrupolar splitting as function of system composition (fig. 7.4.5(4)).

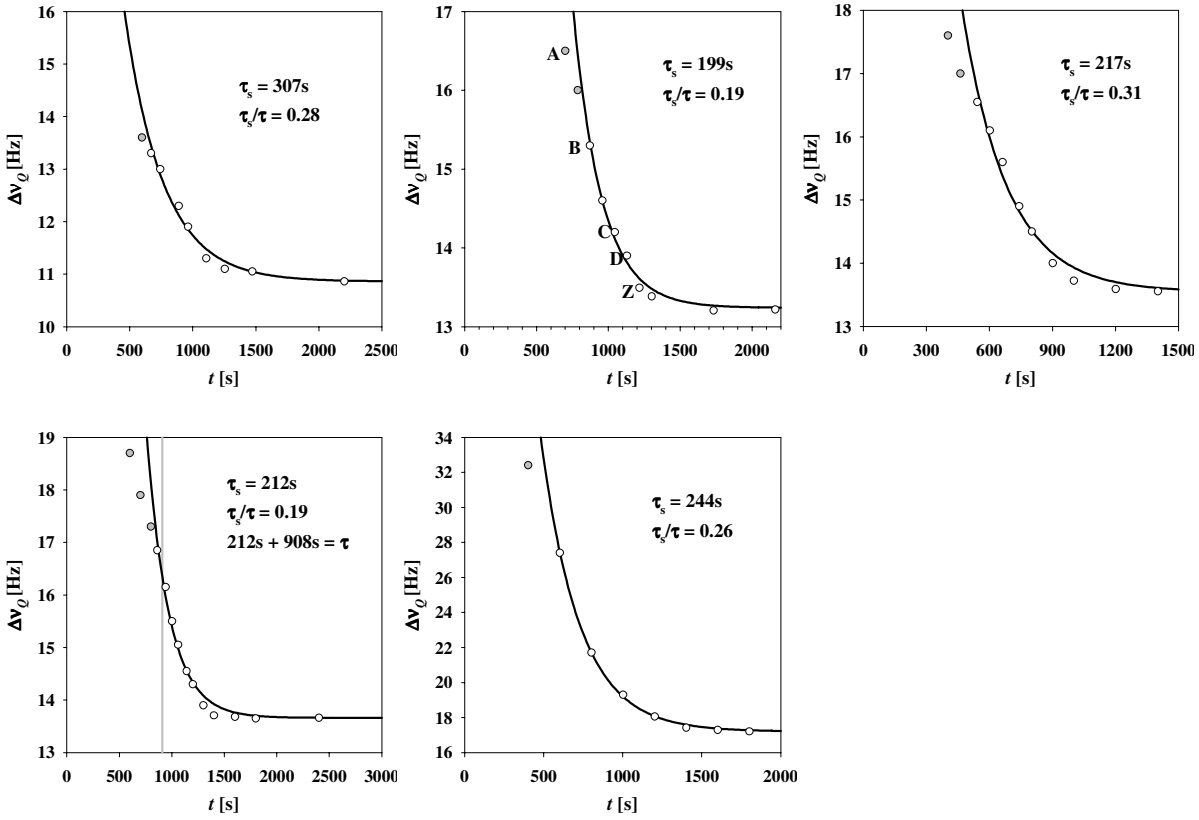

Fig. 7.4.5(4): development of the quadrupolar splitting as function of ϕ_{B+C} for a constant magnitude of the temperature jump. Top left to bottom right: ϕ_{B+C}=0.05, ΔT=–1.5°C (DMX-200); ϕ_{B+C}=0.06, ΔT=–1.5°C (DMX-200); FT_24 ϕ_{B+C}=0.06, ΔT=–1.5°C (Varian 360); FT_20 ϕ_{B+C}=0.06 ΔT= -1.3°C (Varian 360), FT_75 ϕ_{B+C}=0.08, ΔT=–1.3°C, (Varian 360).

In the top row temperature jumps of ΔT=-1.5°C are depicted (left to right: ϕ_{B+C}=0.05, 0.06 (DMX-200 spectrometer) and 0.06(Varian 360 spectrometer)). One sees that the difference between the initial splitting and the steady state splitting is smaller for the ϕ_{B+C}=0.05 case and this is also true for established experiments performed at that bilayer volume fraction (Varian 360 spectrometer, data not shown). In the bottom row ΔT=–1.3°C and a ϕ_{B+C}=0.06 (left) and 0.08 experiment are compared. Again it is clear that the less concentrated sample exhibits a smaller difference between the initial and final splitting and so this trend appears to hold over the entire concentration range studied. (The ϕ_{B+C}=0.07 sample was not included as ΔT=-1.0°C on DMX-200 only.) From fig. 7.4.5(2) one might believe that the τ_s/τ ratio is correlated with the difference in initial and final splitting, however fig. 7.4.5(4) shows that this is not the case.

The trend depicted in fig 7.4.5(4) can perhaps be interpreted in the light of the phase behaviour (fig. 7.4.5(3)) and the phase behaviour discussion (section 7.4.5.3) with regard to fig. 7.4.5(2): A constant ΔT at different ϕ_{B+C} leads to different absolute temperatures of the attained lamellar phase. The jump of ΔT=-1.5 of the ϕ_{B+C}=0.05 sample results in the lowest temperature of the experiments of fig. 7.4.5(4) (~35.4°C, see fig. 2.3(1)), while the ΔT=-1.3

jump of ϕ_{B+C}=0.08 leads to ~36.2°C. It is not known if the sponge phase is stable at either of those temperatures, however if a maximum dilution is attained in both cases, the difference between the overall sample concentration and that dilution will of course be greater for the ϕ_{B+C}=0.08 sample. Thus the sponge phase around nuclei in the ϕ_{B+C}=0.08 sample will be able to dilute comparatively more than the one in the ϕ_{B+C}=0.05 case. This could explain the unusually high initially splitting of experiment FT_75.

7.4.5.4 Development of Peak Width

The width of an NMR peak $\Delta\nu_{1/2}$ is determined by three factors:

- by Zeeman and quadrupolar relaxation (see section 7.1.4 and 7.1.8, respectively)
- by inhomogeneity broadening (see section 7.1.5)
- by superposition of multiple signals at different frequencies

Section 7.3.1.6 shows that the width of the L_3-peak increases during the course of a transition, while the width of the L_α-peaks decreases. This occurs in an exponential manner and quite likely even sigmoidally (fig. 7.3.1(29).- (31) analysis). From the discussions in this chapter it is clear that the 3rd point occurs for lamellar peaks from a distribution of the 'crystallite' directors θ_{db} (as in a 3D-powder), especially in the early stages of a transition, and also from a distribution of the ϕ_{B+C}-values in newly created and older nuclei. In section '*the effects of initial nuclei orientation on lineshape*' it was stated that the two types of superpositioning may well account for the observed width development and that peak sharpening at the end of a transition most likely results from the reduction of defects. From the theory of magnetic relaxation (section 7.1.5) it also seems likely that relaxation is stronger (smaller values of T_2) in more confined spaces, i.e. where molecular motion is more anisotropic, so that in case of higher ϕ_{B+C} wider peaks are expected for lamellar phases. All these points give an explanation for the extremely wide lamellar peaks detected initially in experiment FT_75 (ϕ_{B+C}=0.08, see section 7.2.6.2). Likewise, higher viscosity increases relaxation so that the wide peaks of experiment FT_78 ($\eta_{D2O/S}=\eta_0 \cdot 2.261$, see section 7.2.6.2) are no surprise.

The widening of the L_3-peak is more difficult to explain. No differences are apparent in its development with varying ϕ_{B+C} or ΔT, except that in the case of very fast transitions, i.e. very high ΔT (approx. ≤ -2.0°C), the L_3-singlet actually splits into a doublet (fig. 7.2.6(12)) and that this splitting is more pronounced in the ΔT=-3.9°C case than the ΔT=-2.0°C case.

With progression of the transition the sponge phase will presumably become more dilute (section 7.4.5.3) and associated with this is directional diffusion of D_2O. It seems possible that this movement in the confinement of a complex fluid could lead to an increase in magnetic relaxation. Also, there will be increasing bilayer rearrangement, which could also effect the average of D_2O tumbling.

The described splitting of the L_3-singlet could actually result from the remnant, dilute L_3-phase between the lamellar 'crystallites' (which in case of faster transitions has a larger volume fraction) being transformed into a dilute L_α-phase or at least an L_α like state, where a significant amount of passages is still present (akin to what is found for the L_α to L_3 transitions see section 7.4.6). That is to say, in the cases of very large *T*-jumps, supersaturation could be so high that nucleation in the dilute region is *not* suspended after all. The splitting of the 'L_3-peak' becomes larger for the ΔT=-3.9°C jump than for the ΔT=-2.0°C jump simply because the volume fraction of dilute region is larger and can thus be monitored longer in comparison (the NMR signal intensity is proportional to said fraction). One actually sees D_2O diffusion equating the ϕ_{B+C} values of the initially formed concentrated nuclei and later formed dilute nuclei (fig. 7.2.6(12)).

7.4.5.5 The L_3 to L_α Phase Transition Kinetics

In section 7.3.1.2 it was shown at length why the spectra fitting/simulation procedure used was chosen and how the relaxation time constants τ were determined for various experiments. It must be stressed again that there is great confidence in the determined τ-values, as they proved to be independent of the integral determining procedure and the general shape of the φ-development. It was found that the τ-values decay strongly with increased magnitude of the temperature jump and that this decay can be described by a power law. Also, the dependence on ΔT is greater for the $\phi_{B+C} = 0.05$ sample than for $\phi_{B+C} = 0.06$. This lead to the speculation of $1/\tau$ being dependant on ϕ_{B+C} less strongly in case of large ΔT (fig. 7.3.1(21, *right*)). For the sample of increased viscosity very slow phase transitions were monitored, but τ still developed with ΔT according to a power law.

The τ-times of the $\phi_{B+C} = 0.05$ and 0.06 experiments develop towards similar values at high ΔT (fig. fig. 7.3.1(21, *left*)). Of course, the kinetics of cooling begin to influence the determined τ-values for fast transition kinetics, however even the fastest transition plotted (FT_06, $\phi_{B+C} = 0.06$, ΔT=-2.0) required ~500s to completion with τ~335s while sample

cooling requires ~200s (fig. 7.2.6(1)). Thus it appears likely, that the φ-development for fast transitions akin to an exponential rise instead of a sigmoidal one (fig. 7.3.1(15)) results from the cooling kinetics somewhat impeding the formation of lamellar phase at low *t*. Thus the initial φ rise is very strong instead of gradual as for sigmoidal development. However, the τ times will hardly be overestimated for transitions up to ΔT=-2.0°C.

The Kinetics in the Light of the CNT

The decrease in relaxation time constants with an increase of the driving force ΔT has been linked to an increase in nucleation. With that, it is implied that the absolute number of nuclei present dominate the speed of phase transition, and not their growth rate (section 7.4.5.1). In classical nucleation theory (CNT) the nucleation rate *J* is expressed via a *Boltzmann* approach to

$$J = K_J \exp\left(\frac{-\Delta G^*}{k_B T}\right) \qquad \text{eq. 7.4.5(2)}$$

With the assumption that the kinetic prefactor K_J (which is associated with the diffusion of material to a growing nucleus) is roughly constant, an increase in the nucleation rate *J* occurs for a reduction of the nucleation energy barrier ΔG^* (variations in the absolute temperature *T* can be neglected, as only small *T*-jumps are performed). Thus it is of interest to examine how ΔG^* might be influenced by changes of ΔT.

In the nucleation of gaseous particles to spherical clusters of *n* particles of radius r_n, the difference in Gibbs free enthalpy ΔG is a function of *n* (and thus r_n) and ΔG^* its maximum.

$$\Delta G = n \cdot \Delta\mu + 4\pi r_n^2 \sigma \qquad \text{eq. 7.4.5(3)}$$

where $\Delta\mu$ is the difference in chemical potential between a particle in equilibrium in the new state and a particle in equilibrium in the old state ($\Delta\mu = \mu_{new} - \mu_{old} < 0$) and σ is the surface energy of the cluster ($\sigma > 0$). For the following considerations, the validity of eq. 7.4.5(2) and 7.4.5(3) is assumed, even though the physical realities of the complex fluid phases at hand and the simple model of cluster formation from the gas phase are of course vastly different.

Although it is not apparent from the simple model of eq. 3.2(1) (the *average* bending energy E of any lamellar phase is zero), it seems reasonable to assume that for a given concentration ϕ_{B+C} the difference in Gibbs free enthalpy per unit volume (or rather the area of bilayer A therein and thus a unit area) between the equilibrium L_3 phase and an equilibrium L_α phase at lower temperature is larger than if an L_α-phase at higher temperature is considered, i.e. that the magnitude of the supersaturation $\Delta\mu$ increases upon increasing ΔT (Note that since no expansion work is performed during the transitions, E can be equated with an enthalpy and thus $\Delta G = \Delta E - T\Delta S$, where S is the entropy. For the transition at hand $\Delta S < 0$, as a transformation to a more ordered state is observed.). Since the surface energy between a lamellar and a sponge domain can be estimated to $\sigma \approx \kappa / d_\alpha^2$ [70] and the bending rigidity modulus $\kappa_{bi}=2\kappa_{mono}=$ const. (see above) and d_α=const. for an equilibrium lamellar phase of different T (at ϕ_{B+C}=const.), $4\pi r_n^2\sigma =$ const. for different temperature jumps. Thus, it seems likely that the course of ΔG develops with increasing supersaturation $\Delta\mu$ (in first approximation) classically as in fig. 7.4.5(5), i.e. that the nucleation barrier and the critical cluster size decrease. Therefore, it is probable that greater nucleation rates at greater ΔT are indeed the cause of the speeded L_3 to L_α phase transitions.

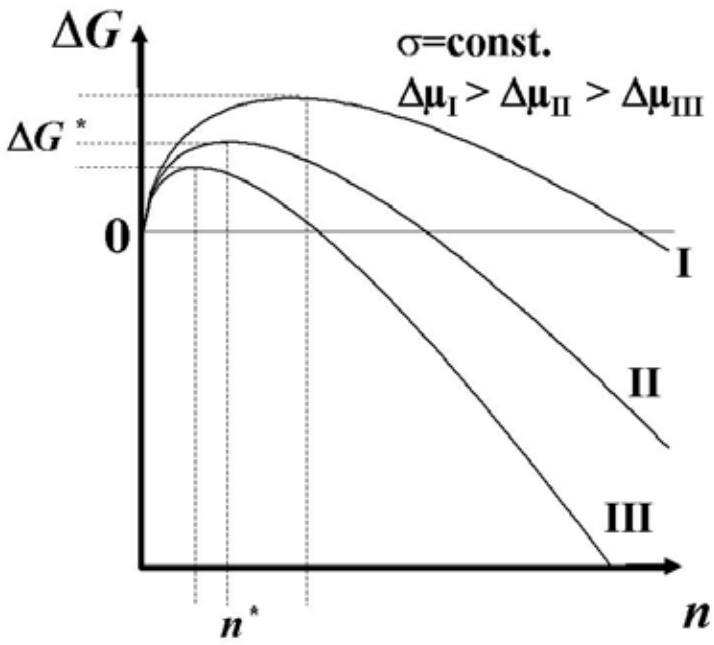

Fig. 7.4.5(5): development of ΔG as a function of particle number n at constant surface energy σ, but varying differences in the chemical potential $\Delta\mu$ of the initial and final system state. For a more negative $\Delta\mu$, the nucleation energy barrier ΔG^* is reduced as is the size of the critical cluster n^* (I to III).

Of course it has been shown experimentally that, when nuclei are initially formed, the bilayer concentration is higher than the equilibrium concentration and accordingly d_α is smaller and σ actually higher. However, the following considerations will show that the formation of a given volume of lamellar phase at higher concentration should release more Gibbs free energy than the formation of one at lower concentration, even though surface tension is higher in the former case. The line of reasoning presented relies on equating a unit area of bilayer surface, of chemical potential μ, to the particle number n of eq. 7.4.5(3).

The scaling invariance (section 3.2) of the L_3 structure applies for the L_α structure as well (for a constant separation ΔT from the L_3-phase), so that the bending energy E per *scaled* unit area is constant for each respective phase, regardless of bilayer concentration ϕ_{B+C}. However, the *bending energy per unit area* is less in the dilute case ($E(\lambda) = E(1)/\lambda^2$, where λ corresponds to the factor of elongation, see section 3.2). Thus if the bending energy is equated with the Gibbs free energy for purposes of estimating trends in the chemical potential of a unit area, then $\mu \propto \phi_{B+C}^2$ since $1/\lambda \propto \phi_{B+C}$ for dilute systems ($\phi_{B+C} << 1$). (This approach assumes that the entropy per unit area of both the L_3 and L_α structure also scale with the square of the concentration, i.e. $S_3 \propto \phi_{B+C}^2$ and $S_\alpha \propto \phi_{B+C}^2$.) In addition, the total area of bilayer A decreases upon dilution ($A \propto \phi_{B+C} \propto 1/\lambda$) so that $n \propto \phi_{B+C}$ and $E \propto \phi_{B+C}^3$.

On the other hand, the surface energy is estimated to $\sigma \approx \kappa/d_\alpha^2$ and since for the inter-lamellar distance $d_\alpha \propto 1/\phi_{B+C}$, $\sigma \propto \phi_{B+C}^2$ results. Judging from these estimates, eq. 7.4.5(3) can be rewritten in the form

$$\Delta G = -A_{in} \cdot \left(f_\mu \cdot \phi_{B+C}\right)^2 + A_s \cdot \left(f_\sigma \cdot \phi_{B+C}\right)^2 \qquad \text{eq. 7.4.5(4)}$$

where f_μ and f_σ are prefactors of the difference in chemical potential per unit area and the surface energy respectively, A_s is the surface area of a lamellar nucleus and A_{in} its internal area, i.e. the area of the lamellar phase it contains. Both CNT and the KJMA model assume spherical nuclei and the same will be done for this discussion. Thus, A_s is easily calculated via

$$A_s = 4\pi r_s^2 \qquad \text{eq. 7.4.5(5)}$$

where r_s is the sphere's radius. A_{in} can be determined when assuming a model nucleus build-up (fig. 7.4.5(6)).

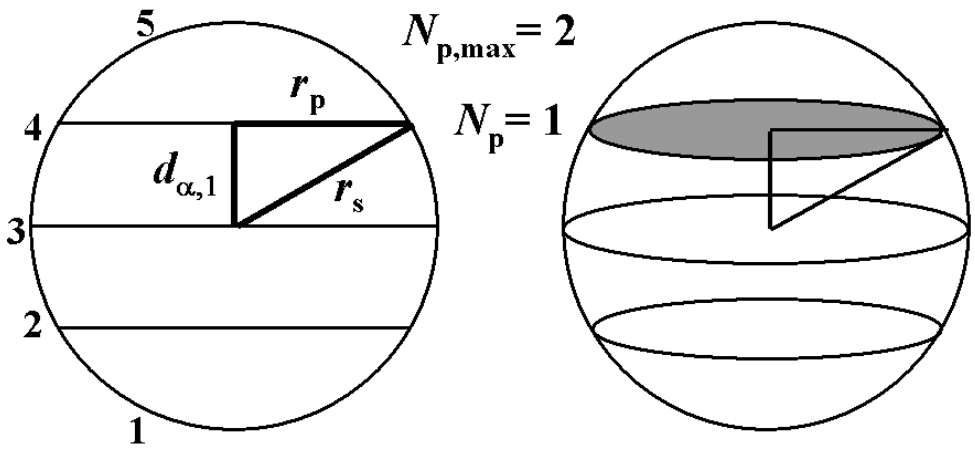

Fig. 7.4.5(6): standard sphere at $\phi_{B+C} = 0.01$, where $N_{p,max} = r_s/d_{\alpha,1} = 2$ and which therefore contains *five* lamellar plains, spaced equally d_α apart, and of which the top and bottom most have an area A_p of zero.

A spherical nucleus in question contains a number of lamellar planes equal to $2N_{p,max}+1$, where

$$N_{p,max} = r_s/d_\alpha \qquad \text{eq. 7.4.5(6)}$$

The circular area A_p of each of these planes can be calculated via its respective radius r_p, which can be derived from simple geometry.

$$A_p = r_p^2 \cdot \pi = \left(r_s^2 - \left(d_\alpha \cdot N_p\right)^2\right) \cdot \pi \qquad \text{eq. 7.4.5(7)}$$

The internal area of the nucleus is then determine by summing over all the individual planes, not forgetting to take the central plane into account

$$A_{in} = r_s^2 \cdot \pi + 2 \sum_{1}^{N_{p,max}} A_p \qquad \text{eq. 7.4.5(8)}$$

If one wishes to considered nuclei of varying bilayer volume fraction, one must designate a value of ϕ_{B+C} as a point of reference. For the purposes of this discussion this will be $\phi_{B+C} = 0.01$ and the distance between lamellae at this concentration will now be termed $d_{\alpha,1}$. The corresponding interbilayer distances at other concentrations $d_{\alpha,\phi}$ are then accessible via

$$d_{\alpha,\phi} = \frac{0.01 \cdot d_{\alpha,1}}{\phi_{B+C}} \qquad \text{eq. 7.4.5(9)}$$

eq. 7.4.5(8) can be cumbersome for large numbers of planes. However, for spheres with a sizeable number of planes the internal area A_{in} can be estimated very accurately via

$$A_{in} = \frac{1}{3}\pi \cdot \phi_{B+C} \cdot \left(\frac{r_s}{d_{\alpha,1}}\right)^3 = \frac{1}{3}\pi \cdot \frac{1}{d_{\alpha,\phi}} \cdot \frac{r_s^{\,3}}{d_{\alpha,1}^2} \qquad \text{eq. 7.4.5(10)}$$

Already for $2N_{p,max}+1 = 9$, i.e. only 7 planes of non-zero area are included, the fraction of the true area to the estimated area is > 0.98. Thus eq. 7.4.5(4) can be rewritten as

$$\Delta G = -\frac{1}{3}\pi \cdot \phi_{B+C} \cdot \left(\frac{r_s}{d_{\alpha,1}}\right)^3 \cdot \left(f_\mu \cdot \phi_{B+C}\right)^2 + 4\pi r_s^2 \cdot \left(f_\sigma \cdot \phi_{B+C}\right)^2 \qquad \text{eq. 7.4.5(11)}$$

The difference in Gibbs free enthalpy can now be calculated as a function of a nucleus' radius for arbitrary ϕ_{B+C}, when assuming values for the prefactors f_μ and f_σ (which are constant for various ϕ_{B+C} and r_s, for a given ΔT). Via differential calculus the critical radius r_s* of a nucleus and its respective energy barrier ΔG* can be determined to

$$r_s^* = \frac{8 \cdot d_{\alpha,1}^3 \cdot f_\sigma^2}{\phi_{B+C} \cdot f_\mu^2} \qquad \text{eq. 7.4.5(12)}$$

$$\Delta G^* = \frac{256 \cdot \pi \cdot d_{\alpha,1}^6 \cdot f_\sigma^6}{3 \cdot f_\mu^4} \qquad \text{eq. 7.4.5(13)}$$

Most notably r_s* is inversely proportional to ϕ_{B+C} and ΔG* is independent of it. Fig. 7.4.5(7) illustrates this fact. However eq. 7.4.5(13) also states that even slight increases of supersaturation $\Delta\mu$ are expected to significantly lower the nucleation barrier as the prefactor experiences a power of four. This trend is even stronger for a reduction of the interbilayer distance $d_{\alpha,1}$ (power of six).

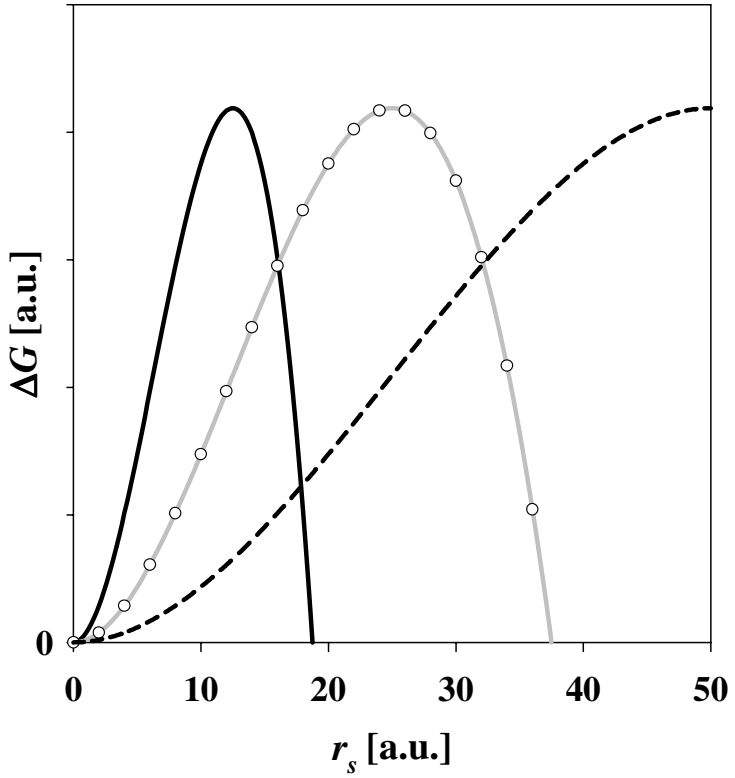

Fig. 7.4.5(7): development of ΔG as function of r_s calculated with eq. 7.4.5(11) with $d_{\alpha,1} = 0.5$ a.u., $f_\mu = 1$ and $f_\sigma = 10$. Curves presented are for concentrations $\phi_{B+C} = 0.02$ (dashed line), 0.04 (grey line) and 0.08 (solid black line). The data points of the $\phi_{B+C} = 0.04$ curve were calculated with eq. 7.4.5(8) to demonstrate the validity of eq. 7.4.5(11)

Since $r_s^* \propto \phi_{B+C}^{-1}$, it follows that $A_s^* \propto \phi_{B+C}^{-2}$ and $A_{in}^* \propto \phi_{B+C}^{-2}$. In other words, ΔG^* is not a function of ϕ_{B+C} since the ratio of internal to surface area of a critical nucleus is constant, i.e.

$$\Delta G^* = -A_{in,1}^* \cdot f_\mu^2 + A_{s,1}^* \cdot f_\sigma^2 \qquad \text{eq. 7.4.5(14)}$$

Thus the developed model cannot account for the increase in transition speed detected for higher concentration, since the nucleation rate J is primarily a function of ΔG^*. However, with an increase in supersaturation (which presumably occurs upon increasing ΔT), higher values of J are expected. Also, it is of importance that $A_{in}^* \propto \phi_{B+C}^{-2}$, because therefore it is plausible that the increase of concentration occurring in a nucleus through the dilution effect can effectively transform a subnucleus into a supernucleus. Importantly, this implies that the probability of a subnucleus surpassing its critical state is increased with the time that such a subnucleus is in existence.

The fact that a strong decrease in phase transition speed is detected in the system of increased viscosity ($\eta_{D2O/S} = \eta_0 \cdot 2.261$, fig. 7.3.1(19)) cannot be explained by considering only

supersaturation and nuclei surface energy. However, from the discussions of the sections above, it appears clear that diffusion is essential in forming the highly concentrated nuclei. This process will be included in the kinetic prefactor K_J of eq. 7.4.5(2) As argued above (see also section 7.4.5.3), at lower supersaturation supernuclei are formed by 'compacting' subnuclei via the dilution effect and thus diffusion is essential. At higher $\Delta\mu$, the process is of less importance, since supernuclei can form without the aid of higher concentration.

It must be stressed that the thermodynamic approach with its spherical nuclei of many lamellar plains is a great oversimplification. In a detailed theoretical discussion, which is beyond the scope of this experimentally based thesis, many aspects remain which need consideration. Instead of estimating $\Delta\mu$ via the bending energy E, the Gibbs free energy G of the initial and final state, as well as any intermediate states must be approximated, taking into account entropic terms such as bilayer fluctuations. In addition to the 'condensation energy' and surface tension energy, the elastic energy and interfacial anchoring energy (energy needed to deviate bilayers from their equilibrium orientation) of the lamellar 'crystallites' are of importance[70]. Finally, inhomogeneities and defects (e.g. focal conic domains) and their distribution within a developing lamellar domain cannot be disregarded[70].

Kinetics in the Light of the Passage Destruction Mechanism

When considering the proposed mechanism of passage destruction (fig. 4.2(2) and (3)) one can speculate on a more localised scale, as to what factors could influence the nucleation barrier ΔG^*. It seems clear that passage destruction can only occur after an unusually strong bilayer fluctuation enables bilayer contact as in fig. 4.2(2) stage 2. The mechanism of passage *formation* is thought of energetically as a 2-step process[68]. For

$$\tau^{-1} = \tau_P^{-1} \cdot \exp\left(-\frac{E_A}{RT}\right) \qquad \text{eq. 7.4.5(15)}$$

H. Leitao stated in ref.[45], that a relaxation rate τ^{-1} of a (phase) transition involving passage formation is the product of a rate (indirectly a probability) τ_P^{-1} of bilayers coming into contact and a probability of a passage to form once contact does occur (2nd term of eq. 7.4.5(15)). He goes on to state that τ_P^{-1} should essentially be controlled by membrane rigidity (κ) and that it is heavily dependent on the interbilayer distance d. On the other hand, the energy barrier of handle formation E_A is expected to be a function of the bilayer properties, i.e. ε, κ_{mono}, $\bar{\kappa}_{mono}$,

and $c_{0,mono}$. He also derives that for the lamellar phase, statistically, there will be one collision of membranes in the elementary volume d_α^3, while for the sponge phase this volume corresponds to $d_3^{(2/\zeta)+1}$, where ζ is the wandering exponent[108], which takes values between zero and one. ζ=0 for a system which is purely controlled by interfacial tension, while ζ=1 when a system shows free membrane behaviour, i.e. is controlled by bending energy only. Therefore, membrane collisions are considerably less likely in an equilibrium L_3 structure than in the equilibrium lamellar structure of equal bilayer composition.

Applying these concepts to the process of passage destruction, it is conceivable that as temperature jumps are performed with greater amplitude, the energy barrier E_A, grows less due to an increase of bending energy through a more negative $\overline{\kappa}_{bi}$ (via the influence of $c_{0,mono}$, section 7.4.1). In other words, the bilayers are under so much tension that when they do meet and stalk formation occurs, it is increasingly likely for this tension to be released by the stalk rupturing in the energetically favourable direction, i.e. passage destruction occurs (fig. 4.2(3) stage (2)→(3)) instead of a return to the original passage conformation (stage (2)→(1)). The 'information' into which direction rupturing has to occur could be mediated by the tension distribution in the stalk. Fig. 4.2(2) stage (2) was formed via an extreme fluctuation of the left bilayer, so that the bending energy density there is particularly high (even though on the scale of the stalk the outer monolayer appears flat) and accordingly this tension is preferably released by pore formation in the horizontal.

The development of the Gibbs free enthalpy is illustrated for the above hypothesis in fig. 7.4.5(8, *left*). The initial state I signifies a passage in the sponge phase and an unusually large bilayer fluctuation must overcome a high energy barrier (II) in order for bilayers to come into contact and form a stalk intermediate (III). The magnitude relation between state I and II is given by the interbilayer distance d_3. Through pore formation and subsequent rupturing of a small section of bilayer (see section 4.2), the bilayers separate and return either to the original passage conformation (state I) or passage destruction occurs resulting in a conformation of flat bilayers (state V). With increase of supersaturation the energy barrier (IV) becomes increasingly smaller than state II when viewed in relation to the intermediate state III.

In order to abide to consistency, the above considerations must also be applied to possible passage *formation* occurring in newly formed lamellar domains (fig. 7.4.5(8, *right*)). Since $d_\alpha < d_3$ the probability of bilayer contact is actually larger in these regions than in the sponge phase ($\tau_P^{-1} \propto d_\alpha^{-3}$, see above). Accordingly the energy barrier (II) between the original state I, consisting of flat bilayers, and a stalk intermediate (III) is smaller than in fig. 7.4.5(8,

left). Also, assuming that stalk formation does occur upon bilayer contact in the sponge phase, it is highly likely that in the lamellar phase the result is the same, since in both situation of contact the bilayer properties are very similar. Thus a local minimum state III will exist. In addition, it was stated above, that a created stalk preferably forms a pore through the bilayer which caused contact through an extreme fluctuation (and is accordingly under high tension), i.e. that the energy barrier IV<II (when viewed for state III and this is especially so for high supersaturation). For the case at hand however, this coincides with the direction passage formation (state VI) and not a return to the initial state I. Obviously though, the L_α-phase is stable and does not form passages in significant amounts although bilayer contact should be frequent. Therefore it seems plausible that it is the process of *pore expansion*, which is necessary to convert a pore to an L_3-like passage, that poses a high energy barrier, so that after a time in the metastable stalk/pore state (III to V), the bilayers will separate to return to the original lamellar structure (I). Note that the minimum at V only serves to emphasise the preferred direction of pore formation from the stalk and that the energy difference between V and IV may literally be nonexistent. In other words, it is more likely that simply the *slope* of the *G* development towards passage formation (IV) form state III is initially less than towards the energy barrier II, so that states III to V form an asymmetric minimum.

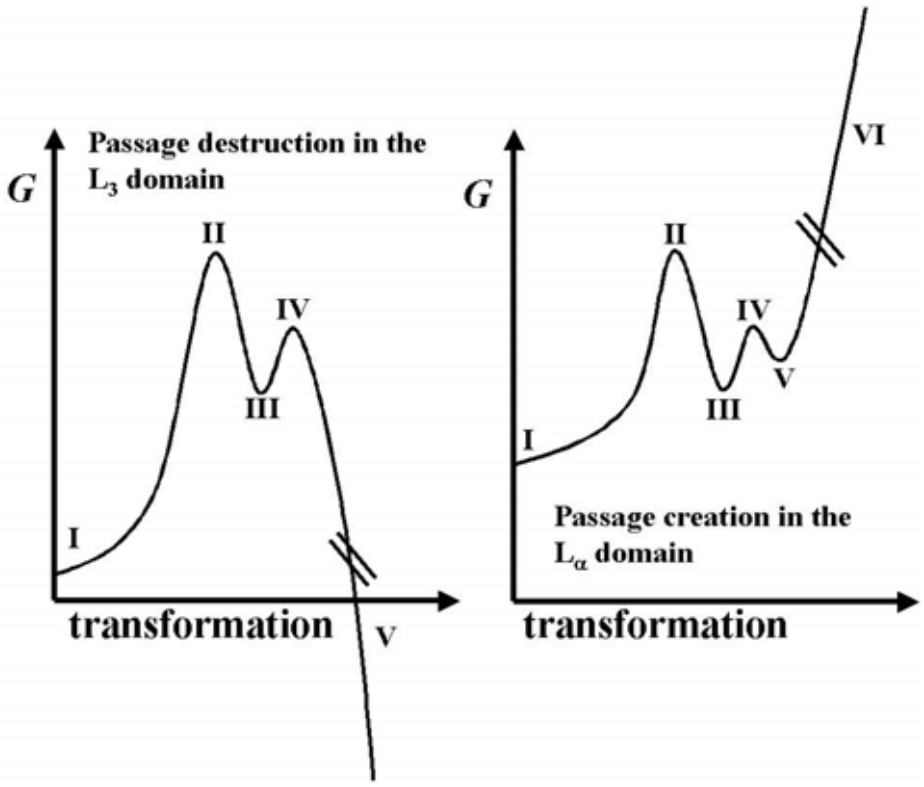

Fig. 7.4.5(8): proposed development of the Gibbs free enthalpy *G* for passage destruction in the L_3 domain (*left*) or passage creation in the L_α domain (*right*) during a sponge to lamellar phase transition. The roman numerals represent different states which are detailed in the text. Note that the enthalpy difference between state III and state IV or II, should not be compared to the difference between state I and II. Also, the minimum state V (*right*)

only serves to emphasise the preferred direction of pore formation in state III and is probably non existent (see text).

Another factor which should influence the transition kinetics is the absolute temperature. It decreases in the case of large ΔT, making the strong fluctuations that bring the bilayers into contact less likely to occur. However, the difference in absolute temperature is minimal in a ΔT=-1.0 or –2.0 jump, while the difference in the relaxation time constants τ is immense (section 7.3.1.4). Interestingly, the energetic reflection on passage destruction presented, can account for the general dependence of τ with ΔT. With increasing ΔT, E_A (which corresponds to the difference between state III and IV in fig. 7.4.5(8)) approaches zero, or simply the probability of the stalk rupturing in the direction of passage destruction approaches unity. Thus, the phase transformation kinetics approach a non-zero minimum value (fig. 7.3.1(21)), since the probability of bilayer contact (the difference between state I and II) is approximately constant. Of course, the kinetics of cooling begins to influence the determined τ-values for fast transition kinetics as discussed at the beginning of this kinetics chapter. Thus it is not implied that the approach towards a possible minimum value seen in fig. 7.3.1(21) corresponds to the theoretical minimum postulated here.

The above stated can also account for the changes in relaxation time with bilayer concentration ϕ_{B+C}. The interbilayer distances d become smaller with increased concentration (for $\phi_{B+C}<<1$, $d \propto \phi_{B+C}^{-1}$), and accordingly the probability of bilayer contact increases ($\tau_P^{-1} \sim \phi_C^{3}$)[109]. Because of the power law dependence of τ with ΔT and the approach of a minimum relaxation time constant, the $1/\tau$ dependence on ϕ_{B+C} is necessarily less for larger ΔT (fig. 7.3.1(21, *right*)), i.e. $1/\tau \propto \phi_{B+C}^{1.2}$ for ΔT=-1.7 and $1/\tau \propto \phi_{B+C}^{4.4}$ for ΔT=-0.8.

Finally, the handle destruction mechanism might also explain as to why L_α domain growth is energetically reduced when compared to the creation of a new nucleus. (Apart from the consideration of the CNT, where a number of nuclei of a given total volume have a greater surface area than a single nucleus of the same volume, and accordingly the single nucleus is energetically favoured.) Passage destruction in the L_3-bulk is the least likely scenario, as bilayer contact probability τ_P^{-1} is lowest there (see above). In the vicinity of an already existing nucleus however, and most certainly at its interface, the bilayers of the passages will have characteristics more similar to those of the lamellae ($\zeta \rightarrow 1$), so that the probability of bilayer contact increases. In fact, it could be shown experimentally that the topological parameter μ_T and therefore the coordination number Z of the passages decreases with reduced distance to the L_3/L_α interface[70] (according to *Porte*[73] $\mu_T \approx Z/4$ so that for an ideal cubic model $\mu_T \approx 1.5$). In addition, d_α of young nuclei is considerably smaller than d_α of the steady state

lamellar phase (section 7.3.1.5) and this shorter distance transmits necessarily to d_3 at the interface because of the continuity of the membranes. Again, this increases the probability of bilayer contact. In fact at said interface[70]

$$\sin\theta_{ep} = \frac{d_\alpha}{d_3} \qquad \text{eq. 7.4.5(16)}$$

where θ_{ep} is the epitaxial angle, a parameter better known in crystallography, which in this case is the angle between the lamellar surface and the L_3/L_α interface (fig. 7.4.5(9)). (In fig. 4.2(1) $\theta_{ep}=0°$, and on this surface of a lamellar 'crystallite' eq. 7.4.5(16) does not apply and d_3 can be of arbitrary size). Eq. 7.4.5(16) has been confirmed experimentally by determining $2\theta_{ep}$ with polarised microscopy [33].

The dilution effect (section 7.4.5.3) may at first seem to contradict the statements of this section, where nuclei growth is considered energetically favourable, due to the reduced distance of d_3 at the interface. One must however keep in mind the continuity of the bilayers and the validity of eq. 7.4.5(16). Thus a zone of dilution will begin at a certain distance from the interface, that is to say the L_3 passages directly at the phase border will still be of small d_3 and thus aid bilayer contact. In case of the interface taking the form of fig. 4.2(1), dilution will be hindered, since the water domain not connected to the L_α crystallite will not be able to expand, because the bilayers represent a barrier for the diffusion of D_2O molecules.

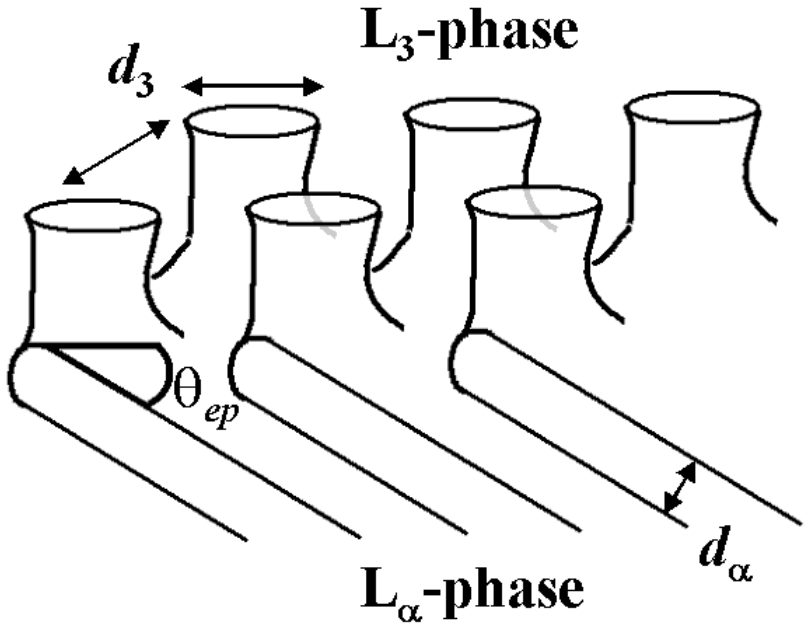

Fig. 7.4.5(9): schematic depiction of an energetically favourable L_3/L_α interface, reproduced from [70]

7.4.6 L_α to L_3Transitions

7.4.6.1 Characteristics of the Phase Transition Mechanism

Up to this point it was apparent through the different lineshape developments that the lamellar to sponge transition occurs through a different process than the sponge to lamellar transition, i.e. not through nucleation and growth. At no point during the transition are three peaks visible, so the coexistence of anisotropic lamellar domains and isotropic sponge domains can be ruled out. (This is of course only true for domain sizes probed by the diffusion of the D_2O molecule, see section 7.4.5.3). Rather, the L_3-phase develops through a number of random fusion events, which create the passages in the multiply connected bilayer structure in such a way that the sample is homogeneous over distances probed by the diffusing water molecules, on a time scale determined by the inverse quadrupolar splitting.

The quadrupolar splitting $\Delta\nu_Q$ results from a residual quadrupolar interaction which is not averaged to zero by the molecular reorientation. In the experiments discussed here, this is due to the presence of MAPA D_2O which has a preferred orientation with respect to the bilayers. Throughout the transition passages are introduced and the bilayers become on average increasingly curved. As a result the D_2O molecules can reach new surface orientation by diffusion, i.e. θ_{nb} is averaged increasingly more effective. (A division of the geometrical term containing θ_{nb} into two terms with θ_{nd} and θ_{db} as in eq. 7.2.1(4) is nonsensical at this point, since the 'decaying' lamellar phase loses its director (see section 7.2.4). When all orientations are accessible, as is the case in the sponge structure, the quadrupolar interaction is averaged to zero and a singlet results. The averaging of the interaction also causes the interaction to become time dependent, and the motion of the molecules within the MAPA regime contributes to the relaxation of the magnetisation. Hence, besides the initial gradual decrease of the quadrupolar splitting, there is also a gradual broadening of the doublet resonances.

The evolution of the spectra can be seen as a result of a gradual decrease of a 'correlation time' τ (note $\tau \neq \tau_c$) describing the change of the preferred orientation of the D_2O molecules as they diffuse along a curved surface. A rough estimate of τ is

$$\tau \approx \frac{r^2}{D} \qquad \text{eq. 7.4.6(1)}$$

where r is the average distance between passages, which more formally can be expressed in terms of an Euler characteristic density, and $D \approx 2 \cdot 10^{-9} m^2 s^{-1}$ the water diffusion coefficient. As the passage density increases, r and thereby τ decrease. The coalescence of the doublet occurs when $\tau \approx 1/\Delta\nu_Q \approx 0.1s$, which is observed experimentally after circa 300s (fig. 7.3.2(18)). Using eq. 7.4.6(1) at this point, one obtains the estimate that $r \approx 10\mu m$. This value can be compared to the characteristic length in the equilibrium sponge phase d_3, which is approximately equal to the average pore size. d_3 ranges from 244nm to 159 nm for ϕ_{B+C}=0.05 to 0.07 (see section 8.7.1).

Due to its homogeneity, the L_α to L_3 phase transition can be seen as continuous on mesoscopic length scales. However, this only refers to the distribution of passages and thereby the overall characteristics of the metastable state. It does not imply that a phase transition of second order, according to the *Ehrenfest* classification, is witnessed. Instead the discontinuities of a first order phase transition[83] are expected and the L_3-phase still thought of as nucleating within the lamellar phase. There is an energy barrier for the formation of a passage[110] and thus each of these events can be considered nucleation. The size of this energy barrier is however small, when compared with the one necessary to incite 'growth' of a nucleus, i.e. passage formation adjacent to an already existing passage. Thus a discussion of the transition in context of the CNT is not possible.

7.4.6.2 The L_α to L_3 Phase Transition Kinetics

In section 7.3.2.2 it was attempted to fit the spectra of the observed phase transitions on the basis of the *chemical exchange* model using a modified McConnell equation, which accounted for a natural linewidth (eq. 7.3.2(2)). However, the model failed in the sense that that the initial quadrupolar splitting value $\Delta\nu_{Q,L}$ could not be kept constant (fig. 7.3.2(2)). Also, it did not manage to describe the lineshape of spectra, where very small splittings were detected, i.e. it determined the time of coalescence too soon (fig. 7.3.2(9)). As stated above, lineshape development depends on the geometrical term including θ_{nb} being averaged increasingly well to zero, due to changes in the diffusion of D_2O. Taking this microscopic description into account, it is no great surprise that the employed model cannot reproduce the lineshapes satisfactorily as it is based on the existence of two states of equal population yielding a singlet at different resonance frequencies in case of slow exchange (section 7.1.9). A quantitative analysis requires the fitting of the NMR band shapes using slow motion theory

for the water dynamics. This however, requires a quantum mechanical treatment of NMR[111] and is therefore beyond the scope of this thesis.

Ignoring the deficiencies of the chemical exchange model, plots of the coalescence parameter χ_P (eq. 7.3.2(3)) as a function of time were generated nevertheless. These show a strong exponential growth with $\tau \approx 20$ to 30s up to the point of coalescence ($\chi_P = 1$), after which the model can yield no further information. Thus the only result is that coalescence is reached very quickly in an exponential manner. However, at the times in question sample heating is still fully in progress (needing ~200s until completion). Therefore the kinetics up to the point of coalescence (which occurs at ~300s independent of sample composition or magnitude of the *T*-jump) are heavily dominated by the heating process and it is conceivable that much faster transitions would take place if heating could be achieved more quickly.

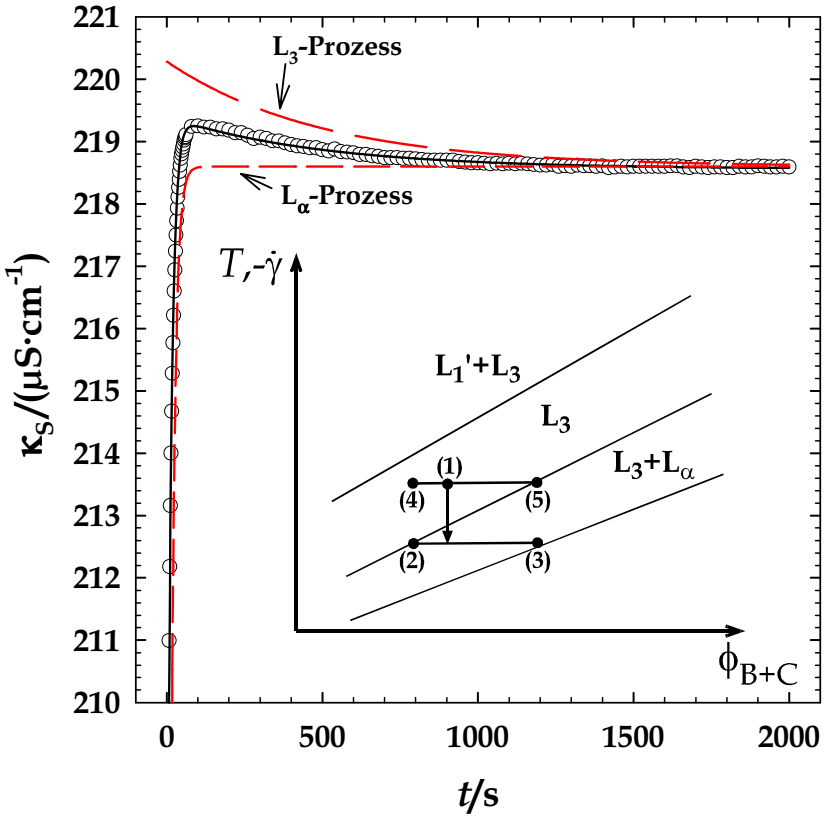

Fig. 7.4.6(1): development of conductivity after the suspension of an isothermal shear experiment. The data points (circles) were fitted with a combination of two exponential functions (solid line), whose individual development is represented by the dashed lines. This figure is taken from ref.[46].

In this context, *Uhrmeister*[46] interpreted isothermal shear experiments, where the lamellar phase relaxes back into the sponge phase, in the following, phenomenological manner. In the experiment presented in fig. 7.4.6(1) a sample of the system H_2O/NaCl – *n*-decane –$C_{12}E_5$ (ω_b=0.45 and ϕ_{B+C}=0.06), was sheared from the L_3 phase into the L_3/L_α coexistence region at a temperature, which corresponds to the middle position of the L_3-

channel at equilibrium. The shearing was stopped (solution at rest at t = 0s) and the relaxation monitored by measuring the conductivity.

Initially there is a strong rise in conductivity and a maximum is quickly attained. The conductivity then relaxes back to its equilibrium L_3 value much more slowly. Thus there are two processes at work and Uhrmeister fitted the data of fig. 7.4.6(1) accordingly, using the sum of two exponential functions (solid line), which yielded relaxation time constants τ_1=12.8s and τ_2=490s. He then went on to give the following explanation for the observed behaviour. The L_3-phase is first sheared into a state, where a dilute L_3-phase(2) is in coexistence with a concentrated lamellar phase(3). This phase separation occurs only on microscopic length scales. Once shearing is suspended, the concentrated lamellar phase(3) transforms into a concentrated L_3-phase(5), which coexists with the dilute L_3-phase(4). This process occurs rapidly (τ_1) and is the cause for the strong increase in conductivity. The then ensuing slow relaxation process (τ_2) is identified with the phases (4) and (5) equilibrating into state (1).

Judging from Uhrmeister's analysis, it appears that *initial* passage formation does occur very rapidly for the lamellar to sponge phase transition for the system at hand. However, τ_1 cannot be interpreted quantitatively since the amount of displacement into the coexistence region is *not* known.

The performed analysis of fitting two Lorentzians to the spectra before coalescence and one for spectra afterwards leads to plots where the development of peak width $\Delta\nu_{1/2}$ is observed as a function of time (section 7.3.2.4). Again, the fast development towards coalescence, which corresponds to the maximum $\Delta\nu_{1/2}$ -value, is apparent. The subsequent reduction of $\Delta\nu_{1/2}$ of the singlet occurs then however in all cases more slowly. The form of said reduction was described by eq. 7.3.2(5), a double exponential decay. First, there is a rapid width decay, which is then followed by much slower peak sharpening. The absolute time at which the process or processes that cause the decay take place, is however well separated from the time needed for sample heating (~200s). Thus, even though the beginning of the L_α to L_3 phase transition kinetic is dominated by the heating process, the later developments are not. Therefore it is clear that the phase transitions are substantially accelerated in comparison with the sponge to lamellar transitions, since an isotropic peak of a width close to the equilibrium width is generally attained within 600s. The acceleration is most obvious for experiment FT_14 (completed at ~600s, fig. 7.3.2(12)) and FT_83 (completed at ~1200s, taking its long period of peak sharpening into account, not visible in fig. 7.3.2(14)), where the reverse transitions yield relaxation time constants τ~3000s. At this

point, one can argue that the difference in rate can be due both to the difference in final temperature and the fact that a homogeneous process is expected to proceed faster than a process involving nucleation and growth.

7.4.6.3 The Kinetics in Light of the Passage Formation Mechanism

The lamellar to sponge phase transition requires the creation of passages and thus necessarily the process of bilayer fusion. The mechanism of passage formation is described in section 4.1 and will serve as a basis for the following discussion. Similarly, eq. 7.4.5(15) describing passage formation as a two-step process and the considerations of *H. Leitao* on the probability of bilayer contact will have to be taken into account (section 7.4.5.5). Fig. 7.4.6(2, *left*), depicts a hypothetical development of the Gibbs free enthalpy for passage formation in the lamellar phase, in analogy to fig. 7.4.5(8).

The initial state I signifies two plane bilayers of the lamellar phase in opposition as illustrated in fig. 4.1(1) stage 1. A large bilayer fluctuation must overcome the moderate energy barrier II in order for bilayers to come into contact and form a stalk intermediate III. Bilayer contact in the lamellar phase is relatively frequent, due to the small value of d_α (in comparison to d_3) and so the magnitude relation between state I and state II is considerably less that the respective one for bilayer contact in the L_3 phase (fig. 7.4.6(2, *right*)). After pore formation, the intermediate can either rupture, causing the bilayers to separate and a return to state I, or the pore can expand leading to the formation of a passage (state V). Akin to the argument given in section 7.4.5.5, pore formation should preferably occur through the bilayer which caused the contact, as it is under high tension. Thus energy barrier IV is smaller than II when viewed in relation to the intermediate state III.

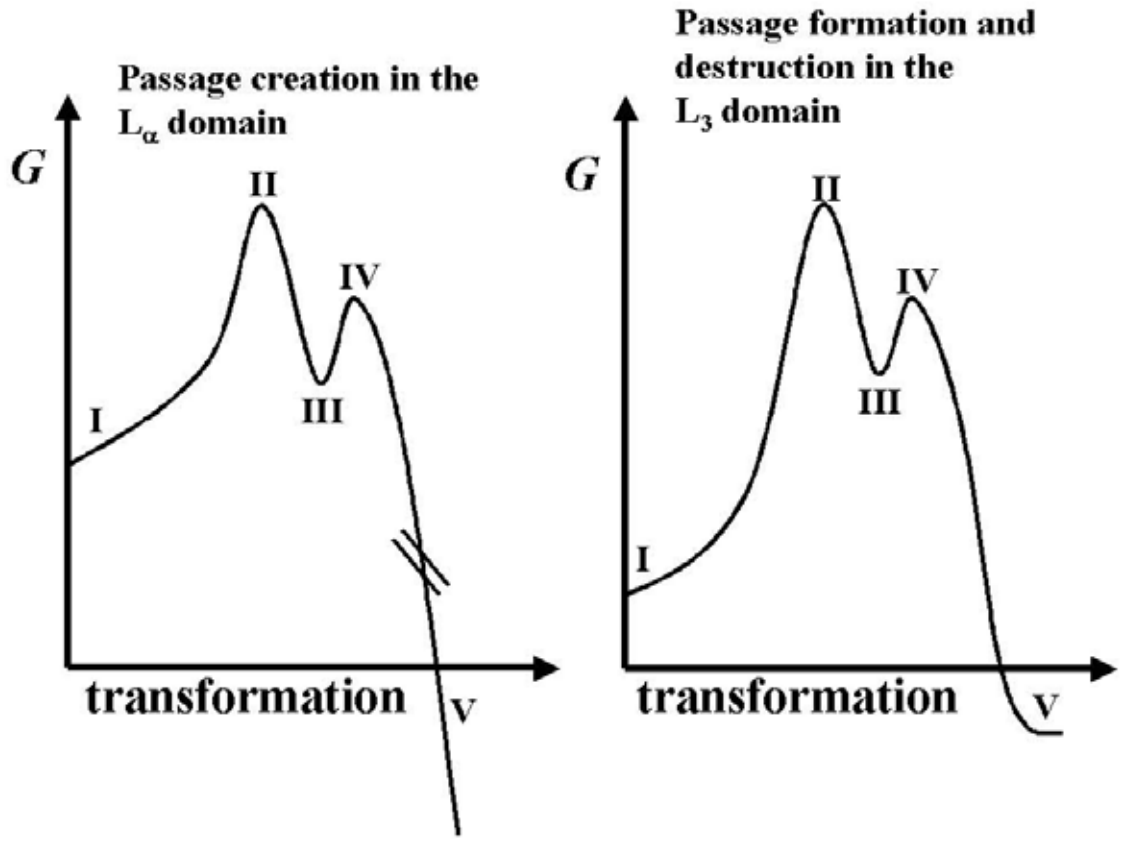

Fig. 7.4.6(2): proposed development of the Gibbs free enthalpy for passage creation in the lamellar phase (*left*) and passage destruction/creation in the pre-equilibrium sponge state. The roman numerals represent different states which are detailed in the text.

Statistically there will be one collision of membranes in the lamellar phase within the elementary volume d_α^3 (section 7.4.5.5) and usually this will result in passage formation. However, once a passage is formed it will expand to the characteristic size d_3 and presumably even a little beyond that, because of a dilution effect as described in section 7.4.5.3. However, this effect should be much less pronounced for the sponge to lamellar transition. Although the L_α phase is only stable at much higher concentration ϕ_α at the target temperature, the L_3-passages can be expanded, i.e. diluted, only relatively little (to ϕ_3') and hence both domain types will remain close to the equilibrium concentration ϕ_0 (fig. 7.4.6(3)). Thus D_2O diffusion should be of only minor importance at this point. Nevertheless, large fluctuations will occur less frequently in the vicinity of an existing L_3-passage, where bilayer contact occurs in the elementary volume $d_3^{(2/\zeta)+1}$ (section 7.4.5.5). In addition, if a second passage does form close to an existing one (connecting the same or adjacent bilayer planes), they will experience a repulsive potential (passage interaction can be viewed as hard core repulsion)[110] and will accordingly spread out. Both concepts sum up to an impressive explanation as to why sponge domain growth does not occur in the L_α to L_3 transitions.

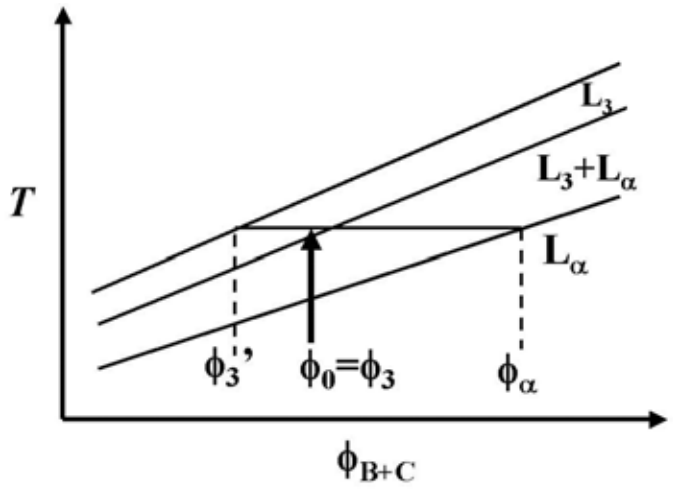

Fig. 7.4.6(3): schematic phase diagram illustrating the desired concentrations in the metastable state. Even in non-equilibrium, the lamellar phase cannot increase to high concentration ϕ_α, since the sponge phase is only stable up to a small dilution ϕ_3'.

From the above contemplations one expects the passage density to increase rapidly and phase transition relaxation rate τ should develop according $\tau \propto \tau_P^{-1} \propto d_\alpha^{-3} \propto \phi_{B+C}^{3}$ (where τ_P^{-1} is the rate of bilayers coming into contact, section 7.4.5.5), i.e. phase transition speeds increase with increasing concentration. Similarly, phase transition speeds should be independent of the magnitude of the *T*-jump, since the final state (and its absolute temperature) is identical for all experiments and since the relations between the energy barriers II and IV should not change with respect to the intermediate III (fig. 7.4.6(2, *left*)). In fact, *Uhrmeister* showed that the relaxation times of positive temperature jump experiments (which lead to an increase in passage density) performed within the L_3-channel only depend upon the target temperature[46]. The τ dependence on ϕ_{B+C} could not be found in the experiments, but with respect to *Uhrmeister's* passage formation time constant τ_1=12.8s and the heating time constant of ~64s (completion at ~200s) this is no surprise.

At coalescence the distance *r* between the passages can be estimated to ~10µm, but d_3 of the equilibrium L_3-phase is at least 40 times smaller for the compositions studied (see above). Thus, passage density still remains to increase considerably beyond this point. However once passage density reaches the point, where notable repulsion exists between them, the introduction of new passages between them will become increasingly difficult. In addition, up to this point there probably exists only a lamellar phase perforated with passages. In order to attain the morphology of the sponge phase the long distance order between the bilayer planes must be lost, i.e. passage direction must be random in 3D space. This could be associated with additional energy barriers.

The decrease of peak width $\Delta\nu_{1/2}$ was described with the help of two exponentials. Thus at a given point in time the slower relaxation process τ_2 begins to dominate. It is

possible that this is the expression of a transition regime, where passage formation becomes energetically more difficult, due to the attainment of a critical passage density and the need to lose lamellar long distance order. The ensuing peak sharpening could then correspond to perfecting the isotropy of the L_3-phase, while attaining a macroscopically uniform passage density.

Also, as passage density increases and a more sponge phase like character is gained, passage *destruction* will become increasingly likely. Fig. 7.4.6(2, *right*) displays proposed development of the Gibbs free enthalpy for passage formation and destruction within the sponge phase. The energy barrier II is high with respect to the initial state I, as interbilayer distance d_3 increases with increasing passage density. From the previous discussions, the energy barrier IV should always be smaller than II, because of the high bending energy of the membrane which caused the bilayers to contact. The energetically favourable state V can correspond to the state after passage destruction *or* formation. Which one will be more favourable will depend upon the local passage density, i.e. passages will preferably form where the density is lower than the equilibrium density and *vice versa*. Thus the sponge phase in equilibrium will consist of a dynamic equilibrium of passage formation and destruction.

From the above contemplations, it is clear why the lamellar to sponge phase transition are considerably faster than the reverse transitions (unless these are performed at excessive supersaturation). Passage formation is generally easier due to smaller distances d_α than d_3 in the bulk or d_3 at the interface of a lamellar nucleus. In addition, there are no major diffusion processes involved in the early stages of passage formation, unlike those required to increase the concentration of the lamellar nuclei. However the energy barrier IV with respect to state III will remain at a significant value, while for the reverse transition it can presumably become non-existent with increasing $\Delta\mu$. Also, reaching true equilibrium (i.e. a uniform passage density) of the L_3-phase can take considerably longer than may be apparent at first glance (and sensitivity of the technique used to monitor the transition is certainly an issue). Later stages of passage formation become increasingly difficult due to increasing values of d_3. Also, passage destruction will occur ever more until a dynamic equilibrium is attained. On the other hand, attaining true equilibrium in the lamellar phase is even more daunting. Defects in the ‘crystallites’ might remain long after the transition is supposedly complete. In addition, the boundary region between the crystallites of different director orientation (2D or 3D powder), will continue to minimise in energy, presumably striving towards a ‘single crystal’ conformation of the entire sample.

7.4.7 The 'Additional Experiments'

The results of the additional experiments (section 7.2.6.4) support the line of discussion followed throughout section 7.4. In section 7.3.3 it was stated, that when reversing the lamellar to sponge transition, the time required until the appearance of well defined lamellar peaks was very short (~140s). In the L_α to L_3 step a state just beyond the point of coalescence was reached. According to the discussion in section 7.4.6.3, this state should correspond to a lamellar phase with a good deal of passage defects, i.e. the distance *r* between the passages is somewhat smaller than 10µm. However, these isolated passages will be destroyed as easily if not easier than those at the L_3/L_α interface in a standard L_3 to L_α transition. Also, it is well possible that the repulsive force between passages will expel some of the passages into the L_3-like boundary region between the 'crystallites' (2D-powder). Furthermore, D_2O will diffuse into this region reducing d_α and thus leading to the large quadrupolar splitting $\Delta\nu_Q$ initially detected.

For the reversing of the sponge to lamellar transition, no exceptional behaviour was detected, only an L_3-singlet was superpositioned over the process. This is expected, since the sponge phase does not 'grow' and likewise the present lamellar nuclei (or rather domains, since they should have grown to considerable size at the EPM at which the transition was reversed) do not 'shrink'. Passages are simply introduced into the lamellar domains, as for a standard L_α to L_3 transition.

Finally, the micellar to lamellar transition appears to be continuous in the sense that this is true for the lamellar to sponge transition, i.e. there is no visible nucleation and growth process of lamellar domains. Instead the character of the state changes homogonously (over distances probed by the diffusing water molecules, on a time scale determined by the inverse quadrupolar splitting) and in an aligned manner (no NMR powder spectrum is registered). From the phase diagram of the system in question (see section 2.2(3)) one might expect a concentrated lamellar phase to separate as the L_1/L_α two phase region is traversed rather slowly (the peak position, related to temperature, shifts for 450s). However, no additional doublet of large splitting was detected within ±150Hz. Then again, the maximum splitting detected at t = 600s was with $\Delta\nu_Q$ = 10.1 Hz notably smaller than the splitting of a steady state lamellar phase of the composition in question ($\Delta\nu_Q$ = 13.7 Hz), indicating that the present phase is either dilute or contains a considerable amount of defects.

8. Small Angle Neutron Scattering (SANS)

Although the previously presented NMR investigations give insight not only into the kinetics of the sponge/lamellar transitions but also into the involved mechanisms, the method is indirect and of low length scale resolution, as it is based upon the diffusion of D_2O probe molecules in interaction with their isotropic/anisotropic environments. In order to obtain direct information on the characteristic length scales of the microstructures present in the complex fluids, either imaging (e.g. electron microscopy) or scattering techniques are necessary. In this thesis, emphasis is placed on the non-invasive scattering of neutrons.

Since the length scales in question are of the nanometer range, both X-rays and neutrons are of the appropriate wavelength for scattering experiments. However, while X-rays interact with the electrons of the target atoms and scattering strength is thus directly dependent on the respective atomic number, neutrons interact with the target nuclei in a non-characteristic manner (with regard to the nucleus mass) and the 'light' atoms (H, D, C; O) that comprise the investigated samples interact much better with neutrons. In addition, the degree of interaction between neutrons and target nuclei sometimes varies greatly between different isotopes of the same element. This gives rise to a technique known as '*contrast variation*' when employing components of selected isotopes and it represents one of the great advantages of neutron scattering over X-ray scattering. Contrast variation is an integral part of the performed experiments (see below). The theory of neutron scattering has been described in several good textbooks[112,54]. The sections below thus focus only on the most basic principles, always in view of the performed experiments.

8.1 Fundamentals of Scattering

Due to the wave-particle duality, an incident neutron beam can be described via the characteristics of waves and as wave functions. The wave vector $\vec{k}_i$ of an incident neutron points in the direction in which the particle travels and its magnitude $\left\|\vec{k}_i\right\|$ is given by $2\pi/\lambda$, where λ equals the *de Broglie* wavelength

$$\lambda = \frac{h}{p} = \frac{h}{m_n \cdot v} = \frac{h}{\sqrt{2m_n \cdot E}} \qquad \text{eq. 8.1(1)}$$

Here m_n is the rest mass of a neutron, p its momentum, v its velocity and E its (kinetic) energy. After interaction with a scattering centre (which in case of SANS is an atomic nucleus), the scattered neutron travels along a new direction described by $\vec{k}_s$. SANS only considers elastically scattered neutrons, i.e. scattering events where no energy is transferred to or received from the scattering centre, and thus $\left\|\vec{k}_s\right\| = 2\pi/\lambda$ also. The change of direction is described by the scattering vector as $\vec{q} = \vec{k}_s - \vec{k}_i$. When one denotes the angle between the incident and scattered neutron as θ and considers that energy is retained in the scattering event, then the magnitude of the scattering vector can be deduced via simple geometry to

$$\left\|\vec{q}\right\| = 2\left\|\vec{k}_i\right\| \cdot \sin\frac{\theta}{2} = \frac{4\pi}{\lambda} \cdot \sin\frac{\theta}{2} \qquad \text{eq. 8.1(2)}$$

By definition $\left\|\vec{q}\right\|$ also contains the refractive index n of the scattering medium as a proportionality constant. However, $n = 1$ for the neutrons in question and thus eq. 8.1(2) holds as it is.

In the theory of diffracting waves[113], an incident planar wave interacts with a scattering centre and results in the propagation of spherically symmetric wavefronts. Wavesfronts from different scattering centres interfere constructively only when they are in phase, i.e. their phase shift due to propagation over different distances is a whole-numbered multiple of the wavelength λ. This is stated by the well known Bragg law

$$n \cdot \lambda = 2d \cdot \sin\frac{\theta}{2} \quad (n = 1, 2, 3\ldots) \qquad \text{eq. 8.1(3)}$$

where d is a characteristic repeat distance between the scattering centres. Eq. 8.1(3) is also applicable for SANS and when one combines the Bragg law with eq. 8.1(2) and considers only the primary reflex ($n = 1$) one obtains

$$d = \frac{2\pi}{\left\|\vec{q}\right\|} \qquad \text{eq. 8.1(4)}$$

Thus a repeat distance d can be determined by observing a maximum in scattering intensity at a given value of $\left\|\vec{q}\right\|$

.

8.2 Geometry of the SANS Experiments

From eq. 8.1(2) it is clear that scattering experiments must be performed with (nearly) monochromatic radiation, i.e. monoenergetic neutrons (λ = const., eq. 8.1(1)) are needed in order to have a definite value of $\|\vec{q}\|$ of at a given angle θ. Also, the incident neutrons must come from essentially a single direction, i.e. the neutron beam must be collimated, so that the angles θ from different scattering events are comparable. (Additionally, the parallelism of the incident neutrons is equivalent with the planarity of the incident neutron waves and this is a condition of the Bragg law anyhow.) Note that the employed neutrons are however not coherent.

SANS experiments are 'static' scattering experiments yielding structural information by measuring the dependence of the average scattering intensity on the angle θ (i.e. $\|\vec{q}\|$). Fig. 8.2(1) illustrates the last steps of the optical path of the neutrons.

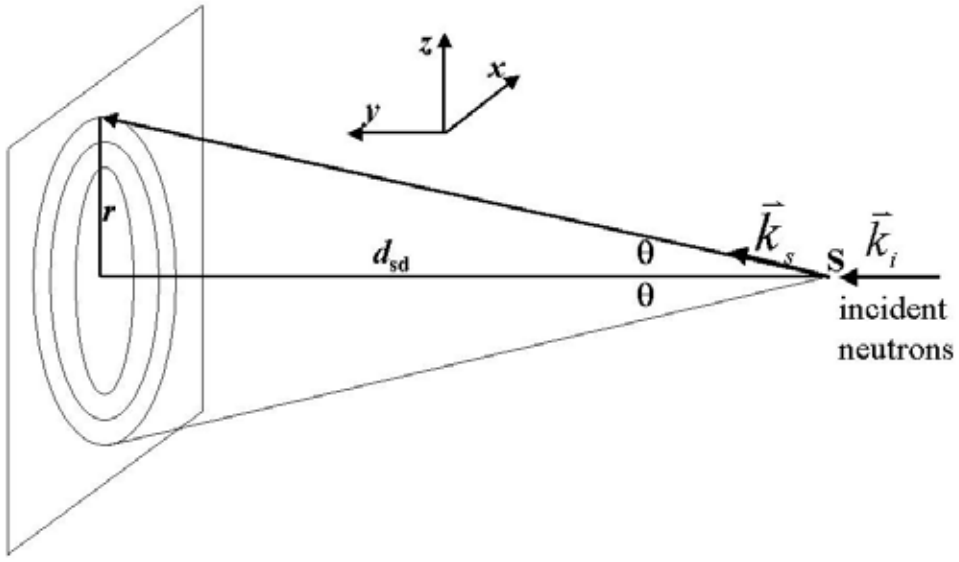

Fig. 8.2(1): the last steps of the optical path of neutrons in SANS experiments. Collimated, monoenergetic neutrons travel along the *y*-axis until they are scattered with the angle θ within the sample (position marked 'S'). They then lead to a 'count' signal on a 2D neutron detector which is located within the *xz*-plane at the distance d_{sd} behind the sample. Disordered and isotropic samples lead to an isotropic scattering pattern, i.e. the scattering intensity is constant at a given distance *r* from the beam centre.

Although neutrons interact much more strongly with the 'light' atoms that comprise the samples than X-rays, this interaction is nevertheless weak and most neutrons pass unhindered through the scattering volume. This primary transmitted beam is absorbed in the 'beam stop' located near the centre of the detector. (Since neutrons are subject to gravity the

actual beam stop position must be adjusted with the sample detector distance d_{sd}.) Due to the small chance of interaction and the short sample path length used (1mm), multiple scattering is not an issue. Of the fraction of neutrons that are scattered, the vast majority is scattered coherently and a disordered or isotropic sample results in an isotropic scattering pattern, i.e. scattering minima/maxima form concentric circles on the detector. Therefore, the correlation between a given position on the detector and the scattering angle θ is given by

$$\tan\theta = \frac{r}{d_{sd}} \qquad \text{eq. 8.2(1)}$$

where r is the distance between a particular position on the detector and the centre of the primary beam. It is clear from fig. 8.2(1) and eq. 8.2(1) that by increasing d_{sd}, smaller angles θ and thus smaller $\|\vec{q}\|$ can be examined. The fraction of neutrons that are actually absorbed by nuclei of the sample is small, due to the type of atoms comprising the samples.

In the experiments, neutrons passed through a velocity selector so that only those of v~659 m/s reached the sample. Therefore $\lambda = 6$Å and $E = 2.3$meV (eq. 8.1(1)) and neutrons of this energy are referred to as *thermal neutrons*. By performing the scattering experiments at four different sample to detector distances (d_{sd} = 1.1, 4.5, 16 and 34m) a q-range of approx. 0.001 Å^{-1} to 0.3 Å^{-1} could be covered, giving insight into length scales from 630 nm to 2 nm (eq. 8.1(2) and 8.1(4)). The samples were contained in flat quartz scattering cells of 1mm internal depth (= neutron path length), which were situated in a home build cell holder. The cell holder itself was mounted on a support to ensure cell alignment with the neutron beam. Temperature within the cell holder was controlled by a water cycle passing through a thermostat. The experiments were carried out on two separate occasions (referred to as the first and second set of experiments) on the instrument D11 at the Institut Laue-Langevin (ILL) in Grenoble, France. For further information regarding the experimental setup and experimental specifics the reader is referred to section 10.5.

8.3 Contrast Variation

In the lamellar and sponge phases there are *two* characteristic structure sizes which are of interest, the repeat distance of the bilayer midplanes *d* and the bilayer thickness $\delta = 2\varepsilon$. A schematic representation of a surfactant bilayer is given in fig. 8.3(1), while the two parameters *d* and 2ε are illustrated by means of the L_3 and L_α-phase structures in fig. 8.3(2).

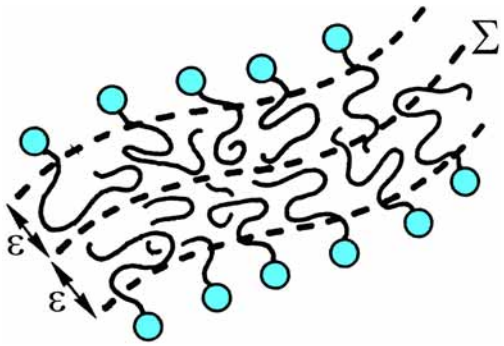

Fig. 8.3(1): schematic representation of a surfactant bilayer build up from two surfactant monolayers back to back (from ref.[114]). The circles represent the hydrophilic surfactant head groups while the tails represent the hydrophobic alkyl chains. The bilayer midplane is denoted with Σ and the distance between Σ and the hydrophobic/philic boundary corresponds to ε, so that the bilayer thickness equals 2ε. The addition of hydrophobic oil causes the bilayer to swell and the distance 2ε to increase.

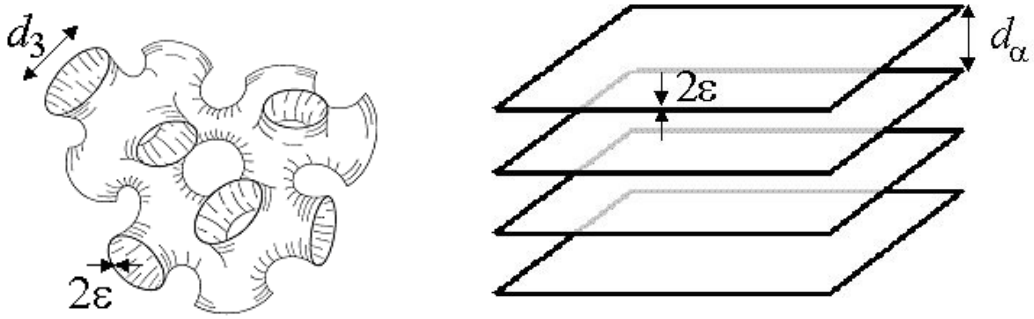

Fig. 8.3(2): schematic representation of the sponge and lamellar structures and the characteristic structure sizes *d* and 2ε. Note that distance *d* is *not* equal in the L_3 and L_α state for a given composition. The illustration of the sponge phase was taken from [45].

Scattering is caused by fluctuations in a medium, as a rule by variations in density. While for electromagnetic radiation the index of refraction of a material can describe these variations, for neutrons differences in the scattering length density ρ_s are decisive. For the scattering intensity $I(q)$ (where $q = \|\vec{q}\|$) in a SANS experiment $I(q) \propto \langle\Delta\rho_s\rangle^2$ is true. ρ_s of a given component consisting of a single type of molecule can be calculated using the characteristic scattering lengths *b* of all its individual atoms according to

$$\rho_s = \sum_i b_i \frac{\rho \cdot N_A}{M} \qquad \text{eq. 8.3(1)}$$

where N_A is *Avogadro*'s number, ρ the macroscopic density and *M* the molar mass. For phases or domains consisting of several components the respective scattering length density ρ_d is calculated via the volume fraction weighted sum of the different ρ_s

$$\rho_d = \sum_i \phi_i \cdot \rho_{s,i} \qquad \text{eq. 8.3(2)}$$

Since the scattering length *b* of the nuclei of different isotopes of the same element can vary drastically, selective use of isotopes can result in large differences of the scattering length density of different components and thus strong scattering. The difference in *b* of the protium (^{1}H) and deuterium (^{2}H) isotope is particularly large, so that contrast variation is exceptionally advantageous for components containing hydrogen.

In order to determine the distances *d* and 2ε, two types of contrast variations are regularly employed, namely bulk and film contrast. The former is obtained by using deuterated water while the components of the bilayer are protonated, the latter when both water and oil are fully deuterated. Fig. 8.3(3) illustrates the density profiles for the two cases.

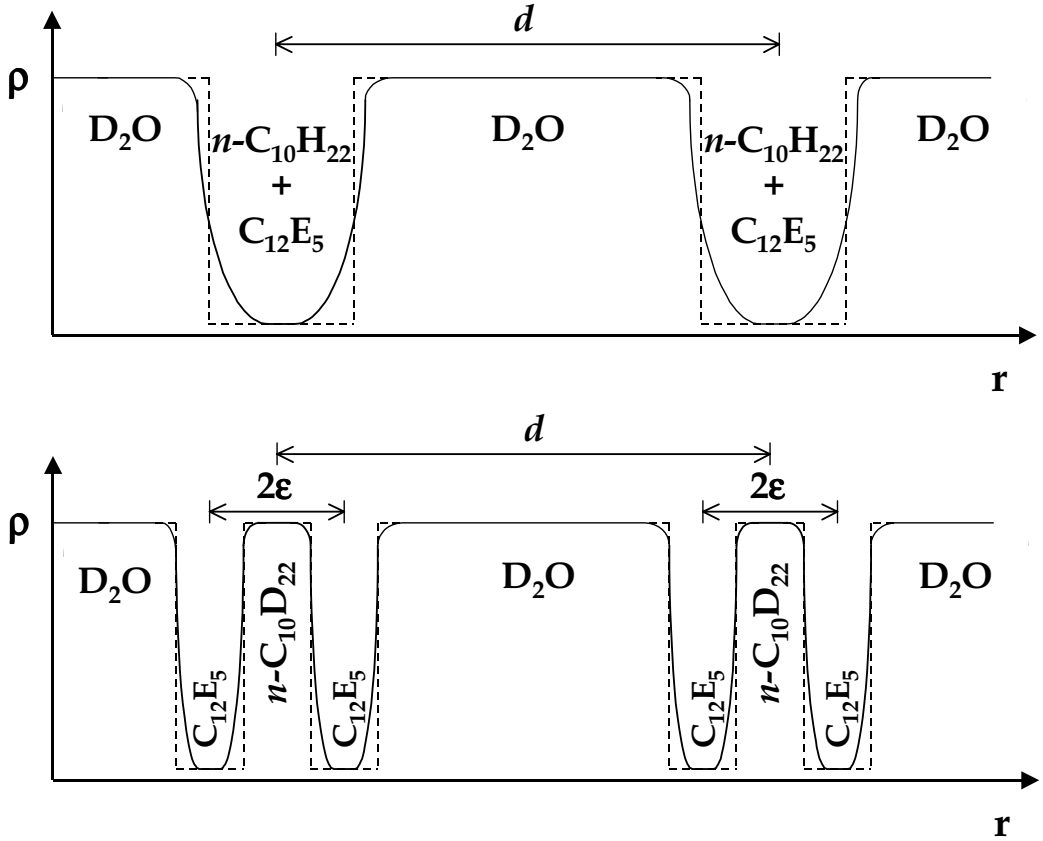

Fig. 8.3(3): approximate scattering length density profile illustrating bulk (top) and film contrast (bottom). For bulk contrast only the hydrophilic component is deuterated, while in film contrast both the hydrophilic component and the hydrophobic oil are deuterated. Thus the distance *d* can be obtained from experiments using bulk contrast, while both distances *d* and 2ε can be obtained using film contrast.

In the ‘ideal’ case of a non-mobile bilayer, without any kind of penetration of molecules of one domain into the molecules of another, one would expect a rectangular scattering length density profile (dashed lines). However, since in reality these factors occur, diffuse boundary layers exist between the different components and the profile is more of a Gaussian shape (solid lines). Although film contrast experiments can yield both the distances d and 2ε, one nevertheless resorts to using bulk contrast to determine the former, as the difference of the average scattering length density $\langle\Delta\rho_s\rangle = \rho_d$ of the bilayer is considerably higher in this case. Also, film contrast could of course be achieved as well by simply using a fully deuterated surfactant, while the water and oil component remain protonated. This however was avoided due to financial considerations.

8.4 Data Processing

The neutron detector at a given distance d_{sd} behind the sample is divided into 64x64 elements of $1cm^2$ each. The data that is obtained is the number of neutrons that arrive at those elements per second (counts per second or cps). Since intensity is an energy per unit of time times unit of area (in SI units $J/(s \cdot m^2)$), the *average* intensity at each element can easily be determined over a given time interval via the area of the element, the cps and the energy of each neutron (eq. 8.1(1)). The magnitude of that time interval is preferred to be minimal, but this is limited by a good signal to noise ratio and therefore by the intensity of the incident neutron beam and the strength with which the sample scatters. In the case of isotropic or disordered samples scattering is isotropic and therefore the detector data can be averaged radially over 2π rad, as each distance r from the beam centre corresponds to the same value of q, and the signal to noise ratio is thus improved.

However, when anisotropic scattering occurs radial averaging cannot be done over all angles. Fig. 8.4(1), depicts raw detector data, i.e. the number of counts that were detected in a (120s) time interval in each $1cm^2$ element of the 64x64 element matrix. After determining the beam centre, a sector of given size is chosen to encompass the area of the detector, where scattering is deemed to be still isotropic, i.e. within this area all elements of distance r from the beam centre have approximately the same number of counts. The data within such a sector is then averaged radially, while any data outside the sector is ignored.

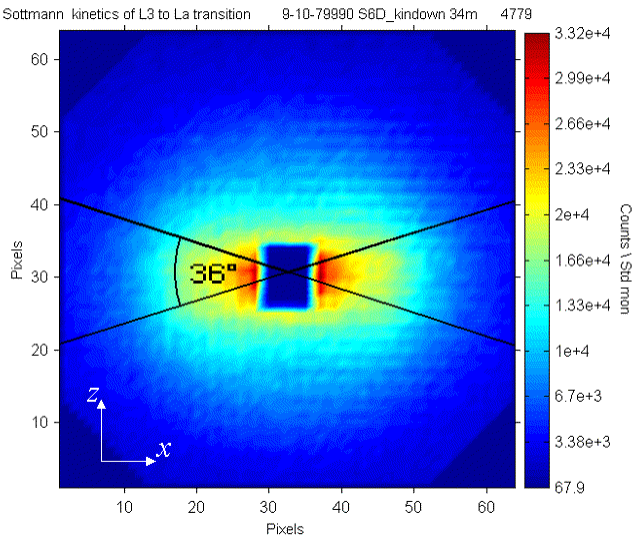

Fig. 8.4(1): anisotropic 2D data set of detector counts with beam stop (centre). When radially averaging and thus reducing data to 1D, only the two marked, opposite sectors were taken into account, thus disregarding the rest. Sector angles θ_s were usually $\theta_s = 36°$ and deviation from the *x*-axis $\varphi = 0°$, but sector size and orientation was modified appropriately if required. This and all similar images were generated by ILL software (Grasp).

When measuring the intensity as a function of q in SANS (or for that matter any scattering) experiments, it is useful to determine the *absolute* scattering intensity $I(q)$ in order to be able to directly compare the obtained results with those of other experiments, which were conducted with alternative instruments, parameters or components. This is achieved by measuring key parameters using a standard substance (usually H_2O) and an empty cell and then calculating $I(q)$ via

$$I(q) = \frac{I_{Sa} - I_{Cd} - \frac{T_{Sa}}{T_{EC}} \cdot \left(I_{EC} - I_{Cd}\right)}{I_{H_2O} - I_{Cd} - \frac{T_{Sa}}{T_{EC,H_2O}} \cdot \left(I_{EC,H_2O} - I_{Cd}\right)} \cdot \frac{T_{H_2O}}{T_{Sa}} \cdot \frac{d\sigma_{H_2O}}{d\Omega} \qquad \text{eq. 8.4(1)}$$

Here T is transmittance $T = I/I_0$, where I_0 is the intensity of the incident neutron beam. The subscripts denote intensity or transmittance values measured for the sample (Sa), the standard substance (H_2O), an empty cell (EC), or the background (Cd, which is determined by blocking the neutron beam with a neutron absorbing cadmium sheet). $d\sigma_{H2O}/d\Omega$ is the differential total scattering cross section of H_2O over the differential solid angle Ω. The scattering cross section of a molecule is closely related to the scattering length values b of its atoms.

8.5 The Equilibrium L_3 State

Scattering spectra of the equilibrium L_3-state were generated at sample-to-detector distances d_{sd} = 1.1m, 4.5m, 16m and 34m, covering a q-range of approx. 0.001 Å^{-1} to 0.3 Å^{-1}. Samples of bilayer volume fractions ϕ_{B+C} = 0.05, 0.06, 0.07, 0.09 and 0.195 were investigated in bulk contrast. The results are plotted in fig. 8.5(1), the absolute intensity is modified by a given factor to facilitate viewing.

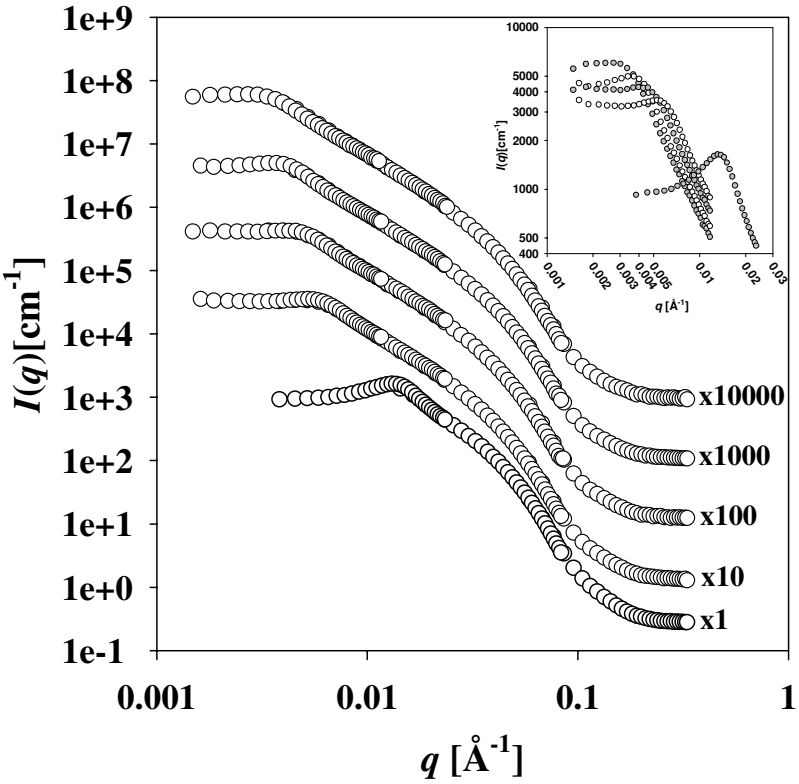

Fig. 8.5(1): bulk contrast SANS plots of the equilibrium L_3-phase of samples of ϕ_{B+C} = 0.05, 0.06, 0.07, 0.09, and 0.195 (top to bottom). The absolute intensities are distorted by a factor given in the graph. (*insert*): scans at a single sample-to-detector distance d_{sd} emphasising the correlation peak. Plot intensities are absolute and samples of increasing ϕ_{B+C} appear from top to bottom.

All plots of fig. 8.5(1) exhibit a peak, which is correlated to the bilayer repeat distance d_3. As expected, the position of this correlation peak is shifted to higher q-values (corresponding to shorter distances d_3) with increasing bilayer volume fraction in accordance with the ideal swelling condition (see eq. 2.2(4)). The peak also becomes progressively more defined, this being most obviously apparent in the case of the ϕ_{B+C} = 0.195 sample. The insert focuses on the q-range in proximity of said correlation peaks and there the plots are presented in unmodified, absolute intensity. The decrease of scattering intensity with increasing ϕ_{B+C} occurs since the scattering intensity is approximately proportional to the repeat distance d^3 at

low q-values. This can be understood through the description of inelastic scattering by *Rayleigh*, where $I \propto r^6$ for spheres (and r equals to a sphere radius). As the volume of the scattering phase is then given by $\phi_{scat} = N \cdot 4/3 \cdot \pi \cdot r^3$, $I \propto \phi_{scat} \cdot r^3$. Thus, for the complex fluids studied here, this expression can be approximated to $I \propto \phi_{B+C} \cdot d^3$.

Generally, when following the plots in the direction of low to high q-values, the intensity first declines proportional to $\sim q^{-2}$ after the correlation peak. This value then transforms to $\sim q^{-4}$, before the intensities reach their final, background values at high q. The decline has been theoretically described[115] for diffuse interfaces to develop according to $\exp(-q^2t^2) \cdot q^{-4}$, where t corresponds to the variance of the diffuseness of the interface (here the surfactant monolayer). Generally, the scattering intensity at high q-values is also proportional to the bilayer volume fraction ϕ_{B+C}. The incoherent background scattering is more intense for samples of higher ϕ_{B+C} due to the increased density of ^{1}H-nuclei, but even in the case of $\phi_{B+C} = 0.195$ below 0.3cm^{-1}. The observed behaviour and the overall appearance of the SANS curves are in accordance with those of sponge phases found in earlier studies[46,45].

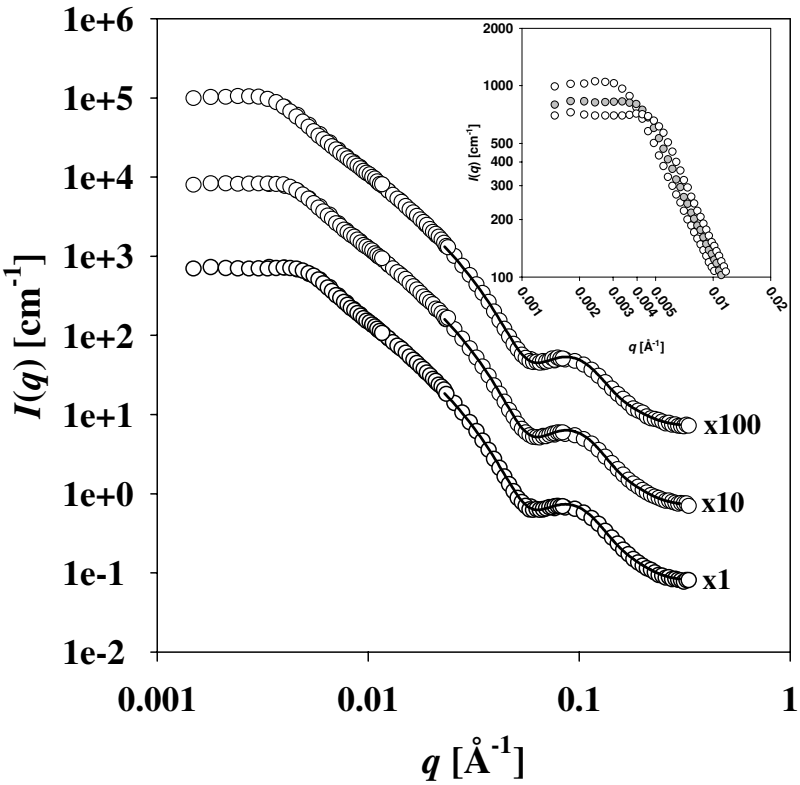

Fig. 8.5(2): film contrast SANS plots of the equilibrium L_3-phase of samples of ϕ_{B+C} = 0.05, 0.06, and 0.07 (top to bottom) The absolute intensities are distorted by a factor given in the graph. The data is fitted with eq. 8.5(1) (solid lines). *insert*: scans at a single sample-to-detector distance d_{sd} emphasising the correlation peak. Plot intensities are absolute and samples of increasing ϕ_{B+C} appear from top to bottom.

Fig. 8.5(2) depicts the results of film contrast investigations on samples of ϕ_{B+C} = 0.05, 0.06, and 0.07. The correlation peaks at low q correspond again to the bilayer repeat distance

d_3, and behave as previously described, although they are much less pronounced. The insert emphasises once more the q-range in the proximity of said peaks and there the plots are presented in unmodified, absolute intensity. Note the considerable differences in scattering intensity when comparing the results with those of the bulk contrast measurements. At q-values of ~0.09 Å^{-1} a further peak resulting from the contrast difference within the bilayer is present. In order to determine the bilayer thickness 2ε, the relevant part of the scattering plots are fitted with[115,116]

$$I(q) = f \cdot \frac{8\pi\phi_{C,i}}{2q^2}\frac{v_C}{a_C}(\Delta\rho)^2 e^{-q^2t^2}\, 0.5(1+\cos(2q\varepsilon)e^{-2\sigma^2q^2}) + I_{incoh} \qquad \text{eq. 8.5(1)}$$

where $\phi_{C,i}$ is the surfactant volume fraction of the interface, v_c the volume of a surfactant molecule and a_c its area, t the diffuseness of the monolayers, σ the invariance of the bilayer and thus σ/ε its polydispersity, I_{incoh} the intensity of the incoherent background scattering and f a factor compensating for inaccuracies in determining the absolute intensity. $\phi_{C,i}$ differs from the overall surfactant volume fraction in that it excludes any surfactant which is solubilised (as a monomere) in the water or oil domain.

The monomeric solubility of $C_{12}E_5$ in water is negligible, but is considerably greater for oil ($\gamma_{mon,B} \approx 0.01$). However, as the oil volume fraction in the samples studied is small, $\phi_{C,i} \approx \phi_C$ can be assumed. Fits made in this manner are satisfactory in describing the position of the local minimum and maximum (solid lines), although there is a systematic deviation to higher $I(q)$ around said maximum. Already from the morphology of the scattering curves, it is apparent that the bilayer thickness is constant in the three samples, as is required of samples of identical ω_b values. The observed behaviour and the overall appearance of the SANS curves are again in accordance with those of sponge phases found in earlier studies[46,45].

In 8.5(3) the scattering behaviour of bulk contrast samples of constant bilayer volume fraction $\phi_{B+C} = 0.06$, but varying viscosity is illustrated. Viscosities were increased by replacing a fraction of the D_2O solvent with sucrose, yielding samples with sucrose mass fractions of ψ=0.230 and 0.340 (corresponding to molar fractions of x=0.0172 and 0.0293 respectively) and viscosities of $\eta_{D2O/S} = \eta_0 \cdot 2.261$ and $\eta_{D2O/S} = \eta_0 \cdot 4.320$ with respect to the D_2O viscosity η_0=1.251 cP. The scattering curve of the $\phi_{B+C} = 0.06$ sample with pure D_2O as the hydrophilic component, which has previously been presented in fig. 8.5(1), is given once more. The appearance of the three plots is very similar. The imperatively common position of

the correlation peaks is evident. The decrease in intensity with increasing sucrose addition (fig. 8.5(3), *insert*) is the result of reducing the scattering length density ρ of the hydrophilic domains (eq. 8.3(2)). Surprisingly, the correlation peak is less defined in samples of higher viscosity, although one would intuitively expect less bilayer undulations here.

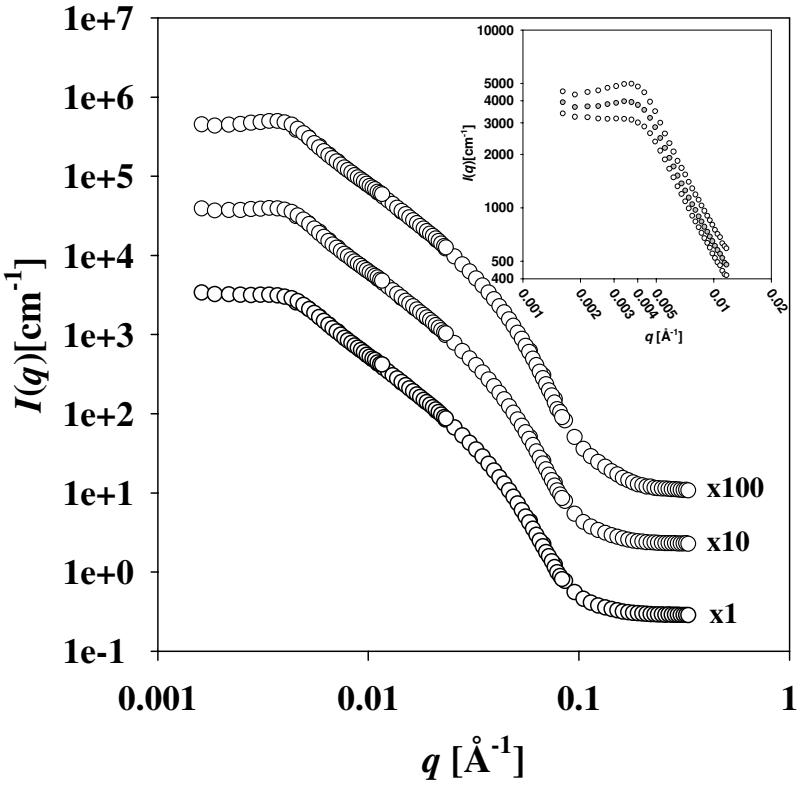

Fig. 8.5(3): bulk contrast SANS plots of the equilibrium L_3-phase of samples of $\phi_{B+C} = 0.06$, but varying viscosity η (η_0=1.251 cP, $\eta_{D2O/S}=\eta_0 \cdot 2.261$ and $\eta_{D2O/S}=\eta_0 \cdot 4.320$; top to bottom). (*insert*): scans at sample-to-detector distance d_{sd}=34.0m emphasising the structure peak. Plot intensities are absolute and samples of increasing η again appear from top to bottom.

8.6 Temperature Jump Experiments

The temperature jump experiments were generally performed after obtaining scattering curves of the initial phase (sponge or lamellar) in equilibrium. The beginning of a transition experiment ($t = 0$) is defined as the point in time at which the temperature of the cell holder was changed to the value of the target temperature. At $t = 0$ accumulation of the first 2D detector data also commenced. Detector count increase continued for an arranged time interval, so that a satisfactory signal to noise ratio was obtained. Subsequently and without delay, the detector counts were set to zero and the next interval of data acquisition began and so on. All intervals of a given experiment were constant and data continued to be collected until the phase transition was deemed complete. A visual examination of the samples was

then carried out to confirm the attainment of the desired one phase region. For bulk contrast samples, the measurements were performed at a single sample-to-detector distance (usually d_{sd}=34m). However, sample-to-detector distances d_{sd} vary in the individual experiments (section 10.5).

After data processing (see above) each of the 2D data acquisition intervals yields a single 1D scattering curve (absolute intensity I as function of q) and thus the experiments are time resolved SANS (TR-SANS) investigations. The longest intervals constituted to 120s (bulk contrast experiments with samples of low ϕ_{B+C}), shorter times could be achieved for the samples of higher concentration and in case of film contrast experiments (section 10.5). Thus moderate time resolution is achieved when monitoring phase transitions of ~1000s to ~3000s. Temperature equilibrium was attained after 150s to 250s (depending on the magnitude of the temperature jump, ΔT = 1.5 to 3.0°C) and occurred therefore fast enough to not significantly interfere with the phase transition kinetics.

8.6.1 The L_3 to L_α phase transition

By following the evolution of neutron scattering in time resolved experiments, one is able to examine the development of scattering peaks correlated to repeat distances and gains insight not only into the kinetics of the phase transitions, but also into the structural and dynamic characteristics of the complex fluids at different length scales. When observing samples of bulk contrast, long range ordering (interbilayer distances) is probed and optical density fluctuations can be detected, while the use of film contrast enables to investigate short range ordering and the bilayer properties.

Fig. 8.6.1(1) displays the typical evolution of the neutron scattering behaviour in time that is observed for L_3-to-L_α phase transitions. Depicted is unprocessed 2D-detector data, i.e. detector counts per detector element, for an experiment in bulk contrast (0.0016Å < q < 0.0177Å). In the first image (a), the correlation peak of the L_3 bilayer repeat distance d_3 is clearly visible. Strikingly, the scattering becomes anisotropic at an advanced point in time (image (d); in this case onset is at t=28min) and this characteristic increases, until it often becomes highly pronounced (f). This unanticipated development occurred in all of the performed experiments, including those of film contrast (0.0125Å<q<0.3303Å), with the exception of those dealing with the sample of highest bilayer volume fraction (ϕ_{B+C} = 0.195). From the previous NMR investigations, it is known that the lamellar phase nucleates within the sponge phase and that the nuclei subsequently grow until all of the L_3-phase is converted

to the new phase. In unperturbed conditions one therefore expects a macroscopic order that is reminiscent of a polycrystalline powder and as such isotropic scattering (see section 7.4.5.1).

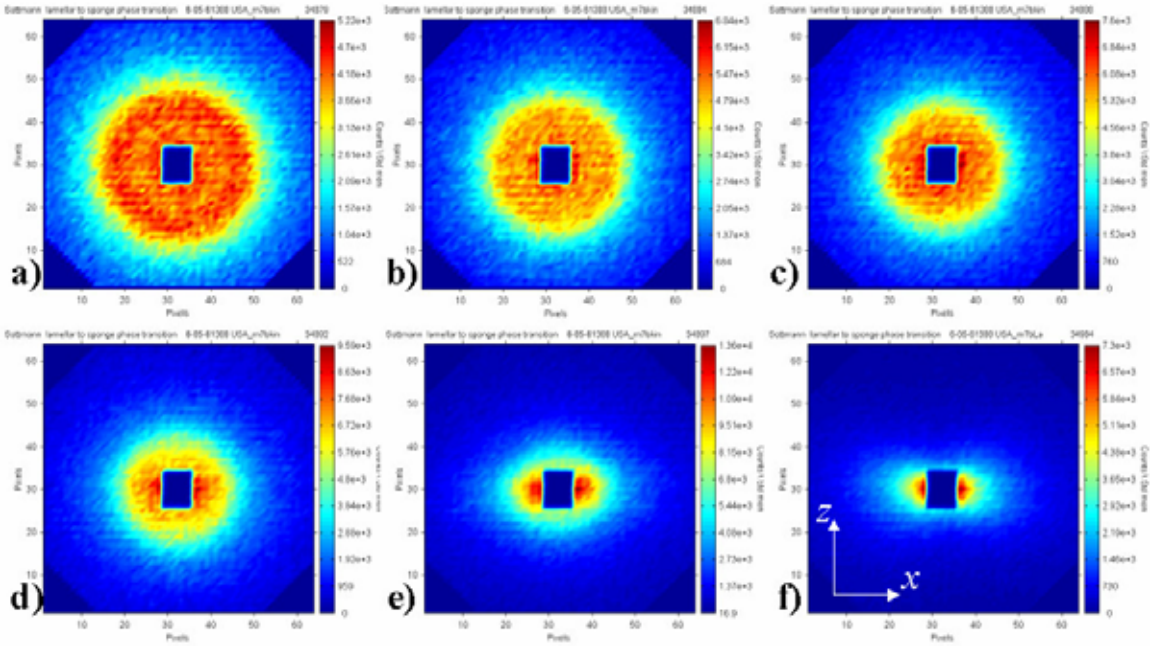

Fig. 8.6.1(1): unprocessed SANS detector data demonstrating the typical emergence and development of anisotropic scattering. Presented is an L_3-to-L_α phase transition experiment with ΔT = -1.5°C at $\phi_{B+C} = 0.07$ (bulk contrast d_{sd} = 34m). The data was recorded at t = 2, 12, 20, 28, 36 and 50 min (images a to f). The approximate form of image d) was defined as the onset of anisotropy. Note that the colours of the individual plots do not correspond to the same number of detector counts.

Here however, one clearly witnesses ordering of lamellae on a macroscopic scale, which is well known from SANS experiments with lamellar phases experiencing shear forces[117,118]. Defining the detector to be in the *xz*-plane (see fig. 8.6.1(1f) and fig. 8.1(1)) and the neutron beam thus parallel to the *y*-axis, the bilayers are predominantly oriented parallel to the *z*-axis (2D-"powder"), and to a considerable fraction even close to the *yz*-plane, since bilayers parallel to the *xz*-plane do not contribute to scattering.

The following trends can be distinguished plainly regarding this surprising phenomenon. Firstly, the time until the onset of anisotropy (onset time) appears to be directly correlated to the kinetics of the observed phase transition (known from NMR experiments); i.e. the anisotropy appears earlier in case of higher bilayer volume fraction ϕ_{B+C}, greater amplitude of the temperature jump ΔT and samples of lower viscosity η (this is addressed in detail in the discussion section 8.7). Interestingly, in the experiments where the anisotropy appears sooner the orientation effect does not become so pronounced. Several samples were shaken after completion of the L_3-to-L_α transition within the cell holder, resulting in actually

increasing the anisotropy in several cases or causing the anisotropic scattering pattern to twist on the detector (i.e. $\varphi \neq 0°$, see fig. 8.4(1)). Finally, probing a single sample with an aperture of d_a=2mm at three positions (4mm apart each) on the z-axis, revealed a gradient of the anisotropy, i.e. the anisotropy grew more pronounced towards the bottom of the sample (fig. 8.6.1(2)).

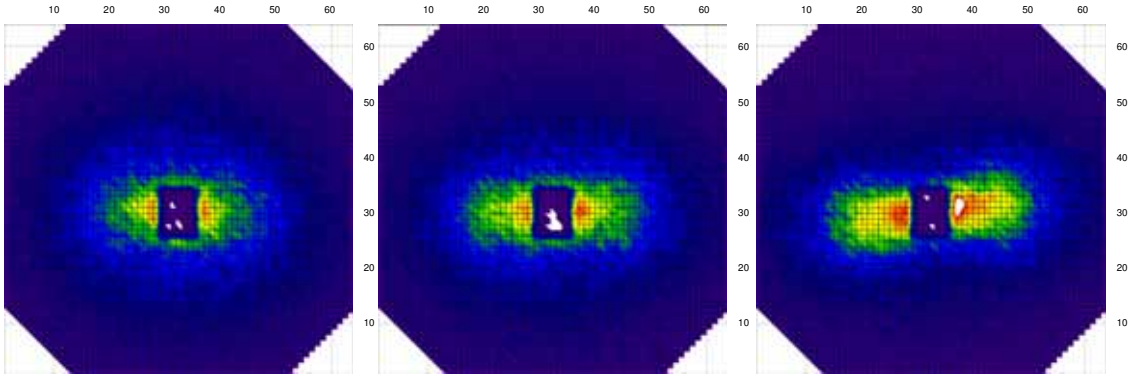

Fig. 8.6.1(2): unprocessed SANS detector data showing an increase in the degree of anisotropy from the top (left) to the bottom (right) of a sample ($\phi_{B+C} = 0.06$, $\eta_{D2O/S}=\eta_0 \cdot 2.261$). Colours represent an identical number of counts in each plot. The centre is occupied by the beam stop.

SANS curves are obtained after radially averaging detector data (in anisotropic cases only a specific sector is considered, see section 8.4) and converting it to absolute scale. The characteristics of L_3-to-L_α phase transitions, which were examined in bulk contrast, can be observed well in the form of the 3D-plots given in fig. 8.6.1(3) and 8.6.1(4), where consecutively acquired scattering curves (absolute intensity as function of scattering vector q) are given at their respective times t. The general scattering curve evolution occurring in sponge to lamellar transitions is similar for almost all the performed experiments, i.e. irrespective of changes of the three studied parameters, ΔT, ϕ_{B+C} and η. (The only exception occurred when investigating a sample of considerably higher bilayer volume fraction, $\phi_{B+C} = 0.195$, fig. 8.6.1(4f) see below). Therefore, the evolution will be described via the transition of a $\phi_{B+C} = 0.06$ sample, which underwent a T-jump of $\Delta T = -1.5°C$ and was monitored at $d_{sd} = 34m$ (fig. 8.6.1(3)). This plot is given again in fig. 8.6.1(4a) for comparison.

At the $t = 0$ mark, a part of the equilibrium L_3-state scattering curve (fig. 8.5(1)) at low q-values is plotted. The L_3-structure correlation peak and the decline of intensity at higher q-values, proportional to q^{-2}, are plainly visible. As the transition begins, the peak actually becomes more defined, due to a general decline in scattering intensity at lower q-values, and shifts to slightly higher q-values. This behaviour is depicted more clearly in fig. 8.6.1(5, *left*) by means of an experiment, where the characteristic is more pronounced. Then, the peak is

shifted continually to lower q-values (surpassing its initial location) while widening somewhat, whereas simultaneously the scattering intensity increases steadily in the low q-region. This segment of the transitions is especially illustrated in fig. 8.6.1(5, *right*) as it is of crucial importance for later analysis.

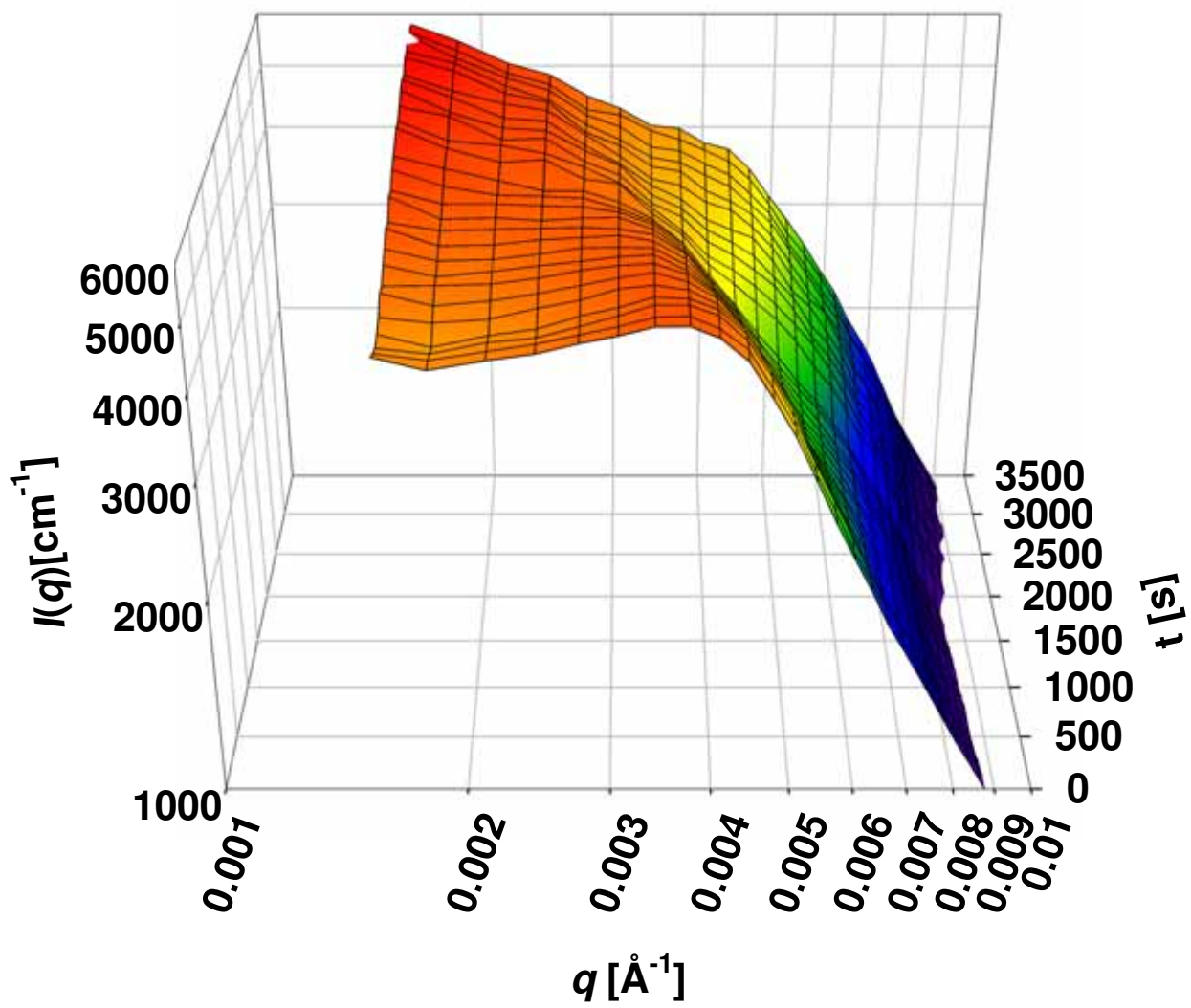

Fig. 8.6.1(3): double logarithmic 3D plot depicting the evolution of the radially averaged and normalised SANS data with time for an L_3-to-L_α transition investigated in bulk contrast (ϕ_{B+C} =0.06, ΔT = -1.5°C, d_{sd} = 34m).

In the experiment of fig. 8.6.1(3) the onset of anisotropy occurs roughly at t = 1500s. At this point the 'L_3-peak' has degraded to the state of a mere shoulder. As the transition continues and the scattering becomes increasingly anisotropic, the intensity in the low q-region persists to rise and therefore said shoulder disappears completely. At this time (~2250s), the change of slope in the displayed q-region appears to be continuous. As time progresses and the order of lamellae increases further, the change of slope in most experiments becomes gradually more discontinuous at a higher but constant q-value, i.e. a new shoulder is formed. This occurs at $q \approx 0.0045 Å^{-1}$ in fig. 8.6.1(3) and this shoulder is now

identified as the Bragg 'peak' of the lamellar phase. It is correlated to the bilayer repeat distance d_3 via eq. 8.1(4). From SANS investigations on the lamellar phase of dilute systems, it is known that these do not exhibit a defined structure factor peak[117].

By means of fig. 8.6.1(4), the influence of changing sample and environmental parameters when studying the L_3-to-L_α transition in bulk contrast will now be examined. In fig 8.6.1(4b), one observes the kinetics of a ϕ_{B+C}= 0.06 sample where the viscosity of the D_2O component has been increased through the addition of sucrose (sucrose mass fractions ψ=0.230, molar fractions x=0.0172, viscosity of the hydrophilic component $\eta_{D2O/S} = \eta_0 \cdot 2.261$ with respect to the D_2O viscosity η_0=1.251 cP). It is remarkably similar to fig. 8.6.1(4a), although the L_3-spectrum at $t = 0$ is of considerably lower scattering intensity. Accordingly the intensity at small q has to rise more strongly, since the two final L_α states are very much alike, both in terms of overall shape and intensity (the Bragg 'peak' is located at $q \approx 0.0045 Å^{-1}$ respectively). Note however, that the transition speed is reduced by a factor of two when compared with fig 8.6.1(4a).

Fig. 8.6.1(4b-d) illustrates the effect of increasing the amplitude of the temperature jump ΔT (ΔT= -1.5, -2.0 and -3.0°C respectively). All experiments where performed on the $\phi_{B+C} = 0.06$ sample of increased viscosity. The initial L_3-state in all three plots is virtually identical, attesting to the good reproducibility of the sponge phase. Again, the final L_α states are very similar in all three cases, i.e. the Bragg 'peaks' are of similar position and intensity. Fig. 8.6.1(4d) appears to show a stronger decrease of scattering intensity after the fast shift of the L_3-peak to lower q-values, but this is only due to the distortion of perspective. Overall the SANS spectra development of the three experiments is virtually analogous, except of course with respect to the time scale. One observes a strong acceleration of the phase transition upon increasing ΔT.

When comparing experiments at different bilayer volume fractions ϕ_{B+C}, (Fig. 8.6.1(4a, e and f); ϕ_{B+C} = 0.06, 0.09 and 0.195), one notices that a constant scattering profile is attained sooner, i.e. the phase transitions terminating sooner, when ϕ_{B+C} is increased. Note however that in the given examples ΔT = -1.5°C for (a), while ΔT = -2.0°C for (e) and (f). In principal, the SANS spectra development of the $\phi_{B+C} = 0.09$ sample is again of the kind previously described, however the development of a Bragg peak (shoulder) could not be observed, although one expects to detect the Bragg peak evermore easily with increasing ϕ_{B+C} [117]. Fig. (f) depicts the transition for a sample of considerably higher ϕ_{B+C} and in order to access the required region of higher q-values, the transition was monitored at d_{sd} = 16m.

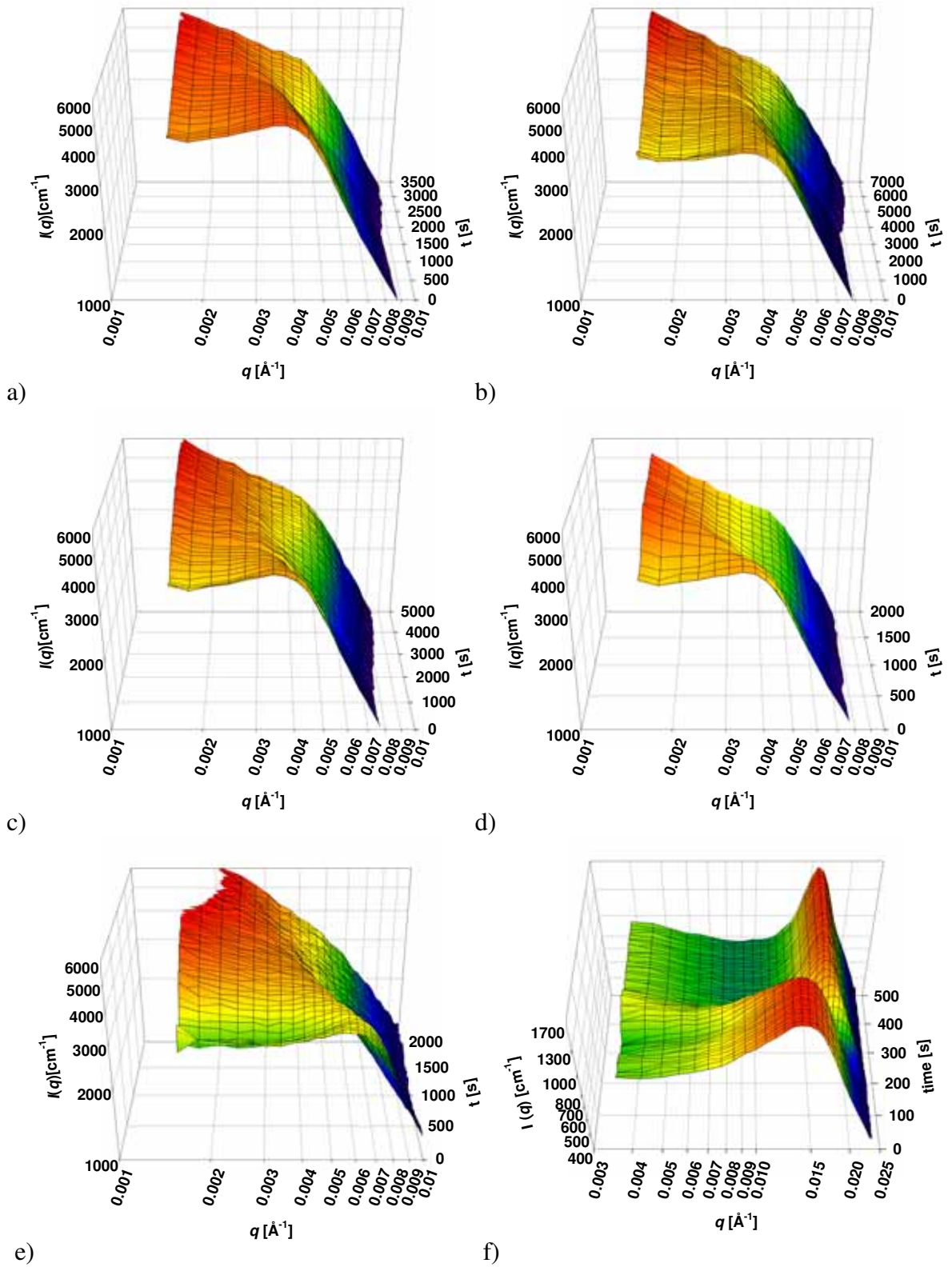

Fig. 8.6.1(4): scattering curves as function of time for L_3-to-L_α phase transitions investigated in bulk contrast. Note the different time scales. Intensity and q scaling are identical except for plot f. a) $\phi_{B+C} = 0.06$, $\Delta T = -1.5$°C b) $\phi_{B+C} = 0.06$, $\Delta T = -1.5$°C, $\eta_{D2O/S} = \eta_0 \cdot 2.261$ c) $\phi_{B+C} = 0.06$, $\Delta T = -2.0$°C, $\eta_{D2O/S} = \eta_0 \cdot 2.261$ d) $\phi_{B+C} = 0.06$, $\Delta T = -3.0$°C, $\eta_{D2O/S} = \eta_0 \cdot 2.261$ e) $\phi_{B+C} = 0.09$, $\Delta T = -2.0$°C f) $\phi_{B+C} = 0.195$, $\Delta T = -2.0$

The SANS curve evolution is evidently dissimilar to those of the dilute samples. Most notably, there is no strong rise of scattering intensity in the low q-region and the lamellar Bragg peak is very distinct. Nevertheless, the L_3-peak is shifted to higher q-values just as the Bragg peak is formed and at this time there is a small but significant increase of intensity in the low q-region. Detailed examination also shows that the L_α-peak emerges at notably higher q-values when compared to its position in the equilibrium state. With exception of the small intensity increase the stated phenomena are not truly visible in the presented illustration. Interestingly, experiments with samples of this high ϕ_{B+C} were the only ones to not exhibit anisotropic scattering behaviour. Lastly, it is important to stress that fig. 8.6.1(4f) most likely does not reflect the kinetics of transition, but rather those of the sample cooling process, since the relaxation time constant in the L_3-phase is over an order of magnitude smaller at this composition[72]. Thus, the spectra of fig. 8.6.1(4f) are all from equilibrium states, i.e. from the L_3/L_α coexistence region during the transition.

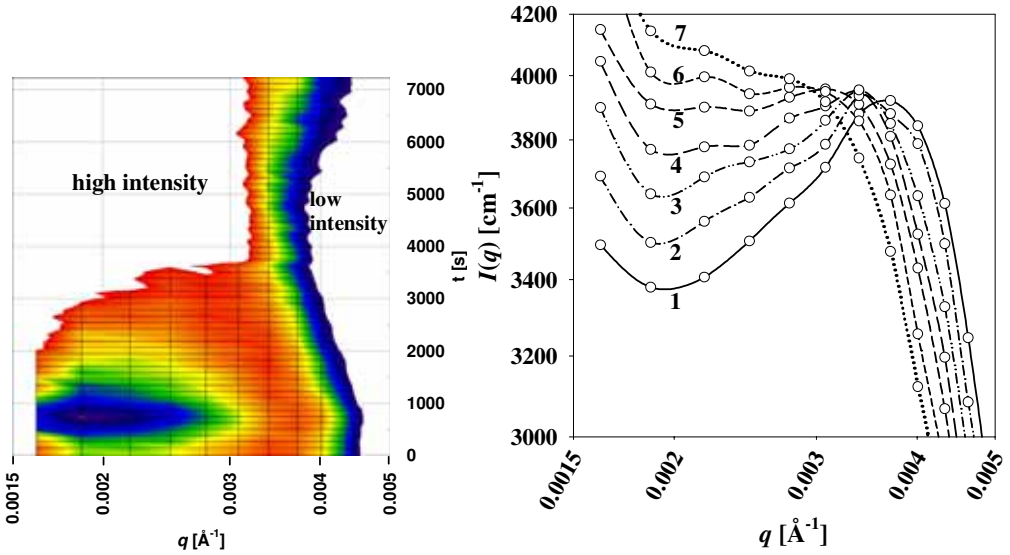

Fig. 8.6.1(5): details of L_3-peak evolution form fig. 8.6.1(4b) ($\phi_{B+C} = 0.06$, $\eta_{D2O/S} = \eta_0 \cdot 2.261$, $\Delta T = -1.5$°C). a) selected intensity profile visualising the shift of the L_3-peak first to higher and then to lower q-values b) double logarithmic plot depicting the shift of the L_3-peak to lower q-values after attaining its maximum definition at ~600s. The chronological order of the plotted spectra is marked by the numbers 1 to 7. It is important to note, that the structure factor peak does not grow significantly in width. This is evident as the sections of strong intensity decay are virtually parallel, i.e. they are shifted to lower q-values in a similar manner as the L_3-peak itself.

The L_3-to-L_α transitions were also monitored for film contrast samples ($\phi_{B+C} = 0.05$, 0.06 and 0.07), alternating between sample-to-detector distances $d_{sd} = 1.1$ and 4.5m and thereby covering a q-range of $0.013\text{Å}^{-1} < q < 0.33\text{Å}^{-1}$. The peaks correlated to the bilayer thickness 2ε (fig. 8.5(2)) retained their characteristics throughout the three transitions, so that the distances 2ε and the polydispersity of the bilayers σ/ε remain constant in each case. In

fact, the only development during the transitions was a slight reduction of scattering intensity, with a minimum at the onset of anisotropy, followed by a return to the original value. Fig. 8.6.1(6). displays the transition of the $\phi_{B+C} = 0.06$ sample.

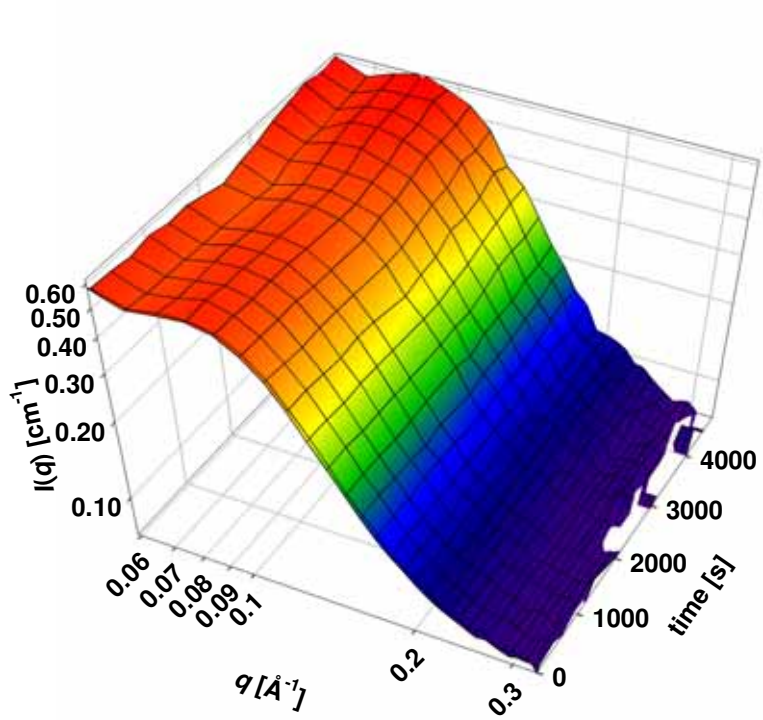

Fig. 8.6.1(6): scattering curves as function of time for an L_3-to-L_α phase transition investigated in film contrast ($\phi_{B+C} =$ 0.06, ΔT = -1.5°C). Only data obtained from the d_{sd} = 1.1m setting is presented.

Here the minimum is located at ~2300s and this coincides with the point in time where the scattering curve of the analogous bulk contrast experiment is devoid of any 'shoulders' (fig 8.6.1(3)). In summary, one finds that there is no evidence for a change in the short range ordering of the bilayer structure, which could have resulted due to the different topology in the L_3 and L_α phases.

8.6.2 The Equilibrium L_α state

That the equilibrium L_α-state does not yield perfectly reproducible scattering behaviour has already become evident in fig. 8.6.1(4e), where a Bragg 'shoulder' failed to form after subjecting the $\phi_{B+C} = 0.09$ sample to a temperature jump of ΔT = -2.0°C. This is due to irreproducibility of the exact state of macroscopic orientation of the lamellar 'crystallites'. In fig. 8.6.2(1, *left*) two comprehensive SANS spectra are presented, which where recorded directly after the completion of their respective phase transitions. Visible is a

great difference between the well defined Bragg peak of the $\phi_{B+C} = 0.195$ sample and the corresponding shoulder, which formed in case of $\phi_{B+C} = 0.06$ ($\eta_{D2O/S} = \eta_0 \cdot 2.261$).

Most samples were shaken after completion of the phase transition resulting in the effects illustrated by fig. 8.6.2(1, *right*). Presented are the scattering curves obtained at $d_{sd} = 34$m of $\phi_{B+C} = 0.06$ (squares) and 0.09 (circles) samples. The significant loss of intensity occurs due to bilayers orientating parallel to the largest sample cell surface, i.e. perpendicular to the neutron beam, and as a result not contributing to scattering. Of course, the absolute scattering intensity is in general a function of the amount of perpendicularly oriented lamellae, and thus even in the unshaken samples subject to chance.

Furthermore, shaking by and large, increases the definition of Bragg peaks ('shoulders'). For the $\phi_{B+C} = 0.09$ sample, there is initially no hint of a 'Bragg shoulder' as the slope of the scattering curve changes continuously (grey circles). After shaking however, a shoulder is detectable at ~0.0068Å^{-1} (white circles). In case of the $\phi_{B+C} = 0.06$ sample, shaking had a more dramatic effect, since an already well discernable 'Bragg shoulder' (grey squares) is transformed into an unusually well pronounced Bragg peak for a sample of such high dilution (white squares). Evidently the peak is also moved to a higher q-value when compared to the 'shoulder' of the non-shaken state.

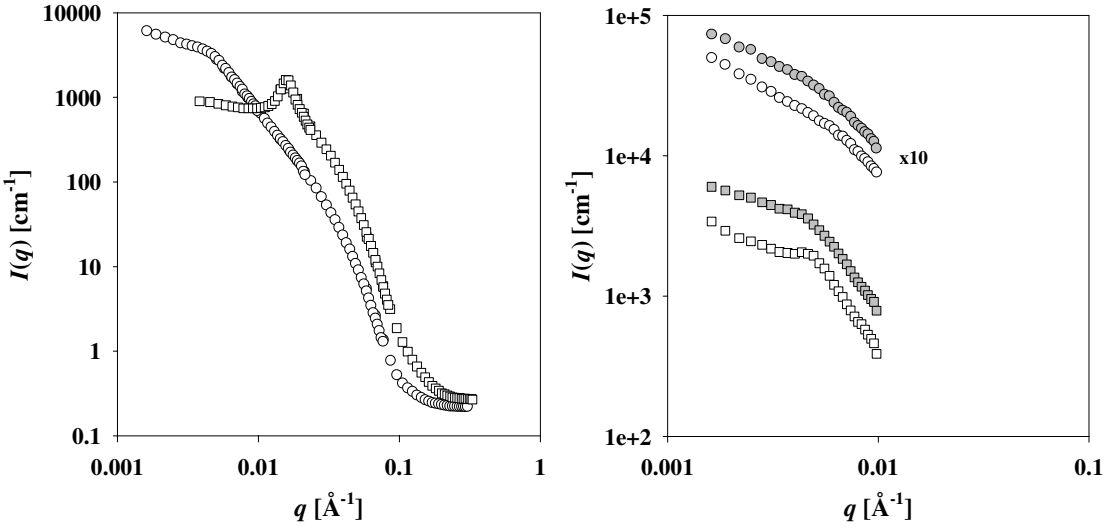

Fig. 8.6.2(1): SANS spectra of equilibrium bulk contrast L_α-phases (*left*): spectra that were recorded directly after completion of the phase transition, i.e. that were not shaken. $\phi_{B+C} = 0.06$, $\eta_{D2O/S} = \eta_0 \cdot 2.261$ (circles); $\phi_{B+C} = 0.195$ (squares); in both cases the samples were subjected to $\Delta T = -2.0$°C (*right*): graph depicting the increase of macroscopic orientation as a result of shaking the samples ($d_{sd} = 34$m only); (grey) scattering prior to shaking; (empty) scattering after shaking; (squares) $\phi_{B+C} = 0.06$, $\Delta T = -1.5$; (circles) $\phi_{B+C} = 0.09$, $\Delta T = -2.0$

As stated previously, the SANS curves of the film contrast samples hardly changed during the L_3-to-L_α transitions in the q-region monitored (fig. 8.6.1(6)). Accordingly, the scattering curves of the steady L_α-states appear very similar to those of the respective

L_3-phases (fig. 8.5(2)). Fig. 8.6.2(2, *left*) depicts the L_α scattering curves of the $\phi_{B+C} = 0.05$, 0.06 and 0.07 samples after shaking. In contrast to the scattering curves attained in bulk contrast, no Bragg 'shoulders' are discernible. Again the relevant region of the data is fitted with eq. 8.5(1) and satisfactory results are obtained using parameters very similar to those of the respective L_3-state fits.

The high degree of concordance between the L_3/L_α scattering curves is demonstrated furthermore by means of the $\phi_{B+C} = 0.07$ sample in fig. 8.6.2(2, *right*). The result from the (shaken) L_α-phase (black) is fitted to the one of the L_3-state (white), after subtraction of the incoherent background in each case and multiplication of the L_α scattering curve by a factor of 1.35. This factor is necessary to account for bilayers perpendicular to the neutron beam not contributing to scattering. The two curves are virtually identical at moderate and high q-values, i.e. differences are only visible in the region of the L_3-peak.

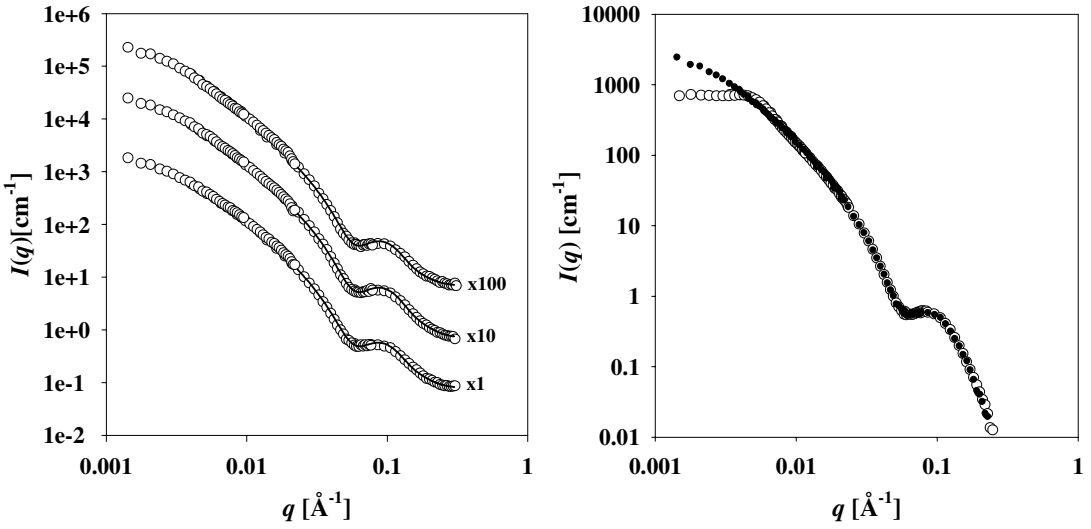

Fig. 8.6.2(2): (*left*): SANS curves of film contrast samples of ϕ_{B+C} =0.05, 0.06 and 0.07 (top to bottom) in the equilibrium L_α-state after shaking; ΔT = -1.5°C. (*right*): fit of the $\phi_{B+C} = 0.07$ L_α-spectrum from the graph on the left (black) to the corresponding L_3-spectrum of fig. 8.5(2) (*right*): after subtraction of the background scattering and multiplication by 1.35.

8.6.3 The L_α to L_3 phase transition

When observing L_α to L_3 phase transition, the general appearance of the SANS spectra evolution is strongly dependent on the initial state, i.e. the condition of the equilibrium L_α-phase. Fig. 8.6.3(1) depicts the scattering development in different experiments, where the sample composition, amplitudes of the temperature jumps ΔT and the beginning state (i.e. shaken or non-shaken) varies. When originating from a non-shaken state the, phase transitions are of the form illustrated in fig. 8.6.3(1a, b). On first inspection, these spectra appear very

similar to those of the opposite transition type given in fig. 8.6.1(4) (note the inversion of the time axis). The Bragg peak, i.e. the lamellar 'shoulder', disappears quickly at constant q, resulting in a spectrum where the scattering intensity declines continuously in the direction of larger q-values. The L_3-peak then appears at low q-values and is shifted to higher ones towards the completion of the phase transition.

There are however also distinct differences. Firstly, there is an obvious discrepancy in terms of transition speed, i.e. the anisotropy disappears quickly (usually within 600s) and the L_3-equilibrium phase is reached at a time at which the L_3-peaks of the L_3-to-L_α transitions are still shifting to lower q-values and are usually quite pronounced. For comparison, note that the transitions of fig. 8.6.3(1a, c, d, e, f) are the exact inversions of those presented in fig. 8.6.1(4c, b, a, e, f) respectively. For a detailed examination of the transition kinetics, the reader is asked to refer to the discussion section. A more significant difference is however, that the L_3-peak appears as soon as the L_α-'peak' has disappeared and when it does, it is very wide before becoming more and more defined as the transition nears completion. Although this phenomenon is not readily visible in fig. 8.6.3(1 esp. a and b), it does occur in all of the observed transitions, but is most distinct when starting with samples that have been shaken previously. One such case is illustrated in fig. 8.6.3(1c) and its L_3-peak formation is detailed in fig. 8.6.3(2). L_3-peaks of such width do not occur in the L_3-to-L_α transitions (compare fig. 8.6.1(5)). Note also that the transitions of fig. 8.6.1(5) and 8.6.3(2) are exact opposites. Again, the transition of fig. 8.6.3(1c) is fast (compare fig. 8.6.1(4b)) and the L_α-'shoulder' disappears quickly its constant q-value.

An exceptional transition behaviour was recorded in case of the $\phi_{B+C} = 0.06$ sample when subjecting it to temperature jump of $\Delta T = +1.5°C$ (fig. 8.6.3(1d). Note that this is the sample that became so extraordinarily well ordered after shaking (fig. 8.6.2(1)). Unlike the transition of fig. 8.6.3(1c), the intensity increase does not occur smoothly and there is a further disruption at a later point ($t \approx 1000$s). It has the longest transition time of all the L_α-to-L_3 transitions (~1500s), even though it a sample where the viscosity was not increased. Furthermore, an amount of anisotropy was retained until ~1400s. However, all of the above mentioned characteristics of the L_α-to-L_3 transitions appear here nevertheless.

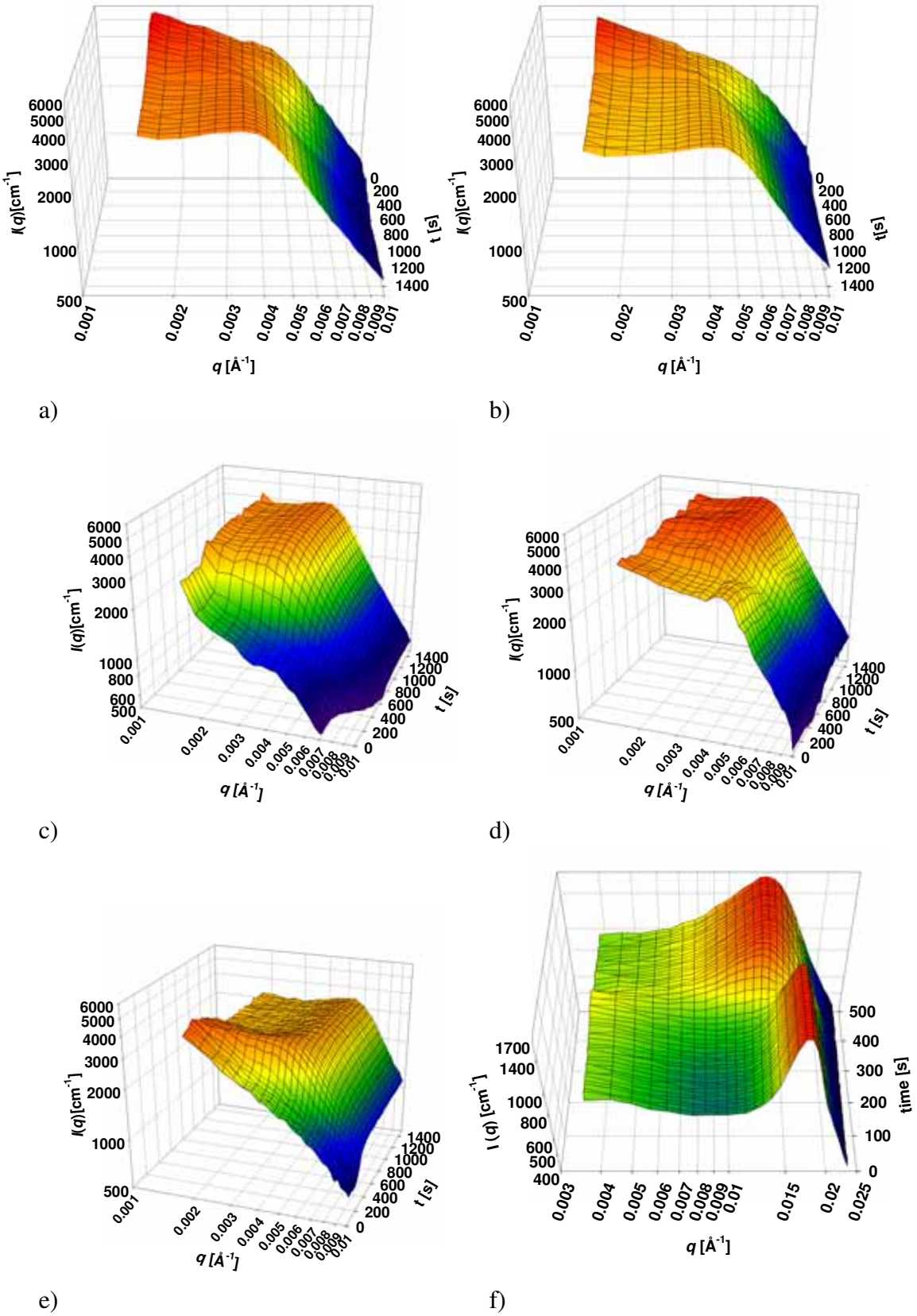

Fig. 8.6.3(1): scattering curves as function of time for L_α-to-L_3 phase transitions investigated in bulk contrast. Intensity, time and q scaling are identical except for plot f. Note however the different directions of the time axes. The initial, equilibrium L_α-states are either of shaken (s) or non-shaken (ns) samples. a) ϕ_{B+C}= 0.06, ΔT = +2.0°C, $\eta_{D2O/S} = \eta_0 \cdot 2.261$, ns b) ϕ_{B+C} = 0.07, ΔT = +1.5°C, $\eta_{D2O/S} = \eta_0 \cdot 2.261$, ns c) ϕ_{B+C} = 0.06, ΔT = +1.5°C, $\eta_{D2O/S} = \eta_0 \cdot 2.261$, s d) ϕ_{B+C} = 0.06, ΔT = +1.5°C, s e) ϕ_{B+C} = 0.09, ΔT = +2.0°C, s f) ϕ_{B+C} = 0.195, ΔT = +2.0°C, ns

Fig. 8.6.3(1e) depicts another transition originating from the shaken state. It is similar to the one of fig. 8.6.3(1c) in all respects, except that the rise of scattering intensity in the low q-region actually surpassed the values of the equilibrium L_3-state. Accordingly, the intensity there decreases again until the completion of the transition. Finally, fig. 8.6.3(1f) illustrates the transition of the concentrated sample, $\phi_{B+C} = 0.195$. It does not exhibit the transition traits as previously described, but is in fact virtually identical to its reverse transition of fig. 8.6.1(4f). This is expected, as the transition kinetics at this concentration are presumably much faster than the kinetics of the sample heating process and thus the scattering curves are recorded for two phase states that are essentially in equilibrium.

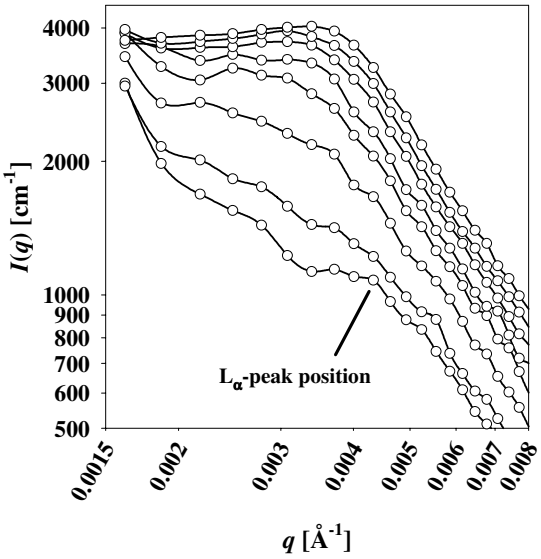

Fig. 8.6.3(2): detail of scattering evolution of the $\phi_{B+C} = 0.06$, $\eta_{D2O/S} = \eta_0 \cdot 2.261$ sample after a temperature jump of $\Delta T = +1.5°C$ (extracted from fig. 8.6.3(1c)). A very wide structure factor peak forms and then narrows continuously, developing toward the familiar L_3-peak shape as the general scattering intensity rises due to the decrease of anisotropy. This behaviour is in strong contrast to the one of the inverse transition presented in fig. 8.6.1(5).

Lamellar to sponge phase transition experiments monitored in film contrast exhibited no changes in scattering behaviour, just as their L_3 to L_α transitions counterparts (data not shown).

8.7 Interpretations of the Experimental Findings

8.7.1 The Sponge and Lamellar Steady States

As stated in section 8.5, the scattering curves of the equilibrium L_3-phase are of the typical form expected for that state[114] and the trends observed in the bulk (fig. 8.5(1)) and film contrast measurements (fig. 8.5(2)) coincide well with the results of earlier studies on the identical[46] or a similar[45] system. New are the results of fig. 8.5(3), where samples of identical bilayer volume fraction ϕ_{B+C}, but varying viscosity are compared (bulk contrast). The correlation peak is less defined at higher viscosity and this is counter intuitive, as one would expect less bilayer undulations in this case. However, in view of the discussion of section 7.4.6, it seems possible that the viscous samples are simply not in a state of true equilibrium (i.e. randomness of passage direction and a uniform passage density had not been attained) and that accordingly the interbilayer distance d_3 is more polydisperse. It is known from scattering experiments on bicontinous microemulsions, and the sponge phase is reminiscent of the structure found there, that systems of greater order lead to a more defined scattering maximum[119].

The equilibrium lamellar phase scattering curves are also of the expected form[120], and at ϕ_{B+C}=0.195 a first-order Bragg peak is clearly defined (fig. 8.6.2(1, *left*)). At high dilution (ϕ_{B+C} <0.10) however, the respective peaks are mere 'shoulders' at best, but this phenomenon is known[26] and stems from a large polydispersity of the interbilayer distance d_α and undulations of the bilayers. In a few cases (e.g. $\phi_{B+C} = 0.09$, $\Delta T = -2.0$; fig. 8.6.2(1, *right*) circle symbols), a Bragg 'shoulder' became detectable only after shaking of the sample, but for the $\phi_{B+C} = 0.06$ sample (squares), this led to the formation of an unusually well pronounced Bragg peak for a sample of such high dilution. Evidently the peak is also moved to a higher q-value when compared to the 'shoulder' of the non-shaken state. Since the undulation properties of the bilayers cannot be altered by having experienced shaking, it is clear that the polydispersity of d_α was reduced by the procedure. The peak shift occurs since the scattering intensity at low q-values is approximately proportional to d_α^3. (see section 8.5). In diluted lamellar phases, Bragg peak sharpening and the mentioned shift have previously been observed after bilayer undulations were reduced[40] (by modifying the system composition with additives).

For the dilute samples, where anisotropic scattering indicates a preferential orientation of the lamellar 'crystallites' in the L_α-state, shaking also led to lower scattering intensities due

to bilayers orienting parallel to the primary glass surface and thus perpendicular to the neutron beam, where they cannot contribute to scattering (fig. 8.6.2(1, *right*)). For the concentrated sample ($\phi_{B+C} = 0.195$) with its isotropic scattering however, the shaking merely caused the structure peak to broaden somewhat (data not shown), implying that the 3D-powder structure is retained, but a slight increase d_α polydispersity occurs. The anisotropy phenomenon will be discussed in more detail further below. Varying the amplitude of the temperature jump ΔT (ΔT = -1.5, -2.0, -3.0) in experiments with the $\phi_{B+C} = 0.06$, $\eta_{D2O/S} = \eta_0 \cdot 2.261$ sample, showed that the lamellar peak position remained constant, irrespective of the absolute temperature (data not shown). This is in accordance with data from investigations of multi lamellar vesicles[117] and dilute lamellar phases[26].

The positions of the L_3- structure peak and the Bragg peak of the lamellar phase are plotted in fig. 8.7.1(1, *left*) as function of the bilayer volume fraction ϕ_{B+C}. In the concentration region studied, good linear fits (solid lines) show that both peak positions are proportional to ϕ_{B+C} (at $\omega_b = \text{const.}$). However, for ideal one-dimensional swelling, theory predicts lines through origin (dashed lines) and this is clearly not the case. Then again, the determined interbilayer distances in the L_3-phases d_3 clearly continue the trend, of the d_3 values determined by *Uhrmeister*[46] (for the identical system), at higher dilution (fig. 8.7.1(1, *right*). (The interbilayer distances d_3 and d_α are calculated via eq. 8.1(4), from the respective position of the L_3 and L_α structure peak, tab. T18 section 11)

In case of the dilute samples, the ratio of the Bragg peak position to that of the L_3-phase varies around 1.3. Exempt from this is the $\phi_{B+C} = 0.05$ sample, where it amounts to 1.54 (the Bragg peak position seems a bit high). In the more concentrated case ($\phi_{B+C} = 0.195$) the ratio equals 1.23. These values are close to the theoretical prediction of 1.5[121] and match a value 1.2 that was determined in an earlier study on the $D_2O - C_{12}E_5$ system[26]. The peak positions for the $\phi_{B+C} = 0.07$ sample of normal viscosity have been omitted from fig. 8.7.1(1 *left*) as both are obviously low. Contamination with water during the sample transfer to the scattering cell could account for this finding.

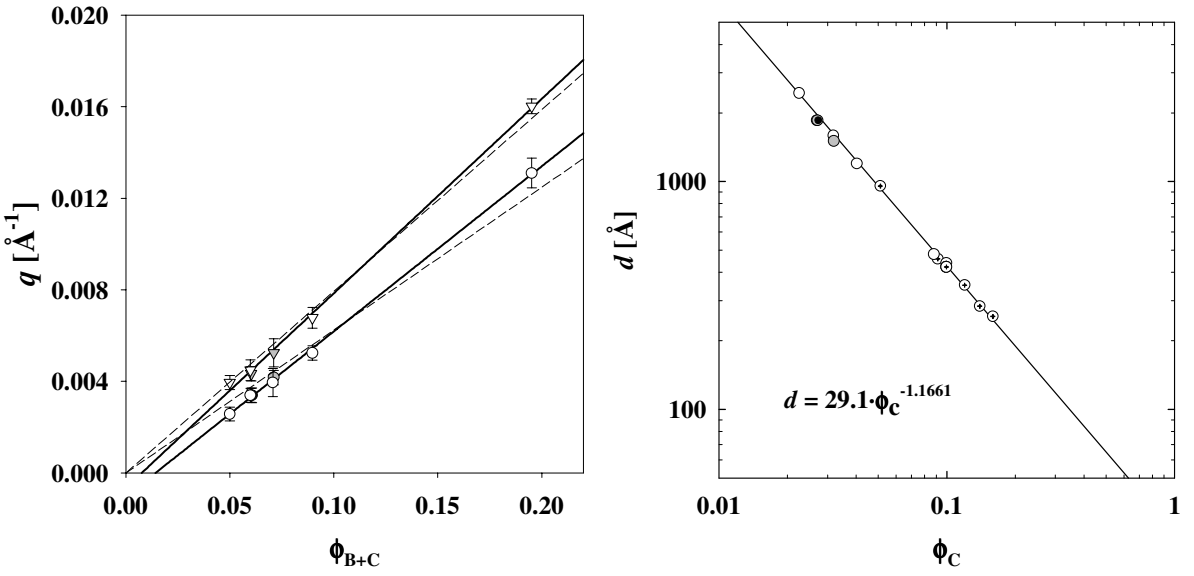

Fig. 8.7.1(1): *left*: structure peak positions of the lamellar (triangles) and sponge (circles) phases. Solid lines represent linear fits, while dashed lines represent linear fits through the origin. Empty symbols refer to samples with a hydrophilic component of standard viscosity (pure D_2O), grey symbols to those with $\eta_{D2O/S}=\eta_0 \cdot 2.261$ and black ones to those with $\eta_{D2O/S}=\eta_0 \cdot 4.320$. When multiple temperature jumps were performed with the same sample, the plotted value is an average. However, in those cases variations in the peak positions were small and the given errors are due mainly to the resolution of the SANS spectra. Data is from bulk contrast experiments only. *right*: interbilayer distance d_3 as function of the surfactant volume fraction on a double logarithmic scale. The symbols denoted with a cross represent data determined by *Uhrmeister* [46] and the linear fit applies only to his data.

The fits to the film contrast scattering curves (fig. 8.5(3) and 8.6.2(2)) yield $2\varepsilon = 51.2$Å which is close to the value of 48.6Å determined by *Uhrmeister* [46] for the same system. Similarly, the other fit parameters of eq. 8.5(1), i.e. the diffuseness of the monolayers t and the invariance of the bilayer σ, also coincide well with the values determined in that previous study (tab. T21, section 11). In summary, the results of the steady state SANS investigations correspond to findings of earlier studies, although samples of higher dilution were examined. This gives confidence in the results of the time resolved experiments, which are discussed in the following section.

8.7.2 TR-SANS, the Kinetic Investigations

The quality of the temperature jump experiments is attested for by the predominantly good reproducibility of the equilibrium L_3-state, i.e. that the scattering spectra before the L_3-to-L_α transition and after the L_α-to-L_3 transition overlap well (data not shown). The NMR experiments revealed that different mechanisms govern the L_3-to-L_α and the L_α-to-L_3 phase transitions. In the former case, there is a nucleation and growth process, while in the latter

uncorrelated bilayer fusion events occur which result in a homogenous distribution of successively formed passages that go on to multiply connect and thus ultimately form the equilibrium sponge phase. The results of the dynamic SANS investigations will be discussed in this knowledge.

The TR-SANS investigations confirm that two different processes do indeed take place in the L_3-to-L_α and the reverse transitions. From the descriptions in fig. 8.6.1(5, *right*) and 8.6.3(2), it is evident that different transition mechanisms are witnessed. That the two processes also differ in terms of time scale is demonstrated below. As the lamellar phase nucleates in the sponge phase, one expects to see the coexistence of L_3 and L_α properties in the respective SANS spectra. This is not the case, but even fully formed lamellar phases of high dilution and low macroscopic order have no outstanding features. The structure shoulder of the L_α-phase forms only after the principal phase transition has long been completed (see below).

The initial shift of the sponge phase structure peak to higher q-values with simultaneous increase in definition (fig. 8.6.1(5, *left*)) should *not* correspond to a decrease of passage density. Although equilibrium sponge phases of lower temperature are composed of fewer passages, and their interbilayer distance d_3 should accordingly be smaller, it is not plausible that such a state could be attained when considering the nucleation and growth mechanism. An overall lower passage density would require the destruction of passages in a non-localised manner and thus each of the destruction incidents would correspond to an energetically non-favourable nucleation event. Instead, it seems likely that a state of less polydispersity of d_3 is realised. With the shift in temperature coincides a shift of the spontaneous curvature H_0 towards zero and consequently the elastic energy E increases, as the mean and Gaussian curvatures H and K, i.e. the overall structure, remain unchanged for the time being (see eq. 3.2(1)). An L_3 structure under such tension could be less mobile and thus less polydisperse. The tension is then released through nucleation and subsequent growth of lamellar domains and the L_3-peak shifts to lower q-values while broadening slightly, i.e. it regains its initial width. Also, the NMR experiments clearly demonstrated that the nucleating L_α-phase is of higher bilayer concentration. The corresponding decrease in bilayer concentration in the sponge phase (dilution effect, section 7.4.5.3) could additionally contribute to the peak shift. The strong increase in scattering intensity in the low q-region could reflect optical density fluctuations (at appropriately long distances) resulting from diffusion processes that evidentially play an important role in ‘crystallite’ growth.

The sponge to lamellar transitions observed for the concentrated sample ($\phi_{B+C} = 0.195$) did not exhibit the characteristics of experiments at higher dilution (fig. 8.6.1(4f)). The detected behaviour can however be explained when assuming that a fast transition is witnessed and that accordingly the kinetics of cooling are monitored. Thus the depicted scattering curves presumably stem from states in equilibrium. This postulation is substantiated by the fact that the final lamellar state is attained in ~250s, which corresponds well with the cooling time required for a $\Delta T = -2.0°C$ jump. In addition, the L_3-peak is shifted to lower q-values during the transition and the lamellar peak emerges at notably higher ones. This is expected, since the L_3-phase has a lower bilayer volume fraction than the lamellar phase, when the two are in coexistence (Lever law, see fig 7.4.5(3)).

In the L_α-to-L_3 transitions the L_α-shoulder disappears as a rule quickly and a very broad structure peak forms subsequently (8.6.3(2)). This peak, that goes on to be more and more defined until the equilibrium L_3-state is reached, apparently reflects the pre L_3-state that first forms from the introduction of passages at uncorrelated locations. As the passage density increases, the peak becomes respectively defined. The strong increase of scattering intensity in experiments that commence from a shaken state arises due to the respective decreasing number of bilayers, which are oriented parallel to the *xz*-plane and therefore do not scatter.

The appearance of anisotropic scattering in the transitions to the lamellar phase was unexpected, as the formation of a macroscopic structure resembling a polycrystalline 3D-powder should result from nucleation in unperturbed conditions (section 7.4.5.1). The scattering pattern observed is presumably caused by a '2D-powder', where the lamellae are essentially parallel to the *z*-axis (fig. 8.2.(1)). Higher order reminiscent of a single crystal (with the lamellae parallel to the *yz*-plane) would result in clearly defined diffraction peaks, i.e. dots on the 2D-dector[26] instead of the observed horizontal band. Notably, the experiments at $\phi_{B+C} = 0.195$ did not lead to the expression of anisotropy, indicating that 'crystallite' orienting requires a significant amount of time, i.e. slow transition kinetics.

One could presume that the appearance of anisotropy is an artefact of the experimental setup. However, it can be excluded that the orientation is caused by the cell walls, as orientation parallel to the largest surface (*xz*-plane) cannot be detected (except indirectly, as reduction in scattering intensity, which does occur upon sample shaking). In addition, section 7.4.5.1 detailed that confinement only induces order in a nucleating lamellar phase over very short distances (50µm). Instead orientation is most likely a result of lamellar crystallites rising within the samples. The nucleating lamellar phase is of lower density than the surrounding L_3-bulk, as its bilayer content is higher. Thus, the 'crystallites' experience a buoyant force and

it seems beneficial, due to fluid dynamic reasons, for the lamellae to orient parallel to their direction of travel (z-axis). This would indeed result in a '2D-powder' structure. In fact, gradients in birefringence (stronger towards the sample top) were detected when studying very long (> 50min) phase transitions in water bath experiments (data not shown).

However, the SANS experiments showed that anisotropy was more pronounced towards the bottom of the sample (fig. 8.6.1(2)) and this may seem to contradict the above explanation. Then again, 'crystallite' density towards the top of the sample would be increased at an early point in time and this crowding could result in crystallites interlocking before the z-orientation is attained. More isolated 'crystallites' towards the bottom of the sample would be less perturbed in their growth phase.

Finally, additional lamellar orientation might result from a slight gradient in temperature, in the direction of the neutron beam, leading to convection. This gradient might exist due to a smaller beam window (and possibly better temperature control) on the source side and a larger one on the detector side (see section 10.5). Again, the lamellae would be expected to orient in their direction of movement, i.e. parallel to the y-axis. Whatever the true cause of preferential lamellar orientation is, the fact remains that there is obviously a strong desire of dilute lamellar to form structures of long range order.

A quantitative analysis of the L_3-to-L_α phase transition kinetics, investigated with TR-SANS in this study, is not possible. Firstly, there is no parameter that can be monitored adequately. The resolution of the L_3-peak position is not precise enough compared to the relatively small amount of shift to lower q-values. Also, the peak is superposed by the general rise in scattering intensity in the low q-region as the transition continues. Following the scattering intensity at constant q-values in time leads to entirely dissimilar results. Additionally, one can not determine the time for the completion of the transitions, as the SANS spectra of the equilibrium lamellar phase persist to evolve, due to the continuing increase in macroscopic order.

Attempts to reproduce the raw detector data in simulations through linear combination of the initial and several presumed final states failed (see below). This method was used successfully previously by *Le et al.* when investigating temperature induced phase transitions from a lamellar to a multi lamellar vesicle phase, while the samples were sheared[117]. However, in the present study this is not possible, as the characteristics of the L_3-phase changes during the transition (expressed by the L_3-peak shift).

Fig 8.7.2(1, *left*) depicts the unprocessed SANS detector data obtained at $t = 890$s of the $\phi_{B+C} = 0.06$, $\Delta T = -1.5$°C transition (fig. 8.6.1(3)). In the *centre*, the result of a linear

combination (least square fit, see section 10.5.4) of the detector data at $t = 0$s (steady state sponge phase) and $t = 1540$s (designated 'steady state' lamellar phase) is presented. It corresponds to 0.48 of the L_3 data and accordingly 0.52 of the L_α data. The *right* plot corresponds to the value $100-(C_{orig}/C_{sim}\cdot 100)$, where C_{orig} and C_{sim} represent the number of detector counts per detector element of the original and simulated data respectively. Thus, positive values give the percentage with which the experimental data was overestimated. The spread of values is in the –20% to +20% range. The fact that a pattern is discernible (instead of a random distribution of deviations), indicates that the experimental data could not be described effectively via the linear combination. Nevertheless, the procedure was carried out at different times t and the fraction of the linear combination, which corresponded to the lamellar steady state, was equated to the volume fraction of lamellar phase φ. The results are plotted in fig. 8.7.2(2) (grey symbols) in direct comparison with the NMR results (white symbols). It is apparent that linear combination cannot serve to describe the sponge to lamellar phase transition kinetics in the TR-SANS experiments.

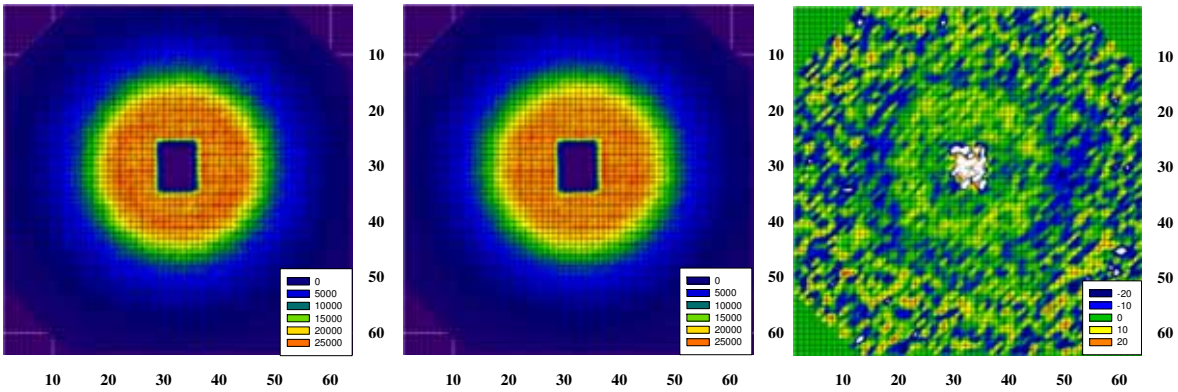

Fig. 8.7.2(1): *left*: 2D-detector data at $t = 890$s of the $\phi_{B+C} = 0.06$, $\Delta T = -1.5$°C transition *centre*: simulated data resulting from linear combination of the equilibrium lamellar and sponge states (48% sponge state). *right*: percentage of deviation.

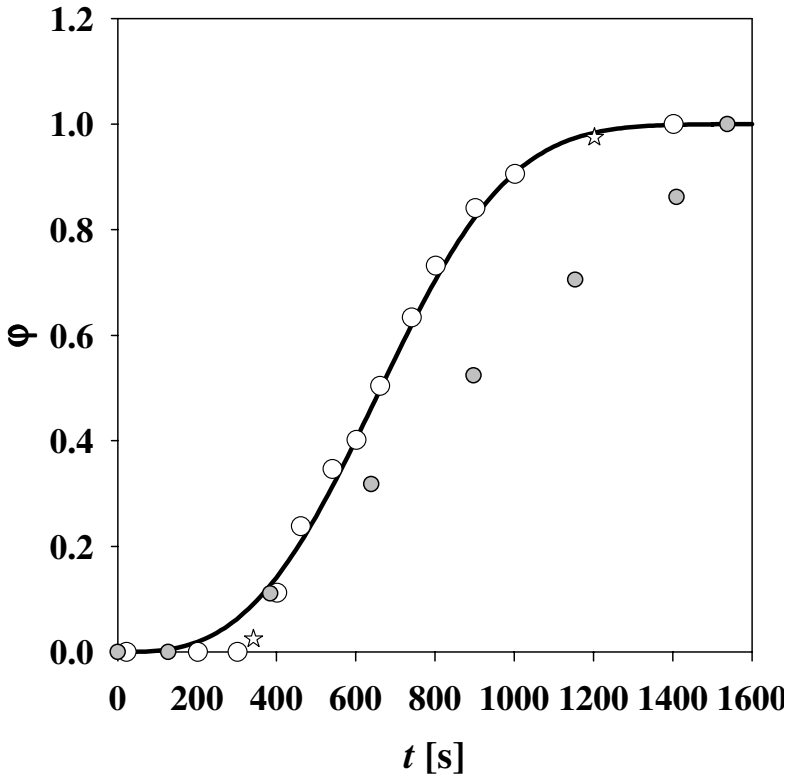

Fig. 8.7.2(2): the lamellar phase volume fraction φ estimated from the linear combination of steady state lamellar and sponge phase detector data (grey) in direct comparison with the NMR result (white).

Fig. 8.7.2(3, *left*) depicts the onset times of anisotropy and compares them with phase transition *completion* times of almost identical samples, obtained from the NMR experiments. One finds only a rough correlation between the two sets of values. Nevertheless, the onset times do appear to be characteristic, as experiments in bulk and film contrast lead to similar results. One finds the same trends in fig. 8.7.2(3, *right*) that the evaluation of the NMR kinetics revealed, i.e. the anisotropy appears later in the cases where the kinetics are slower (lower bilayer volume fraction ϕ_{B+C}, lower magnitude of ΔT and higher viscosity η). In addition, the experiments with the sample of increased viscosity ($\eta_{D2O/S}=\eta_0 \cdot 2.261$, diamonds) show that transition speeds increase non-linearly with variation of ΔT, in accordance with the results of fig. 7.3.1(21).

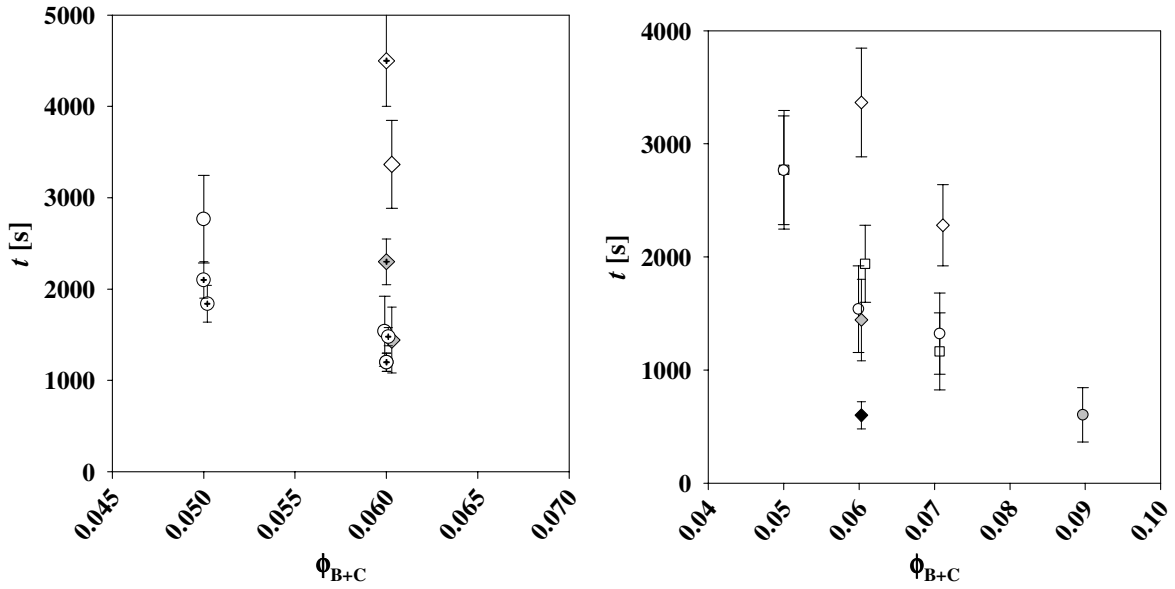

Fig. 8.7.2(3): onset times of anisotropy in L_3-to-L_α transitions. The symbols represent different sample compositions and temperature jumps. (circles): $\eta=\eta_0$ (diamonds): $\eta_{D2O/S}=\eta_0 \cdot 2.261$ (squares): film contrast $\eta=\eta_0$ (empty): ΔT = -1.5 (grey): ΔT = -2.0 (black): ΔT = -3.0 *left*) symbols denoted with a cross represent the phase transition *completion* times of the corresponding samples known from NMR experiments. *right*) onset times of anisotropy of all the performed SANS experiments, exhibiting the trends described in the text.

In cases of slower phase transitions the anisotropy also becomes more pronounced. Slower transition times should correspond to lower nucleation rates and growth speeds, and thus the 'crystallites' are less likely to be perturbed by others and the time available for lamellar orienting is greater before all of the sponge phase is converted and the 'crystallites' interlock. However, macroscopic orientation continues to increase even after the transitions are deemed to be completed: e.g. NMR completion time for the $\phi_{B+C} = 0.06$, ΔT = -1.5°C is approx. 1300s (fig. 8.7.2(3, *left*)). The development of the L_α shoulder occurs much later (2500s, Fig. 8.6.1(3)) and therefore corresponds to the period of peak sharpening in the NMR experiments (section 7.4.5.4). The anisotropy onset times were determined visually by comparing non-processed scattering detector data. The error bars stem from an uncertainty of usually ±3 spectra. The onset times coincide relatively well with the point in time in which the L_3-peak becomes a mere shoulder.

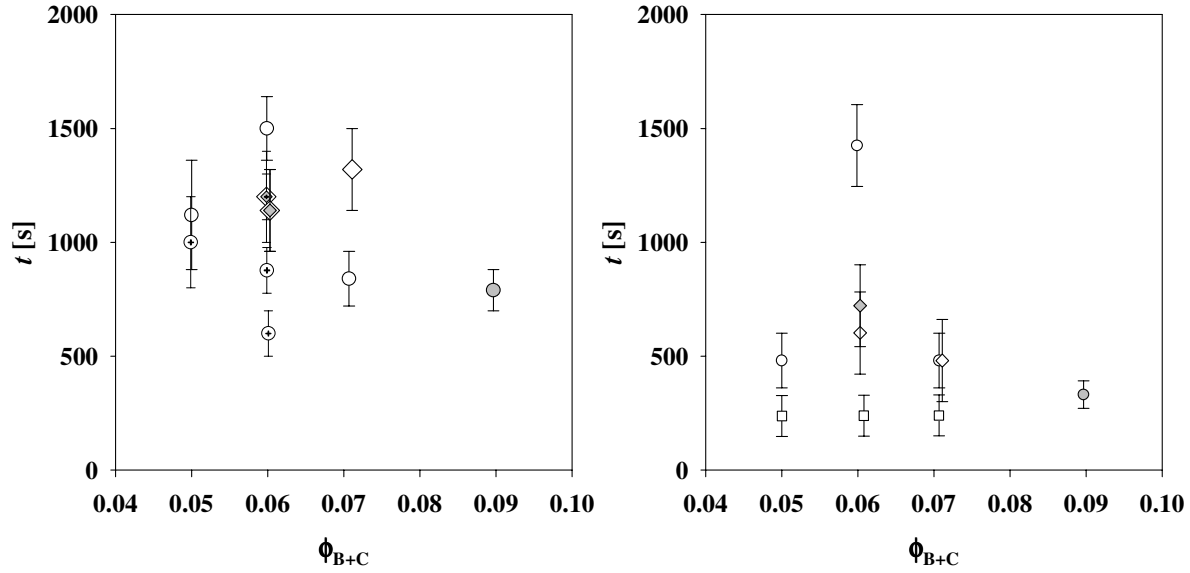

Fig. 8.7.2(4): L_α-to-L_3 transitions. The symbols represent different sample compositions and temperature jumps. (circles): $\eta=\eta_0$ (diamonds): $\eta_{D2O/S} = \eta_0 \cdot 2.261$ (squares): film contrast $\eta=\eta_0$ (empty): $\Delta T = +1.5°C$ (grey): $\Delta T = +2.0°C$ All jumps originated from an equilibrium L_α-phase that experienced previous shaking, except for $\phi_{B+C} = 0.06/\ \eta_{D2O/S} = \eta_0 \cdot 2.261/\ \Delta T = +2.0°C$ and $\phi_{B+C} = 0.07/\ \eta_{D2O/S} = \eta_0 \cdot 2.261/\ \Delta T = +1.5°C$ *left*: Depicted are SANS phase transition completion times and symbols denoted with a cross represent completion times of identical NMR experiments *right*: anisotropy disappearance times.

As opposed to the L_3-to-L_α transitions, the kinetics of the L_α-to-L_3 transitions can be described in terms of the time necessary for their completion, as the formation of changeless SANS spectra corresponding to the L_3 equilibrium state are easily identified in bulk contrast experiments. The respective transition times are plotted in fig. 8.7.2(4, *left*). Notably, these times appear independent of the three varied parameters (ϕ_{B+C}, ΔT and η), when considering the uncertainty of the values. This corresponds to the results of NMR investigations, which were largely completed around 600s and then continued only via sharpening of the L_3-peak. (section 7.4.6.2). NMR phase transition *completion* times are included in fig. 8.7.2(4, *left*) and denoted with a cross. They match the results of the TR-SANS investigations well in three cases ($\phi_{B+C} = 0.05/\Delta T = +1.5$, $\phi_{B+C} = 0.06/\eta_{D2O/S} = \eta_0 \cdot 2.261/\Delta T = +1.5°C$ and $+2.0°C$), in a fourth however there are notable differences ($\phi_{B+C} = 0.06/\Delta T = +1.5$), but this exception will be discussed further below.

In general, the completion times of the TR-SANS experiments show akin to the NMR experiments that the lamellar to sponge transition is considerably faster than the reverse case. The most striking difference is observed for the experiments of increased viscosity. The NMR completion times for $\phi_{B+C} = 0.06/\eta_{D2O/S} = \eta_0 \cdot 2.261/\Delta T = -1.5°C$ and $-2.0°C$ correspond to ~4500s and 2250s (8.7.2(3, *left*)). The completion times of the reverse ($\Delta T = +1.5°C$ and $+2.0°C$) TR-SANS experiments are ~1200s in both cases. (Note that none of the determined

TR-SANS completion times are significantly influenced by the heating kinetics as this process is completed in 150s to 250s). Therefore, sample viscosity is clearly of less importance for the lamellar to sponge transition than for the reverse case and it seems likely that this due to diffusion processes dominating the kinetics of the nucleation and growth mechanism.

In analogy to the decreased transition times, the anisotropy generally disappears quickly (within 600s, i.e. during 35-65% of the transition time the samples scatter anisotropically) and this phenomenon is also independent of the variable parameters (fig. 8.7.2(4, right). Exceptional behaviour is exhibited however in the $\phi_{B+C} = 0.06/\Delta T = +1.5$ experiment, where the sample scatters anisotropically to a minimal degree almost until completion of the transition. This sample was ordered extraordinarily well upon shaking and took longest to complete the transition to the sponge phase. Its distinctive transition behaviour has been illustrated in fig. 8.6.3(1d).

Although this is only the result of a single experiment, which must still be reproduced in order to be conclusive, it appears that a state which has attained predominantly L_3-character can still retain anisotropic ordering from its lamellar origin (the possibility of phase separation is excluded due to visual examination of the final state). Considering this and the general independence of the kinetics from the variable parameters, it seems plausible that the rate determining factor of the L_α-to-L_3 transitions is the disruption of macroscopic order. The faster completion times in the NMR experiments might appear to refute this hypothesis, as the lamellar phases are highly ordered in that case (2D-powder like). However, this order is present only in one dimension and in the respective SANS experiments the shear forces of shaking could have resulted in greater order, since a 2D-powder arrangement is already present after the *T*-jump. Thus NMR experiments with lamellar phases that are virtually completely ordered (single crystal like) are needed in order to examine if this significantly increases transition speeds. Such order should be attainable by applying shear forces in thin, flat cuvettes and introduction into strong magnetic fields.

9. Summary

The fusion and fission of biological membranes, i.e. of fluid amphiphilic bilayers, is an integral part of cellular and subcellular processes and accordingly a key area of research in the fields of biochemistry and biophysics. However, most of the associated studies dealing with the mechanisms of bilayer fusion/fission are either of a purely theoretical nature or numerical simulations. Up to now only little experimental work has actually been performed and the current state of affairs appears as yet unsatisfactory. In this thesis, the subject is approached on a most basic level, by studying thermally induced transitions between two complex fluid phases, the sponge or L_3-phase and the lamellar or L_α-phase. Both phases exhibit highly dynamic, extended bilayer surfaces, which are generated through self-assembly. However, the topology of the bilayer is different in both phases: while the isotropic L_3-phase consist of a continuous membrane of multiply connected passages extending in three dimensions (which separates two continuous, interwoven and independent water domains), the anisotropic L_α-phase is composed of stacks of bilayer sheets (fig. 2(1)). Thus, passage formation/bilayer fusion necessarily occurs when transforming the well defined state of zero passages of the lamellar phase into the sponge phase, while accordingly passage annihilation/bilayer fission characterises the reverse transition (fig.4.1(1) and 4.2(2)).

In the investigations here, a mixture of water (D_2O) – oil (*n*-decane) – and nonionic surfactant ($C_{12}E_5$) is used to study L_3/L_α phase transitions, which are triggered by an abrupt change in temperature. This model system is attractive since its strongly temperature dependent microstructure and phase behaviour are well-known and understood, enabling thus the estimation of mechanical properties of the bilayer (i.e. spontaneous curvature and the bending constants). The experiments are performed at a constant surfactant to oil plus surfactant ration ω_b =0.45 and at high dilution (bilayer volume fraction $0.05< \phi_{B+C} <0.09$, fig. 2.3(1)). The former condition ensures constant bilayer thickness 2ε at all times, while the latter slows down the sponge/lamellar phase transition kinetics to such an extend, that the application of investigation techniques with relatively low time resolution, namely deuterium nuclear magnetic resonance (^{2}H-NMR) spectroscopy and time resolved small angle neutron scattering (TR-SANS), becomes possible. These techniques allow better insight into both the kinetics and the mechanisms of the phase transitions in question. The use of ^{2}H-NMR proves to be particularly advantageous, since different, characteristic ^{2}H-NMR patterns of the two phases (i.e. singlet for the isotropic L_3 phase and a simple doublet for the anisotropic L_α phase), allow for a rigorous examination of the L_3/L_α transition. In addition, TR-SANS studies yield direct information on the changes in the present microstructures.

Both transitions, i.e. the L_3-to-L_α and the L_α-to-L_3 are investigated varying three key parameters: the amplitude of the temperature jump ΔT, the bilayer volume fraction ϕ_{B+C} and the viscosity η of the hydrophilic component (modified via sucrose addition). ΔT represents the driving force of the transition, since temperature determines the monolayer spontaneous curvature c_0, and thus the saddle splay modulus of the bilayers $\overline{\kappa}_{bi}$, which, in interaction with the bilayer Gaussian curvature K_{bi}, gives the bilayer bending energy E (eq. 7.4.1(3)).

In the L_3-to-L_α transition process, the ^{2}H-NMR spectrum initially consists of a singlet originating from the isotropic L_3-phase. As time progresses, an L_α-doublet appears and subsequently grows in intensity, while simultaneously the central L_3-peak diminishes, until it vanishes completely and only the doublet of the steady L_α-state remains. (fig. 7.2.6(2)). This behaviour shows clearly that a nucleation and growth process is present. Analysing these results enables the calculation of the integrals of the L_α and L_3 signal. From this, it is found that the L_α phase volume fraction φ increases sigmoidally with time and there is there is direct experimental evidence that young supernuclei (see section 6.1) are of considerably higher bilayer volume fraction than the equilibrium state (fig. 7.3.1(22-27)). The φ-development is successfully described by a nucleation and growth model of *Kolmogorov*, *Johnson*, *Mehl* and *Avrami* (KJMA), yielding that nuclei grow with approximately the same speed in three dimensions and that continuous/progressive nucleation occurs for slow ($\tau > 1000$s) phase transitions (KJMA exponent α=4, fig. 7.3.1(9,10)). For fast phase transitions (i.e. $\tau < 1000$s), continuous nucleation is suspended at an advanced point in time (α=3, fig. 7.3.1(14,15)). This view is supported both by experimental evidence of peak shape development (fig. 7.4.5(1)) and the theoretical consideration, that the formation of nuclei of high ϕ_{B+C} causes a *dilution effect* in the surrounding L_3-phase (fig. 7.4.5(3)).

Also from NMR experiments, relaxation time constants τ are determined with great confidence ($\Delta\tau \pm 50$s). Generally, it is found that τ decays strongly with increased magnitude of the ΔT, i.e. an L_3-to-L_α transition becomes faster. This decay can be described by a power law. Additionally, the dependence of τ on ΔT is greater for the $\phi_{B+C} = 0.05$ sample than for $\phi_{B+C} = 0.06$. This leads to the speculation that τ is less strongly dependant on ϕ_{B+C}, in case of large ΔT (fig. 7.3.1(21,*right*)) For the sample of increased viscosity, very slow phase transitions are monitored, but τ still develops with ΔT according to a power law.

Another type of NMR experiment decoupled nucleation from growth by allowing a sample to experience a short temperature minimum (fig 7.3.4(1)). The experiments show that, under the premise that kinetics are dominated by the nucleation rate J and not by the growth speed, J increases with increase of magnitude of ΔT (fig. 7.3.4(2)). This should be due to an increase in supersaturation $\Delta\mu$. Evidence for this increase comes from experiments where, for

large ΔT, continuous nucleation is not suppressed by the dilution effect, but rather a dilute L_α-phase nucleates from diluted L_3-regions (fig. 7.2.6(12)). Also, for large ΔT supernuclei form before the dilution effect can strongly increase their concentration (fig. 7.4.5(2)).

For the L_3-to-L_α transition, the TR-SANS experiments start from a typical scattering curve of an equilibrium L_3-phase, whose peak then sharpens and shifts to a higher value of the scattering vector q (fig. 8.6.1(5,*left*)). This can be attributed to a decrease in polydispersity of the interbilayer distance d_3 and/or undulations of the bilayers and the cause of this phenomenon is presumably an initial increase in tension in the bilayer structure, i.e. of bending energy E. As time progresses the trend reverses and the L_3-peak broadens and shifts strongly to lower q values. Later on, surprisingly, an anisotropic scattering pattern appears, which can be attributed ultimately to the buoyancy of 'L_α-crystallites'. For the diluted system ($\phi_{B+C} \leq 0.09$), typical L_α–scattering curves could not be observed. However, for a higher membrane volume fraction ($\phi_{B+C} = 0.195$), TR-SANS results show a well defined Bragg peak and the phase transition kinetics at this concentration are clearly faster than the kinetics of heating/cooling (fig. 7.2.6(1)). The initial appearance of anisotropy is used as a signature for the transformation kinetics and thus confirms the kinetic trends found by NMR.

In the reverse progress, that is the L_α-to-L_3 transition, the ^{2}H-NMR experiments show completely different behaviour. An experiment begins with a well-defined L_α doublet and, as the transition progresses, the L_α peaks draw closer and closer together, until they coalesce in a broad singlet, which then goes on to sharpen continuously until completion of the transition. It is thus evident that this process develops through a completely different mechanism than the L_3-to-L_α transition (i.e. not a nucleation and growth process). The L_α peaks coalescence is fast (~ 200, fig 7.3.2(18)), however the following reduction of peak width is somewhat slower, so that not until ~ 600s (independent of the ΔT, ϕ_{B+C} and η) a well defined L_3 singlet is attained. Subsequent peak sharpening is slow, implying that a critical passage density has been attained and that continuation towards true equilibrium is impeded (e.g. fig. 7.3.2(10)). The L_α–to-L_3 transition is in most cases much faster (~ 600s) than the reverse case (~ 300-4000s). The NMR findings are qualitatively confirmed by TR-SANS (fig. 8.6.3(1)). However one SANS measurement, performed on an unusually well ordered sample (fig. 8.6.2(1,*right*)), showed remarkable spectra development (fig. 8.6.3(1d)) while retaining an anisotropic characteristic for an abnormally long time (fig. 8.7.2(4,*right*)). This intriguingly indicates that, for the L_α-to-L_3 transition, a rate determining factor could be the disruption of long range lamellar order. In summary, the L_α-to-L_3 transition is characterised through locally uncorrelated passage formation, so that the ensuing structure is homogeneous over distances probed by the diffusing water molecules, on a time scale determined by the quadrupolar splitting. Direct

kinetic evaluation of the transition on the basis of *chemical exchange* using a modified McConnell equation (eq. 7.3.2(2)) proved insufficient and future analysis will have resort to slow motion theory.

As the L_3-to-L_α transition is found to occur through a nucleation and growth process, a model on the basis of the classical nucleation theory (CNT), which usually describes gas-liquid transitions, is proposed to describe the effect of nucleation on the Gibbs free energy of the system. It relies on estimating the supersaturation $\Delta\mu$, via the scaling of the bending energy E with concentration, and describing L_α-nuclei as spheres of a given surface energy $A\sigma$ and internal lamellar area (fig. 7.4.5(6)). The model fails to explain the observed acceleration of transition speeds with increase of ϕ_{B+C}. Instead it calculates a constant nucleation barrier ΔG^* independent of ϕ_{B+C}. However, it does predict smaller critical nuclei r_s^* with increase in ϕ_{B+C} and yields smaller values of ΔG^* and r_s^* for increases in $\Delta\mu$. Finally, it shows that subnuclei attaining higher concentration via the dilution effect could transform into supernuclei.

Considerations on the basis that passage formation/destruction is a two step process (eq. 7.4.5(15)) and a theory of *Leitao*, which states that bilayer contact probability is determined by interbilayer distance d, clarify why the L_3/L_α phase transition exhibit direction dependent transformation mechanisms. In addition, the ΔT, ϕ_{B+C}, η dependence of τ of the L_3-to-L_α transitions can be comprehended qualitatively, as these parameters control the contact events that lead to passage formation. Additional experiments reversing phase transitions while in progress support the explanations of the mechanisms (section 7.2.6.4)

In conclusion, this thesis represents the first systematic study of nucleation and growth in a microemulsion-type system. Furthermore, the presented results should serve as a basis to improve the theoretical description of L_3/L_α phase formation as well as bilayer fusion and fission and give an impulse to further employ time resolved ^{2}H-NMR spectroscopy in the study of phase transitions.

10. Appendices **218**

10.1 Materials **218**

10.2 Sample Preparation **218**

10.3 Determining of the Equilibrium Phase Behaviour **219**

10.4 ^{2}H-NMR Experiments **220**

10.4.1 The NMR Apparatus 220
10.4.2 The 90° Pulse Sequence 222
10.4.3 Preliminary ^{2}H-NMR Experiments 224

Sample Preparation and Insertion into the Spectrometer 224
Shimming 226
Spectra Acquisition, Time Keeping and Time Resolution 226
The Phase Transition Experiment 227
The Rate of Temperature Equilibration 228

10.4.4. Established ^{2}H-NMR experiments 229

Experimental Improvements 229
The Rate of Temperature Equilibration 230
Details of the Experiments Separating Nucleation from Growth 233

10.4.5 Algorithms 234

10.5 SANS Experiments **236**

10.5.1 Experimental Setup 236
10.5.2 SANS Experimental Procedure 237
10.5.3 Data Processing 239
10.5.4 Algorithm 239

11. Tables **240**

11.1 Components and Stock Solutions **240**

11.2 Phase Diagrams **241**

11.3 Preliminary NMR Experiments **242**

11.4 Established NMR Experiments **243**

11.5 General NMR Tables **248**

11.6 SANS Experiments **249**

10. Appendices

10.1 Materials

The surfactant *n*-dodecylpentaoxyethylene ($C_{12}E_5$) was purchased from Bachem AG (Weil am Rhein, Germany; 96.9% pure), Fluka (Buchs SG, Switzerland; purity>98%) as well as Nikko Chemicals (Tokyo, Japan, purity>98%). The hydrophobic component *n*-decane was obtained from Sigma-Aldrich Chemie GmbH (Munich, Germany) and the D_2O (99.9% pure) and the fully deuterated *n*-decane $C_{10}D_{22}$ (99% pure) from Cambridge Isotope Laboratories, Inc. (Andover, USA) The sucrose (99% pure) was purchased from Merck & Co., Inc. All components were used as supplied.

10.2 Sample Preparation

All samples were prepared by weight in 10ml test tubes with screw caps by diluting stock solutions of the surfactant and oil component (surfactant to oil plus surfactant volume ratio ω_b = 0.45) with D_2O. This resulted in samples with masses of 1.5g to 3.2g. Volume fractions were calculated by solely taking the substance densities into account ($C_{12}E_5$: 0.97 g cm^{-3}, *n*-decane: 0.73 g cm^{-3}, D_2O: 1.11 g cm^{-3}, $C_{10}D_{22}$: 0.845 g cm^{-3}), thereby disregarding any deviations due to the true partial molar volumes. Samples with higher viscosities were produced by diluting with two different D_2O/sucrose solutions as hydrophilic component. These solutions had a sucrose mass fraction of ψ=0.230 and 0.340, which corresponds to a molar fraction of x=0.0172 and 0.0293. Their densities were determined via a DMA 602 densimeter from Chempro to be δ=1.192 and 1.238 g cm^{-3} respectively. After measuring drop times in a ball-draw Haake viscosimeter, their viscosities were calculated to be $\eta_{D2O/S}$=2.828 and 5.404 cP which corresponds to $\eta_{D2O/S} = \eta_0 \cdot 2.261$ and $\eta_{D2O/S} = \eta_0 \cdot 4.320$, where η_0=1.251 cP is the viscosity D_2O. Density and viscosity measurements were carried out at 20.0°C. Note that the viscosities of the complex fluids themselves was not determined and that viscosity is a function of temperature.

10.3 Determining of the Equilibrium Phase Behaviour

Throughout this thesis, determination of the phase behaviour was restricted to the identification of the upper phase boundary of the lamellar phase and the two phase boundaries of the L_3-phase. The resulting phase diagrams are given in section 2 and their numerical values can be found in the appropriate tables of section 11. In all cases the same procedure was employed, i.e. the boundaries were determined visually in water bath experiments.

For this purpose, samples were fully submerged in a transparent ~10 litre tank, where temperature was controlled to within ±0.02 via a thermostat. Phase boundaries could then be identified by finding two neighbouring phases with a certain temperature interval between them and then subsequently dividing this interval by two, until only one of the phases remained to be observed. The L_3-phase could be distinguished with relative ease through its lucidity, since the two phase coexistence regions situated at higher and lower temperatures are considerably more turbid upon formation. Identification of the upper L_α boundary proved to be more difficult, as both the pure lamellar phase and an L_3/L_α mixture close to that boundary are very cloudy. In these cases, samples were generally allowed to equilibrate for ~1h or more to observe the onset of macroscopic phase separation, i.e. droplet formation. In addition crossed polarisers were used in recognising the birefringent lamellar phase and the streaming birefingent sponge phase.

Note that due to the increasingly slow transition kinetics, it becomes ever more difficult and time consuming to determine phase boundaries at low bilayer volume fraction. Also, when dealing with samples of the type and composition in question, experience showed that it is an absolute prerequisite for the well sealed test-tubes to be fully submersed in the temperature regulating water, and furthermore, that the air space above the liquid meniscus must be kept as minimal as possible. If this later condition is not met, the phase behaviour is not reproducible, i.e. the phase boundaries of the L_3-phase are found at higher as well as lower temperatures (several tenths of °C).

10.4 ^{2}H-NMR Experiments

The ^{2}H-NMR investigations were performed on two different occasions at Lund University, Sweden. Preliminary experiments were carried out on a Bruker DMX-200 spectrometer at the Department of Physical Chemistry 1. Further experiments were executed at a later date on a Varian 360 spectrometer of the Department of Biophysical Chemistry. This section begins with a general description of the hardware and operation (from a technical perspective) of NMR spectrometers. A section giving an explanation of the 90° single pulse sequence follows and further on experimental specifics are presented. Lastly, details concerning data processing are clarified.

10.4.1 The NMR Apparatus

Fig. 10.4.1(1) depicts the essential components of an NMR spectrometer schematically.

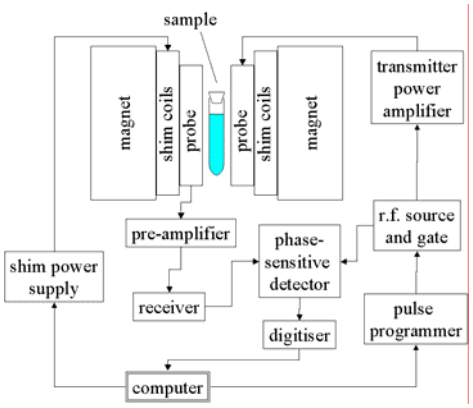

Fig. 10.4.1(1): schematic representation of an NMR spectrometer with its main components. The arrows denote the directions of signal/information transmittal. Further components, which are necessary to perform more complicated experiments (e.g. those necessary for creating a gradient in the magnetic field) and the field-frequency lock circuitry, have been omitted.

The magnet: The heart of an NMR spectrometer is its superconducting electromagnet, which produces the powerful (several Tesla), nearly homogenous, and quite stable magnetic field $\vec{B}$. It is fashioned of special material wire wound into a coil, which exhibits its superconducting properties at very low temperatures. Thus, it is immersed in liquid helium (4.2K) and contained within a Dewar vessel, which in turn is located inside a second Dewar vessel containing liquid nitrogen (77.4K). The latter Dewar acts as a thermal buffer to the

surrounding ambient temperature (~293K). A strong current flows inside the coil virtually without resistance, giving rise to $\vec{B}$.

The shim coils: The magnetic field however is not perfect, i.e. it contains minor spatial inhomogeneities, which occur due to magnet design, materials in the probe, variations in the thickness of the sample tube, sample permeability, and ferromagnetic materials around the magnet. The shim coils correct these inhomogeneities, by producing small magnetic fields opposing the defects. The magnetic imperfections exist in a variety of functional forms (linear, parabolic, etc.) and appropriate arrangements of shim coils, all with the appropriate amount of current, are required to counter them. Thus, there are up to 20 different parameters which need to be optimised to attain a more homogenous magnetic field. The optimum shim current settings are found by either minimizing the linewidth, maximizing the size of the FID, or maximizing the signal from the field lock (see below). Finally, the sample is located in the very centre of the magnet bore and it is generally spun with approximately 15Hz to further reduce magnetic field inhomogeneity.

In addition, the static field $\vec{B}$ is not sufficiently stable for high-resolution NMR (furthermore it decays slowly in strength over time). This is countered by an electronic device, which is known as a field-frequency lock. Its circuitry is not depicted in fig. 10.4.1(1). Essentially, a second NMR experiment is performed continuously and automatically by the spectrometer at all times. Deuterium is usually present in high concentrations in NMR experiments, as deuterated solvents are commonly utilised. Thus, the resonance frequency of deuterium is determined, by exciting the nuclei with appropriate r.f. radiation and, via a feedback loop between a correcting coil and the phase sensitive detector, $\vec{B}$ is constantly corrected/stabilised.

The probe: The probe of an NMR device contains the r.f. coils (Helmholtz coils), that generate $\vec{B}_1$, which rotates the bulk magnetisation $\vec{M}$ (e.g. into the *xy*-plane). These same coils also detect the transverse components of the magnetisation as they precess in the *xy*-plane, as these induce a weak (10^{-9}-10^{-5} V) electromotive force within the coils. The probe also includes the temperature controlling circuitry. Sample temperature is regulated by a stream of cooled or heated air, which flushes around the sample tube, and is monitored by a thermocouple within the air stream.

The r.f. signal modulation and signal detection: the r.f. source is a very stable crystal oscillator or synthesiser unit, which continuously produces a signal of sine form. All frequencies of the spectrometer are derived from it. The gate unit controls amplitude, phase, and width of the signal, which are indirectly controlled by the pulse programmer, which

switches the phase and turns the r.f. signal on and off. Naturally, all parameters are set by the operator via the computer. The initially weak signal from the gate unit is amplified from milli Watts to tens or even hundreds of Watts. Usually, rectangular pulses are created, but other shapes (e.g. Gaussian) can be produced as well. The latter however requires a so called linear amplifier. After the transmitter pulse has been applied the FID can be detected in the form of induced electromotive forces in the r.f. coils. Following amplification, the signals are transferred to the phase sensitive detector via a receiver. This detector requires a reference frequency, which is derived from the r.f. source, in order to assure phase coherence. Finally, the signals from the detector are passed to the analogue-to-digital converter or simply digitiser and then stored in the computer.

10.4.2 The 90° Pulse Sequence

All the NMR experiments presented in this thesis required the same simple pulse sequence. It contains only a single 90° pulse and is represented in fig. 10.4.2(1).

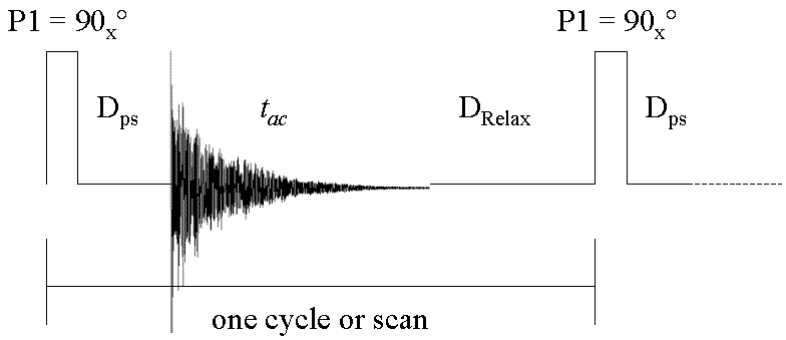

Fig. 10.4.2(1): the general pulse sequence used for *all* NMR experiments of this thesis, with exciting pulse, FID, and delay times. Note that only a schematic description is given and that the time axis is not to scale.

The sequence begins with a rectangular 90° pulse, emitted along the *x*-axis of the laboratory frame, P1. As a result, the bulk magnetisation $\vec{M}$ is forced onto the *y*-axis and its transversal component subsequently precesses in the *xy*-plane with the Larmor frequency ν_L (section fundamentals). As the probe circuitry needs to recover from the effects of the strong excitation pulse, the electromagnetic force induced in the receiver coils is not registered until a pre-scan delay time D_{ps} has passed. This delay is on the order of 200µs. Afterwards, the FID, which decreases exponentially with T_2^* (section 7.1.4), is detected during the acquisition time t_{ac}.

In many experiments, the signal to noise ratio is not satisfactory after Fourier transforming a single FID. However, this ratio can be arbitrarily improved simply by repeating a given NMR experiment a number of times (one speaks of multiple scans or cycles) and letting the intensities of the individual FIDs sum up before performing the Fourier transformation. This is possible, because a FID is an interferogram anyhow and thus the signals of several FIDs of the same *steady state* sample interfere positively, while their respective noise tends to interfere negatively. However, before a second pulse, i.e. a second cycle, can be applied, the sample spins should return to their thermal equilibrium distribution according to Boltzmann (eq. 7.1.2(3)), otherwise saturation will occur after the system has been subjected to a series of pulses (see section 7.1.4). As one approaches saturation, the FID signal intensity decreases continuously, so that the advantage of using multiple cycles is lost. Consequently, a relaxation delay D_{Relax} is needed after the acquisition time. This delay should amount to $\geq 5T_1$. However, the occurrence of saturation is not a critical problem in modern pulse NMR spectroscopy, since the signals obtained after Fourier transformation are only affected with respect to their integral and not regarding their linewidth (as the steady state solutions of the Bloch equations imply (eq. 7.1.4(1)).

The described sequence is the simplest possible and known as a single pulse experiment, as only one pulse is used per cycle. It basically contains only two important variable parameters (if one excludes D_{ps}, for which a default value is given by the spectrometer manufacturer, and D_{relax}, since saturation is not truly an issue. This is especially true, if the number of scans per spectrum is low). The life-span of the pulse P1 determines how far the vector of the magnetisation is flipped towards the *xy*-plane, i.e. the angle of the pulse (section 7.1.3). This angle can be optimised to attain the 90°-value by means of a simple experiment, where the pulse life-span is varied empirically, and is usually of the order of 10µs. But in case of single pulse experiments, even the angle of the pulse is not overly significant, as a deviation from the 90° optimum simply leads to a signal of lower intensity. However, with respect to the acquisition time t_{ac}, it is essential that this time period is sufficiently lengthy for the FID to decay fully, since truncation of the FID leads to highly undesirable artefacts in the frequency spectrum (a sinc-component). An excessively long acquisition time on the other hand has no ill effects, if one disregards the increase of gathered data and corresponding consumption of computer memory.

The following relation exists between the acquisition time t_{ac}, the number of data points obtained in the time domain N_{td}, and the width of the spectrum in the frequency domain W_{sp}.

$$t_{ac} = N_{td} \cdot t_{dw} = \frac{t_{dw}}{W_{sp}} \qquad \text{eq. 10.4.2(1)}$$

where t_{dw} is the dwell time. It corresponds to the time period between the acquisition time and the width of the data points of the FID and it is usually determined indirectly by the operator, when (s)he selects the acquisition time and the width of the frequency spectrum to be investigated (usually several thousand Hertz).

10.4.3 Preliminary ^{2}H-NMR Experiments

The initial ^{2}H-NMR experiments were performed on a Bruker DMX-200 spectrometer. The 200 value states that the resonance frequency of protons is located at 200MHz and accordingly the magnetic field possesses a magnitude of ~4.7T. Consequently, the Larmor frequency ν_L of deuterium is situated therefore at 30.7 MHz, as g_I(D) = 0.85745. The relationship between the magnetic field strength and the resonance frequency of a nucleus can be calculated with eq. 7.1.2(5).

The investigations focused on three component samples consisting of D_2O, *n*-decane, and $C_{12}E_5$. The surfactant to oil plus surfactant volume ratio was kept constant at $\omega_b = 0.45$, while the bilayer volume fraction ϕ_{B+C} was varied (ϕ_{B+C} = 0.05, 0.06, and 0.07). L_3-to-L_α and L_α-to-L_3 phase transitions were induced by abruptly changing the temperature of the air flow streaming around the sample tube. Therefore, each sample remained within the spectrometer for the entire duration of an experiment and did not have to be disturbed in any way. Accordingly, reduction of magnetic field inhomogeneities through spinning of the samples was not an option, as the phase transitions were to be studied in the absence of any non-equilibrium forces. The magnitude of the temperature jump ΔT, which represents the driving force of the transitions, was also altered.

Sample Preparation and Insertion into the Spectrometer

Prior to the NMR experiments, the upper phase boundary of the lamellar phase and phase boundaries of the L_3-phase of each sample were determined visually via water bath experiments (section 10.2). In the NMR experiments, a minimal air space above the sample

liquid proved to be of particular importance, because the use of full length (approx. 20cm) NMR-tubes of 10mm diameter turned out to be futile. In those cases, droplets of unknown composition condensed on the glass wall above the sample, due to the existence of a temperature gradient along the length of the tube. In retrospect, this gradient should not have been unanticipated, since the temperature of the studied fluid is simply controlled by a stream of heated air coming from underneath the sample tube. The phase behaviour of such samples phase was generally shifted to higher temperatures, indicating that the droplets were of higher than average oil content.

In order to counter the described effects, the samples were flame sealed approx. 2cm above the liquid meniscus. This however posed a new problem, because NMR samples need to be situated in a special fixture before being lowered down into the NMR apparatus using a long string. The fixture ensures that a sample is centred within the magnet, but requires sample tubes to be in the excess of 12cm in length. The dilemma was solved temporarily by flame sealing the samples in glass tubes of approx. 8mm diameter and inserting those in standard length, 10mm wide precision NMR tubes. The minute space between the two tubes was filled with water (H_2O) for better thermal conduction (fig. 10.4.3(1)).

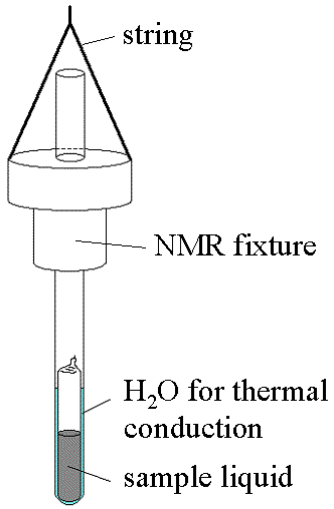

Fig. 10.4.3(1): sample containment for preliminary NMR experiments. Samples are flame sealed in test-tubes of approx. 8mm diameter and then placed within tubes of 10mm radius. Excess space (extremely exaggerated in the illustration) is filled with H_2O for improved thermal conduction.

For a phase transition experiment, a sample of the set-up above was first made to attain the desired initial state (e.g. the L_3-state) by submersing the whole arrangement in an external water bath. After drying of the outer tube, the configuration was then introduced into the spectrometer, which had been previously adjusted to the temperature corresponding to the initial state. The sample was subsequently left to equilibrate for tens of minutes, while

repeated, short, visual checks ensured that it remained in the required one phase region. Once it was certain that the temperature inside the magnet was accurate (the display of the spectrometer listed a temperature which was offset from the actual one in a non-constant manner), manual shimming, i.e. homogenisation of the magnetic field through the variation of 20 parameters, could commence.

Shimming

Shimming is achieved by iteratively optimising the results of consecutively performed 90°-pulse experiments (described above). In the isotropic L_3-phase, the result of such an experiment, after Fourier transformation of the FID, is a single peak at the ^{2}H-resonance frequency of the ^2H_2O (section 7.2.1). In general, the method of choice was to maximise the intensity of the registered peak, while simultaneously maintaining/attaining its greatest possible symmetry. This second condition was of higher priority, as soon as good line widths (e.g. <5Hz) were achieved. The continuous repetition of the pulse experiment and subsequent Fourier transformation of the FID occurs automatically in the described situation. In unfortunate cases, the shimming procedure took more than two hours. Likewise, removal of a sample from the spectrometer sometimes led to the complete loss of magnetic field homogeneity, even if said sample was reintroduced only seconds later.

Spectra Acquisition, Time Keeping and Time Resolution

An actual NMR phase transition experiment could commence once shimming was completed. However, the only essential difference to the afore described shimming procedure lies in a superior signal to noise ration of the acquired spectra, i.e. again a 90°-pulse experiment was performed and accordingly a single peak was registered as long as the sample remained in its L_3 state. At an early stage of the investigations, 24 cycles were conducted to receive a single spectrum. This number was later reduced to four, when it became obvious that the signal to noise ratio was still excellent with this setting. Accordingly, the time needed to receive a single spectrum was reduced. Of course when observing a changing, non-steady system, only an average of the states existing during that period is recoded, so that a minimal spectra acquisition time is preferable in those cases. The experiments with four scans took only 13s, so that with respect to the long duration of sponge to lamellar transitions (tens of minutes), the results can be considered as moments in time in which an almost steady state is

observed. It is important to note, that the total time needed to acquire a spectrum t_{sac} can *not* simply be calculated as the sum of the individual time segments of the pulse sequence multiplied by the number of cycles. This is due to software routines between the individual scans which require significant time of their own. Thus, for exact time keeping, the experimental determination of t_{ac} was necessary.

A 200 MHz spectrometer is relatively weak when compared to modern, state of the art spectrometers, which operate in the 600 or even 800 MHz range (for protons), and additionally deuterium nuclei generate a comparatively weak magnetic moment ($\gamma(^2H)/\gamma(^1H) = 0.154$), thus resulting in a respectively low sample magnetisation $\vec{M}$ ($\left\|\vec{M}\right\|(^2H) / \left\|\vec{M}\right\|(^1H) = 0.063$, when considering the same number of atomic nuclei; eq. 7.1.2(4)). Nevertheless, good time resolution could be achieved, due to the large amount of deuterated sample material present, e.g. the water is fully deuterated and 99.9% pure and constitutes ~94 % of the sample by volume.

The Phase Transition Experiment

When a phase transition was induced through change of the spectrometer temperature, it was monitored by consecutively recording ^{2}H-NMR spectra, each being the result of the same number of scans. In order to reduce the amount of data gathered, an additional delay time was often introduced after the receipt of each spectrum. The total number of spectra to record had to be determined prior to the start of the experiment. Thus, the transition times had to be estimated beforehand and the additional delay time chosen accordingly. However, the recording of spectra could often be aborted prematurely, when the target spectrum (for the L_α-phase a doublet) was deemed to be unchanging. After completion of a temperature jump experiment, the samples were quickly examined visually in order to determine if the desired one phase region was truly obtained. Crossed polarisers were used to help in identifying the lamellar phase. Sometimes, in order to maintain the magnetic field shimmed, the visual inspection was neglected and a second temperature jump (the exact inverse of the first one) was conducted immediately.

The launch of the spectra acquisition program was synchronised with the initiation of the temperature change, so that the time axis of the phase transition experiments is determined directly through the sequential number of the spectra. The acquisition time values in the experiments ranged from 1.2 to 1.5s and the width of the frequency domain spectrum from

5000 to 2000 Hz. Obviously, the spectra presented in section 7.2.6 represent only a selection of the recorded frequency data, but the excluded regions are devoid of any signal.

The Rate of Temperature Equilibration

The experiments require the kinetics of the temperature variation to be significantly faster than the objective kinetics of the phase transition. The former were determined through use of a thermocouple, which was placed within pure water (H_2O) of average sample volume. Thermocouples of the type T were employed. Their sensor consists of copper and constantan, the latter being an alloy of copper and nickel (Cu55Ni45), and cover a temperature range from -200°C to 350°C. They have a moderately good output of ~43µV/°C and in this case an accuracy of ±0.1°C. The output and consequently the accuracy of a thermocouple is affected by strong magnetic fields. Thus, temperature measured in this way in the NMR apparatus might be offset from the actual temperature. Furthermore, even the determination of temperature differences (intervals) may not be accurate. Due to these considerations, temperature intervals calculated from the display temperature of the spectrometer are the basis of the results of this thesis.

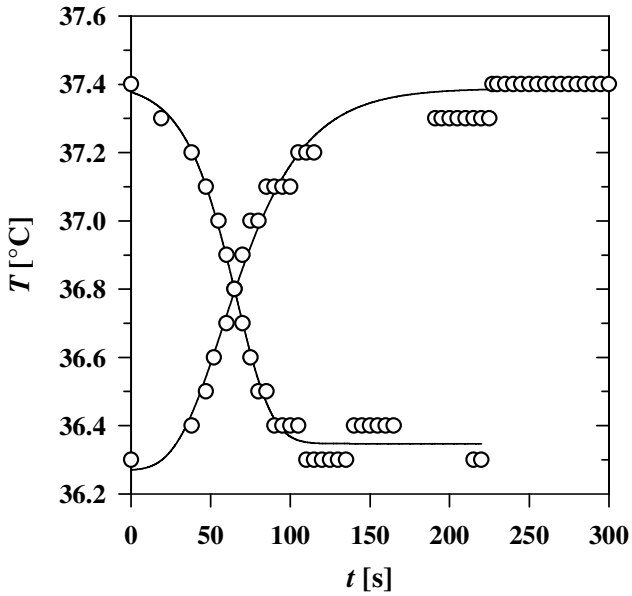

Fig. 10.4.3(2): exemplary heating and cooling kinetics. Temperature equilibrium is reached in approx. 200s. The error of the registering thermocouple corresponds to ±0.1°C.

In order to accelerate the rate of temperature equilibration, at the beginning of a jump, the air stream temperature was *set* to reach a temperature up to 2°C below/above the concrete target temperature. However, care was taken to ensure that the actual temperature of the air stream (measured by a temperature sensor of the spectrometer) never dropped below or rose

above the target temperature. As soon as the actual temperature approached the vicinity of the target temperature, the air stream temperature was *set* to the actual target temperature, which would be attained shortly thereafter. Result for both heating and cooling are present in fig. 10.4.3(2). Temperature equilibration is attained at approx. 200s. A more comprehensive analysis of the heating and cooling kinetics, relevant for the bulk of the experiments, is presented in the next section.

10.4.4 Established ^{2}H-NMR Experiments

The second set of experiments was performed on an NMR spectrometer with the following components/characteristics: The magnet was a 360MHz widebore Oxford magnet with Oxford shim coil and an 18-shim shim power supply from Oxford. The probe stack was a modified Nicolet and the temperature controller a Stellar VTC90. The spectrometer itself was a modified Varian Unity Plus 400MHz with a two channels and deuterium lock. The controlling computer was a Sun Ultra 10 with Solaris 8 operating system.

Experimental Improvements

The only essential difference in hardware (with respect to the performed experiments), when compared to the preliminary investigations, was the magnet type, i.e. its field strength. Since the resonance frequency of protons is located at 360MHz, the magnetic field accordingly possesses a magnitude of ~8.5T and the Larmor frequency ν_L of deuterium is situated at 55.2 MHz. Sample containment was improved upon, by resorting to flame sealing the test fluid in 10mm NMR tubes and connecting these to a full length tube of the same kind using superglue (fig. 10.4.4(1)). Due to the use of precision NMR tubes, gluing of a straight connection became feasible.

Through the presence of a higher field strength and increased sample volume, spectra of excellent signal to noise ratios could be obtained using merely a single cycle. In this manner, the time resolution was increased to ~2s. This ensured snap-shot like spectra, i.e. spectra corresponding to a single state, in even the fastest of the studied transitions (approx. 600s for completion). Additionally, using 10mm tubes maximised the sample volume to glass surface area ratio. This is significant as nucleation of the L_α-phase was to be studied in the bulk, i.e. nucleation on the glass walls had to be reduced to a minimum. In all other respects, the

transitions from sponge to lamellar phase and *vice versa* are in accordance with the description given in section 10.4.3.

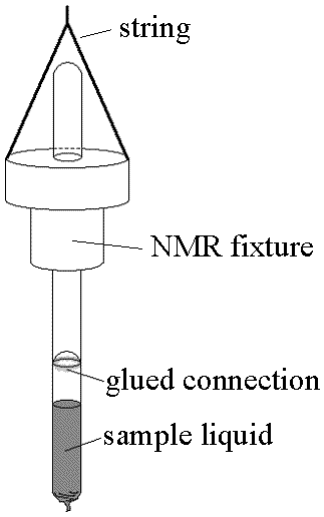

Fig. 10.4.4(1): improved sample containment. The sample liquid is flame sealed in a 10mm precision NMR glued accurately in line with another, full-length tube of the same kind.

The Rate of Temperature Equilibration

Akin to the preliminary experiments, the kinetics of temperature equilibration were determined using a thermocouple placed within an amount of H_2O corresponding to an average sample volume. Initially, the rate of temperature equilibration was determined for the case, where the temperature of the air stream is simply set to the target temperature. 10mm NMR tubes are used. In fig. 10.4.4(2a and 3a) the results of such experiments with varying amplitudes of the temperature jump ΔT are plotted. In the respective b) figures, the data was normalised, which results in reducing the plots to a single curve. The normalised data was then fitted using the least squares method and a three parameter exponential function

$$y = y_0 + a\left(1 - e^{-bx}\right) \qquad \text{eq. 10.4.4(1)}$$

where y and x correspond to $\Delta T/\Delta T_{max}$ and t respectively and y_0, a and b are constants. Additionally, the restriction $y_0 + a = 1$ (for a positive change of temperature) or -1 (for a negative change of temperature) was employed. Thus, the heating and cooling process follows an exponential evolution and its time constant $\tau = 1/b$ is seemingly independent of ΔT.

Temperature equilibration occurs after ~450s. The starting temperature of the negative jumps and the final temperature of the positive ones corresponded to $T \approx 37.3$°C, i.e. a temperature where the system in question is in the middle of the L_3-phase when $\phi_{B+C} = 0.06$.

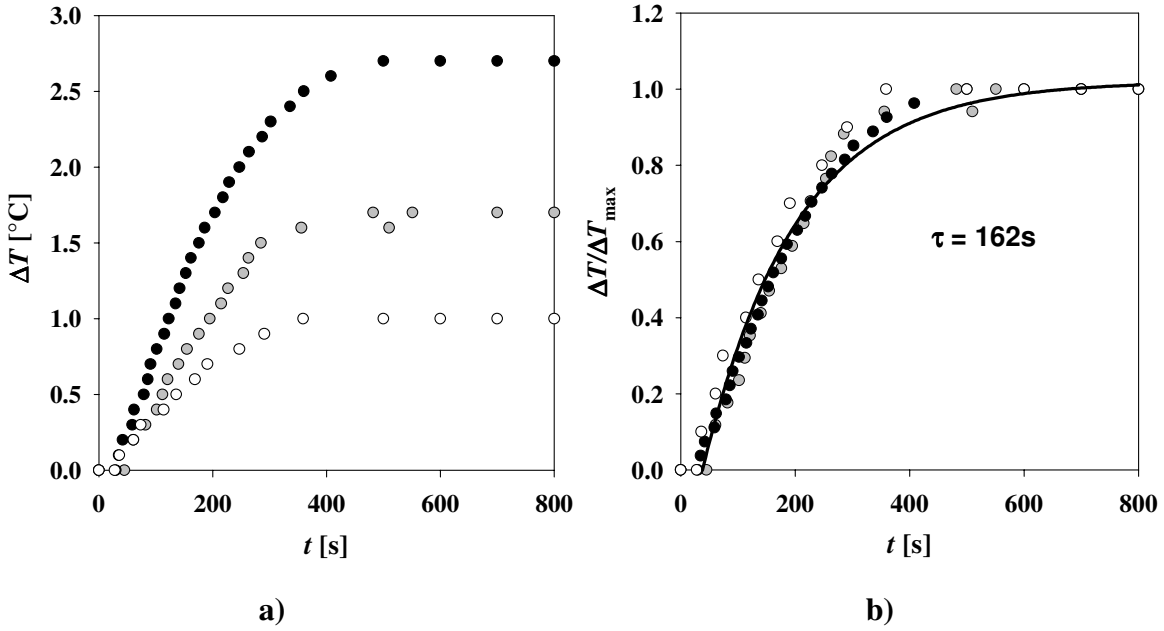

Fig. 10.4.4(2): a) illustration of the heating kinetics of H_2O in a 10mm tube when the temperature of the air stream is set to the target temperature. $\Delta T = 1.0$ (empty), 1.7 (grey) and 2.7°C (black circles) b) the data of figure a, normalised by dividing each value by the (maximum) final value of the appropriate curve.

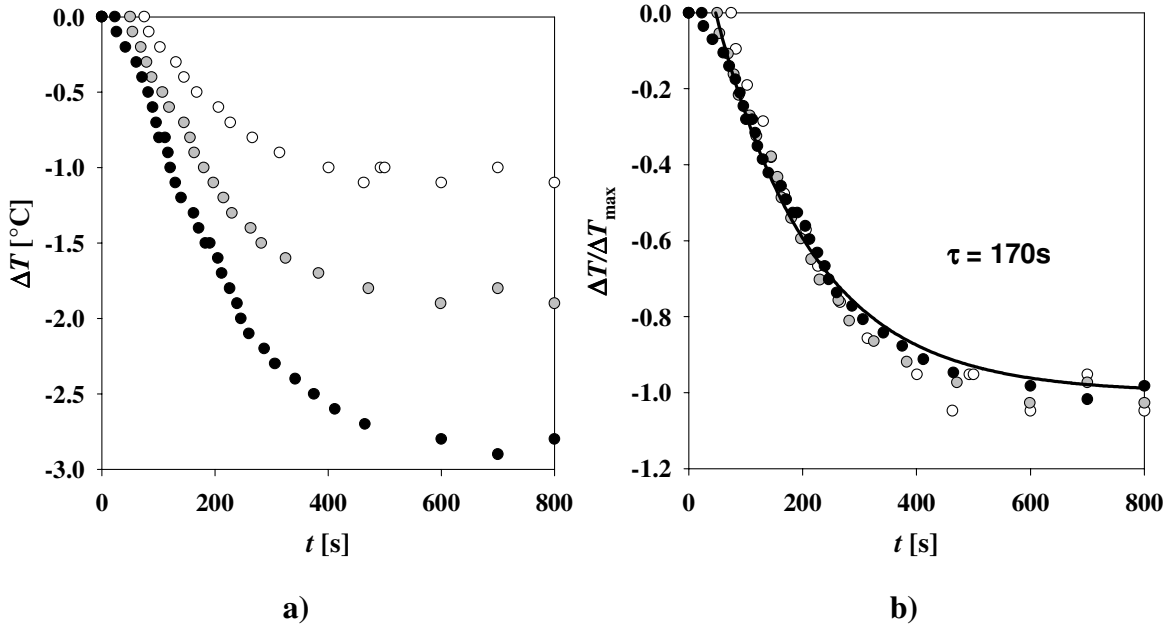

Fig. 10.4.4(3): a) illustration of the cooling kinetics of H_2O in a 10mm tube when the temperature of the air stream is set to the target temperature. $\Delta T = -1.05$ (empty), -1.85 (grey) and -2.85°C (black circles) b) the data of figure a, normalised by dividing each value by the absolute of the final (maximum) value of the appropriate curve.

In order to increase the speed of the temperature equilibration times, the temperature regulating air stream was overheated (for positive temperature jumps) or undercooled (for negative temperature jumps) past the target temperature, for an exactly defined and controlled increment of time. This time is depended upon the amplitude of the actual temperature jump being performed and it is summarised in the table below. The degree of overheating/ undercooling was *set* to 2.0°C beyond the target temperature. However, the air stream temperature did not necessarily reach this extreme value, especially if the overheat/undercool time was low. Additional experiments with the thermocouple next to the wall, showed that the samples themselves are not overheated/undercooled. Nine experiments of the heating kinetics and eight of the cooling kinetics were performed, using varying amplitudes of the temperature jumps and overheating/undercooling times (fig. 10.4.4(4, 5)).

ΔT [°C]	t [s]
0.8	40
0.9 to 1.1	55
1.3	60
1.5	71
1.7 to 2.0	90

Tab. 10.4.4(1): times used to overheat/undercool the air stream by *setting* the temperature 2.0°C past the target temperature as function of the amplitude of the actual temperature jump. Times are identical for L_3-to-L_α and L_α-to-L_3 transitions.

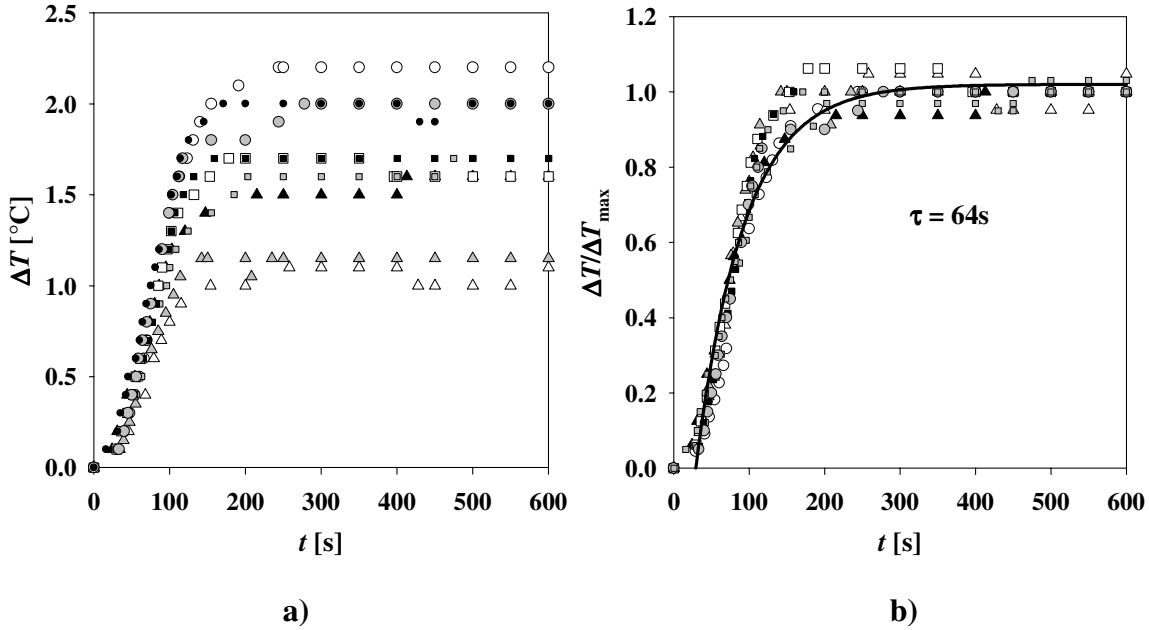

Fig. 10.4.4(4): a) heating kinetics of H_2O of average sample volume in a 10mm NMR tube. The air stream temperature was *set* to surpass the target temperature by 2°C for a specific amount of time (tab. 10.4.4(1)). b) the normalised data of figure a. The thermocouple has an error of ±0.1°C.

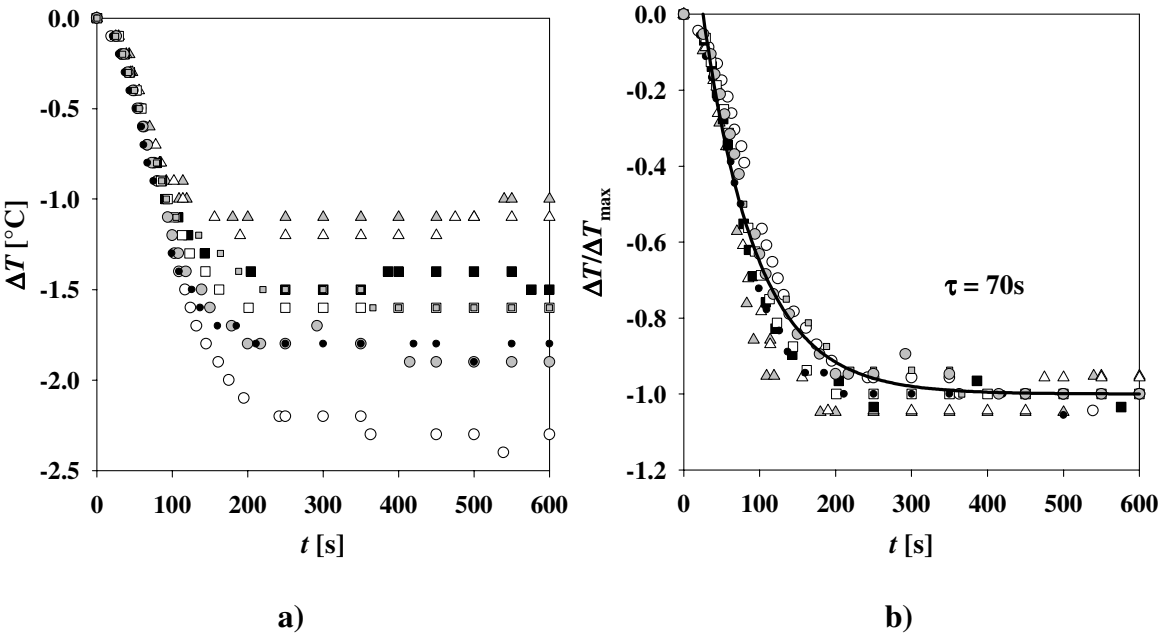

Fig. 10.4.4(5): a) cooling kinetics of H_2O of average sample volume in a 10mm NMR tube. The air stream temperature was *set* to surpass the target temperature by 2°C for a specific amount of time (see table above). b) the normalised data of figure a. The thermocouple has an error of ±0.1°C.

Fits to the normalised data of fig. 10.4.4(4 and 5), akin to those of fig. 10.4.4(2 and 3), show that there is a significant increase in equilibration speed, when using the overheating/undercooling method. Although the equilibration behaviour can not truly be described by an exponential any longer, the plotted lines serve as a guide and it is clear that temperature equilibration is reached around 200s, when one considers the error of the thermocouple (±0.1°C). Thus, the heating and cooling kinetics of the 360MHz spectrometer, basically coincide with those determined for the 200MHz spectrometer.

Details of the Experiments Separating Nucleation from Growth

The experiments in question were performed on the 360MHz spectrometer. Care was taken throughout the sample handling processes, to keep sample perturbation through shaking at a minimum. Also, the time required for transferring a sample between heating blocks (transition between segment III and IV) and between the 'hot block' and the spectrometer (transition between segment IV and V) was very small, ~1s in the former case and ~5s in the latter. Thus, effects on the temperature profile are minimal and can be neglected.

The heating blocks themselves, had 10mm bore holes, thereby providing excellent contact between the sample tube and the temperature regulating metal. Initial use of water baths as temperature regulating units proved to be impracticable, as samples needed to be

dried before being returned to the spectrometer (transition between segment IV and V). This turned out to cause too much perturbation, take too long and simply effect temperature too greatly. Likewise, it became necessary to implement a 'hot block', since otherwise the time for altering the minimum temperature to the target temperature requires ~200s in the spectrometer (even when this process is accelerated through overheating the air stream, see above).

Extensive tests were performed to optimise the residence time of the sample in each of the segments (II-IV). The temperature of H_2O, corresponding to average sample volume, was measured in a 10mm NMR tube with a thermocouple both at the wall and its core. Special care was taken to ensure that in the most critical part of the experiment, i.e. the rapid sample cooling in air at room temperature, the sample temperature at the glass wall did not drop below the desired minimum.

10.4.5 Algorithms

Below follows code written for 'user defined' equations as part of the 'Regression Wizard' of the SigmaPlot program, version 9.0:

1) Sum of three Lorentzians fit

Equation

```
f=(a/(1+((x-x0)/b)^2))+(c/(1+((x-m0)/d)^2))+(e/(1+((x-n0)/g)^2))
fit f to y
```

Variables

```
x = col(1) ' {{prevmin: 0.000000}} {{prevmax: 10.000000}}
y = col(2)
'Automatic Initial Parameter Estimate Functions
peaksign(q)=if(total(q)>q[1]; 1; -1)
xatymin(q;r)=xatymax(q;max(r)-r)
```

Initial Parameters ***(values are from of a specific fit)***

```
a = if(peaksign(y)>0; max(y); min(y)) "Auto {{previous: 0.0750611}}
b = fwhm(x;abs(y))/2 "Auto {{previous: 2.03943}}
x0 = if(peaksign(y)>0; xatymax(x;y); xatymin(x;y)) "Auto {{previous: 119.834}}

c = if(peaksign(y)>0; max(y); min(y)) "Auto {{previous: 0.0172524}}
d = fwhm(x;abs(y))/2 "Auto {{previous: 3}}
m0 = if(peaksign(y)>0; xatymax(x;y); xatymin(x;y)) "Auto {{previous: 127.935}}

e = if(peaksign(y)>0; max(y); min(y)) "Auto {{previous: 0.072157}}
g = fwhm(x;abs(y))/2 "Auto {{previous: 2.02497}}
n0 = if(peaksign(y)>0; xatymax(x;y); xatymin(x;y)) "Auto {{previous: 137.884}}
```

Constraints ***(values are examples of a specific fit)***

```
b>0
d>0
```

g>0
b<4.1*g
g<4.1*b
a<4.1*e
e<4.1*a

m0>126
m0<129
n0>135
n0<160
x0>104
x0<125

b>1
b<4
d>0.5
d<5
g>1
g<4

a>0.003
c>0
e>0.003

c<a
c<e

2) Modified McConnell equation (eq. 7.3.2(2))

Equation
AA=x
BB=TZ

f=Inten*(((6.2832*(AA-BA))^2)*1/BB+((1/BB^2)+(2*P/BB)+(((6.2832*BD)^2)/4))*(1/BB+2*P))
/(((6.2832*(AA-BA))^2-(1/BB^2)-(2*P/BB)-((6.2832*BD)^2)/4)^2+4*(6.2832*(AA-BA))^2*((1/BB)+P)^2)
fit f to y

Variables
x = col(1) ' {{prevmin: 0.000000}} {{prevmax: 10.000000}}
y = col(2)
'Automatic Initial Parameter Estimate Functions
peaksign(q)=if(total(q)>q[1]; 1; -1)
xatymin(q;r)=xatymax(q;max(r)-r)

Initial Parameters (values are from of a specific fit)
P = fwhm(x;abs(y))/2 "Auto {{previous: 17}}
TZ = fwhm(x;abs(y))/2 "Auto {{previous: 0.1977}}
Inten = if(peaksign(y)>0; max(y); min(y)) "Auto {{previous: 1.96419}}
BA = if(peaksign(y)>0; xatymax(x;y); xatymin(x;y)) "Auto {{previous: 113.967}}
BD = if(peaksign(y)>0; xatymax(x;y); xatymin(x;y)) "Auto {{previous: 8.79637}}

Constraints (values are examples of a specific fit)
P>0.000000000001
P>100
TZ>0.025
TZ<0.3

Inten>1

BA>113
BA<115
BD>3
BD<15

10.5 SANS Experiments

The SANS experiments were performed on two different occasions at the D11 instrument of the Institut Laue-Langevin (ILL) in Grenoble, France. These are referred to as the first and second set of experiments. During the first set, samples with D_2O as the hydrophilic component and $\phi_{B+C} = 0.05$, 0.06, and 0.07 of both bulk and film contrast were studied, while during the second the $\phi_{B+C} =$ 0.06 bulk contrast experiments were repeated and samples of higher bilayer volume fraction ($\phi_{B+C} = 0.09$ und 0.195) and higher viscosities (D_2O+sucrose) were investigated in bulk contrast. Sample preparation occurred just as described in section 10.2.

10.5.1 Experimental Setup

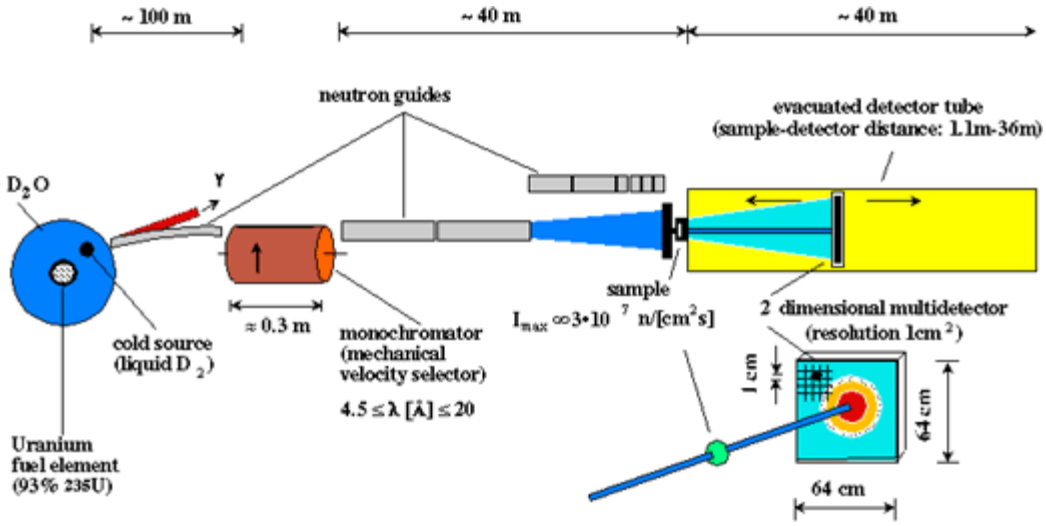

Fig. 10.5.1(1): the beam line of the D11 instrument (from ref.[122])

Fast neutrons of high energy and short wavelength are produced via nuclear fission in the reactor. Before these particles can be used to perform SANS experiments they must be slowed considerably in order to be of shorter wavelength. This process is termed moderation and occurs by letting the neutrons pass through a 'cold source' of liquid D_2, where they lose kinetic energy via inelastic scattering. Afterwards, the beam is monochromated, i.e. only neutrons of a select velocity and thus wavelength pass a helical slot velocity selector (from Dornier, $\Delta\lambda/\lambda$=0.09). For all of the experiments $\lambda = 6$Å. The neutrons are then collimated by a series of moveable glass guides. Depending on the type of divergence needed, guides can be inserted at different distances from the sample. The neutrons then pass through the sample,

where they are scattered, before reaching the evacuated detector tube, at whose end a 2D neutron detector is located. This is a ^{3}He gas detector (from Cerca) and consists of 64x64 elements of 1cm^2 each (detector dead time = 0.85µs). The investigated q-range can be altered by changing the sample to detector distance (see section 8.2).

The sample fluid is contained in a quartz cell of 1mm optical length, which in turn is located in a metal cylinder, with a small bore for the incident neutrons on one side and a larger one for the scattered ones on the other. Apertures of various sizes can be used to limit the diameter of the incident beam (see below). The temperature of the cylinder is controlled to within (at least) ±0.05°C by letting water of the appropriate temperature stream around it. The whole cell is mounted on a support to ensure alignment with the neutron beam.

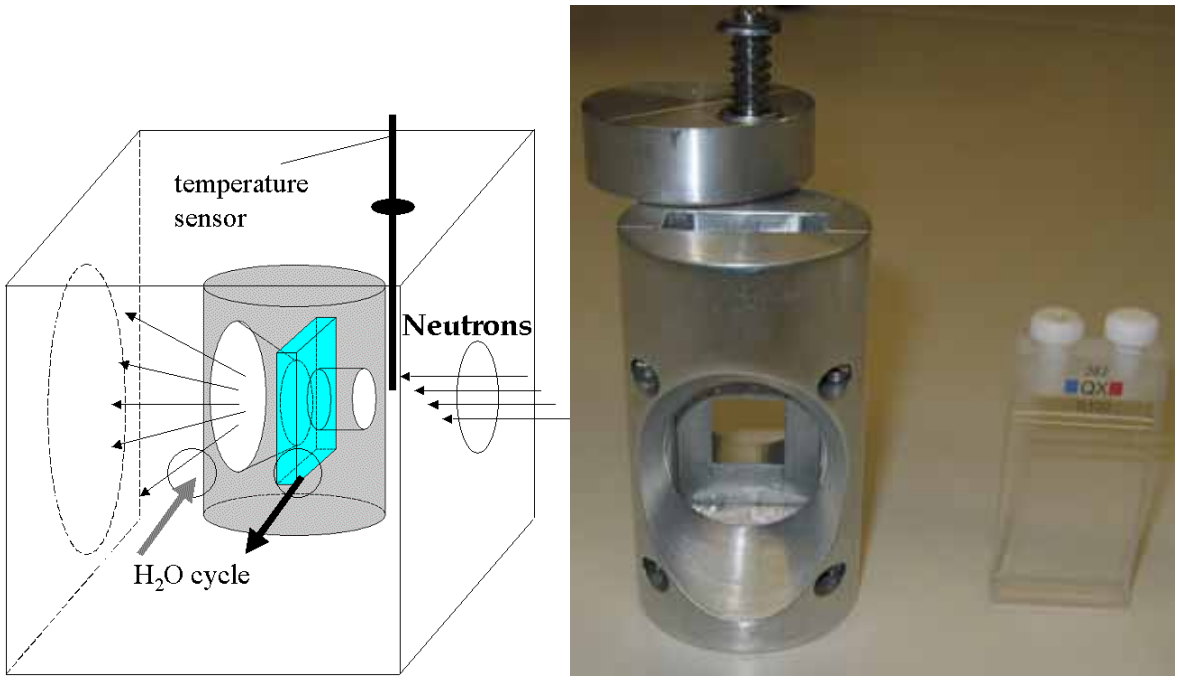

Fig. 10.5.1(2): *left*: schematic depiction of home-build cellholder, where temperature control occurs through a water cycle. The sample is located in a rectangular quartz cell (centre), which in turn is placed in a metal cylinder for good thermal conductivity (grey). The incident neutrons enter the cell from the right. *right*: photo of actual metal cylinder (viewed from downstream) and quartz cell.

10.5.2 SANS Experimental Procedure

Thermal neutrons of wavelength λ=6Å and sample-to-detector distances of d_{sd}=1.1m, 4.5m, 16m and 34m resulted in covering a q-range of approx. 0.001 Å^{-1} to 0.3 Å^{-1}. The neutron beam was collimated by inserting a glass guide at the appropriate guide-to-sample distance (in case of bulk contrast samples d_{gs}=8m, 16.5m, 16.5m and 34m respective to the sample-to-detector distances given prior, while in case of film contrast samples d_{gs}=5.5 m, 8.0m, 16.5m and 34m).

Sample solutions were transferred form 10ml test tubes with pipettes to Hellma cells of synthetic quartz (SUPRASIL) of the QS and QX type with 1mm internal neutron path length after heating them to their isotropic L_3 state in a water bath. Special care needed to be taken to avoid phase separation and thus the possibility to alter ϕ_{B+C} during the fast transfers. During the first set of experiments the cells had an internal width of 9mm, thus making the use of an aperture of diameter d_a=5mm necessary, while during the second this width equalled 18mm, therefore enabling the use of an aperture of d_a=10mm.

This study focuses primarily on monitoring the transition processes between the L_3 and L_α phases. (However, SANS spectra of the respective equilibrium states were also recorded.). These transitions were induced by altering the temperature of water, which streamed through the cell holder, and thus the one of the sample. Temperature equilibration times were on the order of 150s to 250s depending on the amount of the temperature change (ΔT = 1.5 to 3.0°C) and therefore fast enough to not significantly interfere with the phase transition kinetics. Through visual inspection of the initial and final state, it was confirmed that the samples were in the desired one phase region.

The phase transition kinetics were monitored for bulk contrast samples at d_{sd}=34.0m (giving insight into the 0.0016Å < q < 0.0177Å region), while for the film contrast samples the sample-to-detector distance was alternated back and forth between d_{sd}=4.5m and 1.1m (0.0125Å < q < 0.3303Å). Exempt from this was the case of the ϕ_{B+C} = 0.195 bulk sample, where d_{sd}=16.0m (0.0038Å<q<0.0234Å). In order to maximise the time resolution in the TR-SANS experiments, one requires a neutron flux as high as possible and so, the ILL reactor was chosen. In the first set of experiments, spectra with tolerable signal to noise ratios for the bulk contrast samples could be obtained every 120s, as the detector counts per second (cps) varied between 3700 and 4100cps. Therefore, moderate to good time resolution was achieved when regarding processes of time scales from 1000s to 3000s (known from previous NMR experiments). Spectra for film contrast samples were obtained every 50s (d_{sd}=1.1m) and 90s (d_{sd}=4.5m), as the cps were respectively higher, but altering the detector distance took approx. 100s. In the second set, due to using a larger aperture, good signal to noise ratios were achieved when using 120s detection intervals for the ϕ_{B+C}= 0.05, 0.06, and 0.07 samples and counts did not drop below 10000cps. For the ϕ_{B+C}= 0.09 and 0.195 samples the intervals could be reduced to 30s and 10s respectively. In the later case, the use of an attenuator became necessary in order to prevent detector overflow.

10.5.3 Data Processing

In case of isotropic scattering, reduction of the two-dimensional datasets to one-dimensional ones could be achieved by radially averaging the raw data detector counts over all angles with ILL software (*rnils*). The data was then converted to absolute scale via the procedure described in section 8.4 (ILL software: *spolly*). Scattering data for water in the d_{sd}=16.0m and 34.0m cases was extrapolated from the d_{sd}=4.5m result. In case of anisotropic 2D data sets reduction to 1D was more complex. The data of each detector element was first converted to absolute value as described above (ILL software: *anpoly*) and only then radially averaged by regarding sectors where the scattering appeared to be largely isotropic (ILL software: *areg*).

10.5.4 Algorithm

Below follows code of the 'Regression Wizard' of the SigmaPlot program, version 9.0, which fits a plane to a 3D distribution of values. This code was modified through certain constraints and could then be used to determine the linear combination of 2D detector data.

Linear combination

Equation
f=a*x+b*y
fit f to z

Variables
x = col(1) ' {{prevmin: 0.000000}} {{prevmax: 10.000000}}
y = col(2) ' {{prevmin: 0.000000}} {{prevmax: 5.000000}}
z = col(3)
'Automatic Initial Parameter Estimates
F(q;r)=ape(q;r;1;0;1)

Initial Parameters (values are from of a specific fit)
a = F(x;z)[2] "Auto {{previous: 0.138396}}
b = F(y;z)[2] "Auto {{previous: 0.861604}}

Constraints (values are examples of a specific fit)
a>0
a<1
b>0
b<1
a+b=1

11. Tables

The following abbreviations are used in the 'comment' columns or table headers to identify samples or experiments:

- PE = 'preliminary experiments', this refers to NMR experiments that were carried out on the Bruker DMX-200 spectrometer during the first stay in Lund.

- EE = established experiments, this refers to NMR experiments that were carried out on the Varian 360 spectrometer during the second stay in Lund. Note that all established experiments have an experiment number (FT_xx).

- FC = 'film contrast', refers to SANS samples of film contrast composition. Note that the mass given in the '*n*-decane' column refers to fully deuterated *n*-decane ($C_{10}D_{22}$).

- BC = 'bulk contrast', refers to SANS samples of bulk contrast composition.

- VD2 and **VD5** are used to describe sample compositions, i.e. the respective stock solution (see components and stock solutions below) was employed when the sample was produced. Note that the mass given in the 'D_2O' column refers to the mass of the appropriate D_2O/sucrose mixture.

- $\eta_{D2O/S} = \eta_0 \cdot 2.261$ and **$\eta_{D2O/S} = \eta_0 \cdot 4.320$** are employed to indicate experiments which were carried out using samples with increased viscosity of the D_2O component. The former denotation indicated the use of stock solution VD2, the latter VD5.

11.1 Components and Stock Solutions

Tab. T1: densities ρ and molar masses M of components employed (n.r. = not required).

	ρ [g/cm^3]	**M [g/mol]**
H_2O	0.998	18.016
D_2O	1.105	20.028
***n*-decane**	0.730	142.29
***n*-decane (D22)**	0.845	164.42
$C_{12}E_5$	0.967	406.61
Sucrose	n.r.	342.3
D_2O η = 2.828cP	1.1923	n.r.
D_2O η = 5.404cP	1.2379	n.r.
H_2O η = 2.5cP	1.1048	n.r.
H_2O η = 5.0cP	1.1620	n.r.

Tab. T2: composition of sucrose stock solutions. x corresponds to the sucrose molar fraction.

Name	Comment	*m* (H_2O) [g]	*m*(sucrose) [g]	ρ [g/cm^3]	η [cP]	x(sucrose)
VH2	H_2O η = 2.5cP	40.0120	13.5235	1.1048	2.5	0.0175
VH5	H_2O η = 5.0cP	34.9990	20.6796	1.1620	5.0	0.0302
VD2	D_2O η = 2.828cP	20.2976	6.0630	1.1923	2.828	0.0172
VD5	D_2O η = 5.404cP	10.3741	5.3498	1.2379	5.404	0.0293

Tab. T3: stock solutions of *n*-decane/$C_{12}E_5$. Note that stock solution STL3F was prepared using fully deuterated *n*-decane ($C_{10}D_{22}$). ψ correspond to the surfactant mass fraction.

Name	*m* ($C_{12}E_5$) [g]	*m* (*n*-decane) [g]	ρ (decane) [g/cm^3]	ω_b	ψ ($C_{12}E_5$)
STL1	0.2229	0.2046	0.73	0.4513	0.521
STL2	2.0165	1.8621	0.73	0.4498	0.520
STL3F	0.7372	0.7859	0.845	0.4505	0.484
STL4	0.7415	0.6845	0.73	0.4499	0.520
STL5	1.4229	1.3150	0.73	0.4496	0.520

11.2 Phase Diagrams

In tables T4, the data points of the phase boundaries of fig. 2.3(1) and fig. 2.3(2) are given. Phase boundaries for the systems of D_2O with increased viscosity are given in the SANS section (Tab. T16).

Tab. T4.1: phase boundaries of the D_2O – *n*-decane – $C_{12}E_5$ system

ϕ_{B+C}	L_α/L_3+L_α [°C]	L_3+L_α/L_3 [°C]	$L_3/L_1'+L_3$ [°C]
0.0401	36.20	36.70	37.10
0.0499	36.25	36.90	37.25
0.0599	36.30	37.10	37.50
0.0704	–	37.40	37.80
0.0804	36.65	37.52	37.79
0.0897	–	37.70	38.00
0.1005	–	37.80	38.06
0.1096	36.52	37.88	38.19
0.1201	36.96	37.99	38.39
0.1390	37.07	38.42	38.70
0.1952	–	39.00	39.40
0.1961	37.65	38.99	39.39

Tab. T4.2: *Uhrmeister*[46] phase boundaries for the H_2O/NaCl – *n*-decane – $C_{12}E_5$ system *minus* 0.6°C

ϕ_{B+C}	L_α/L_3+L_α [°C]	L_3+L_α/L_3 [°C]	$L_3/L_1'+L_3$ [°C]
0.0881	–	37.78	38.12
0.1169	–	38.02	38.51
0.1457	–	38.40	38.89
0.1741	–	38.65	39.17
0.2023	–	39.07	39.71

Tab. T4.3: phase boundaries of the H_2O – *n*-decane – $C_{12}E_5$ system

ϕ_{B+C}	L_α/L_3+L_α[°C]	L_3+L_α/L_3 [°C]	$L_3/L_1'+L_3$ [°C]
0.0603	38.26	39.16	38.96
0.0801	38.75	39.66	39.45

Tab. T4.4: phase boundaries of the H_2O/sucrose – *n*-decane – $C_{12}E_5$ system (VH2, x=0.0175)

ϕ_{B+C}	L_α/L_3+L_α[°C]	L_3+L_α/L_3 [°C]	$L_3/L_1'+L_3$ [°C]
0.0500	29.49	29.85	30.16
0.0600	29.56	30.15	30.31
0.0700	29.49	30.30	30.46
0.0800	29.56	30.37	30.55
0.0998	29.75	30.45	31.43

Tab. T4.5: phase boundaries of the H_2O/sucrose – *n*-decane – $C_{12}E_5$ system (VH5, x=0.0302)

ϕ_{B+C}	L_α/L_3+L_α [°C]	L_3+L_α/L_3 [°C]	$L_3/L_1'+L_3$ [°C]
0.0597	23.07	23.17	23.26
0.0805	23.17	23.57	23.76
0.1001	23.36	23.96	24.16

11.3 Preliminary NMR Experiments

Tab. T5: compositions and phase boundaries of samples used in the preliminary ^{2}H-NMR experiments (Bruker DMX-200 spectrometer). Samples were prepared with STL1.

ϕ_{B+C}	L_α/L_3+L_α[°C]	L_3+L_α/L_3 [°C]	$L_3/L_1'+L_3$ [°C]	*m* (D_2O)[g]	*m*(*n*-decane) [g]	*m*($C_{12}E_5$) [g]
0.0502	36.20	36.95	37.30	1.7867	0.0341	0.0371
0.0601	36.40	37.25	37.65	1.7770	0.0410	0.0447
0.0702	36.40	37.30	37.90	1.7571	0.0478	0.0521

Tab. T6: negative temperature jump experiments performed in the preliminary ^{2}H-NMR experiments. T_i and T_f are the initial and the final temperatures of the spectrometer respectively. τ is the relaxation time constant. Those times marked with a * correspond to the times of the triple peak moment (TPM). τ_s is the relaxation time constant of the development of the quadrupolar splitting. $\Delta\nu_{Q,L}$ corresponds to the quadrupolar splitting of the steady state lamellar phase.

ϕ_{B+C}	T_i [°C]	T_f [°C]	ΔT [°C]	τ [s]	τ_s [s]	τ_s/τ	$\Delta\nu_{Q,L}$ [Hz]
0.0502	37.1	36.1	-1.0	2900*	–	–	10.77
0.0502	37.1	35.6	-1.5	1080	307	0.28	10.88
0.0502	37.1	35.1	-2.0	390*	–	–	10.90
0.0601	37.5	36.2	-1.3	1750	–	–	12.94
0.0601	37.5	36.0	-1.5	1050	199	0.19	13.24
0.0702	37.3	36.3	-1.0	1750	290	0.17	15.73

Tab. T7: positive temperature jump experiments performed in the preliminary ^{2}H-NMR experiments.

ϕ_{B+C}	T_i [°C]	T_f [°C]	ΔT [°C]	coalescence time [s]
0.0502	36.0	37.1	1.1	303
0.0601	36.3	37.5	1.2	303
0.0601	36.0	37.5	1.5	271
0.0601	35.5	37.5	2.0	300

11.4 Established NMR Experiments

Tab. T8: compositions and phase boundaries of samples used in the established ^{2}H-NMR experiments (Varian 360 spectrometer). Samples were prepared with STL2.

Comment	ϕ_{B+C}	L_α/L_3+L_α [°C]	L_3+L_α/L_3 [°C]	$L_3/L_1'+L_3$ [°C]	$m(D_2O)$ [g]	m(*n*-decane) [g]	$m(C_{12}E_5)$ [g]
–	0.0499	36.25	36.90	37.25	2.3946	0.0948	0.0493
–	0.0599	36.30	37.10	37.50	2.3966	0.1151	0.0598
–	0.0700	–	37.30	37.80	2.0000	0.1135	0.0590
–	0.0795	36.80	37.45	37.90	2.0951	0.1364	0.0709
VD2	0.0598	28.50	29.00	29.35	2.2079	0.0473	0.0513

Tables T9: negative temperature jump experiments performed in the established ^{2}H-NMR experiments. T_2* represent the effective time constants of the transverse relaxation, determined from the width of the steady state sponge (L_3) peak and lamellar (L_α) peaks respectively. See Tab. T6 for further symbol definitions.

Tab. T9.1: negative temperature jump experiments undertaken with the ϕ_{B+C} = 0.06 sample

Exp. No.	T_i [°C]	T_f [°C]	ΔT [°C]	τ [s]	τ_s [s]	τ_s/τ	$\Delta\nu_{Q,L}$ [Hz]	T_2* (L_3) [s]	T_2* (L_α) [s]
FT_03	33.4	31.7	-1.7	720	193	0.27	14.22	0.1634	0.1379
FT_04	33.4	31.7	-1.7	550	201	0.37	13.72	0.2073	0.1744
FT_06	33.4	31.4	-2.0	316*	–	–	13.65	0.2054	0.1915
FT_08	33.4	32.5	-0.9	1720	376	0.22	13.86	0.2045	0.1879
FT_10	33.4	32.5	-0.9	1000	311	0.31	13.79	0.1982	0.1835
FT_12	33.5	31.6	-1.9	510	166	–	13.63	0.2058	0.1947
FT_13	33.5	32.6	-0.9	2270	453	0.20	14.04	0.2113	0.1761
FT_16	33.5	32.4	-1.1	1430	275	0.19	13.59	0.1790	0.1542
FT_17	33.5	32.4	-1.1	1170	229	0.20	13.64	0.1886	0.1669
FT_20	33.5	32.2	-1.3	1120	212	0.19	13.66	0.1785	0.1623
FT_22	33.5	32.0	-1.5	650	205	0.32	13.92	0.1877	0.1720
FT_24	33.5	32.0	-1.5	700	217	0.31	13.55	0.2078	0.1902
FT_26	33.6	32.8	-0.8	2776*	–	–	13.69	0.1849	0.1495
FT_29	33.6	32.8	-0.8	2400	551	0.23	13.63	0.1772	0.1541
FT_31	33.6	32.8	-0.8	2916	–	–	13.59	0.1889	0.1465
FT_32	33.6	32.6	-1.0	1850	343	0.19	13.75	0.2011	0.1468
FT_33	33.6	32.6	-1.0	1700	306	0.18	13.63	0.1963	0.1467

Tab. T9.2: negative temperature jump experiments undertaken with the ϕ_{B+C} = 0.05 sample

Exp. No.	T_i [°C]	T_f [°C]	ΔT [°C]	τ[s]	τ_s [s]	τ_s/τ	$\Delta\nu_{Q,L}$ [Hz]	T_2* (L_3) [s]	T_2* (L_α) [s]
FT_43	33.1	32.2	-0.9	3843*	–	–	10.59	0.1564	0.1198
FT_45	33.0	32.0	-1.0	2203*	–	–	10.77	0.1657	0.1529
FT-47	33.1	32.1	-1.0	1843*	–	–	10.64	0.1606	0.1502
FT_48	33.1	32.1	-1.0	2280	482	0.21	10.62	0.1622	0.1401
FT_50	33.1	31.9	-1.2	2353*	–	–	10.73	0.1667	0.1202
FT_51	33.1	31.6	-1.5	1323*	–	–	10.83	0.1768	0.1509
FT_52	33.1	31.4	-1.7	543*	–	–	10.83	0.1712	0.1611
FT_53	33.1	31.2	-1.9	573*	–	–	10.87	0.1711	0.1630
FT_54	33.1	31.6	-1.5	1150	298	0.26	10.74	0.1671	0.1464
FT_56	33.1	32.0	-1.1	2193*	–	–	10.58	0.1656	0.1490

Tab. T9.3: negative temperature jump experiments undertaken with the ϕ_{B+C} = 0.07 sample

Exp. No.	T_i [°C]	T_f [°C]	ΔT [°C]	τ [s]	τ_s [s]	τ_s/τ	$\Delta\nu_{Q,L}$ [Hz]	T_2* (L_3) [s]	T_2* (L_α) [s]
FT_69	33.8	29.9	-3.9	260*	–	–	15.90	0.1183	–

Tab. T9.4: negative temperature jump experiments undertaken with the ϕ_{B+C} = 0.08 sample

Exp. No.	T_i [°C]	T_f [°C]	ΔT [°C]	τ [s]	τ_s [s]	τ_s/τ	$\Delta\nu_{Q,L}$ [Hz]	T_2* (L_3) [s]	T_2* (L_α) [s]
FT_73	33.9	32.4	-1.5	825*	–	–	–	–	–
FT_75	33.9	32.6	-1.3	950	244	0.26	17.20	0.1850	0.1061

Tab. T9.5: negative temperature jump experiments undertaken with the ϕ_{B+C} = 0.06, $\eta_{D2O/S}$ =η_0·2.261 (VD2) sample. The ** symbol signifies an estimated τ-value.

Exp. No.	T_i [°C]	T_f [°C]	ΔT [°C]	τ [s]	τ_s [s]	τ_s/τ	$\Delta\nu_{Q,L}$ [Hz]	T_2* (L_3) [s]	T_2* (L_α) [s]
FT_77	26.2	24.2	-2.0	1338*	–	–	–	–	–
FT_78	26.2	24.3	-1.9	1450	406	0.28	15.64	0.0580	0.0655
FT_80	26.2	25.1	-1.1	6940**	–	–	–	–	–
FT_82	26.2	24.7	-1.5	2913*	–	–	–	–	–
FT_84	26.2	24.5	-1.7	2673*	–	–	14.96	–	–

Tables T10: positive temperature jump experiments performed in the established ^{2}H-NMR experiments. 'T_2* for P=0'corresponds to the effective time constant of the transverse relaxation determined from the fits of the modified McConnell equation to the steady state lamellar phase doublet.

Tab. T10.1: positive temperature jump experiments undertaken with the ϕ_{B+C} = 0.06 sample.

Exp. No.	T_i [°C]	T_f [°C]	ΔT [°C]	coalescence time [s]	T_2* for P=0
FT_05	31.7	33.4	1.7	291	0.1870
FT_07	31.4	33.4	2.0	368	–
FT_09	32.5	33.4	0.9	273	0.1842
FT_11	32.5	33.4	0.9	338	0.1903
FT_14	32.6	33.5	0.9	228	0.1612
FT_18	32.4	33.5	1.1	265	0.1758
FT_21	32.2	33.5	1.3	288	0.1698
FT_23	32.0	33.5	1.5	313	0.1750
FT_25	32.0	33.5	1.5	265	0.1977
FT_28	32.8	33.6	0.8	240	0.1758
FT_30	32.8	33.6	0.8	215	0.1642
FT_38	32.6	33.6	1.0	192	–
FT_41	32.6	33.6	1.0	209	–

Tab. T10.2: positive temperature jump experiments undertaken with the ϕ_{B+C} = 0.05 sample.

Exp. No.	T_i [°C]	T_f [°C]	ΔT [°C]	coalescence time [s]	T_2* for P=0
FT_44	32.2	33.1	0.9	182	0.1491
FT_46	32.0	33.1	1.1	292	0.1566
FT_49	32.1	33.1	1.0	212	0.1464
FT_55	31.6	33.1	1.5	242	0.1592
FT_58	32.1	33.1	1.0	302	–

Tab. T10.3: positive temperature jump experiments undertaken with the ϕ_{B+C} = 0.06, $\eta_{D2O/S} = \eta_0 \cdot 2.261$ (VD2) sample.

Exp. No.	T_i [°C]	T_f [°C]	ΔT [°C]	coalescence time [s]	T_2* for P=0
FT_79	24.3	26.2	1.9	260	0.0612
FT_81	25.1	26.2	1.1	212	0.0603
FT_83	24.7	26.2	1.5	252	0.0620

Tab. T11: details of temperature jumps, where the nucleation and the growth phase were decoupled (ϕ_{B+C} = 0.06).

Exp. No.	T_i [°C]	T_f [°C]	ΔT [°C]	τ [s]	ΔT_{min} [°C]	$\Delta\nu_{Q,L}$ [Hz]	T_2* (L_α) [s]
FT_36	33.6	32.6	-1.0	950	-2.0	13.48	0.1609
FT_37	33.6	32.6	-1.0	1280	-1.5	13.51	0.1588
FT_39	33.6	32.6	-1.0	1420	-1.5	13.66	0.1514
FT_40	33.6	32.6	-1.0	750	-2.0	13.27	0.1615

Tab. T12: agreement between the time of the TPM and the relaxation time constant τ

Exp. No.	τ [s]	TPM [s]	τ / TPM
FT_03	720	683	1.054
FT_04	550	515	1.068
FT_08	1720	1683	1.022
FT_10	1000	962	1.040
FT_12	510	454	1.123
FT_13	2270	2194	1.035
FT_16	1430	1351	1.058
FT_17	1170	1089	1.074
FT_20	1120	1062	1.055
FT_22	650	602.5	1.079
FT_24	700	682.5	1.026
FT_29	2400	2193	1.094
FT_31	2916	2702	1.079
FT_32	1850	1762	1.050
FT_33	1700	1602.5	1.061
FT_48	2280	2103	1.084
FT_54	1150	1083	1.062

Tab. T13: the relaxation time constants τ, resulting from simulations of the KJMA equation to the developments of the lamellar phase volume fraction φ, match the τ-value determined from a least square *fit* very well.

Exp. No.	Δ*T* [°C]	KJMA α (fit)	τ (fit) [s]	τ/ τ (fit)
FT_03	-1.7	2.739	742	0.97
FT_04	-1.7	2.370	574	0.96
FT_08	-0.9	4.146	1728	1.00
FT_10	-0.9	2.487	1005	1.00
FT_12	-1.9	3.366	520	0.98
FT_13	-0.9	4.789	2274	1.00
FT_16	-1.1	3.937	1433	1.00
FT_17	-1.1	3.457	1182	0.99
FT_20	-1.3	3.656	1134	0.99
FT_22	-1.5	2.669	675	0.96
FT_24	-1.5	2.806	742	0.94
FT_29	-0.8	3.681	2369	1.01
FT_31	-0.8	4.029	2908	1.00
FT_32	-1.0	3.867	1877	0.99
FT_33	-1.0	3.425	1723	0.99

11.5 General NMR Tables

Tab. T14: average quadrupolar splittings of the equilibrium lamellar phases

Comment	ϕ_{B+C}	$\Delta\nu_{Q,L}$ [Hz]	error ± [Hz]
PE	0.0502	10.87	0.2
PE	0.0601	13.17	0.2
PE	0.0702	15.73	0.2
EE	0.0499	10.70	0.12
EE	0.0599	13.69	0.15
EE	0.0700	15.82	0.2
EE	0.0795	17.11	0.2
EE, $\eta_{D2O/S} = \eta_0 \cdot 2.261$	0.0598	15.36	0.2

Tab. T15: n corresponds to the number of MAPA D_2O molecules per surfactant molecule and S_{qn} is an order parameter. $\Delta\nu_Q(\text{max})$ is the quadrupolar splitting which would result in the lamellar phase if only MAPA D_2O would be present. The quantities given below are calculated using n = 5.75, and χ = 255kHz.

Comment	ϕ_{B+C}	$\Delta\nu_{Q,L}$ [Hz]	$n \cdot S_{qn}$	S_{qn}	$\Delta\nu_Q$(max) [Hz]
PE	0.0502	10.87	0.056	0.0097	1847
PE	0.0601	13.17	0.056	0.0097	1849
PE	0.0702	15.73	0.056	0.0098	1872
EE	0.0499	10.70	0.055	0.0096	1836
EE	0.0599	13.69	0.058	0.0101	1936
EE	0.0700	15.82	0.057	0.0099	1893
EE	0.0795	17.11	0.054	0.0093	1785

11.6 SANS Experiments

Tab. T16: compositions and phase boundaries of samples used in the SANS experiments

Comment	ϕ_{B+C}	L_α/L_3+L_α [°C]	L_3+L_α/L_3 [°C]	$L_3/L_1'+L_3$ [°C]	$m(D_2O)$ [g]	m(*n*-decane) [g]	$m(C_{12}E_5)$ [g]
FC, STL3F	0.0500	36.63	37.35	37.42	3.2108	0.0707	0.0664
FC, STL3F	0.0608	36.65	37.57	37.62	3.2104	0.0869	0.0816
FC, STL3F	0.0707	36.80	37.59	37.72	3.1678	0.1008	0.0945
BC, STL4	0.0500	36.25	37.17	37.23	3.2342	0.0616	0.0667
BC, STL4	0.0707	36.40	37.43	37.49	3.1882	0.0877	0.0951
BC,STL4	0.0897	–	37.70	38.00	2.4934	0.0889	0.0962
BC, STL4	0.1952	–	39.00	39.40	2.5393	0.2228	0.2414
BC, STL5	0.0599	37.13	37.37	36.58	1.4925	0.0344	0.0373
BC, STL5, VD2	0.0502	28.90	29.00	28.50	1.5082	0.0268	0.0291
BC, STL5, VD2	0.0603	29.07	29.18	28.64	1.5073	0.0326	0.0353
BC, STL5, VD2	0.0711	29.12	29.20	28.71	1.5035	0.0388	0.0419
BC, STL5, VD5	0.0607	22.99	23.18	22.53	1.5071	0.0316	0.0342

Tab. T17.1:. negative temperature jump experiments with the time *t* until onset of anisotropic scattering.

Comment	ϕ_{B+C}	T_i [°C]	T_f [°C]	ΔT [°C]	*t* aniso. onset [s]	error ± [s]
BC	0.0500	37.31	35.82	-1.5	2766	480
BC	0.0599	37.24	35.75	-1.5	1538	384
BC	0.0707	37.40	35.90	-1.5	1322	360
BC	0.0897	37.85	35.86	-2.0	604	240
BC	0.1952	39.12	37.12	-2.0	–	–
BC	0.1952	39.12	37.11	-2.0	–	–
BC, $\eta_{D2O/S} = \eta_0 \cdot 2.261$	0.0603	29.14	27.64	-1.5	3366	480
BC, $\eta_{D2O/S} = \eta_0 \cdot 2.261$	0.0603	29.12	27.17	-2.0	1442	360
BC, $\eta_{D2O/S} = \eta_0 \cdot 2.261$	0.0603	29.12	26.17	-3.0	600	120
BC, $\eta_{D2O/S} = \eta_0 \cdot 2.261$	0.0711	29.19	27.71	-1.5	2280	360
BC, $\eta_{D2O/S} = \eta_0 \cdot 4.320$	0.0607	23.08	21.60	-1.5	–	–
FC	0.05	37.46	35.96	-1.5	2771	525
FC	0.0608	37.63	36.14	-1.5	1940	340
FC	0.0707	37.73	36.23	-1.5	1165	340

Tab. T17.2: positive temperature jump experiments with the time *t* until the disappearance of anisotropic scattering and the time *t* until *completion* of the phase transition process.

Comment	ϕ_{B+C}	T_i [°C]	T_f [°C]	ΔT [°C]	shaken?	*t* aniso. disappear [s]	error ± [s]	*t* completion [s]	error ± [s]
BC	0.0500	35.78	37.30	1.5	s	481	120	1120	240
BC	0.0599	35.75	37.24	1.5	s	1425	120	1500	140
BC	0.0707	35.90	37.37	1.5	s	481	120	840	120
BC	0.0897	35.86	37.85	2.0	s	332	60	790	90
BC	0.1952	37.12	39.12	2.0	s	–	–	--	--
BC	0.1952	37.11	39.08	2.0	ns	–	–	--	--
BC, $\eta_{D2O/S} = \eta_0 \cdot 2.261$	0.0603	27.64	29.12	1.5	s	602	180	1140	180
BC, $\eta_{D2O/S} = \eta_0 \cdot 2.261$	0.0603	27.17	29.12	2.0	ns	722	180	1140	180
BC, $\eta_{D2O/S} = \eta_0 \cdot 2.261$	0.0711	27.71	29.19	1.5	ns	481	180	1320	180
BC, $\eta_{D2O/S} = \eta_0 \cdot 4.320$	0.0607	21.60	23.14	1.5	ns	–	–		
FC	0.0500	35.96	37.45	1.5	s	238	90	--	--
FC	0.0608	36.14	37.62	1.5	s	239	90	--	--
FC	0.0707	36.23	37.72	1.5	s	240	90	--	--

Tab. T18: q-values of the scattering maximum for the L_3 and L_α equilibrium phase and the corresponding bilayer repeat distances d_3 and d_α(from BC experiments only).

Comment	ϕ_{B+C}	ϕ_c	q (max,L_3) [Å^{-1}]	d_3 [nm]	q (max,L_α) [Å^{-1}]	d_α [nm]	d_3/d_α
–	0.0500	0.0225	0.0026	244	0.0039	159	1.54
–	0.0599	0.0269	0.0034	185	0.0045	140	1.32
–	0.0707	0.0318	0.0040	159	–	–	–
–	0.0897	0.0404	0.0052	120	0.0068	93	1.29
–	0.1952	0.0878	0.0131	48	0.0160	39	1.22
$\eta_{D2O/S} = \eta_0 \cdot 2.261$	0.0603	0.0271	0.0034	185	0.0043	145	1.28
$\eta_{D2O/S} = \eta_0 \cdot 2.261$	0.0711	0.0320	0.0042	151	0.0053	120	1.26
$\eta_{D2O/S} = \eta_0 \cdot 4.320$	0.0607	0.0273	0.0034	185	–	–	–

Tab. T19: scattering lengths *b* of various isotopes

	^{1}H	^{2}H (D)	^{12}C	^{16}O
***b* [10^{-15}m]**	-3.741	6.671	6.6511	5.803

Tab. T20: scattering length densities ρ_s of the components employed

	$\rho_s \cdot 10^{-10}$ [cm^{-2}]
D_2O	6.3895
***n*-decane (H22)**	-0.4879
***n*-decane (D22)**	6.5999
$C_{12}E_5$	0.1297

Tab. T21: fit parameters of the film contrast spectra fits for the equilibrium sponge (L_3) and lamellar phase (L_α), for the three samples studied ($\Delta\rho$ = 6.47·10^{-6} Å^{-2}, a_c=48Å^2, v_c=698Å^3). For the same system, *Uhrmeister*[46] determined ε = 24.3, t = 5.85 and σ = 7.3.

	L_3	L_α	L_3	L_α	L_3	L_α
ϕ_{B+C}	0.0500	0.0500	0.0608	0.0608	0.0707	0.0707
$\phi_{C,i}$	0.0225	0.0225	0.0274	0.0274	0.0318	0.0318
f	0.60	0.55	0.60	0.60	0.60	0.45
t	5.9	6.2	5.9	5.9	5.9	5.9
ε	25.6	25.6	25.6	25.6	25.6	25.6
σ	7.1	6.9	7.0	7.0	7.2	7.2
I_{incoh}	0.072	0.070	0.072	0.072	0.080	0.080

Tab. T22: NMR *completion* times for negative temperature jump experiments

Comment	ϕ_{B+C}	ΔT [°C]	*t* completion [s]	error ± [s]
PE	0.0502	-1.5	1840	200
PE	0.0601	-1.5	1480	100
FT_54	0.0499	-1.5	2100	200
FT_22	0.0599	-1.5	1200	100
FT_24	0.0599	-1.5	1200	100
FT_77	0.0598	-2.0	2300	250
FT_82	0.0598	-1.5	4500	500

Tab. T23: NMR *completion* times for positive temperature jump experiments

Comment	ϕ_{B+C}	ΔT [°C]	*t* completion [s]	error ± [s]
PE	0.0601	1.5	600	100
FT_55	0.0499	1.5	1000	200
FT_25	0.0599	1.5	877	100
FT_83	0.0598	1.5	1200	200
FT_79	0.0598	2.0	1200	100

12. References

[1] C. E. Fairhurst, S. Fuller, J. H. Gray, M.C. , and G. J. T. Tiddy, in *Handbook of liquid crystals*, edited by J. Goodby, G. W. Gray, H. W. Spiess, V. Vill, and D. Demus (Wiley-VCH, 1998), Vol. 3, pp. 341.

[2] M. C. Holmes and M. S. Leaver, in *Phase transitions in complex fluids*, edited by P. Tole´dano and A. M. Figueiredo Neto (World Scientific, 1998).

[3] S. Hyde, S. Andersson, K. Larsson, Z. Blum, T. Landh, S. Lidin, and B. W. Ninham, *The Language of Shape. The role of curvature in condensed matter: physics, chemistry and biology*. (Elsevier Science B.V., 1997).

[4] D. F. Evans and H. Wennerstoem, *The colloidal domain: where physics, chemistry and biology meet*, second ed. (Wiley-VCH, 1999).

[5] A. S. Kabalnov, A. V. Pertzov, and E. D. Shchukin, Journal of Colloid and Interface Science **118** (2), 590 (1987).

[6] A. S. Kabalnov, K. N. Makarov, A. V. Pertzov, and E. D. Shchukin, Journal of Colloid and Interface Science **138** (1), 98 (1990).

[7] P. A. Winsor, *Solvent properties of amphiphilic compounds*. (Butterworth, London, 1954).

[8] L. M. Prince, *Microemulsions*. (Academic Press, New York, 1977).

[9] M. Kahlweit, R. Strey, and G. Busse, J. Phys. Chem. **94** (10), 3881 (1990).

[10] M. Kahlweit and R. Strey, Angewandte Chemie International Edition in English **24** (8), 654 (1985).

[11] M. Kahlweit, R. Strey, and G. Busse, Physical Review E **47** (6), 4197 LP (1993).

[12] J. M. Seddon, A. Squires, O. Ces, R. H. Templer, J. Woenckhaus, and R. Winter, in *Self-Assembly*, edited by B. H. Robinson (IOS Press, Amsterdam, 2003), pp. 212.

[13] P. Laggner and M. Kriechbaum, Chemistry and Physics of Lipids **57**, 121 (1991).

[14] K. TAINAKA and Y. I. Y, EUROPHYSICS LETTERS **15** (4), 399 (1991).

[15] P. White and J. Powell, Bulletin of Mathematical Biology **59** (4), 609 (1997).

[16] A. M. van der Bliek, J. Cell Biol. **151** (2), 1F (2000).

[17] X. Li and S. J. Gould, J. Biol. Chem. **278** (19), 17012 (2003).

[18] L. V. Chernomordik, V. A. Frolov, E. Leikina, P. Bronk, and J. Zimmerberg, J. Cell Biol. **140**, 1369 (1998).

[19] L. V. Chernomordik, G. B. Melikyan, and Y. A. Chizmadzhev, Biochim. Biophys. Acta **906**, 309 (1987).

[20] G. W. Kemble, T. Danieli, and J. M. White, Cell **76**, 383 (1994).

[21] G. B. Melikyan, J. M. White, and F. S. Cohen, J. Cell Biol. **131**, 679 (1995).

[22] G. B. Melikyan, W. D. Niles, V. A. Ratinov, M. Karhanek, J. Zimmerberg, and F. S. Cohen, J. Gen. Physiol. **106**, 803 (1995).

[23] J. Zimmerberg, R. Blumenthal, D. P. Sarkar, M. Curran, and S. J. Morris, J. Cell Biol. **127**, 1885 (1994).

[24] A. F. Smeijers, A. J. Markvoort, K. Pieterse, and P. A. J. Hilbers, JOURNAL OF PHYSICAL CHEMISTRY B **110** (26), 13212 (2006).

[25] D. Anderson, H. Wennerstroem, and U. Olsson, Journal of Physical Chemistry **93** (10), 4243 (1989).

[26] R. Strey, R. Schomäcker, D. Roux, F. Nallet, and U. Olsson, J. Chem. Soc., Faraday Trans. **86** (12), 2253 (1990).

[27] G. Porte, J. Phys. Cond. Matter **4** (45), 8649 (1992).

[28] B. Balinov, U. Olsson, and O. Söderman, Journal of Physical Chemistry **95** (15), 5931 (1991).

[29] R. Strey, W. Jahn, G. Porte, and P. Basserau, Langmuir **6**, 1635 (1990).

[30] I. Carlsson and H. Wennerström, Langmuir **15**, 1966 (1999).
[31] T. D. Le, U. Olsson, H. Wennerström, and P. Schurtenberger, Phys. Rev. E **60** (4), 4300 (1999).
[32] M. Buchanan, L. Starrs, S. U. Egelhaaf, and M. E. Cates, Phys. Rev. E **62** (5), 6895 (2000).
[33] Y. Iwashita and H. Tanaka, Physical Review Letters **95**, 047801 (2005).
[34] C. Schmidt and H. W. Spiess, in *Handbook of Liquid Crystals*, edited by D. Demus, J. W. Goodby, G. W. Gray, H. W. Spiess, and V. Vill (Wiley-VCH, Weinheim, 1998), Vol. 1, pp. 595.
[35] A. Fischer, H. Hoffmann, P. Medick, and E. Rössler, J. Phys. Chem. B **106**, 6821 (2002).
[36] D. J. Mitchell, G. J. T. Tiddy, L. Waring, T. Bostock, and M. P. McDonald, Journal of Chemical Society. Faraday Transactions **79**, 975 (1983).
[37] U. Olsson, P. Ström, O. Söderman, and H. Wennerstöm, Journal of Physical Chemistry **93** (11), 4572 (1989).
[38] J. C. Lang and R. D. Morgan, Journal of Chemical Physics **73** (11), 5849 (1980).
[39] K. Fukuda, U. Olsson, and U. Würz, Langmuir **10** (9), 3222 (1994).
[40] M. Jonströmer and R. Strey, J. Phys. Chem. **96**, 5993 (1992).
[41] C. L. Sassen, L. M. Filemon, T. W. d. Loos, and J. d. S. Arons, J. Phys. Chem. **93**, 6511 (1989).
[42] M. Kahlweit and R. Strey, Angew. Chem. **97**, 655 (1985).
[43] M. Leaver, U. Olsson, H. Wennerström, R. Strey, and U. Würz, J. Chem. Soc., Faraday Trans. **91** (23), 4269 (1995).
[44] R. Strey, W. Jahn, M. Skouri, J. Marignan, G. Porte, and U. Olsson, *Structure, Dynamics of Strongly Interacting Colloids*. (Kluwer, Amsterdam, 1992).
[45] A. Wehling, *The dynamics of L_3 phases*. (Cuvillier Verlag, Göttingen, 2001).
[46] P. Uhrmeister, *Inaugural-Dissertation, Selbstorganisierende Netzwerke in Mikroemulsionen*. (Cuvillier Verlag, Köln, 2002).
[47] U. Olsson and P. Schurtenberger, Langmuir **9**, 3389 (1993).
[48] M. Kahlweit, R. Strey, P. Firman, D. Haase, J. Jen, and R. Schomäcker, Langmuir **4** (3), 499 (1988).
[49] M. Kahlweit, R. Strey, R. Schomäcker, and D. Haase, Langmuir **5** (2), 305 (1989).
[50] P. Firman, D. Haase, J. Jen, M. Kahlweit, and R. Strey, Langmuir **1** (6), 718 (1985).
[51] W. Helfrich, Z. Naturforsch. **28C**, 693 (1973).
[52] P. G. Nilsson and B. Lindman, J. Phys. Chem. **87**, 4756 (1983).
[53] G. J. T. Tiddy, Phys. Rep. **57**, 1 (1980).
[54] G. L. Squires, *Introduction to Theory of Neutron Scattering*. (Cambridge University Press, Cambridge, 1978).
[55] R. Strey, Colloid & Polymer Science **272** (8), 1005 (1994).
[56] T. Sottmann and R. Strey, in *Fundamentals of interface and colloid science*, edited by J. Lyklema (Elsevier Academic Press, 2005), Vol. V Soft Colloids.
[57] G. Porte, M. Delsanti, I. Billard, M. Skouri, J. Appell, J. Marigan, and F. Debeauvais, J. Phys. II France **1**, 1101 (1991).
[58] M. Skouri, J. Marignan, J. Appell, and G. Porte, J. Phys. II France **1**, 1121 (1991).
[59] D. C. Morse, Phys. Rev. E **50**, R2423 (1994).
[60] D. L. Gibbons, M. C. Vaney, A. Roussel, A. Vigouroux, B. Reilly, J. Lepault, M. Kielian, and F. A. Rey, Nature **427**, 320 (2004).
[61] R. Jahn, T. Lang, and T. C. Sudhof, Cell **112**, 519 (2003).
[62] Y. Kozlovsky and M. M. Kozlov, Biophys. J. **82**, 882 (2002).
[63] V. S. Markin and J. P. Albanes, Biophys. J. **82**, 693 (2002).
[64] M. M. Kozlov and V. S. Markin, Biofizika. **28**, 255 (1983).

[65] V. S. Markin, M. M. Kozlov, and V. L. Borovjagin, Gen. Physiol. Biophys. **3**, 361 (1984).
[66] L. Yang and H. W. Huang, Science **297**, 1877 (2002).
[67] L. Yang and H. W. Huang, Biophys. J. **84**, 1808 (2003).
[68] P. Sens and S. A. Safran, Europhys. Lett. **43**, 95 (1998).
[69] C. Quilliet, C. Blanc, and M. Kleman, Phys. Rev. Lett. **77**, 522 (1996).
[70] O. D. Lavrentovich, C. Quilliet, and M. Kléman, J. Phys. Chem. B **101**, 420 (1997).
[71] D. P. Siegel, Biophys. J. **65**, 2124 (1993).
[72] T. D. Le, U. Olsson, H. Wennerström, P. Uhrmeister, B. Rathke, and R. Strey, J. Phys. Chem. B **106** (36), 9410 (2002).
[73] D. Anderson, U. Olsson, and H. Wennerström, J. Phys. Chem. **93**, 4243 (1989).
[74] D. Kashchiev, *Nucleation Basic Theory with Applications*. (Butterworth-Heinemann, 2000).
[75] P. G. Debenedetti, *Metastable Liquids: Concepts and Principles*. (Princeton University Press, Princeton, New Jersey, 1996).
[76] A. Kolmogorov, Bull. Acad. Sci. URSS (Sci. Mat. Nat.) **3**, 355 (1937).
[77] W. A. Johnson and P. A. Mehl, Trans. Am. Inst. Mining and Metallugical Engineers **135**, 416 (1939).
[78] M. Avrami, J. Chem. Phys. **7**, 1103 (1939).
[79] M. Avrami, J. Chem. Phys. **8**, 212 (1940).
[80] M. Avrami, J. Chem. Phys. **9**, 177 (1941).
[81] K. Avramova, Cryst. Res. Technol. **37** (5), 491 (2002).
[82] A. Abragam, *The Principles of Nuclear Magnetism*. (Oxford University Press, London, 1961).
[83] P. W. Atkins, *Physikalische Chemie*, 2nd ed. (VCH, Weinheim, 1996).
[84] P. T. Callaghan, *Principles of Nuclear Magnetic Resonance Microscopy*. (Oxford University Press, New York, 1991).
[85] A. Carrington and A. D. McLachlan, *Introduction to Magnetic Resonance*. (Harper & Row, New York, 1967).
[86] R. K. Harris, *Nuclear Magnetic Resonance Spectroscopy*. (Pitman Books Ltd., London, 1983).
[87] S. W. Homans, *A Dictionary of Concepts in NMR*. (Clarendon Press, Oxford, 1989).
[88] N. Bloembergen, E. M. Purcell, and R. V. Pound, Phys. Rev. **73** (1948).
[89] K. Rendall, G. J. T. Tiddy, and M. A. Trevethan, Journal of Colloid and Interface Science **98** (2), 565 (1984).
[90] N.-O. Persson and B. Lindman, Journal of Physical Chemistry **79** (14), 1410 (1975).
[91] H. M. McConnell, J. Chem. Phys. **28**, 430 (1958).
[92] J.-i. Fukasawa, C.-D. Poon, and E. T. Samulski, Langmuir **7**, 1727 (1991).
[93] K. Rendall and G. J. T. Tiddy, J. Chem. Soc., Faraday Trans. 1 **80**, 3339 (1984).
[94] H. Wennerström, N.-O. Persson, and B. Lindman, Am. Chem. Soc., Symp. Ser. **9**, 253 (1975).
[95] J. Grandjean and P. Laszlo, in *Dynamics of Solutions and Fluid Mixtures by NMR*, edited by J.-J. Delpuech (Wiley, Chichester, 1995), pp. 232.
[96] R. P. W. J. Struis, J. d. Bleijser, and J. C. Leyte, J. Phys. Chem. **91**, 1639 (1987).
[97] M. Gotter, R. Strey, U. Olsson, and H. Wennerström, Faraday Discuss. **129**, 327 (2005).
[98] H. Wennerström, personal communication.
[99] G. Gompper and D. M. Kroll, Phys. Rev. Lett. **81**, 2284 (1998).
[100] D. Dunmur and K. Tariyama, in *Handbook of Liquid Crystals*, edited by D. Demus, J. W. Goodby, G. W. Gray, H. W. Spiess, and V. Vill (Wiley-VCH, Weinheim, 1998), Vol. 1, pp. 204.

[101] L. M. Blinov, in *Handbook of Liquid Crystals*, edited by D. Demus, J. W. Goodby, G. W. Gray, H. W. Spiess, and V. Vill (Wiley-VCH, Weinheim, 1998), Vol. 1, pp. 477.

[102] B. J. Forrest and L. W. Reeves, Chem. Rev. **81** (1), 1 (1981).

[103] C. R. S. II, J. E. Schaff, and J. H. Prestegard, Biophys. J. **64**, 1069 (1993).

[104] P. Ram and J. H. Prestegard, Biochim. Biophys. Acta **940**, 289 (1988).

[105] C. Rosenblatt, Phys. Rev. A **24**, 2236 (1981).

[106] D. Capitani, C. Casieri, G. Briganti, C. L. Mesa, and A. L. Segre, J. Phys. Chem. B **103**, 6088 (1999).

[107] G. Briganti, A. L. Segre, D. Capitani, C. Casieri, and C. L. Mesa, J. Phys. Chem. B **103**, 825 (1999).

[108] L. Peliti, in *Fluctuating Geometries in Statistical Mechanics and Field Theory*, edited by F. David, P. Ginsparg, and Z. Zinn-Justin (Elsevier, 1996), pp. 195.

[109] W. Helfrich, Z. Naturforsch. **33A**, 305 (1978).

[110] L. Golubovic, Phys. Rev. E **50**, 2419 (1994).

[111] E. Meirovitch and J. H. Freed, Chem. Phys. Lett. **64**, 311 (1979).

[112] S. W. Lovesey, *Theory of Neutron Scattering from Condensed Matter: Nuclear Scattering*. (Clarendon, Oxford, 1984).

[113] W. Massa, *Kristallstrukturbestimmung*, 2. ed. (Teubner, Stuttgart, 1996).

[114] G. Porte, J. Appell, P. Bassereau, and J. Marignan, J. Phys. France **50**, 1335 (1989).

[115] R. Strey, J. Winkler, and L. Magid, J. Phys. Chem. **95**, 7502 (1991).

[116] G. Porod, edited by O. Glatter and O. Kratky (Academic Press, New York, 1982).

[117] T. D. Le, U. Olsson, K. Mortensen, J. Zipfel, and W. Richtering, Langmuir **17** (4), 999 (2001).

[118] M. Bergmeier, M. Gradzielski, H. Hoffmann, and K. Mortensen, J. Phys. Chem. B **103**, 1605 (1999).

[119] H. Leitao, M. M. T. d. Gama, and R. Strey, J. Chem. Phys. **108** (10), 4189 (1998).

[120] F. Nallet, D. Roux, and S. T. Milner, J. Phys. France **51**, 2333 (1990).

[121] S. T. Milner, S. A. Safran, D. Andelman, M. E. Cates, and D. Roux, J. Phys. France **49**, 1065 (1988).

[122] http://www.iff.fr/YellowBook/D11/

Erklärung:

Ich versichere, dass ich die von mir vorgelegte Dissertation selbständig angefertigt, die benutzten Quellen und Hilfsmittel vollständig angegeben und die Stellen der Arbeit - einschließlich Tabellen und Abbildungen -, die anderen Werken im Wortlaut oder dem Sinn nach entnommen sind, in jedem Einzelfall als Entlehnung kenntlich gemacht habe; dass diese Dissertation noch keiner anderen Fakultät oder Universität zur Prüfung vorgelegen hat; dass sie, abgesehen von unten angegebenen Teilpublikationen, noch nicht veröffentlich worden ist sowie, dass ich eine solche Veröffentlichung vor Abschluss des Promotionsverfahrens nicht vornehmen werde. Die Bestimmungen der Promotionsordnung sind mir bekannt. Die von mir vorgelegte Dissertation ist von Prof. Dr. R. Strey betreut worden.

Köln, den 13. November 2006

Teilpublikationen:

M. Gotter, R. Strey, U. Olsson, H. Wennerström, "Fusion and fission of fluid amphiphilic bilayers", *Faraday Discuss.*, **129**, 327 (2005)

M. Gotter, T. Sottmann, R. Strey, U. Olsson, H. Wennerström, "Monitoring of sponge (L_3) and lamellar phase (L_α) formation kinetics: An investigation of fluid amphiphilic bilayer fusion and fission", *Proceedings of the 33. Topical Meeting on Liquid Crystals*, Paderborn, (2005)